Arctic Sea Ice in Tide Models

Vasulkar, A.N.

DOI
10.4233/uuid:5e4ec5d2-0a70-4b53-ba33-11ffccbfadab

Publication date
2024

Document Version
Final published version

Citation (APA)
Vasulkar, A. N. (2024). *Arctic Sea Ice in Tide Models*. [Dissertation (TU Delft), Delft University of Technology]. https://doi.org/10.4233/uuid:5e4ec5d2-0a70-4b53-ba33-11ffccbfadab

Arctic Sea Ice in Tide Models

Amey N.Vasulkar

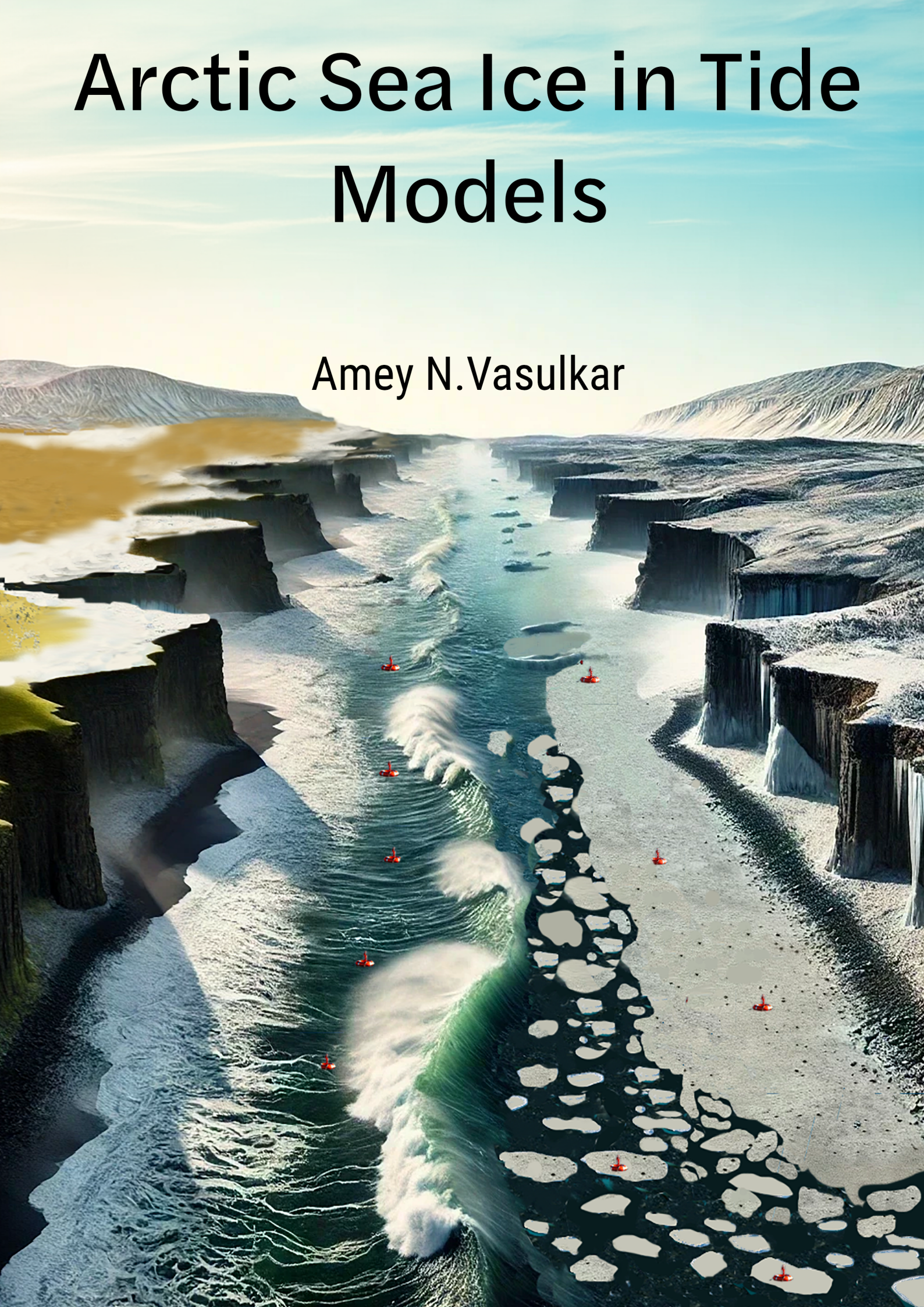

ARCTIC SEA ICE IN TIDE MODELS

ARCTIC SEA ICE IN TIDE MODELS

Dissertation

for the purpose of obtaining the degree of doctor
at Delft University of Technology
by the authority of the Rector Magnificus, prof. dr. ir. T.H.J.J. van der Hagen,
chair of the Board for Doctorates
to be defended publicly on
Thursday 19 September 2024 at 12:30 o'clock

by

Amey Nandkumar VASULKAR

MSc. Applied Mathematics, Delft University of Technology, the Netherlands,
MSc. Scientific Computing, Technical University of Berlin, Germany,
born in Pune, India

This dissertation has been approved by the promotors.

Composition of the doctoral committee:

Rector Magnificus	chairperson
Prof. dr. ir. M. Verlaan	Delft University of Technology, *promotor*
Dr. ir. D.C. Slobbe	Delft University of Technology, *copromotor*
Prof. dr. ing. R. Klees	Delft University of Technology, *promotor*
Independent members:	
Prof. dr. J. D. Pietrzak	Delft University of Technology
Prof. dr. R. S. W. van de Wal	Utrecht University
Prof. dr. H. M. Schuttelaars	Delft University of Technology
Dr. ir. P. B. Smit	Sofar Ocean Technologies, USA
Prof. dr. ir. A. W. Heemink	Delft University of Technology, reserve member

Keywords: Global Ocean Tide Models, Ice-Ocean Dissipation Parameterization, Sea Ice Oscillations, Optimization, Free Drift Sea Ice, Tidal Frequency Shift

Printed by: https://www.proefschriftspecialist.nl/ on 100% recycled paper.

Cover by: Cumulative effort where the base image is generated through prompting DALL-E followed by manual edits from Sharayu Kore, and the cover layout by Sneha Gokhale

ISBN 978-94-6366-918-4
EAN/ISBN 978-94-6366-927-6

An electronic copy of this dissertation is available at
https://repository.tudelft.nl/.

आतां अज्ञान अवघे हरपें |
विज्ञान निःशेष करपें |
आणि ज्ञान ते स्वरूपें |
होऊनि जाईजे ||

.....

Now, let all ignorance be destroyed,
Let knowledge eliminate all that remains,
And let one become,
The very form of wisdom itself.

Dnyaneshwari, Chapter 7 Verse 7

SUMMARY

Climate change is causing rapid transformations in the Arctic, most notably the significant decline in sea ice cover. As Arctic sea ice recedes at an alarming rate, it has become increasingly evident that these changes have far-reaching implications across various domains.

This thesis embarks on an evaluation of one such domain, the relationship between Arctic sea ice and global tides, addressing a critical gap in existing global hydrodynamic tidal models. Global models currently do not account for tidal energy dissipation due to sea ice, nor do they consider the impact of variations in sea ice cover on tides. Seasonal variations in sea ice cover are known to modulate tides due to ice-water frictional dissipation, and the ongoing decline in sea ice due to climate change further highlights the need for accurate modeling of this dissipation. Global tidal models play a crucial role in many fields, including but not limited to navigation and coastal flood management. The importance of global tidal models further underscores the need for an efficient parametrization to account for sea ice-induced tidal dissipation. This led to the first research objective of this thesis: to develop a physically consistent parameterization for modelling sea ice-induced dissipation in barotropic global tide models.

Chapter 2 discusses the physics of air-ice-ocean interactions to model the dissipation while addressing the challenges in acquiring accurate sea ice drift velocities on tidal time scales. A parametric method is introduced to incorporate sea ice dissipation into tidal modelling without direct coupling to a sea ice model. In this approach, the dissipation from the three sea ice regimes: landfast ice, drifting sea ice with internal stresses, and free-drift sea ice is modelled separately. Notably, this chapter reveals that the landfast sea ice can have a significant influence on the seasonal modulation of the M_2 tide going upto 0.25 m in regions like the Hudson Bay. This emphasizes the need for further research on the long-term effects of declining Arctic sea ice.

In chapter 3, we assess the dissipation of tides caused by free drift sea ice. In deep and open ocean areas without wind influence, this dissipation is negligible. However, for shallow water regions like the Spitzbergen Shelf this dissipation is unknown. We analyse this dissipation using a beacon dataset and a physics-based ice model in the Barents Sea region. The findings suggest that the dissipation from free drift sea ice is negligible (2-3% of the bottom frictional stress) under the low wind conditions.

The details of the new parameteric approach to model the dissipation of tidal energy from sea ice is given in Chapter 4. This new approach divides the sea ice cover into regions dominated by either Vertical Shear (VS) or Horizontal Shear (HS) energy dissipation, based on a non-dimensional Friction Number (F) that depends on sea ice thickness and concentration. Performance assessment using the seasonal modulation of the M_2 tidal component was done by comparing to observations from altimetry and tide gauges. It is seen that the new parameterization has larger correlation (0.6) with the altimetry-

data than the current state-of-the-art methods (0.4). As compared to tide gauge observations, the new parameterization has lower differences for all the tide gauges compared to the current state-of-the-art approache. This improved parameterization is more suitable to study the impact of sea ice (and its decline) on tides due to its consideration of sea ice thickness and concentration which is absent in the current state-of-the-art approaches.

During the development of this approach, a significant limitation emerged due to the absence of accurate and time-specific observations of tidal currents or tidal water levels in the Arctic region. Consequently, we explored the potential of GNSS buoy data as a new source of information on tidal currents. As a response, our second research objective was to formulate a method for deriving tidal current constituents from GNSS buoy data in the Arctic. This led to the development of a novel method, termed the 'Model-derived fitting method', detailed in Chapter 5.

Traditional methods for tidal harmonic analysis prove insufficient in the complex Arctic environment characterized by spatial and temporal variations in tidal amplitudes and phases and the presence of sea ice. The proposed method is evaluated through case studies in the Barents Sea, Chukchi Sea, and Baffin Bay, demonstrating its accuracy, robustness, and operational capabilities. It includes comparisons with model values and mooring observations, which confirms its effectiveness in estimating tidal currents, especially in regions with dominant barotropic or baroclinic tidal currents. Furthermore, the study reveals a phase shift observed by the buoy data due to the mean flow of the buoy, similar to Doppler shift effects, particularly in baroclinic tide regions.

The thesis successfully achieved the research objectives by addressing critical questions related to impact of sea ice on tides, introducing innovative parameterizations, and exploring new data sources for tidal current estimation. The thesis advances our understanding of Arctic tidal dynamics and water-ice interactions. It provides valuable insights and tools for future research and practical applications in the Arctic region.

SAMENVATTING

Klimaatverandering veroorzaakt snelle veranderingen in het Noordpoolgebied, met name de aanzienlijke afname van de zee-ijsbedekking. Nu het zee-ijs in het Noordpoolgebied in een alarmerend tempo smelt, wordt het steeds duidelijker dat deze veranderingen grote gevolgen hebben.

Globale getijmodellen houden momenteel geen rekening met de dissipatie van getijenergie door zee-ijs, noch met de invloed van variaties in zee-ijs. Het is bekend dat seizoensgebonden variaties in zee-ijsbedekking het getij kan veranderen door energie dissipatie als gevolg van wrijving tussen ijs en water. De voortdurende afname van zee-ijs als gevolg van klimaatverandering benadrukt de noodzaak van nauwkeurige modellering van dit effect. Globale getij modellen spelen een cruciale rol in de scheepvaartsector en overstromingsbeheer. Dit leidde tot het eerste onderzoeksdoel van dit proefschrift: het ontwikkelen van een fysisch consistente parameterisatie voor het modelleren van zee-ijs geïnduceerde dissipatie in barotrope modellen voor globaal getij.

Hoofdstuk 2 bespreekt de fysica van lucht-ijs-oceaan interacties die nodig zijn om de dissipatie te kunnen modelleren. Verder worden de uitdagingen in het verkrijgen van nauwkeurige drijfsnelheden van zee-ijs besproken. Er wordt een parametrische methode geïntroduceerd om de dissipatie van zee-ijs op te nemen in getijdenmodellering zonder directe koppeling met een zee-ijsmodel. Hierbij beschrijven we de dissipatie van de drie zee-ijsregimes: landijs, drijvend zee-ijs met interne spanningen en vrij drijvend zee-ijs. Dit hoofdstuk onthult met name dat het vasteland ijs een significante invloed kan hebben op de seizoensgebonden modulatie van het M_2 getij tot 0.25 m in regio's zoals in de Hudsonbaai. Dit benadrukt de noodzaak voor verder onderzoek naar de langetermijneffecten van afnemend Arctisch zee-ijs.

In hoofdstuk 3 beschrijven we de dissipatie van getij veroorzaakt door vrij drijvend zee-ijs. In diepe en open oceaangebieden zonder windinvloed is deze dissipatie verwaarloosbaar. Voor gebieden met ondiep water, zoals de Spitsbergen continentaal plat, was deze dissipatie echter onbekend. We analyseerden deze dissipatie met behulp van een baken dataset en een natuurkundig ijsmodel van het Barentszzeegebied. De bevindingen suggereren dat de dissipatie van vrij drijfijs verwaarloosbaar is (2-3% van de bodemwrijvingsspanning) in de perioden met weinig wind.

De details van de nieuwe parameterbenadering voor het modelleren van de dissipatie van getijdenenergie door zee-ijs worden beschreven in hoofdstuk 4. Deze nieuwe benadering verdeelt de zee-ijs gebieden in gebieden die worden gedomineerd door ofwel verticale schuifspanning (VS) of horizontale schuifspanning (HS), gebaseerd op een niet-dimensionaal wrijvingsgetal (F) dat afhankelijk is van de dikte en concentratie van het zee-ijs. De seizoensgebonden modulatie van de M_2 getijcomponent hebben we vergeleken met waterstandsmetingen en altimetrie.

Het blijkt dat de nieuwe parameterisatie een grotere correlatie (0,6) heeft met de al-

timetrie gegevens dan de huidige geavanceerde methoden (0,4). De vergelijking met metingen liet zien dat de nieuwe parameterisatie lagere verschillen voor alle getijdemetingen dan de huidige state-of-the-art benadering. De parameterisatie die wij hebben geïntroduceerd is beter omdat rekening wordt gehouden met de dikte en concentratie van zee-ijs in tegenstelling tot de huidige methoden.

Tijdens de ontwikkeling van deze parameterisatie kwam een belangrijke beperking naar voren, namelijk de afwezigheid van nauwkeurige en tijd specifieke waarnemingen van getijdenstromingen en waterstanden in het Noordpoolgebied. Daarom onderzochten we het potentieel van GNSS-boeigegevens als een nieuwe bron van informatie over getijdenstromingen. Het tweede onderzoeksdoel was daarom het ontwikkelen van een methode voor het afleiden van getijstroomcomponenten uit GNSS-boeigegevens in het Noordpoolgebied. De nieuwe methode, genaamd de 'Model-derived fitting method', wordt beschreven in hoofdstuk 5

Traditionele methoden voor harmonische getijanalyse blijken ontoereikend in de complexe Arctische omgeving die wordt gekenmerkt door grote ruimtelijke en temporele variatie. De voorgestelde methode is geëvalueerd aan de hand van casestudies in de Barentszzee, de Tsjoektsjenzee en de Baffinbaai. Deze studies lieten de nauwkeurigheid, robuustheid en operationele mogelijkheden van de methode zien. Vergelijkingen met modelwaarden en meetwaarnemingen lieten de effectiviteit van de methode zien voor het schatten van getijdenstromingen, vooral in regio's met dominante barotrope of baroklinische stromingen. Verder vonden we een faseverschuiving in de boei data als gevolg van de gemiddelde stroming van de boei, vergelijkbaar met dopplerverschuivingseffecten, vooral in baroklinische getijdengebieden.

In deze dissertatie zijn de onderzoeksdoelen met succes bereikt met betrekking tot de invloed van zee-ijs op getijden, de introductie van innovatieve parameterisaties, en het onderzoeken van nieuwe schattingen van getijdenstromingen. Het proefschrift bevordert ons begrip van de getijdendynamiek in het Noordpoolgebied en de interacties tussen water en ijs. Het biedt waardevolle inzichten en hulpmiddelen voor toekomstig onderzoek en praktische toepassingen in het Noordpoolgebied.

1

INTRODUCTION

Since 1979, satellite data shows that the Arctic sea ice extent has decreased by approximately 13% per decade relative to the 1981-2010 average.

Source: NSIDC/NOAA

1

1.1. BACKGROUND

1.1.1. INFLUENCE OF SEA ICE ON GLOBAL TIDES

Global operational hydrodynamic tidal models currently do not account for the dissipation of tidal energy due to sea ice, which occurs through frictional shear stress at the ice-water interface (Sverdrup, 1927; Kleptsova & Pietrzak, 2018). These models also overlook the impact of variations in sea ice cover on tides, including both seasonal variations and the long-term decline in sea ice cover.

Seasonal variation in sea ice cover, particularly between winter and summer, is known to cause significant modulation of tides due to ice-water frictional dissipation (e.g., St-Laurent et al., 2008; Müller et al., 2014; Kagan and Sofina, 2010). In their analysis of the seasonal modulation of the M_2 tidal constituent, St-Laurent et al., 2008 identified modulation as the differences between the winter (March) and summer (September) values. Their findings highlight a considerable amplitude modulation of up to ±0.15 m in regions like the Foxe Basin and Eastern Hudson Bay, where summer amplitudes range from 0.6 to 0.8 m.

Climate change has contributed to a continuous decline in sea ice cover, with current summer Arctic sea ice extent shrinking by 12.2% per decade (U.S. National Ice Center, 2020) (see Figure 1.1). The Intergovernmental Panel on Climate Change (IPCC)'s Special Report on Global Warming of 1.5°C (Hoegh-Guldberg et al., 2018) projects persistent Arctic warming, leading to a further declining sea ice.

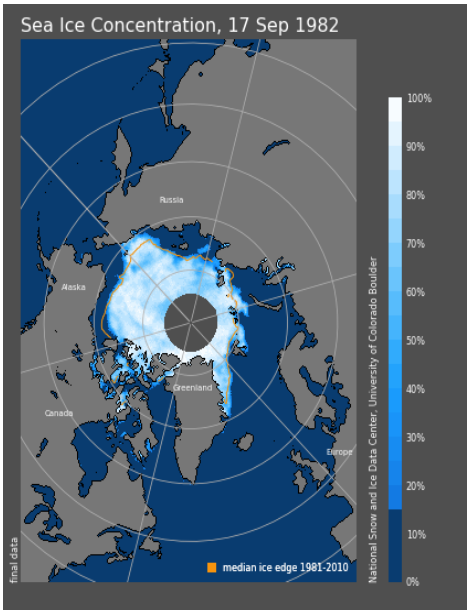

(a) Summer Sea ice extent in 1982

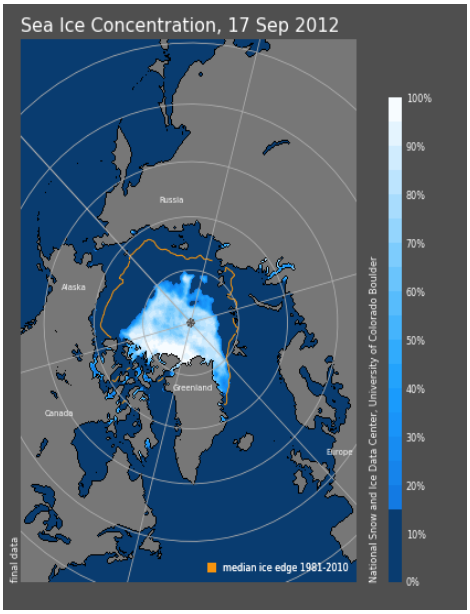

(b) Summer Sea ice extent in 2012

Figure 1.1.: Summer sea ice extent in the Arctic Ocean in September 1982 and 2012. September 2012 has the lowest summer sea ice extent on record. Source: National Snow and Ice Data Center (NSIDC)

The decline of sea ice implies reduced dissipation of tidal energy, potentially resulting in larger tidal amplitudes reaching the shore (Pickering et al., 2017). The global effects of declining sea ice on tides are unknown, and no studies have specifically focused on this issue, as global tidal models do not account for sea ice-induced dissipation. However, various regional studies in the Arctic (e.g. Kleptsova and Pietrzak, 2018; Kowalik, 1981; Murty and Polavarapu, 1979; Rotermund et al., 2021, among others) have documented changes in local tides due to ice-water friction from ice cover.

Previously, the modulation of tides by sea ice, through dissipation, was considered less significant than other errors in global models, and thus, often overlooked (Kleptsova & Pietrzak, 2018; Rotermund et al., 2021). However, these models have improved considerably over the past few decades, owing to advancements in both modelling techniques and data assimilation from satellite altimetry and tide gauges (Stammer et al., 2014). As such, the sea ice-induced dissipation of tides is no longer negligible and needs to be included in global operational tide-surge models.

The integration of sea ice-induced dissipation into tidal models is anticipated to not only refine global tidal predictions but also to gain an in-depth understanding of both the long-term trends and seasonal variations in sea ice on global tides. As we progress towards enhancing the accuracy and comprehensiveness of global tidal models, we are naturally led to acknowledge their fundamental importance.

1.1.2. IMPORTANCE OF GLOBAL TIDAL MODELS

Global hydrodynamic tidal models are indispensable for a broad spectrum of applications including navigation, shipping, coastal engineering, ecological health management, and flood risk assessment.

These models are particularly crucial for coastal flood management and early warning systems (Horsburgh et al., 2017), providing the accurate predictions necessary for effective marine and coastal planning.

Coastal flooding poses a growing threat to coastal communities worldwide (Jonkman, 2005), driven by a combination of sea level rise, storm surges, and tides. The impact of this threat is expected to be further exacerbated by climate change in the future (Paz & Negro, 2011). Data from the National Oceanic and Atmospheric Administration (NOAA) (National Oceanic & Administration, 2018) indicates an increase in coastal flooding days in the U.S. over the past decade. This is particularly noticeable on the east coast (Figure 1.2) and is attributed to climate change.

Furthermore, global hydrodynamic tidal models are also used to correct for tides in high-resolution global ocean general circulation and tide models with assimilation from satellite altimetry (Arbic, 2022). Inaccuracies in tidal estimates from tidal models can affect ocean forecasts' accuracy.

Given the wide ranging applications, producing accurate estimations from global tidal models is paramount. Addressing this need, it is essential to model the dissipation from sea ice on tides (Samaras & Karambas, 2021), a significant yet often overlooked factor in global tidal behaviour.

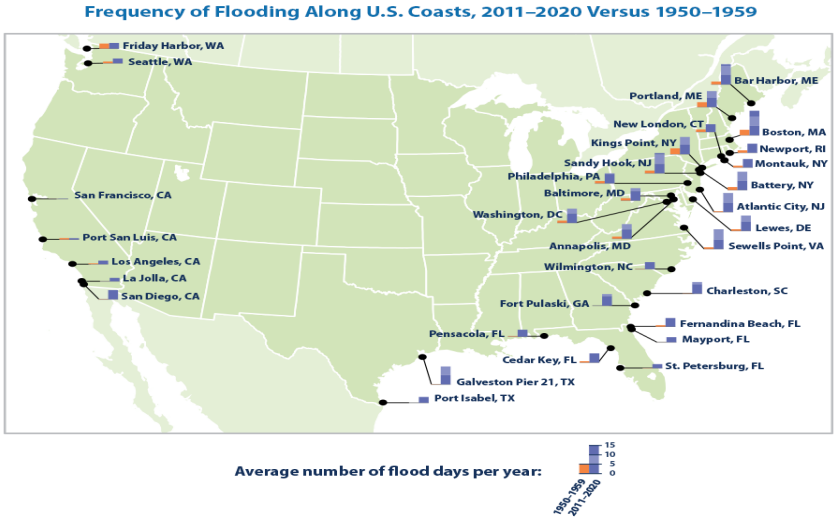

Figure 1.2.: Comparison between two decades (1950-59 and 2011-20) of the average number of flood days per year along U.S. Coasts. Source: NOAA

1.2. PREVIOUS WORK

Global hydrodynamic tide models require an accurate and physically-consistent representation of sea ice-water dissipation. Validation and calibration against observational data are essential to ensure the accuracy and reliability of these models.

1.2.1. SEA ICE MATERIAL AND DYNAMICS

Understanding sea ice material and dynamics is fundamental for accurately modelling sea ice-induced dissipation. Arctic sea ice is not a single solid mass; instead, it comprises numerous smaller pieces. This sea ice landscape features various elements, including leads, deformed ice, and ice floes (see Leppäranta, 2011a). On a scale, typically between 10 m and 100 m, the solid sea ice lid becomes destabilized and fractures into smaller pieces known as ice floes (Leppäranta, 2011b). However, our study focuses on the impact of Arctic-wide sea ice, which exists on a much larger spatial scale, typically covering areas around ~ 1000 km. In such large-scale studies, the continuum scale of sea ice, namely the ice field, is considered, rather than individual ice floes. Therefore, from this point on, all references to sea ice will refer to a sea ice field. These ice fields can be broadly classified into 3 subcategories based on their dynamics, as illustrated in Figure 1.3. These categories include:

- **Landfast ice:** Sea ice that remains fastened to the coast, over shoals or between grounded ice bergs. This ice is immobile and sometimes also referred to as *fast ice*
- **Drift Ice:** Sea ice that is floating on the ocean surface and moving under the influence of wind and ocean currents. This category broadly encompasses all sea ice that is *not landfast*. A drift ice field can be further divided into two sub-categories:
  - *Free drift ice:* A drifting sea ice field where the internal stresses in the field are negligible compared to the external forces implying the internal stresses having no impact on the drift of the ice field.
  - *Drift ice with strong internal stresses:* A drifting sea ice field where the internal stresses in the field are significant compared to the external forces having an impact on the drift of the ice field.

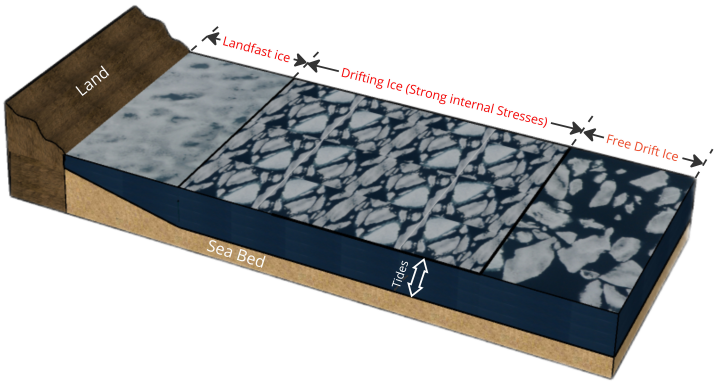

Figure 1.3.: Schematic of sea ice division.

The drift of sea ice can be effectively modelled using sea ice drift equations, which are derived from Newton's second law with the continuum mechanics assumption of an ice field (Leppäranta, 2011c). This field experiences internal stress due to interactions among various ice floes and is modelled by knowing the sea ice field's rheology (Leppäranta, 2011d).

1.2.2. CURRENT STATE-OF-THE-ART MODELLING APPROACHES

Dissipation between sea ice and water depends on the relative velocity between them (McPhee, 1982; Pease et al., 1983). Evaluating this requires inputs of sea ice velocities influenced by tides and storm surges on a tidal time scale. However, many sea ice models typically omit tidal forcing (Heil & Hibler, 2002), and remote sensing products only provide mean total velocities on daily to monthly scales.

Thoroughly and accurately accounting for sea ice-induced dissipation necessitates the use of a 3D global coupled ocean tide-sea ice model, such as STORMTIDE (Müller et al., 2014) or HYCOM (Arbic et al., 2010). These models are suitable for runs on smaller time scales while becoming computationally prohibitive for longer runs like climatology. The computational costs also limit their operational use for coastal warning systems.

Most of the current operational 2D global hydrodynamic tidal models, including FES2014 (Lyard et al., 2021) and Global Tide and Storm Surge Model (GTSM) (Verlaan et al., 2015), either partially or completely neglect the interaction between sea ice and tides. Sea ice models often exhibit numerical instabilities which necessitate case-by-case resolution to achieve convergence (Cheng, 2002). Integrating these challenging sea ice models with 2D tidal operational models is not an option due to the relatively high resolution of the tidal models which are built with computational efficiency in mind (Wang & Bernier, 2023).

To overcome these challenges, recent regional Arctic tidal models (e.g. (Kleptsova & Pietrzak, 2018; Cancet et al., 2016)), have partially accounted for the sea ice-tide dissipation by using mean monthly sea ice cover, with all sea ice treated as landfast ice. In this approach, the ice-friction stress is modelled similarly to the existing bottom frictional stress, but, with a drag coefficient resembling the ice-water interface.

1.2.3. AVAILABLE OBSERVATIONS FOR MODEL VALIDATION AND CALIBRATION

Seasonal modulation of tides is evaluated as March-September differences in the tidal amplitudes and phases. Observations of this modulation can serve as a metric for calibrating or validating models that consider sea ice-induced dissipation. Tidal water level constituents from tide gauges and satellite altimetry provide crucial data for this purpose.

In the Arctic, the tidal constituent datasets from Kowalik and Proshutinsky, 1994 and ArcTiCA (Hart-Davis et al., 2023) are among the most comprehensive datasets derived from tide gauge measurements. However, these datasets do not include seasonal modulation of tidal constituents and are limited by constituents derived from historical data back to the 1800s.

Regional datasets from the Canadian Arctic region (Fisheries and Ocean Canada-MEDS, 2019) and the Russian Arctic (Kulikov et al., 2020) (Figure 1.4) provide seasonal modulation for the M_2 tide, but they also have limitations. Some rely on historical data, while others lack specific references to the year of data collection.

Altimetry data from the TOPEX/Poseidon and Jason series of satellites are widely used to obtain tidal constituent estimates, as seen in works like EOT20 (Hart-Davis et al., 2021), TPX09 (Egbert & Erofeeva, 2002), and X-TRACK (Birol et al., 2017). However, these satellites do not cover the polar regions, reaching only up to $\pm 66^\circ$ latitudes. In the last decade, SAR altimetry missions like CryoSat-2 (Wingham et al., 2006) and Sentinel-3 (Donlon et al., 2012) have provided Arctic altimetry data, extending up to 88°N. Bij de Vaate et al., 2021 utilised data from these missions to compile a dataset of the seasonal modulation of the M_2 tide in the Arctic. Although

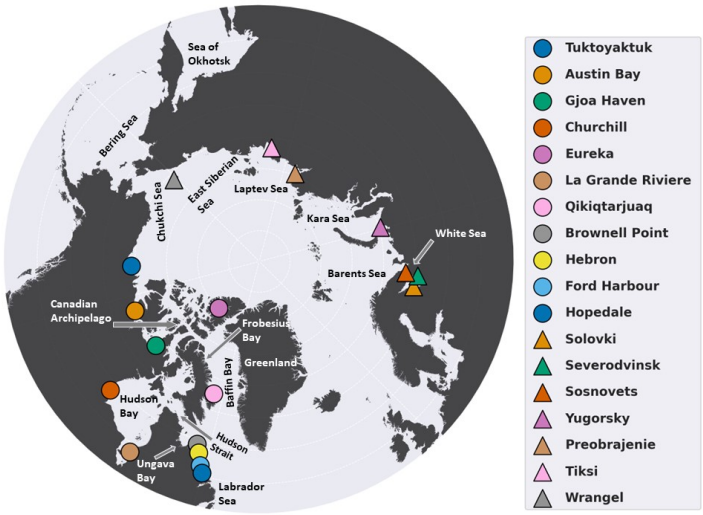

Figure 1.4.: Tidge gauge locations with their respective names in the legend. The dots represent tide gauges from Fisheries and Ocean Canada-MEDS, 2019 and triangles represent tide gauges from Kulikov et al., 2020.

valuable for model validation, it's important to note that this seasonal modulation is an average over the years of the satellite missions, rather than specific to any single year.

Despite their limitations, these two datasets–the tide gauges (Figure 1.4) and the altimetry-derived product from Bij de Vaate et al., 2021– are the only available resources for validation and calibration in the Arctic. There are challenges in installing new tide gauges in the remote Arctic conditions, as highlighted by Ray, 2016.

1.3. MOTIVATION

1.3.1. UNDERSTANDING THE DYNAMICS OF SEA ICE-TIDE DISSIPATION

The current state-of-the-art modelling approach has two main limitations. Firstly, it assumes a fixed sea ice cover with sea ice velocities set to zero. This assumption leads to an overestimation of dissipation compared to the actual dissipation when the sea ice is drifting. Given that the average maximum extent of landfast ice in a year is just 12% of the total Northern Hemisphere wintertime sea ice cover (Mahoney, 2018), the overestimation of dissipation can lead to a larger tidal dampening. Secondly, this approach does not consider the physics of interaction between drifting sea ice and tides, thus omitting sea ice parameters such as thickness and concentration which are important for ice drift response to winds and tides (e.g. Heil and Hibler, 2002).

Sea ice fields can be categorized into three types: Landfast, free drift, and drifting with strong internal stresses, each interacting with tides differently. Landfast sea

ice is the extremum case which is straightforward to implement using the bottom frictional stress. However, free drift and drifting ice with strong internal stresses present more complex modelling challenges.

In free drift sea ice, the absence of wind and internal stresses results in identical velocities for both ice and water (McPhee, 1978). This analysis, primarily conducted in deep and open ocean contexts, leaves uncertainties regarding sea ice-tide dissipation in shallow water regions and in presence of winds.

While, drifting sea ice with strong internal stresses exhibits velocities influenced by these stresses, alongside external forces such as winds and tidal currents (Leppäranta, 2011c). The resulting relative velocity between sea ice and tides necessitates a representation of internal stresses to assess dissipation accurately.

Moreover, wind presence alters the movement of sea ice drift relative to ocean-tide currents (McPhee, 1978). Heil and Hibler, 2002 tackled this complexity by developing a boundary layer-embedded model for sea ice drift, which was later coupled with a barotropic ocean model. While comprehensive, this coupled model faces significant computational challenges. In the absence of wind, sea ice and ocean-tide currents typically move in parallel, albeit at different velocities. Therefore, our focus is modelling on scenarios without wind influence, specifically the tidal dissipation from drifting sea ice under strong internal stresses.

1.3.2. ENHANCING ARCTIC TIDE MODELS WITH BUOY DATA

The lack of sufficient datasets in the Arctic for calibrating and validating tidal models underscores the need to explore alternative data sources. Global Navigation Satellite System (GNSS) buoy drifter data and its derived ocean and tidal velocities have been available globally, excluding the Arctic, for a couple of decades (Poulain & Centurioni, 2015). Recently, Arctic buoy data has become publicly accessible through programs like the International Arctic Buoy Programme (IABP) and expeditions such as MOSAiC (Bliss et al., 2022). These buoys, capable of tracking surface ocean currents with temporal sampling as frequent as every 15 min, are well-suited for observing tidal currents. Tidal current constituent estimates derived from these buoys offer an additional resource for calibrating and validating tidal models.

The challenge in deriving tidal current constituent estimates from buoy-tracked surface currents lies in their dynamic nature. The movement of buoy in space means that traditional tidal harmonic analysis techniques, which assume static measurement points, are not directly applicable due to spatial and temporal variations in amplitudes and phases. Recent studies (Poulain & Centurioni, 2015; Kodaira et al., 2016) have modified traditional tidal harmonic analysis and incorporating averaging techniques to extract tidal current constituents from buoy data. However, their methods are more suitable for barotropic tidal estimates and do not fully address the unique challenges posed by the Arctic region. For instance, the presence of sea ice restricts buoy data availability, hence, accurate estimates are needed from single buoy trajectories. Moreover, there are large baroclinic regions in the Arctic with significant spatio-temporal variability in the tidal constituents of Arctic currents (Baumann et al., 2020). These issues render the averaging approach of the above studies inapplicable in the Arctic. Consequently, there is a pressing

need in the Arctic for methodologies capable of deriving tidal constituents from buoy-tracked tidal currents. These methods must be applicable to both barotropic and baroclinic regions and account for variations in amplitude and phase along single buoy trajectories.

1.4. AIM AND RESEARCH QUESTIONS

The objective of this thesis is twofold: First, to develop a physically-consistent parametrization for the ice-water frictional stress that can be used in barotropic global tide models without modelling tide resolving currents in a 3D coupled ice-ocean model framework; and second, to devise a method for deriving tidal constituents from GNSS buoy data in the Arctic, thereby introducing a new data source for the calibration and validation of tidal models.

For the first objective, the analysis will utilize the Global Tide and Storm Surge Model (GTSM) (Verlaan et al., 2015) developed by Deltares, with a particular focus on the seasonal modulation of the M_2 tidal constituent. The following research questions will be answered:

1. **What is the extent and magnitude of the impact of seasonal variations in landfast sea ice on the model-derived seasonal modulation of M_2 tide in the Arctic, and what are the implications for tides away from the landfast ice?**
   To investigate the impact of landfast sea ice on tides, we acquired the landfast sea ice configurations for winter and summer from a dataset provided by National Snow and Ice Data Center (NSIDC) for the years 2013 and 2017. The dissipation from landfast ice was implemented in GTSM. Subsequently, the seasonal modulation of the M_2 tide was computed as the difference between March and September amplitudes and phases to reveal the influence of landfast ice.

2. **How significant is the tidal dissipation from free drift sea ice field on tides under the presence of varying wind speeds and in shallow water regions?**
   The impact of tidal dissipation from free drift sea ice fields under varying wind conditions and in shallow water regions was evaluated using a GNSS buoy dataset. This dataset had buoys drifting in the tidally dominant Spitsbergen Shelf region. The buoy trajectories showed oscillatory loops indicative of tidal current influences. A physics-based point ice model was developed to systematically examine tidal dissipation characteristics from free drift ice under different wind speed scenarios.

3. **To what extent can the dissipation from all three categories of Arctic sea ice–Landfast, free drift, and drift under strong internal stresses–on tides be accurately modelled with the new physically-consistent parameterization?**
   The three categories: Landfast, free drift and drifting sea ice with strong internal stresses have different dissipation characteristics. To model them in a physically-consistent and accurate way a new parameterization was developed to model the dissipation from all forms of sea ice in a tidal model. Departing from the traditional three categories, we divided the sea ice field into two

regimes: Vertical Shear (VS) and Horizontal Shear (HS). VS represents the dissipation arising from the relative velocity between sea ice and tides, where the sea ice velocity is approximately 0. On the other hand, HS accounts for the dissipation resulting from the shear due to internal stresses in the sea ice field. The performance of this new parameterization was evaluated by computing the seasonal modulation of the M_2 tide and comparing to altimetry-derived product Bij de Vaate et al., 2021 and tide gauge output (Figure1.4)

4. **How can tidal harmonic constituents of tidal currents be obtained from single buoy trajectories, accounting for the spatial and temporal variations in amplitude and phase along these trajectories? What is the validity of the resulting method in estimating tidal currents in both barotropic and baroclinic regions?**
   We derived a method for conducting tidal harmonic analysis on the buoy-derived tidal velocities. This method accounts for the space-time variation in the amplitudes and phases along a single buoy trajectory. The estimates of the method are validated using buoys in 3 different regions: the Barents Sea, Chukchi Sea (both barotropic) and Baffin Bay (baroclinic).

1.5. OUTLINE OF THE THESIS

In Chapter 2, we describe the GTSM, including its governing equations and the drift equations of sea ice along with its challenges and our approach to modelling the sea ice in tidal models. Following this, we provide results with the landfast ice implementation in GTSM and answer research question 1. Chapters 3, 4, and 5 focus on research questions 2, 3, and 4, respectively. Finally, we summarize the conclusions of this thesis and provide recommendations for future work.

REFERENCES

Sverdrup, H. U. (1927). Dynamics of tides on the North Siberian Shelf. *Geofys. Publr.*, *4*, 1–75.

Kleptsova, O., & Pietrzak, J. D. (2018). High resolution tidal model of Canadian Arctic Archipelago, Baffin and Hudson Bay. *Ocean Modelling*, *128*, 15–47. https://doi.org/10.1016/j.ocemod.2018.06.001

St-Laurent, P., Saucier, F. J., & Dumais, J. F. (2008). On the modification of tides in a seasonally ice-covered sea. *Journal of Geophysical Research: Oceans*, *113*(C11), 11014. https://doi.org/10.1029/2007JC004614

Müller, M., Cherniawsky, J. Y., Foreman, M. G., & Von Storch, J. S. (2014). Seasonal variation of the M 2 tide. *Ocean Dynamics*, *64*(2), 159–177. https://doi.org/10.1007/s10236-013-0679-0

Kagan, B. A., & Sofina, E. V. (2010). Ice-induced seasonal variability of tidal constants in the Arctic Ocean. *Continental Shelf Research*, *30*(6), 643–647. https://doi.org/10.1016/J.CSR.2009.05.010

U.S. National Ice Center. (2020). U.S. National Ice Center Arctic and Antarctic Sea Ice Concentration and Climatologies in Gridded Format, Version 1 [G10033]. https://doi.org/https://doi.org/10.7265/46cc-3952

Hoegh-Guldberg, O., Jacob, D., Taylor, M., Bindi, M., Brown, S., Camilloni, I., Diedhiou, A., Djalante, R., Ebi, K. L., Engelbrecht, F., Guiot, J., Hijioka, Y., Mehrotra, S., Payne, A., Seneviratne, S. I., Thomas, A., Warren, R., & Zhou, G. (2018). Impacts of 1.5žC Global Warming on Natural and Human Systems. An IPCC Special Report. In V. Masson-Delmotte, P. Zhai, H.-O. Pörtner, D. Roberts, J. Skea, P. R. Shukla, A. Pirani, W. Moufouma-Okia, C. Péan, R. Pidcock, S. Connors, J. B. R. Matthews, Y. Chen, X. Zhou, M. I. Gomis, E. Lonnoy, T. Maycock, M. Tignor & T. Waterfield (Eds.). Cambridge University Press. https://doi.org/10.1017/9781009157940.005

Pickering, M. D., Horsburgh, K. J., Blundell, J. R., Hirschi, J. J., Nicholls, R. J., Verlaan, M., & Wells, N. C. (2017). The impact of future sea-level rise on the global tides. *Continental Shelf Research*, *142*, 50–68. https://doi.org/10.1016/J.CSR.2017.02.004

Kowalik, Z. (1981). A Study of the M-2 Tide in the Ice-Covered Arctic Ocean. *Modeling, Identification and Control: A Norwegian Research Bulletin*, *2*(4), 201–223. https://doi.org/10.4173/mic.1981.4.2

Murty, T. S., & Polavarapu, R. J. (1979). Influence of an ice layer on the propagation of long waves. *Marine Geodesy*, *2*(2), 99–125. https://doi.org/10.1080/15210607909379342

Rotermund, L. M., Williams, W. J., Klymak, J. M., Wu, Y., Scharien, R. K., & Haas, C. (2021). The Effect of Sea Ice on Tidal Propagation in the Kitikmeot Sea,

Canadian Arctic Archipelago. *Journal of Geophysical Research: Oceans*, *126*(5), e2020JC016786. https://doi.org/10.1029/2020JC016786

Stammer, D., Ray, R. D., Andersen, O. B., Arbic, B. K., Bosch, W., Carrère, L., Cheng, Y., Chinn, D. S., Dushaw, B. D., Egbert, G. D., Erofeeva, S. Y., Fok, H. S., Green, J. A. M., Griffiths, S., King, M. A., Lapin, V., Lemoine, F. G., Luthcke, S. B., Lyard, F., … Yi, Y. (2014). Accuracy assessment of global barotropic ocean tide models. *Reviews of Geophysics*, *52*(3), 243–282. https://doi.org/10.1002/2014RG000450

Horsburgh, K., Losada, I., Vousdoukas, M., Weisse, R., & Wolf, J. (2017). Hydrological Risk: Wave Action, Storm Surge and Coastal Flooding. In K. Poljanek, M. Marín Ferrer, T. De Groeve & I. Clark (Eds.), *Science for disaster risk management 2017: Knowing better and losing less*. Publications Office of the European Union. https://doi.org/10.2788/688605

Jonkman, S. N. (2005). Global perspectives on loss of human life caused by floods. *Natural Hazards*, *34*(2), 151–175. https://doi.org/10.1007/S11069-004-8891-3/METRICS

Paz, R., & Negro, V. (2011). Urban Coastal Flooding and Climate Change. *Journal of Coastal Research-ICS2011 (Proceedings)*.

National Oceanic & Administration, A. (2018). *Patterns and Projections of High Tide Flooding along the US coastline using a common impact threshold* (tech. rep.). NOAA Technical Report NOS CO-OPS 086. https://tidesandcurrents.noaa.gov/publications/techrpt86_PaP_of_HTFlooding.pdf

Arbic, B. K. (2022). Incorporating tides and internal gravity waves within global ocean general circulation models: A review. *Progress in Oceanography*, *206*, 102824. https://doi.org/10.1016/J.POCEAN.2022.102824

Samaras, A. G., & Karambas, T. V. (2021). Modelling the Impact of Climate Change on Coastal Flooding: Implications for Coastal Structures Design. *Journal of Marine Science and Engineering*, *9*(9). https://doi.org/10.3390/JMSE9091008

Leppäranta, M. (2011a). Drift ice material. *The Drift of Sea Ice*, 11–63. https://doi.org/10.1007/978-3-642-04683-4{_}2

Leppäranta, M. (2011b). Introduction. *The Drift of Sea Ice*, 1–9. https://doi.org/10.1007/978-3-642-04683-4{_}1

Leppäranta, M. (2011c). Equation of drift ice motion. *The Drift of Sea Ice*, 143–184. https://doi.org/10.1007/978-3-642-04683-4{_}5

Leppäranta, M. (2011d). Sea ice rheology. *The Drift of Sea Ice*, 107–141. https://doi.org/10.1007/978-3-642-04683-4{_}4

McPhee, M. G. (1982). *Sea ice drag laws and simple boundary layer concepts, including application to rapid melting* (Report 82-4). United States Army Cold Regions Research; Engineering Laboratory.

Pease, C. H., Salo, S. A., & Overland, J. E. (1983). Drag measurements for first-year sea ice over a shallow sea. *Journal of Geophysical Research*, *88*(C5), 2853. https://doi.org/10.1029/JC088iC05p02853

Heil, P., & Hibler, W. D. (2002). Modeling the High-Frequency Component of Arctic Sea Ice Drift and Deformation. *Journal of Physical Oceanography*, *32*(11), 3039–3057. https://doi.org/10.1175/1520-0485(2002)032<3039:MTHFCO>2.0.CO;2

Arbic, B. K., Wallcraft, A. J., & Metzger, E. J. (2010). Concurrent simulation of the eddying general circulation and tides in a global ocean model. *Ocean Modelling*, *32*(3-4), 175–187. https://doi.org/10.1016/j.ocemod.2010.01.007

Lyard, F. H., Allain, D. J., Cancet, M., Carrère, L., & Picot, N. (2021). FES2014 global ocean tide atlas: Design and performance. *Ocean Science*, *17*(3), 615–649. https://doi.org/10.5194/OS-17-615-2021

Verlaan, M., De Kleermaeker, S., & Buckman, L. (2015). GLOSSIS: Global storm surge forecasting and information system. *Australasian Coasts & Ports Conference 2015: 22nd Australasian Coastal and Ocean Engineering Conference and the 15th Australasian Port and Harbour Conference*, 229–234.

Cheng, B. (2002). On the numerical resolution in a thermodynamic sea-ice model. *Journal of Glaciology*, *48*(161), 301–311. https://doi.org/10.3189/172756502781831449

Wang, P., & Bernier, N. B. (2023). Adding sea ice effects to a global operational model (NEMO v3.6) for forecasting total water level: approach and impact. *Geoscientific Model Development*, *16*(11), 3335–3354. https://doi.org/10.5194/gmd-16-3335-2023

Cancet, M., Andersen, O., Lyard, F., Shulz, A., Cotton, P., & Benveniste, J. (2016). A New High Resolution Tidal Model in the Arctic Ocean. *Living Planet Symposium*, 67. https://ui.adsabs.harvard.edu/abs/2016ESASP.740E..67C

Kowalik, Z., & Proshutinsky, A. Y. (1994). The Arctic Ocean Tides. American Geophysical Union (AGU). https://doi.org/10.1029/gm085p0137

Hart-Davis, M., Howard, S., Ray, R., Andersen, O., Padman, L., Nilsen, F., & Dettmering, D. (2023). Arctic Tidal Constituent Atlas (ArcTiCA): A database of tide elevation constituents for the Arctic region from 1800 through present day. https://doi.org/10.18739/A2D795C4N

Fisheries and Ocean Canada-MEDS. (2019). Canadian Tides and Water Levels Data Archive. https://tides.gc.ca/tides/en/stations

Kulikov, M. E., Medvedev, I. P., & Kondrin, A. T. (2020). Features of Seasonal Variability of Tidal Sea-level Oscillations in the Russian Arctic Seas. *Russian Meteorology and Hydrology*, *45*(6), 411–421. https://doi.org/10.3103/S1068373920060047/FIGURES/3

Hart-Davis, M., Dettmering, D., Piccioni, G., Schwatke, C., Passaro, M., & Seitz, F. (2021). EOT20: A new global empirical ocean tide model derived from multi-mission satellite altimetry. *The EGU General Assembly*. https://doi.org/10.5194/EGUSPHERE-EGU21-2037

Egbert, G. D., & Erofeeva, S. Y. (2002). Efficient Inverse Modeling of Barotropic Ocean Tides. *Journal of Atmospheric and Oceanic Technology*, *19*(2), 183–204. https://doi.org/https://doi.org/10.1175/1520-0426(2002)019<0183:EIMOBO>2.0.CO;2

Birol, F., Fuller, N., Lyard, F., Cancet, M., Niño, F., Delebecque, C., Fleury, S., Toublanc, F., Melet, A., Saraceno, M., & Léger, F. (2017). Coastal applications from nadir altimetry: Example of the X-TRACK regional products. *Advances in Space Research*, *59*(4), 936–953. https://doi.org/10.1016/J.ASR.2016.11.005

Wingham, D. J., Francis, C. R., Baker, S., Bouzinac, C., Brockley, D., Cullen, R., de Chateau-Thierry, P., Laxon, S. W., Mallow, U., Mavrocordatos, C., Phalippou, L., Ratier, G., Rey, L., Rostan, F., Viau, P., & Wallis, D. W. (2006). CryoSat: A mission to determine the fluctuations in Earths land and marine ice fields. *Advances in Space Research*, *37*(4), 841–871. https://doi.org/10.1016/J.ASR.2005.07.027

Donlon, C., Berruti, B., Buongiorno, A., Ferreira, M. H., Féménias, P., Frerick, J., Goryl, P., Klein, U., Laur, H., Mavrocordatos, C., Nieke, J., Rebhan, H., Seitz, B., Stroede, J., & Sciarra, R. (2012). The Global Monitoring for Environment and Security (GMES) Sentinel-3 mission. *Remote Sensing of Environment*, *120*, 37–57. https://doi.org/10.1016/J.RSE.2011.07.024

Bij de Vaate, I., Vasulkar, A. N., Slobbe, D. C., & Verlaan, M. (2021). The Influence of Arctic Landfast Ice on Seasonal Modulation of the M2 Tide. *Journal of Geophysical Research: Oceans*, *126*(5), e2020JC016630. https://doi.org/10.1029/2020JC016630

Ray, R. D. (2016). On Measurements of the Tide at Churchill, Hudson Bay. *http://dx.doi.org/10.1080/07055900.2016.1139540*, *54*(2), 108–116. https://doi.org/10.1080/07055900.2016.1139540

Mahoney, A. R. (2018). *Landfast Sea Ice in a Changing Arctic* (tech. rep.). Arctic Program NOAA. https://arctic.noaa.gov/Report-Card/Report-Card-2018/ArtMID/7878/ArticleID/788/Landfast-Sea-Ice-in-a-Changing-Arctic

McPhee, M. G. (1978). A simulation of inertial oscillation in drifting pack ice. *Dynamics of Atmospheres and Oceans*, *2*(2), 107–122. https://doi.org/10.1016/0377-0265(78)90005-2

Poulain, P. M., & Centurioni, L. (2015). Direct measurements of World Ocean tidal currents with surface drifters. *Journal of Geophysical Research: Oceans*, *120*(10), 6986–7003. https://doi.org/10.1002/2015JC010818

Bliss, A., Hutchings, J., Anderson, P., Anhaus, P., Belter, H. J., Berge, J., Bessonov, V., Cheng, B., Cole, S., Costa, D., Cottier, F., Cox, C. J., Torre, P. R. D. L., Divine, D. V., Emzivat, G., Fang, Y.-C., Fons, S., Gallagher, M., Geoffrey, M., … Zuo, G. (2022). Raw files for sea ice drift tracks from the Distributed Network of autonomous buoys deployed during the Multidisciplinary drifting Observatory for the Study of Arctic Climate (MOSAiC) expedition 2019 - 2021. https://doi.org/10.18739/A2WW77163

Kodaira, T., Thompson, K. R., & Bernier, N. B. (2016). Prediction of M2 tidal surface currents by a global baroclinic ocean model and evaluation using observed drifter trajectories. *Journal of Geophysical Research: Oceans*, *121*(8), 6159–6183. https://doi.org/10.1002/2015JC011549

Baumann, T. M., Polyakov, I. V., Padman, L., Danielson, S., Fer, I., Janout, M., Williams, W., & Pnyushkov, A. V. (2020). Arctic tidal current atlas. *Scientific Data 2020 7:1*, *7*(1), 1–11. https://doi.org/10.1038/s41597-020-00578-z

2

TOWARDS SEA ICE-TIDE DISSIPATION IN TIDAL MODELS-APPLICATION TO LANDFAST ICE

This chapter focuses on modelling the impact of sea ice dissipation on tides within a generic 2D barotropic tidal framework, applied specifically to the Global Tide and Storm Surge Model (GTSM). We begin by examining the physics of air-ice-ocean interactions, essential for integrating sea ice dissipation into tidal dynamics. A part of this study addresses the challenge of acquiring accurate sea ice drift velocities on tidal time scale, a crucial factor in the modelling. Our new approach involves a parametric method to incorporate sea ice dissipation into tidal modeling without direct coupling to a sea ice model thus, moving away from computing the sea ice drift velocities.

A key finding from implementing this approach on landfast ice is the substantial influence of seasonal variations in landfast ice on the seasonal modulation of the M_2 tidal constituent in the Arctic. This significant impact of varying landfast ice conditions on Arctic tidal patterns highlights a need for research in potential long-term effects of the ongoing Arctic sea ice decline.

Sect. 2.5 of this chapter has been published in Bij de Vaate et al., 2021:

Bij de Vaate, I., **A. N. Vasulkar**, D. C. Slobbe, and M. Verlaan (May 2021). The Influence of Arctic Landfast Ice on Seasonal Modulation of the M2 Tide. Journal of Geophysical Research: Oceans 126(5), e2020JC016630. DOI: 10.1029/2020JC016630

2.1. Introduction

Sea ice affects tides and storm surges by modifying the air-sea momentum flux through the additional friction to the underlying ocean flow. Accurately modeling this additional friction-induced dissipation is crucial for predicting tides, sea level changes, and assessing coastal flooding risks. Dissipation is dependent on the relative velocity between the water and ice (Pease et al., 1983), which requires sea ice velocities on a tidal time scale. There is no publicly available dataset which can provide these velocities. The primary method to obtain such velocities involves using a 3D global coupled ice-ocean tide model that accounts for ice thermodynamics, dynamics, transport, and ridging (Hunke et al., 2010), and solving for sea ice drift on tidal time scales. However, most such models (e.g. STORMTIDE (Müller et al., 2014) and HYCOM (Arbic et al., 2010)) are not operational but typically limited to specific time periods due to high computation costs.

An alternative, easier option is a partial coupling which involves solving the ice-momentum equation with the tidal model where the ice concentration and thickness are obtained from external datasets. Yet, this method comes with its own set of challenges. Accurately solving sea ice and tidal equations together demands a thorough understanding of sea ice rheology and precise modelling of internal stress gradients within the sea ice. Such coupling processes are time-intensive, costly, and yet encounter issues like 'artificial inertial response' due to mass imbalances (Steele et al., 1997; Hibler et al., 2006). Considering these challenges, we focus on a parameteric approach to modelling sea ice dissipation on tides in 2D barotropic tidal models.

In developing a dissipation parameterization, we model the dissipation from each of the three sea ice regimes–landfast ice, drifting sea ice with strong internal stresses, and free drift sea ice–separately in a barotropic tidal model. For landfast ice, which is stationary, the dissipation implementation is straightforward through the existing bottom frictional stress in tidal models. Landfast ice significantly affects local hydrodynamics by reducing the interaction between the atmosphere and the underlying ocean (Mahoney et al., 2014) but its effects far from the source are not known. In the winter about 1.65 million km^2 in the Arctic are covered by landfast ice, while in summer there is no landfast ice (Li et al., 2020). This seasonal variation in landfast ice coverage may lead to tidal modulation due to variation of landfast ice-induced dissipation, but the extent of its impact across the Arctic is not fully understood.

In this chapter, we begin with a comprehensive overview of the Global Tide and Storm Surge Model (GTSM) utilized in this thesis. We then explore the physics of the air-ice-ocean interface to know the forcing underlying the sea ice-induced tidal dissipation. Following this, we discuss the integration of such dissipation into tidal models where we examine the sea ice drift and associated challenges encountered in solving the sea ice drift equation. This points to the challenges in obtaining sea ice velocities on a tidal time scale, leading to our approach for parameterizing sea ice-induced tidal dissipation. This parameterization is then applied specifically to landfast ice.

In this context, we analyse the effects of seasonal variations in landfast ice on the

Arctic M_2 tide, examining both winter and summer configurations. This provides insights into the extent to which landfast ice causes an Arctic tidal modulation.

2.2. GLOBAL TIDE AND SURGE MODEL (GTSM)

2.2.1. MODEL DETAILS AND BATHYMETRY

The Global Tide and Surge Model version 4.1 (referred to as the GTSM) (Verlaan et al., 2015; Muis et al., 2016; Irazoqui Apecechea et al., 2017) is used in this thesis. The model is implemented in the Delft3D Flexible Mesh suite from Deltares and is developed on an unstructured grid with a resolution starting from 25 km in open oceans to 2.5 km near the coasts. This unstructured grid addresses issues with singularity at the North Pole and thinning in the longitudinal direction in high latitudes to prevent numerical difficulties while allowing a computationally cost-effective solution (Kernkamp et al., 2011). A visual representation of the GTSM grid around the North Pole can be found in Figure 2.1.

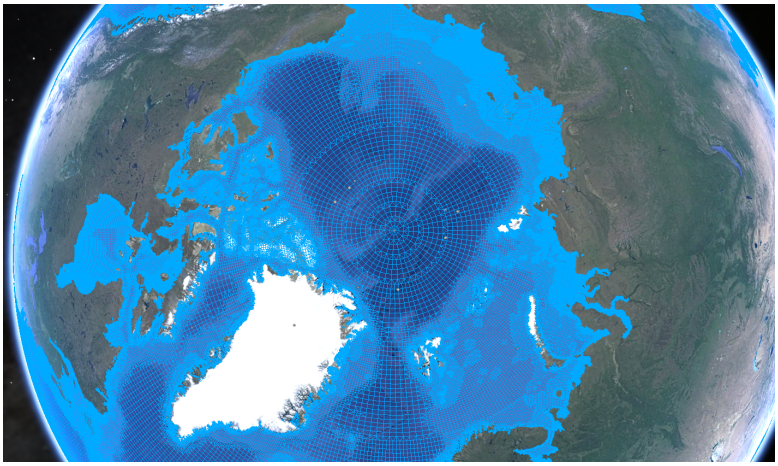

Figure 2.1.: Grid of GTSM in the Arctic region starting with a node on the North Pole

The model uses the GEBCO2019[1] gridded bathymetry which includes IBCAOv3[2] for the Arctic Bathymetry (GEBCO Bathymetric Compilation Group, 2019). GTSM has been calibrated globally for bathymetry using FES2014 derived water levels (Wang et al., 2021).

2.2.2. GOVERNING EQUATIONS

GTSM employs the depth-averaged shallow water equations with no lateral boundaries. The model incorporates the full tide-generating potential for forcing the tides. Additionally, it also includes parameterized forms of Self Attraction

[1]The General Bathymetric Chart of the Oceans
[2]The International Bathymetric Chart of the Arctic Ocean version 3

and Loading (SAL) and internal tidal wave drag, both vital in larger open oceans (Irazoqui Apecechea et al., 2017). The resulting governing equations for continuity and momentum are:

$$\frac{\partial \zeta}{\partial t} + \nabla.(H_d \boldsymbol{u}_t) = 0, \tag{2.1}$$

$$\frac{\partial \boldsymbol{u}_t}{\partial t} + f e^{i\pi/2} \boldsymbol{u}_t + \boldsymbol{u}_t.\nabla \boldsymbol{u}_t = -g\nabla(\zeta_n) + \nu_w(\nabla^2 \boldsymbol{u}_t) + \frac{\boldsymbol{\tau}_b}{\rho_w H_d} + \frac{\boldsymbol{\tau}_{IT}}{\rho_w H_d} + \frac{\boldsymbol{\tau}_{aw}}{\rho_w H_d}, \tag{2.2}$$

where:

ρ_w = density of water
$\zeta(t)$ = water level relative to the model's reference surface
$\boldsymbol{u}_t$ = barotropic depth-averaged tidal water velocity
H_d = total water depth given by $H_b + \zeta$ with H_b being the bathymetry
ν_w = horizontal kinematic viscosity of water
g = acceleration due to gravity
f = Coriolis parameter
ζ_n = net water level obtained from $\zeta - \zeta_{SAL} - \zeta_{EQ}$
ζ_{SAL} = SAL effect
ζ_{EQ} = equilibrium tide
$\boldsymbol{\tau}_{IT}$ = internal tides frictional stress
$\boldsymbol{\tau}_b$ = bottom frictional stress
$\boldsymbol{\tau}_{aw}$ = air-water surface frictional shear stress (also known as wind stress)

2.3. AIR-ICE-OCEAN INTERFACIAL FORCES

Interfacial forces between air, sea ice and ocean give insights into the dissipation from sea ice on tides. Sea ice that floats on the ocean surface acts as a boundary layer between the ocean and atmosphere, adding an extra layer in which movement occurs as a result of external forces. Figure 2.2 illustrates the relevant interfacial forces in the air-ice-ocean system. The ice and water surface interact through a shear stress induced by the relative velocities between the two layers. This extra force contributes to the momentum equations of sea ice and water as an external force term. The equation for the ice-water shear stress, based on the quadratic drag law from McPhee, 1982, is given by:

$$\boldsymbol{\tau}_{iw} = \rho_w C_w |\boldsymbol{u}_i - \boldsymbol{u}_t| (\boldsymbol{u}_i - \boldsymbol{u}_t), \tag{2.3}$$

where, $\boldsymbol{\tau}_{iw}$ is the shear stress from ice on water, C_w the drag coefficient for ice-water, $\boldsymbol{u}_i$ the velocity of the ice. The negative of $\boldsymbol{\tau}_{iw}$ is denoted by $\boldsymbol{\tau}_{wi}$ and represents the water-ice shear stress vector.

Likewise, the air-ice shear stress is given by:

$$\boldsymbol{\tau}_{ai} = \rho_a C_a |\boldsymbol{u}_i - \boldsymbol{u}_a| (\boldsymbol{u}_a - \boldsymbol{u}_i), \tag{2.4}$$

where $\boldsymbol{\tau}_{ai}$ is the shear stress from air on ice, ρ_a the density of air, C_a the drag coefficient for air-ice, $\boldsymbol{u}_a$ the velocity of air, and $\boldsymbol{u}_i$ the velocity of ice. The negative of $\boldsymbol{\tau}_{ai}$ is denoted by $\boldsymbol{\tau}_{ia}$ and represents the ice-air shear stress vector.

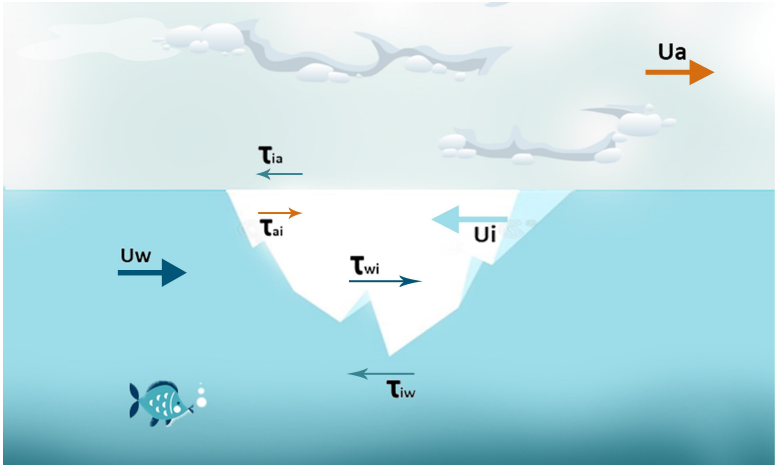

Figure 2.2.: Graphic illustrating the shear stresses in the air-ice-ocean system. $\boldsymbol{\tau}_{wi}$ and $\boldsymbol{\tau}_{iw}$ are water-ice and ice-water stresses, respectively and $\boldsymbol{\tau}_{ai}$ and $\boldsymbol{\tau}_{ia}$ are air-ice and ice-air stresses, respectively.

2.4. INCLUDING SEA ICE DISSIPATION IN BAROTROPIC TIDAL MODELS

In areas covered by sea ice, the momentum equation of water (Equation (2.2)) is modified by replacing the air-water wind stress ($\boldsymbol{\tau}_{aw}$) with the ice-water shear stress ($\boldsymbol{\tau}_{iw}$), to include the sea ice-induced shear stress. Thus, the modified momentum equation is:

$$\frac{\partial \boldsymbol{u}_t}{\partial t} + f e^{i\pi/2}\boldsymbol{u}_t + \boldsymbol{u}_t.\boldsymbol{\nabla}\boldsymbol{u}_t = -g\boldsymbol{\nabla}(\zeta_n) + \nu_w(\boldsymbol{\nabla}^2\boldsymbol{u}_t) + \frac{\boldsymbol{\tau}_b}{\rho_w H_d} + \frac{\boldsymbol{\tau}_{IT}}{\rho_w H_d} + (1-\alpha)\frac{\boldsymbol{\tau}_{aw}}{\rho_w H_d} + (\alpha)\frac{\boldsymbol{\tau}_{iw}}{\rho_w H_d}, \tag{2.5}$$

where $\alpha = H(c)$ is a Heaviside function of sea ice concentration (c) which takes the value 1 when there is sea ice present (i.e. $c > 0$) and 0 when there is no sea ice. For the case of landfast ice, $\alpha = 1$ when sea ice concentration corresponds to landfast ice else, it is zero. In the absence of winds, one is just left with the sea ice-induced shear stress in the region of sea ice cover.

In this equation, to accurately include the dissipation from sea ice as per Equation (2.3), sea ice velocities influenced by tides on a tidal time scale are required. However, obtaining these velocities necessitates a 3D global coupled ice-ocean-tide model. As discussed in Sect. 2.1, such models are not feasible for high-resolution operational models due to their extensive computational demands. Alternatively, there is a partial coupling approach which we will explore in additional detail next, also presents significant challenges.

2.4.1. Partially Coupled Approach

In this approach, we solve the sea ice momentum equation (Equation (2.6)) with the sea ice concentration and thickness prescribed from external datasets along with the tidal momentum equation. The upcoming sub-sections will delve into the specific challenges in this approach including but not limited to the challenges encountered when solving the sea ice momentum equation.

The Drift of Sea Ice

According to Leppäranta, 2011, the motion of a drifting sea ice field is 2D on the ocean surface. This 2D drift equation for a sea ice layer floating on the sea surface is derived by integrating Newton's second law of motion in 3D over the sea ice thickness. Doing so, relies on three assumptions from continuum mechanics, namely, (1) ice field of continuum particles (ice floes) with associated density, (2) forcing due to internal stress field from ice floes and (3) Eulerian or Lagrangian frame of reference. The resulting momentum equation in 2D is as follows:

$$\rho_i h_i \left(\frac{\partial \boldsymbol{u}_i}{\partial t} + \boldsymbol{u}_i . \boldsymbol{\nabla} \boldsymbol{u}_i + f \boldsymbol{u}_i e^{-i\pi/2} \right) = -\rho_i h_i g \boldsymbol{\nabla} \zeta - h_i \boldsymbol{\nabla} p_a + \boldsymbol{\nabla} . \boldsymbol{\sigma} + \boldsymbol{\tau}_{ai} + \boldsymbol{\tau}_{wi}, \tag{2.6}$$

where h_i is the sea ice thickness, ρ_i the density of sea ice ($\sim 925\,\mathrm{kg/m^3}$), $\boldsymbol{u}_i$ the ice velocity, p_a the atmospheric pressure, and $\boldsymbol{\sigma}$ the 2D internal stress. The remaining terms have the same meaning as in Equation (2.5). Notably, most sea ice models solving for this momentum equation provide sea ice velocities on daily, weekly or monthly time scales (Heil & Hibler, 2002).

Internal Stresses in an Ice Field

The modelling of internal stresses in a sea ice momentum equation is perhaps one of the most important and challenging aspects. In an ice field, the internal stresses are not typically determined by the stress-strain relationship of ice (i.e., a solid material). Rather, they result from the stresses induced between ice floes resisting strain or shear. Various constitutive laws and associated models assume different rheologies of sea ice fields, such as simple Newtonian linear viscous, non-linear viscous, plastic viscous, and elastic-viscous-plastic (e.g. Campbell, 1965, Coon, 1974, Rothrock, 1975, Hibler III, 1979). Of these, the elasto-viscous-plastic (EVP) rheology of Hunke and Dukowicz, 1997 is the most commonly used in sea ice models (Ólason et al., 2022). This model is a numerically efficient implementation of the previously well-known viscous-plastic (VP) rheology proposed by Hibler III, 1979. The expression relating the internal stresses to the strain rate tensor according to this VP model is given by:

$$\boldsymbol{\sigma} = \zeta \dot{\epsilon_I} + 2\eta \dot{\epsilon} - \frac{P}{2}, \tag{2.7}$$

where $\zeta(h_i, A)$ and $\eta(h_i, A)$ are the horizontal (2D) bulk and shear viscosities (units kg/s), respectively, P is the strength of the sea ice field, $\dot{\epsilon_I}$ and $\dot{\epsilon}$ are the components of the strain rate tensor. This term plays a crucial role in drifting sea ice by serving as passive drag, similar to the water-ice drag (Steele et al., 1997).

COMPARISON TO TIDAL MOMENTUM EQUATION

On comparing to the momentum equation of the shallow water equations (Equation (2.5)), it is seen that the role of sea ice thickness corresponds to that of the total water depth, ice-water friction corresponds to bottom friction, and the internal stress field of ice corresponds to horizontal viscous stress in water. The constancy of velocity of sea ice in the vertical direction is also valid for 2D barotropic tide models. In the absence of wind and internal stresses in deeper oceans, both the momentum equations are similar leading to similar behaviour of sea ice to tides. Due to these similarities in the equations, solving for both the sea ice and tide momentum equation is a possible alternative.

CHALLENGES IN THIS APPROACH

While solving for the sea ice drift equation, the most time consuming aspect is the sub-cycling (breaking down to smaller time steps) for the EVP solver for ice dynamics (Hunke & Dukowicz, 1997). Furthermore, the simplified partial coupling neglects mass transport which can lead to an 'artificial inertial response' in the presence of tides and winds (Hibler et al., 2006). As a result, accurately obtaining sea ice velocities on a tidal time scale using this method is not only computationally expensive, but also lacks accuracy.

2.4.2. OUTLINE OF THE PARAMETERIC APPROACH

In light of the operational and accuracy limitations associated with both fully and partially coupled approaches, we propose shifting our focus towards a more straightforward parametric approach. This approach is designed to incorporate sea ice-induced dissipation into tides within a 2D barotropic model, without necessitating a direct coupling to a sea ice model or solving for sea ice velocities.

Our parameterization focusses on the physics of ice-tide interaction while taking into account the drifting sea ice motion too. This is a deviation from the current state-of-the-art parameteric approaches of assuming a fixed sea ice cover. To achieve this, we adopt a comprehensive approach that encompasses the three regimes of sea ice dynamics giving us the following:

- **Landfast ice:** As a stationary and fixed form of sea ice, the dissipation from landfast ice can be included in a barotropic tidal model in a manner similar to the fixed sea bed.
- **Free drift sea ice:** In shallow water regions, in the absence of internal stresses and winds, terms such as bottom friction and horizontal viscosity of water contribute to a relative velocity between sea ice and water. Hence, it becomes imperative to analyse this physical interaction to accurately model dissipation (Chapter 3).
- **Drifting sea ice with strong internal stresses:** In the absence of winds, the motion of sea ice is primarily driven by ocean currents. Here, the internal stresses within the sea ice field impose a passive drag on the water, which

can be effectively incorporated into tidal models through a parameterization approach that takes into account the physics governing its interaction with tides (Chapter 4).

In this approach, modeling the landfast ice term proves to be easiest and aligns with the methodology employed in various state-of-the-art regional tidal models (e.g., Cancet et al., 2016; Kleptsova and Pietrzak, 2018). We incorporated the landfast ice component into GTSM and investigated its seasonal impact on the tides.

2.5. Effect of Seasonal Variations in Landfast Ice

2.5.1. Data and Methods

GTSM was used to study the impact of seasonal variations in landfast ice cover on the seasonal modulation of the M_2 tide. Here, we ignored the winds. The frictional dissipation due to landfast ice was modelled by adding the frictional stress ($\boldsymbol{\tau}_{iw}$) to the existing bottom frictional stress. In doing so, we used Equation (2.3), where the ice velocity was set to zero, and the drag coefficient is 5.5×10^{-3} in accordance with McPhee, 1982.

The ice-water frictional stress was introduced only for the regions of landfast ice cover which were modelled by means of polygons outlining their extent (Cancet et al., 2016). These polygons were created using gridded landfast ice charts at 10 km resolution obtained from U.S. National Ice Center, 2020. The estimated effect of seasonal variations in landfast ice on seasonal modulation of tides was determined by comparing M_2 amplitudes and phases from two GTSM simulations with seasonal limiting cases of landfast ice cover. We followed the approach of St-Laurent et al., 2008 and used the landfast ice covers of March and September, corresponding to the annual maximum and minimum landfast ice cover respectively. Simulations were done for 2013 and 2017 to assess the impact of inter-annual variations in landfast ice cover. These years had the maximum and minimum fast ice cover, respectively, within the time span of 2010–2019 (Li et al., 2020). In both years there was a negligible amount of landfast ice cover in September leading to the first limiting case of an ice-free surface. The March landfast ice-extents are shown in Figure 2.3

Simulations were run for two spring-neap cycles (i.e., 29.5 days), preceded by a 7-days spin up time. Hourly water levels were saved for a domain covering the region north of $60°N$, extended by the Hudson Bay area; $50°N$ $60°N$, $100°$ $-45°W$. Subsequently, tidal constants were estimated using UTide (Codiga, 2011) for the major constituents K_1, O_1, Q_1, P_1, N_1, M_2, S_2 and K_2. The period of 29.5 days corresponds to two spring-neap cycles and is sufficiently long for disentangling M_2 from the other tidal constituents involved in the analysis. Note that this period does not allow accurate separation of S_2 and K_2, and K_1 and P_1, as this requires a timespan of 182.6 days (Foreman & Henry, 1989). Although this may have a minor effect on the estimation of M_2, it will not impact our analysis since we compare amplitudes/phases between March and September. These months are half a year apart and therefore in phase with the semi-annual cycle resulting from the superposition of these constituent pairs. Nodal corrections were applied to

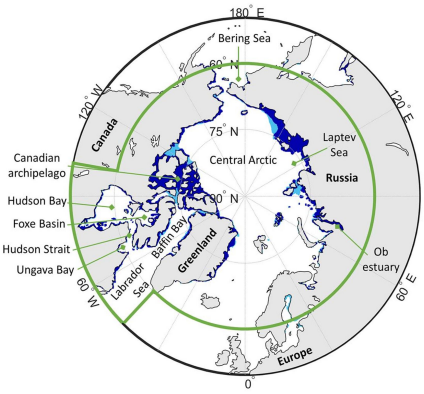

Figure 2.3.: Arctic landfast ice extent for March 11, 2013 (light and dark blue) and March 9, 2017 (dark blue), obtained from updated dataset of U.S. National Ice Center (2009). Note that the ice cover of 2017 completely overlaps that of 2013. The green line indicates the domain of this study.

eliminate amplitude differences caused by the 18.6 years nodal cycle. This allows direct comparison between estimated M_2 phases and amplitudes from the different simulations.

2.5.2. RESULTS AND DISCUSSION

Model simulated seasonal modulation for 2013 (Figure 2.4a) showed considerable differences in amplitude and phase between March and September. The amplitude differences were negative (i.e., September amplitudes larger than March) in the Canadian Archipelago and on the Russian shelf, Hudson Bay, positive in Baffin Bay and some region outside the Frobesius Bay, and close to zero in the Arctic Ocean and European seas. Meanwhile, the phase differences were negative (i.e., September phase advance than March) in the Hudson Bay, Ungava Bay, and some part of the Siberian Shelf, and mostly positive in the remaining areas, with maximum phase differences around $\pm 40°$.

In comparison to 2013, the difference of M_2 amplitude between March 2017 and March 2013 is seen in Figure 2.4b. The model-derived amplitude and phase differences caused by the smaller landfast ice cover of 2017 (not shown here) display a similar pattern as in the case of 2013. In most of the domain, there is little difference between the March amplitudes of both years. However, the differences are significant in Hudson Bay and nearby regions; up to 0.05 m ($\sim 20\%$). In general, this results in reduced differences between March and September amplitudes in 2017. Negative differences in amplitude are reduced by up to 0.05 m in Hudson Bay and positive differences in Hudson Bay (east) and Baffin Bay are reduced by about 0.02 m. Seasonal modulation is larger in 2017 (up to 0.02 m) than in 2013 in the east of the

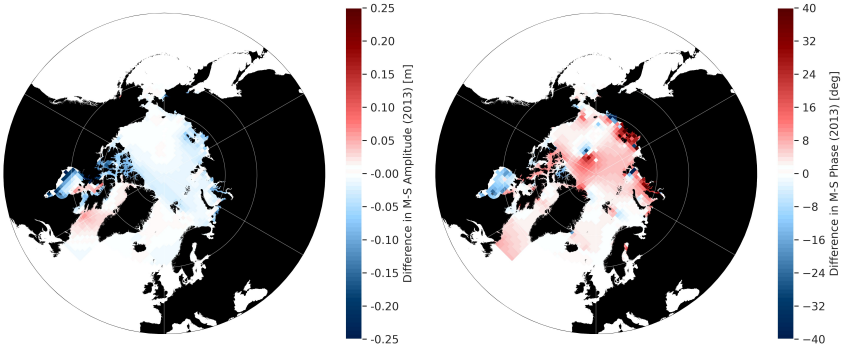

(a) Seasonal modulation of M_2 for 2013

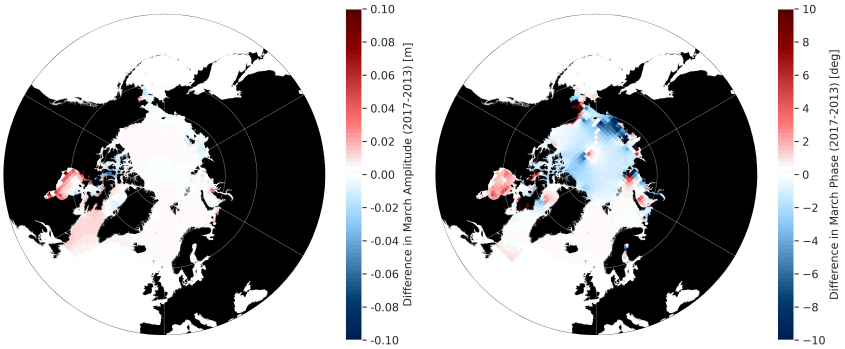

(b) Difference of M_2 amplitudes and phase between 2017 and 2013

Figure 2.4.: Model-derived difference in amplitude and phase for 2013 (Figure 2.4a) and between March 2017 and March 2013 (20172013; different color scale) (Figure 2.4b). Negative values in Figure 2.4a imply larger amplitudes in September while for phases it implies a phase advance. Similarly, negative values in Figure 2.4b imply a larger amplitude in 2013 and a phase advance in 2013. Data have been interpolated to a stereographic grid for plotting.

Canadian Archipelago and in Labrador Sea. The east of the Canadian Archipelago is not covered by landfast ice in 2017, while it was in 2013, and has a lower M_2 amplitude in March 2017 than in 2013. This results in a larger amplitude difference in March with respect to September. In the Labrador Sea, the March amplitude of 2017 is more positive than that of 2013. In March 2017, Hudson Bay experiences less phase advance than in March 2013. In the Central Arctic, the Canadian archipelago, Baffin Bay and on the Russian shelf, phase delay is reduced as well.

The study demonstrated that the seasonal variation of landfast ice can significantly impact the seasonal modulation of tides in the Arctic with values being up to 0.25 m. The presence of landfast ice leads to local energy dissipation which typically results in a decrease of the amplitudes in March with an increase of landfast ice. However, it is noteworthy that in other regions, amplitudes can actually increase as a consequence of the variation in dissipation. The simulations on the effect of landfast ice on tides were carried out for two years representing maximum and minimum ice cover since 2011. The results revealed that although the largest differences in ice cover between the years occurred in the Canadian Archipelago and on the Russian shelf, the alteration of landfast ice cover also affected the seasonal modulation of M_2 amplitudes in Hudson and Baffin Bay, with differences of up to 0.05 m. The observed relationship between seasonal variations in landfast ice extent and tide modulation, along with the effect of landfast ice changes influencing distant tides, suggests a potentially significant impact of ongoing Arctic sea ice decline.

Although, these are purely model-based results, a detailed comparison of these with altimetry-derived modulation is available in Bij de Vaate et al., 2021 where it is clear that accounting for only landfast ice is not sufficient to accurately model the effect of sea ice on tides. The drifting sea ice can also have an impact on tides and needs to be accounted for in the model.

2.5.3. CONCLUSIONS

We took the first steps of our parameteric approach by including the dissipation from landfast ice in GTSM. Through a dedicated study, we explored the influence of seasonal variations in landfast ice on the seasonal modulation of the Arctic M_2 tide. Notably, the results revealed that the landfast ice can lead to a tidal modulation of up to 0.25 m in the Arctic, particularly in regions like the Hudson Bay. Moreover, these findings underscore the necessity for additional research to understand the long-term implications of the continuing decline in Arctic sea ice.

REFERENCES

Bij de Vaate, I., Vasulkar, A. N., Slobbe, D. C., & Verlaan, M. (2021). The Influence of Arctic Landfast Ice on Seasonal Modulation of the M2 Tide. *Journal of Geophysical Research: Oceans*, *126*(5), e2020JC016630. https://doi.org/10.1029/2020JC016630

Pease, C. H., Salo, S. A., & Overland, J. E. (1983). Drag measurements for first-year sea ice over a shallow sea. *Journal of Geophysical Research*, *88*(C5), 2853. https://doi.org/10.1029/JC088iC05p02853

Hunke, E. C., Lipscomb, W. H., Turner, A. K., Jeffery, N., & Elliott, S. (2010). CICE: the Los Alamos Sea Ice Model Documentation and Software User's Manual (Version 4.1).

Müller, M., Cherniawsky, J. Y., Foreman, M. G., & Von Storch, J. S. (2014). Seasonal variation of the M 2 tide. *Ocean Dynamics*, *64*(2), 159–177. https://doi.org/10.1007/s10236-013-0679-0

Arbic, B. K., Wallcraft, A. J., & Metzger, E. J. (2010). Concurrent simulation of the eddying general circulation and tides in a global ocean model. *Ocean Modelling*, *32*(3-4), 175–187. https://doi.org/10.1016/j.ocemod.2010.01.007

Steele, M., Zhang, J., Rothrock, D., & Stem, H. (1997). The force balance of sea ice in a numerical model of the Arctic Ocean. *JOURNAL OF GEOPHYSICAL RESEARCH*, *102*(C9), 61–82. https://doi.org/10.1029/97JC01454

Hibler, I. D., Roberts, A., Heil, P., Proshutinsky, A. Y., Simmons, H. L., & Lovick, J. (2006). Modeling M2 tidal variability in Arctic Sea-ice drift and deformation. *Annals of Glaciology*, *44*, 418–428. https://doi.org/10.3189/172756406781811178

Mahoney, A. R., Eicken, H., Gaylord, A. G., & Gens, R. (2014). Landfast sea ice extent in the Chukchi and Beaufort Seas: The annual cycle and decadal variability. *Cold Regions Science and Technology*, *103*, 41–56. https://doi.org/10.1016/J.COLDREGIONS.2014.03.003

Li, Z., Zhao, J., Su, J., Li, C., Cheng, B., Hui, F., Yang, Q., & Shi, L. (2020). Spatial and Temporal Variations in the Extent and Thickness of Arctic Landfast Ice. *Remote Sensing 2020, Vol. 12, Page 64*, *12*(1), 64. https://doi.org/10.3390/RS12010064

Verlaan, M., De Kleermaeker, S., & Buckman, L. (2015). GLOSSIS: Global storm surge forecasting and information system. *Australasian Coasts & Ports Conference 2015: 22nd Australasian Coastal and Ocean Engineering Conference and the 15th Australasian Port and Harbour Conference*, 229–234.

Muis, S., Verlaan, M., Winsemius, H. C., Aerts, J. C., & Ward, P. J. (2016). A global reanalysis of storm surges and extreme sea levels. *Nature Communications 2016 7:1*, *7*(1), 1–12. https://doi.org/10.1038/ncomms11969

Irazoqui Apecechea, M., Verlaan, M., Zijl, F., Le Coz, C., & Kernkamp, H. (2017). Effects of self-attraction and loading at a regional scale: a test case for the Northwest European Shelf. *Ocean Dynamics*, *67*(6), 729–749. https://doi.org/10.1007/s10236-017-1053-4

Kernkamp, H. W., Van Dam, A., Stelling, G. S., & De Goede, E. D. (2011). Efficient scheme for the shallow water equations on unstructured grids with application to the Continental Shelf. *Ocean Dynamics*, *61*(8), 1175–1188. https://doi.org/10.1007/S10236-011-0423-6/TABLES/2

GEBCO Bathymetric Compilation Group. (2019). *The GEBCO_2019 Grid - a continuous terrain model of the global oceans and land* (tech. rep.). British Oceanographic Data Centre, National Oceanography Centre, NERC, UK. GEBCO.

Wang, X., Verlaan, M., Apecechea, M. I., & Lin, H. X. (2021). ComputationEfficient Parameter Estimation for a HighResolution Global Tide and Surge Model. *Journal of Geophysical Research: Oceans*, *126*(3), e2020JC016917. https://doi.org/10.1029/2020JC016917

McPhee, M. G. (1982). *Sea ice drag laws and simple boundary layer concepts, including application to rapid melting* (Report 82-4). United States Army Cold Regions Research; Engineering Laboratory.

Leppäranta, M. (2011). Equation of drift ice motion. *The Drift of Sea Ice*, 143–184. https://doi.org/10.1007/978-3-642-04683-4{_}5

Heil, P., & Hibler, W. D. (2002). Modeling the High-Frequency Component of Arctic Sea Ice Drift and Deformation. *Journal of Physical Oceanography*, *32*(11), 3039–3057. https://doi.org/10.1175/1520-0485(2002)032<3039:MTHFCO>2.0.CO;2

Campbell, W. J. (1965). The wind-driven circulation of ice and water in a polar ocean. *Journal of Geophysical Research*, *70*(14), 3279–3301. https://doi.org/10.1029/jz070i014p03279

Coon, M. C. (1974). MECHANICAL BEHAVIOR OF COMPACTED ARCTIC ICE FLOES. *JPT, Journal of Petroleum Technology*, *26*, 466–470. https://doi.org/10.2118/3956-PA

Rothrock. (1975). The Mechanical Behavior of Pack Ice. *Annual Review of Earth and Planetary Sciences*, *3*(1), 317–342. https://doi.org/10.1146/annurev.ea.03.050175.001533

Hibler III, W. D. (1979). A Dynamic Thermodynamic Sea Ice Model. *Journal of Physical Oceanography*, *9*(4), 815–846. https://doi.org/https://doi.org/10.1175/1520-0485(1979)009<0815:ADTSIM>2.0.CO;2

Hunke, E. C., & Dukowicz, J. K. (1997). An ElasticViscousPlastic Model for Sea Ice Dynamics. *Journal of Physical Oceanography*, *27*(9), 1849–1867. https://doi.org/10.1175/1520-0485(1997)027

Ólason, E., Boutin, G., Korosov, A., Rampal, P., Williams, T., Kimmritz, M., Dansereau, V., & Samaké, A. (2022). A New Brittle Rheology and Numerical Framework for Large-Scale Sea-Ice Models. *Journal of Advances in Modeling Earth Systems*, *14*(8), e2021MS002685. https://doi.org/10.1029/2021MS002685

Cancet, M., Andersen, O., Lyard, F., Shulz, A., Cotton, P., & Benveniste, J. (2016). A New High Resolution Tidal Model in the Arctic Ocean. *Living Planet Symposium*, 67. https://ui.adsabs.harvard.edu/abs/2016ESASP.740E..67C

Kleptsova, O., & Pietrzak, J. D. (2018). High resolution tidal model of Canadian Arctic Archipelago, Baffin and Hudson Bay. *Ocean Modelling*, *128*, 15–47. https://doi.org/10.1016/j.ocemod.2018.06.001

U.S. National Ice Center. (2020). U.S. National Ice Center Arctic and Antarctic Sea Ice Concentration and Climatologies in Gridded Format, Version 1 [G10033]. https://doi.org/https://doi.org/10.7265/46cc-3952

St-Laurent, P., Saucier, F. J., & Dumais, J. F. (2008). On the modification of tides in a seasonally ice-covered sea. *Journal of Geophysical Research: Oceans*, *113*(C11), 11014. https://doi.org/10.1029/2007JC004614

Codiga, D. L. (2011). *Unified Tidal Analysis and Prediction Using the UTide Matlab Functions* (tech. rep. September). University of Rhode Island. https://doi.org/10.13140/RG.2.1.3761.2008

Foreman, M. G., & Henry, R. F. (1989). The harmonic analysis of tidal model time series. *Advances in Water Resources*, *12*(3), 109–120. https://doi.org/10.1016/0309-1708(89)90017-1

3

TIDAL DISSIPATION FROM FREE DRIFT SEA ICE

One of the major challenges facing global hydrodynamic tidal models is the modelling of the interaction between sea ice and tides in high-latitude waters. Recent studies have shown strong seasonal correlation between sea ice and tides. Hence, it is important to accurately model the effect of sea ice in a tidal model. Presence of sea ice leads to a frictional dissipation of tides. Most models either completely ignore sea ice or partly include it by assuming a fixed sea ice cover (landfast ice). However, sea ice can also be drifting and the nature of dissipation between drifting sea ice and tides is partly unknown.

We assess the dissipation of tides due to free drift sea ice. In the absence of wind, this is negligible in the deeper and open ocean. For the shallow water regions, however, this dissipation is unknown. Here, we evaluate this dissipation for the Spitzbergen Shelf region using a beacon dataset showing strong free drift subdaily sea ice oscillations and a physics based point ice model. Two analyses were done which compared the model and observed motion. The analyses showed that for winds speeds below $8\,\mathrm{m/s}$ *and with low subdaily signals, the subdaily free drift sea ice motion is strongly connected to the tides and that the frictional dissipation is low.*

In the context of global tide and storm surge models, the dissipation from free drift sea ice on tides should be evaluated based on the region (deep ocean or shallow water) and existing wind conditions. In the presence of strong winds the dissipation between free drift sea ice and air can be significant on a subdaily scale even if there are no subdaily signals in the wind itself.

This chapter is based on Vasulkar et al., 2022 as:

Vasulkar, A., Verlaan, M., Slobbe, C., & Kaleschke, L. (2022). Tidal dissipation from free drift sea ice in the Barents Sea assessed using GNSS beacon observations. Ocean Dynamics, 72(8), 577597. DOI: 10.1007/s10236-022-01516-w

3.1. INTRODUCTION

Hydrodynamic global tide models have improved significantly in the past couple of decades due to a combination of improved modelling and data assimilation. Yet, these models still face challenges in high-latitude waters (poleward of ±66° latitude) (Stammer et al., 2014; Kleptsova & Pietrzak, 2018). Among these challenges is the fact that most of these global tidal models either completely or partly ignore the interaction between sea ice and tides. This also applies to a model we are co-developing with Deltares, named, Global Tide and Surge Model (GTSM (Verlaan et al., 2015; Muis et al., 2016)). Apart from global tidal models, there are some regional tidal models for the Arctic like Padman and Erofeeva, 2004 and Chen et al., 2009 which perform well. Of these too, Padman and Erofeeva, 2004 do not consider sea ice while the AO-FVCOM model of Chen et al., 2009 is a 3D model coupled to a sea ice model. Yet, these models are regional and are not suitable to study the effects of sea ice on tides globally.

Sea ice leads to a dissipation of tidal energy. The magnitude and nature of this energy loss is still a topic of ongoing research (Stammer et al., 2014). The friction generated by tides at the sea ice-ocean interface is a potential mechanism for this tidal energy dissipation (Kleptsova & Pietrzak, 2018). The stress from this friction can be represented in a model through a simple parameterization where the stress is proportional to the square of the relative velocity between sea ice and tidal velocity (McPhee, 1982; Pease et al., 1983). Some global tidal models that partly include the sea ice assume all of the sea ice to be stationary/time-invariant (landfast ice) with annual mean state (Stammer et al., 2014). This simplifies the relative velocity to just the velocity of water/tides. But, sea ice is also drifting and the sea ice area is seasonally varying.

Recent studies (Kleptsova & Pietrzak, 2018; Kagan & Sofina, 2010; Müller et al., 2014; Bij de Vaate et al., 2021) have shown strong seasonal correlation between sea ice and the tidal constituents. Kleptsova and Pietrzak, 2018 dealt with this problem by using a monthly sea ice concentration field while assuming all the sea ice to be stationary. However, this still ignores the fact that only 12% of the northern hemisphere wintertime sea ice cover is landfast ice (Mahoney, 2018) while, the remaining fraction is drifting sea ice.

In the case of drifting sea ice, modelling the water-ice frictional stress requires the relative velocity between sea ice and water. To evaluate this, one would need sea ice velocities on subdaily timescales from models which include tidal forcing. Such models, if any, should be 3D ice-ocean coupled models which would correctly resolve the effect of ice on water and vice versa and should include tides. Such a dataset of sea ice velocities is not known to be publicly available and in fact, many sea ice models typically omit tidal forcings (Heil & Hibler, 2002). On the other hand, remote sensing derived products provide the mean total velocities at weekly/monthly resolution so these cannot be used either. That said, most of the hydrodynamic tide models are 2D and in these models it would suffice to include an efficient parameterization of the frictional dissipation from drifting sea ice on tides.

It is unknown how much drifting sea ice contributes to the dissipation of tides. The work of Kleptsova and Pietrzak, 2018 suggests that the impact could be

significant. In fact, integrated over a large domain even quite small dissipation at the ice-tide interface could be relevant for large scale tide modelling. Our long term aim is to estimate the amount of energy loss between drifting sea ice and tides and if significant find a parameterization that can be used in global tide models. To estimate the energy loss, it is important to understand the interaction between the drifting sea ice motion and tides and the underlying physics.

The motion of drifting sea ice can be divided into motions at subdaily and longer time scales. The subdaily sea ice motion interacts with tides and is therefore important for our study. This subdaily motion is essentially formed by sea ice oscillations containing both inertial oscillations, attributed to inertial forcing (coriolis force) (Hunke & Dukowicz, 1997; McPhee, 1978), and tidal oscillations (Pease et al., 1983). The proportion of inertial or tidal component in the oscillations helps evaluate the relative motion between sea ice and tides. There are a few regional studies (Pease et al., 1995; Hibler et al., 2006; Kowalik & Proshutinsky, 1994) which investigated the interaction between the subdaily sea ice drift and tides. All these studies were performed to study the effect of tides on sea ice drift and deformation and not vice versa, i.e., the effect of sea ice on the dissipation of tides. Nevertheless, they shed light on the nature of the subdaily sea ice motion and its relationship with tides.

Pease et al., 1995 in their harmonic analysis of the Argos buoys in the Barents Sea continental shelf region observed that the M_2 tidal constituent in the subdaily sea ice motion was a magnitude larger than the inertial oscillation. Also, Kowalik and Proshutinsky, 1994 using their model for the Arctic Central Basin noted that the subdaily sea ice motion is dominated by tides but not inertial forces. This was in contrast to Hibler et al., 2006 who, using a sea ice model proposed by Heil and Hibler, 2002, showed that in the subdaily sea ice oscillations of the Arctic Central basin, the inertial effects dominate and are enhanced by tidal forcing. This contradiction could be attributed to the different sea ice models used by Kowalik and Proshutinsky, 1994 and Hibler et al., 2006. On the other hand, Pease et al., 1995 and Kowalik and Proshutinsky, 1994 had similar conclusions of tides being a dominant aspect of subdaily sea ice motion, the relative magnitude of inertial oscillations in both the studies was different. The difference here, might be a result of different magnitudes of internal stresses in the drifting ice field in the central Arctic and the Barents Sea region. This adds to the complexity as drifting sea ice field with and without significant internal stresses and based on the region of the Arctic could have different dissipation on the tides.

On this context, we propose to divide the sea ice field into two regimes: sea ice drifting under strong internal stresses and under weak/no internal stresses (Zubov, 1945). The latter is also referred to as *free-drift* (McPhee, 1980). Consequently, the interaction of each regime with tides needs to be studied separately. In this paper, we only consider free drift sea ice field and its dissipation on tides thereof.

It is noted in McPhee, 1978; Leppäranta, 2011a that in free drift and no-wind conditions, the sea ice and water velocities are equal under steady state. This implies that there will be no dissipation at the sea ice-tide interface. In fact, under low winds with no subdaily signal too, it can be seen that such a dissipation is negligible

(Omstedt et al., 1996). But these analyses assumed deep and open oceans. It is not clear whether and how strong the dissipation is in case of strong winds or in shallow water regions (i.e. depths< 50 m) where the bottom friction is significant or in straits where vorticity of the current is affected.

Here, we focus on studying the dissipation in scenarios of shallow water regions and strong winds. For this study, we have GNSS observations of beacons in a free drift sea ice field showing sea ice oscillations at a temporal resolution of 15 min in the shallow water region of the Barents Sea, south-east of Svalbard. Moreover the tides are also strong in this region.

Our aim is to analyse the oscillations from this dataset and assess the dissipation of tides due to free drifting sea ice in such shallow water region. This analysis would give us a methodology which could help in assessing such dissipation for the global tidal models.

Analysing the sea ice oscillations would require separating the tidal and inertial oscillations. In the Barents sea region, the semidiurnal tidal frequencies, particularly M_2, and inertial frequencies are close to each other (Furevik & Foldvik, 1996; Middleton & Denniss, 1993). Thus, in an harmonic analysis of the time series of buoy positions, similar to Pease et al., 1995, long time series are required to separate them and satisfy the Rayleigh criterion. The beacon dataset we have, does not satisfy this requirement. Moreover the inertial frequency varies with latitude and the beacon data cannot be considered homogeneous. So, it is impossible to separate the signal from inertial and tidal parts based on their frequency alone. Hence, in this paper, a *physics-based approach* is used by developing a point ice model to help separate the inertial and tidal signals/oscillations from the subdaily free drift sea ice oscillations. From now on, these are simply referred to as *sea ice oscillations* but the reader should bear in mind that these are free drift sea ice oscillations.

Using the point ice model and observations, two analyses are presented. The first evaluates the correlation between the sea ice oscillations and the tidal currents/tides which sheds light on the relative motion between the two. The second one assesses the causality of the sea ice oscillations by performing a forcing sensitivity analysis. Here, the point ice model is used to conduct a sensitivity analysis on the sea ice oscillations from the forcing in the model and in effect, determine the significant cause of the sea ice oscillations. Knowing this forcing responsible for the cause of sea ice oscillation coupled with the information on relative motion between sea ice oscillations and tidal currents helps us compute the dissipation between free drift sea ice-tide interface in the shallower region of the Barents Sea and understand its significance thereoff.

The chapter is structured as follows: Section 3.2 describes the buoy observations and their validation for the free drift assumption. Following this, there is point ice model description and validation in Section 3.3. In Sections 3.4, and 3.5, we present and discuss the results of the two analyses. Section 3.6 gives insight into the energy dissipation and finally, we end by summarising the main findings and concluding remarks.

3.2. BUOY OBSERVATIONS

During an experiment for testing a sea ice forecast and ship route optimisation system in the Barents Sea (Kaleschke et al., 2016) in March 2014, an array of 15 drifting ice buoys (Kaleschke & Müller, 2022) (beacons[1]; as they were called by their manufacturer and henceforth referred to as in this paper) were deployed from an aircraft. Their purpose was to determine the origin of the sea ice and see if the ice thickness changes are caused by ice dynamics or ice growth and melting. The beacons had an in-built GNSS receiver with the beacon positions sampled at a

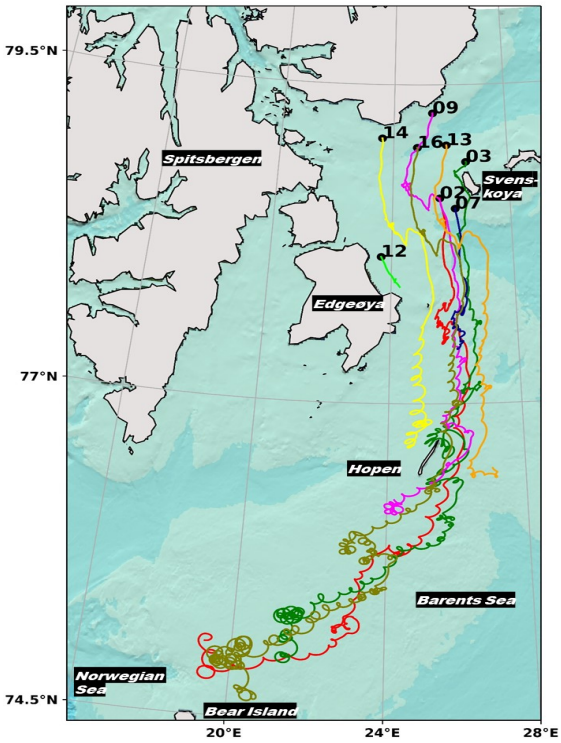

Figure 3.1.: The trajectories for 8 out of the 15 beacons starting from March 16. The remaining beacons were either damaged or lost after deployment. The original experiment intended for the beacons to transmit data for a period in March, but some of the beacons were even operational till the end of May.

frequency of 15 min. Based on the beacon positions, the velocity of the beacons was computed using a forward difference scheme. The beacon trajectories (Figure 3.1) started in the Barents Sea, east of Svalbard. Initially, the trajectories are seen to move south and then turn south-west over the shallow Spitsbergen bank. The clockwise loops formed by the trajectories are the sea ice oscillations, and these move in a

[1] Compact Air Launched Ice Beacons (CALIB) were used as ice beacons. The CALIB is a buoy which may be launched from an aircraft.

coiled manner as the oscillations have a mean drift to the south-west.

A high correlation between these sea ice oscillation loops in beacon trajectories and the magnitude of tidal currents is evident from Figure 3.1 and 3.2. Tidal currents in Figure 3.2 are computed using the in-house global tidal model, GTSM, and plotted for March 31 at 00:00am. It can be said that the beacons move under strong tidal currents. These strong currents are not a result of some local time specific event but, in fact, this region of Spitsbergen bank is known to have high tidal currents (Kowalik, 1979; Gjevik & Straume, 1989). Thus, the oscillations observed in beacon trajectories below the 78°N latitude in the Spitsbergen bank are a result of inertial as well tidal forces as also noted in the study of Pease et al., 1995.

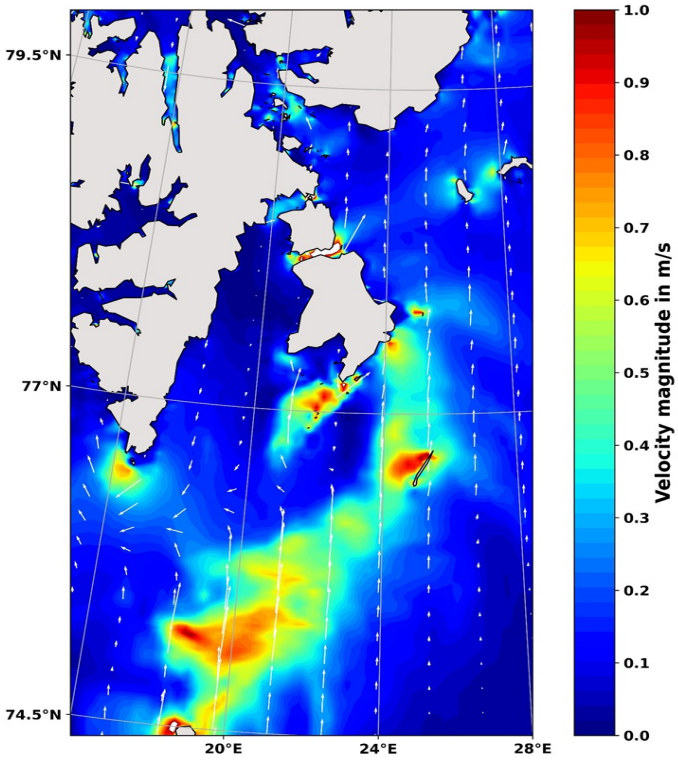

Figure 3.2.: Plots showing contours of tidal velocity magnitude with arrows showing the movement of tidal currents on March 31 at 00:00am. The plot is obtained by computations on GTSM. The length of the velocity vectors is scaled according the velocity magnitude.

The tidal currents seem to go from south to north while the beacon movements are north to south. This could be due to south-westerly winds as seen in the tidal ice dynamics study of Dmitriev et al., 1991 for the same area. In fact, Dmitriev et al., 1991 studied that under strong tidal forcing, elliptical shape traces are formed in the ice field signifying a tidal ice drift in the Marginal Ice Zone areas with ice concentration around 70%. These elliptical traces are essentially the sea ice

oscillations. In our Barents Sea experiment too, these sea ice oscillations are possible in the marginal ice zone with low sea ice concentrations.

The sea ice field conditions for parts of the beacon trajectories can be found in Kaleschke et al., 2016. It is seen that, (Figure 3 in the reference) during the experiment, in the region between Edgeøya and Svenskoya the sea ice had high compactness with no signs of leads. This implies that in this region there were high internal stresses. In fact, the stresses were so high that the ice was (almost) stationary and some of the beacons got stuck (see beacon 12 Figure 3.1). These high internal stresses could be a reason for the lack of oscillations observed in this region of the beacon trajectories. Now, as the beacons move south and start oscillating below the 78°N latitude it is important to know the nearby sea ice concentration. Using the high resolution (3.125 km) AMSR2 daily sea ice concentration product (Beitsch et al., 2014), the field of sea ice concentration is plotted for April 3 (Figure 3.3) along with all, then operational, beacon (6 of the 8) trajectories.

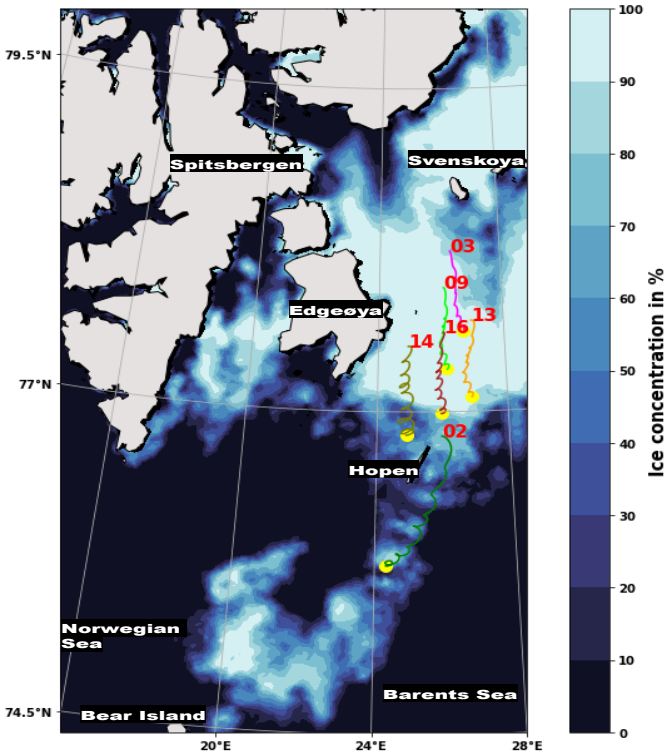

Figure 3.3.: Sea ice concentration obtained from the AMSR2 product for April 3. The individual beacon tracks are shown starting from March 31 with the yellow coloured markers showing the beacon positions on April 3.

The trajectories started from March 31 as post this date, all the beacons were well below 78°N latitude. On April 3, the beacons are mostly in the marginal ice zones

with sea ice field concentrations lower than 80%. Such zone is usually composed of relatively small ice floes and not a compact sheet and hence, the internal stresses in the ice field are low. For the beacon 09, which appears to be in a high concentration field, the sea ice field is far away from the coast of Edgeøya or Hopen for the ice field to have any forcing from the boundaries. In such sea ice, the internal ice stresses are relatively low. That said, this argument is also valid, later in time, when the beacons move towards south west and the ice field in the region extends up to Bear Island. Although, the arguments here are based on sea ice concentration field for one day, they are valid for concentration fields on other days as well. In Online Resource 3, one can find the sea ice concentrations for other days along with the beacon trajectories and one can also compare between the AMSR2 product and another sea ice product.

Based on these arguments, we can assume that the beacons move in sea ice field having low/no internal stresses and having concentrations mostly below 80%. In such a field, a free drift can be considered as a good approximation (McPhee, 1980; Leppäranta & Omstedt, 1990). Consequently, in this paper, we consider the beacon trajectories starting from March 31 and assume they are free drifting.

3.3. POINT ICE MODEL

We analyse the interaction between free drift sea ice and tides mathematically in an effort to validate the free drift equations governing the point ice model.

3.3.1. MATHEMATICAL ANALYSIS OF GOVERNING EQUATIONS

The governing equation of tides and free drift sea ice are compared. The momentum equation of tides in 2D hydrodynamic tidal models is essentially, the shallow water equations, given by:

$$\frac{d\boldsymbol{u}_t}{dt} + fe^{i\pi/2}\boldsymbol{u}_t = -g\boldsymbol{\nabla}\zeta_t - \frac{\boldsymbol{\tau}_b}{\rho_w H} + \nu\boldsymbol{\nabla}^2\boldsymbol{u}_t - \frac{\boldsymbol{\tau}_{wi}}{\rho_w H}, \tag{3.1}$$

where $\boldsymbol{u}_t$ is the water tidal velocity vector, ρ_w is the density of water, H is the water depth, ν is the kinematic viscosity of water, $fe^{i\pi/2}$ is the complex Coriolis parameter, $g(9.81\,\mathrm{m/s^2})$ is the acceleration due to gravity, $\boldsymbol{\tau}_b$ is the bottom frictional stress from the sea bed, $\boldsymbol{\nabla}\zeta_t$ is the pressure gradients from tidal sea surface heights and $\boldsymbol{\tau}_{wi}$ is the water-ice frictional stress at ice-water interface.

On the other hand, the sea ice free drift equation (Leppäranta, 2011a) in density averaged form is as follows:

$$\frac{d\boldsymbol{u}_i}{dt} + fe^{i\pi/2}\boldsymbol{u}_i = -g\boldsymbol{\nabla}\zeta + \frac{\boldsymbol{\tau}_{ai}}{\rho_i h_i} + \frac{\boldsymbol{\tau}_{wi}}{\rho_i h_i}, \tag{3.2}$$

where $\boldsymbol{u}_i$ is the ice-velocity, ρ_i is the density of sea ice, h_i is the sea ice thickness. Forcing $\boldsymbol{\tau}_{ai}$ is the frictional stress between the air-ice interface and likewise, $\boldsymbol{\tau}_{wi}$ is the water-ice frictional stress. $\boldsymbol{\nabla}\zeta$ is the gradient of sea surface heights.

Now, in the free drift sea ice equations, the forcing from sea surface heights and relative motion between ice-water interface consists of both, the ocean general

circulation and tidal component. As we are comparing to governing equation for tides, consider only the tidal oceanic forcing in the free drift Equation (3.2).

Comparing Equation (3.1) and (3.2) shows that the Left Hand Side (LHS) are the same implying the homogeneous solutions, and consequently the inertial solutions, will be the same in both the cases.

Comparatively, the Right Hand Side (RHS), both the Equation (3.1) and (3.2) have similar terms apart from the bottom friction drag and diffusion term in the tidal equations and wind/air-ice drag in the ice drift equations. In deeper and open oceans, for the tidal model Equation (3.1), the bottom frictional stress will be small for larger depths ($H >> 1$) and can be neglected. Furthermore, as there are no straits or regions in open oceans which can cause strong vorticity the viscous diffusion term is also negligible. On the other hand, in the case of free drift model Equation (3.2), under no wind, the drag from the wind is not present.

Ultimately, in both the cases (Equation (3.1) and (3.2)) only two terms remain on the RHS of the equations-the gradients from the sea surface heights which is same in both the cases and the water-ice frictional stress but with a different scaling based on ocean depth.

Thus, we can say that both the tidal model equations and ice drift equation are similar and can expect the sea ice drift to be similar to the tides in such a situation of deeper and open oceans. This conclusion is in accordance with McPhee, 1978 who also make these simplifications.

Then, an integrated ice-ocean equation would have only the pressure gradient forcing from the sea surface heights on the RHS as the external forcing driving the ocean and sea ice together. As a result, the cause of free drift sea ice oscillations is the same as the cause of tides i.e. the gradients of sea surface heights, implying that the dissipation between sea ice and tides is non-existent.

Based on this analysis, it is clear that for shallow water regions, strong vorticity regions, like straits, and for strong winds there is a velocity difference between sea ice and tides and as such, this might lead to dissipation in the interface. Now we describe our point model in the next section.

3.3.2. MODEL FORMULATION

To use a physics-based approach for separating the tidal and inertial signals, a point ice model was developed with free drift assumption in the Spitsbergen Shelf region. The model governing equations are given by Equation (3.2). As noted in Leppäranta, 2011a the air-pressure gradient term in the ice-drift is minor and can be neglected.

It should be noted that we assume a constant sea ice density of $\rho_w = 920\,\mathrm{kg/m^3}$ and a constant sea ice thickness $h_i = 1\,\mathrm{m}$. The sea ice velocity, $\boldsymbol{u}_i (= [u_i, v_i]^T)$ is a velocity vector of a point particle which makes d/dt as the total derivative. Here, u_i is the west-east/longitudinal or zonal velocity and v_i is the south-north/latitudinal or meridional velocity. Each of the beacon trajectories can then be simulated in time, based on point particles for each beacon, which are released at the start of the beacon trajectories at $t = 0$.

The shear stress terms based on a quadratic drag law (McPhee, 1982; Brown, 1981)

are given by:

$$\boldsymbol{\tau}_{ai} = \rho_a C_a (\boldsymbol{u}_a - \boldsymbol{u}_i)|\boldsymbol{u}_a - \boldsymbol{u}_i|, \tag{3.3}$$

$$\boldsymbol{\tau}_{wi} = \rho_w C_w (\boldsymbol{u}_w - \boldsymbol{u}_i)|(\boldsymbol{u}_w - \boldsymbol{u}_i)|, \tag{3.4}$$

where ρ_a (1.2 kg/m^3) and ρ_w (1024 kg/m^3) are densities of air and water respectively, $\boldsymbol{u}_a$ is the surface air velocity, $\boldsymbol{u}_w$ is the surface water velocity, $C_a (= 1.2 \times 10^{-3})$ and $C_w (= 5.5 \times 10^{-3})$ are the coefficients of drag between the air-ice and water-ice interface whose values are obtained from McPhee, 1982 and Brown, 1981 and assumed to be constant. Wind drag is a term used interchangeably to refer to air-ice drag in this paper.

The point ice model represented by Equation (3.2) is an Ordinary Differential Equation (ODE) with a time dependent non-linear inhomogeneous term. To evaluate the inhomogenous component in the model, we would need the wind and water velocities as well as the sea surface heights at each time instant. Now, this model is a simple, *standalone* sea ice model implying there is no coupling to any tidal, atmospheric or ocean circulation model. So, the simplification is that the required water levels, water velocities and wind data are obtained from existing and validated models or published datasets. These are then interpolated in space and time to the observed positions of the beacons at the respective time. This gives us a time series for wind and water velocities and gradients of sea surface heights with the values at each time being essentially the value from the corresponding dataset/model at the beacon position for the time. This serves a two-fold purpose, first by giving the point ice model the required data to compute the shear stress' and sea level gradient forcing in the model. And second, that interpolating the data to real-time beacon positions can be thought of as a one-way coupling or feedback between the point ice model and the other models.

Once these datasets are obtained, our point ice model is discretized using a Runge-Kutta 2 method with a constant time step of 30 s. The model then simulates only the ice velocities based on the forcing as per Equation (3.2) where the external forcing are based on actual beacon positions.

3.3.3. EXTERNAL DATASETS/MODELS

Three datasets (Table 3.1) are used to obtain the water levels, water velocities and wind data. The wind velocities are obtained from the ERA5 hourly reanalysis product (Hersbach et al., 2018), while, for the water velocities we need two different dataset as the beacons are forced by both the ocean general circulation currents (ocean currents) and the tidal currents. Hence, the water velocity ($\boldsymbol{u}_w$) is obtained as a linear combination of both, i.e. $\boldsymbol{u}_w = \boldsymbol{u}_o + \boldsymbol{u}_t$, where $\boldsymbol{u}_o$ is the ocean currents component in water velocity and $\boldsymbol{u}_t$ is tidal currents component in water velocity. Similarly, the sea surface gradients are computed as the sum of the gradients from the sea surface heights obtained from the ocean general circulation model and tidal model ($\nabla\zeta_o + \nabla\zeta_t$, where the subscripts o and t denote ocean and tide respectively). The ocean circulation data are obtained from a global ocean analysis forecast product of CMEMS (Copernicus Marine Service, 2014) and the tidal data is obtained

from the GTSM (Verlaan et al., 2015; Muis et al., 2016). After obtaining the data from the datasets, they are processed to derive the respective time series for each beacon needed to run the point ice model. The time series for velocities follow from the space-time linear interpolation. For the pressure gradient computation, spatial interpolations used a cubic 4 point interpolation and temporal interpolations were linear. The spatial gradients were computed using finite differences over a distance of 2.5km. The grid step for the gradient computation is large compared to the beacon movement in the small model time step (30s). The 30s time step for the point ice model is only needed for stability of the explicit scheme and can likely be increased for an implicit scheme. The main time scale here, is tidal and on these time scales, grid step of 2.5km is enough as tides do not change significantly over very short distances in open water.

Type	Dataset	Grid Resolution	Time Res.	Variables	Time Span (2014)
Winds	ERA5 hourly reanalysis (Hersbach et al., 2018)	$0.25^\circ \times 0.25^\circ$	hourly	u10, v10 (10 m wind)	March 1 to May 16
Ocean	GLOBAL OCEAN ANALYSIS FORECAST E.U. Copernicus Marine Service, 2014	$1/12^\circ$	hourly	u, v, ssh at 0.45 m depth	March 15 to May 16
Tides	Global Tide and Surge Model v3.0 (Verlaan et al., 2015; Muis et al., 2016)	5 to 25km	15mins	u, v, ssh	March 15 to May 16

Table 3.1.: Description of the operational or published datasets for wind, ocean and tides and the corresponding variables used to build the point model.

3.3.4. MODEL VALIDATION

The point model simulated beacon velocities are obtained with the initial condition for the model runs given by the observed initial velocity. These simulated velocities are compared to the observed velocities for all the beacons. Here, we show comparison for beacon 16 (Figure 3.4) where it is seen that the modelled time series' are very similar to the observed, especially in the initial part, for both, the longitudinal u_i and latitudinal v_i velocity. But, in time as the errors accumulate the differences increase between the modelled and observed values. Also, both, u_i and v_i velocities, have similar order of magnitude in modelled and observed values. The plots for remaining beacons show a similar behaviour (see Online Resource 1).

In the next test, we integrated the modelled velocities to obtain the simulated beacon positions and compared those to the observed ones. The velocity integration started with initial beacon position being obtained from the beacon observations. In general, we observe differences (Figure 3.5) in the model-simulated beacon trajectories and corresponding observed trajectories for all 6 beacons. But, the generic shape of the trajectories is captured fairly well. Particularly, the modelled beacon 14 (Figure 3.5e) seems to have almost the same trajectory as observed. Beacons 03 and 16 (Figure 3.5d, 3.5f) have the longest trajectories and their overall trajectories appear to be rotated clockwise (or towards west) in the simulations compared to the observations. Similar rotations are observed for trajectories of beacons 09 and 13 (Figure 3.5c, 3.5d). The largest differences are seen for the simulated trajectory of beacon 02 (Figure 3.5a). Further, it is noteworthy that in

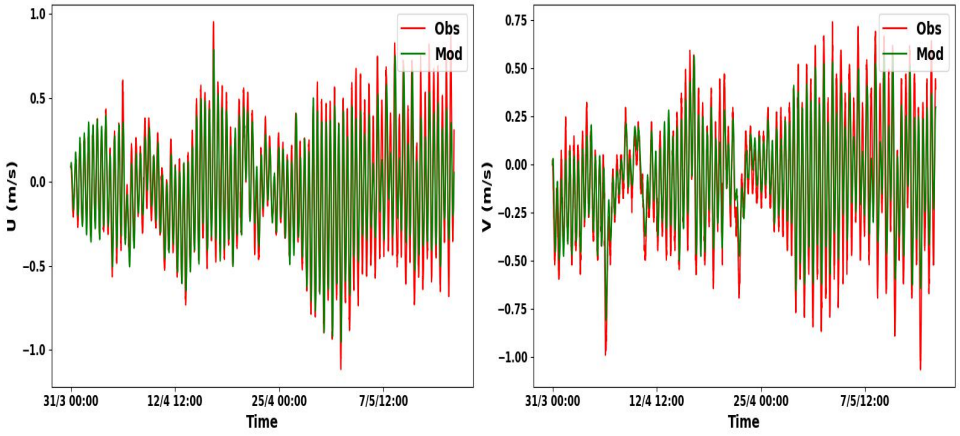

Figure 3.4.: Time series plot for the longitudinal (u_i) (U in plot) and latitudinal (v_i) (V in plot) velocities for beacon 16. Observations are in red and point model simulations are in green. Time on the $x-$axis is given in format DD/M HH:MM with year being 2014. The velocities are plotted at the same time of the observations of the beacon positions, and thus, are separated by a time step of 15 min.

the plot we can only see differences in locations of the beacons but there may be differences in time as well. Another noteworthy aspect is that the modelled trajectories of beacons 03 and 09 (Figure 3.5b and 3.5c) tend to go over the land boundary. This can be attributed to the fact that forward integration is used in our model and thus, it would not know about the presence of land bodies while computing the trajectory.

These discrepancies noted in the trajectories could have numerous reasons. First and foremost, the forward integration accumulates the velocity errors. Second, the model parameters (ice thickness and drag coefficients) are assumed to be constant, whereas in reality they could vary. Third, this point model is forced using output from external ocean, tidal and atmospheric models. Thus, there is no feedback from the ice solution on the ocean or tidal solutions. This could lead to artificial sea ice tidal response (Hibler et al., 2006). But using in-situ beacon positions, gives a priori knowledge of the ice response and hence, this factor can be alleviated to some extent. Additionally, the uncertainties or errors in the ocean, tidal and atmospheric models can also propagate in the point model simulations. Finally, the observed trajectories seem to move faster south of 76° latitude. This can be caused by the errors in ocean currents or winds, but also by the model itself. This is especially noticeable for the worse performing beacon 02 (Figure 3.5a).

Nonetheless, our study focuses on the subdaily motion and the above observed discrepancies in trajectories should not be of major concern if the subdaily motion is correctly modelled. As seen from the plots (Figure 3.5), not only the shape of the trajectories but also the clockwise loops (sea ice oscillations) are captured in the simulations. An analysis of these subdaily loops of the simulations will shed light on

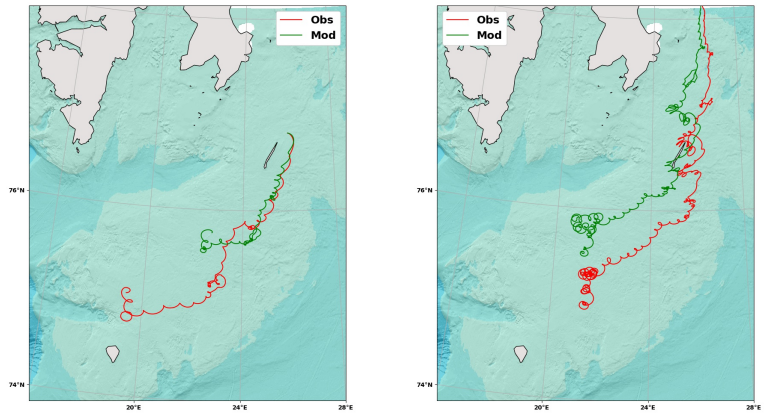

(a) 02

(b) 03

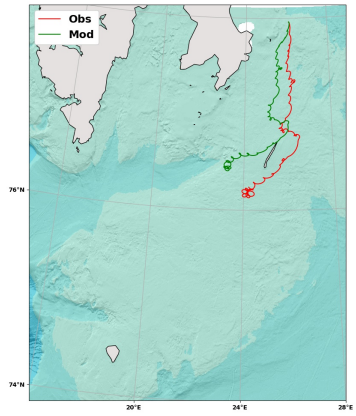

(c) 09

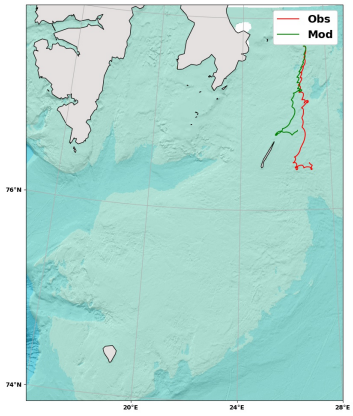

(d) 13

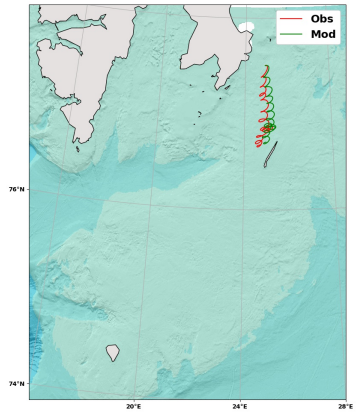

(e) 14

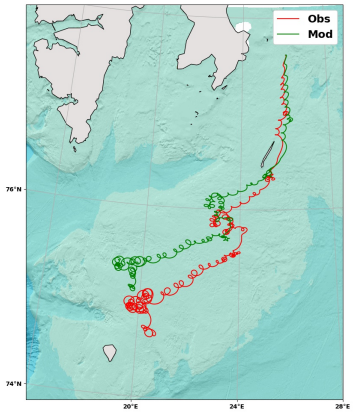

(f) 16

Figure 3.5.: Modelled drift trajectories for the beacons against the observed trajectories. The caption under each figure gives the beacon number. All the modelled trajectories are computed using a constant ice thickness of 1.0 m. The start date and time for all the simulations is chosen as March 31, 00:00 am because post this all the beacon trajectories are below 78°N latitude.

the validity of our model.

The sea ice motion, as also seen in beacon trajectories, is made up of subdaily oscillations superposed with daily mean drift. The equation for this is given by:

$$\boldsymbol{u}_i = \boldsymbol{u}_{it} + \boldsymbol{u}_{io}, \tag{3.5}$$

where $\boldsymbol{u}_i$ is the sea ice velocity vector or, in this case, the beacon velocities, $\boldsymbol{u}_{it}$ represents the subdaily oscillations (high-frequency) in the sea ice velocity and $\boldsymbol{u}_{io}$ is the mean drift (low-frequency) in the sea ice velocity.

Next, we aim to validate the model-derived variability at subdaily time scales. In doing so, we will compare for beacons 02, 03, 09, and 16 the spectra of the model-derived time series to the spectra of the observation-derived ones. Beacons 13 and 14 are excluded from this analysis, because their length does not allow resolving the tidal frequencies M_2 and S_2 dominant in the area of interest. This requires a minimum length of 14 days (Rayleigh criterion). The spectra are computed using a discrete Fourier transform (DFT), where a scaling of $2/N$ (N is the number of points in the truncated signal) is applied to obtain the amplitudes. Given our interest in the subdaily oscillations and to reduce spectral leakage, prior to the DFT a high-pass filter is applied. Spectral leakage is the inevitable consequence of applying a DFT to a finite data record. The high-pass filtering has been conducted by subtracting the low-pass filtered time series from the all-pass filtered time series. Here, we have used a Hamming low-pass filter with a cut-off frequency of 24 h (given the 15 min sampling interval this corresponds to a length of 97 ($N_w = 97$)). To remove the part of the low-pass filtered signal affected by the warming-up and cooling-down phase of the filter, we should remove the first and last $N_w - 1$ data points. Given the fact that our time series are quite short (between 16.8 and 46.0 days), we decided to remove only the first and last $(N_w - 1)/2 = 48$ data points. The resulting time series, shortened by one day, are denoted by $\boldsymbol{u}_{it} = [\delta u, \delta v]^T$, where west-east/longitudinal (δu) and south-north/latitudinal (δv) velocity time series are the subdaily oscillations in respective directions.

To further reduce spectral leakage, we truncated the high-pass filtered time series such that they include (approximately) an integer number of tidal cycles. Given the dominance of M_2 (period of 12.42 h) and S_2 (period of 12 h), the length of the time series should be an integer number of 15 days. As such, we truncated the length of beacons 02 and 09 by 0.8 and 0.9 days, respectively.

The resulting amplitude and phase spectra are plotted in Figure 3.6, along with the M_2, S_2, MU_2, and M_4 tidal and Coriolis/inertial frequencies (corresponding to 74.7°N and 79°N latitudes).

The first and most important aspect from the spectra is that the (peak) maximum amplitude for all the beacons occurs at a frequency which is close to the semi-diurnal tidal and inertial frequencies corresponding to 74.7°-79°N latitudes. In this region of the Barents Sea, M_2, S_2, and inertial forces are dominant as noted in Section 3.2. Thus, these observed peaks have a physical origin. However, the magnitudes of these observed maximum amplitudes vary for each beacon, ranging from 0.1 m/s to 0.2 m/s with beacon 09 (Figure 3.6e,3.6f) having the lowest and beacon 16 (Figure 3.6g,3.6h) having the largest amplitudes. It should be noted that this Fourier

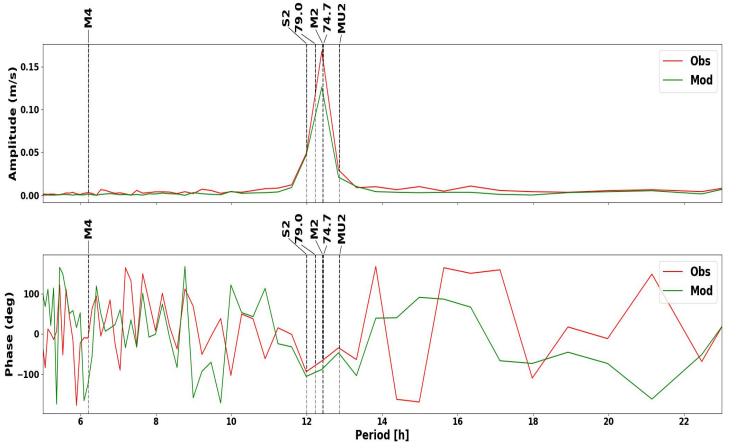

(a) 02:U

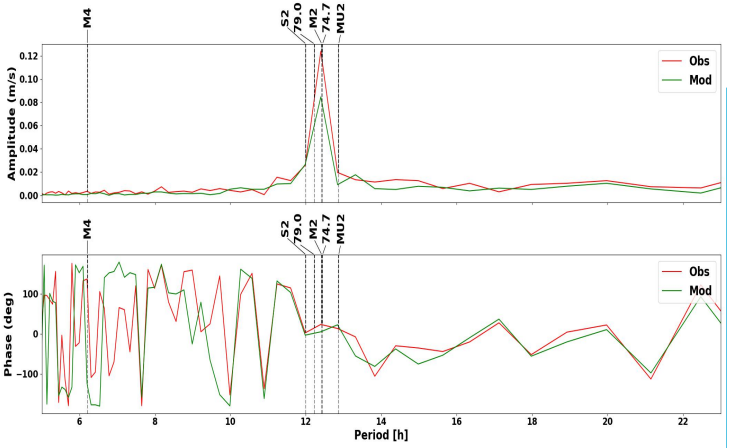

(b) 02:V

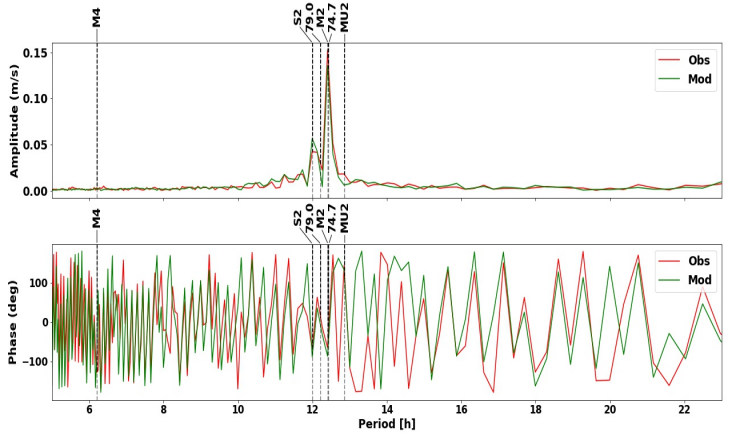

(c) 03:U

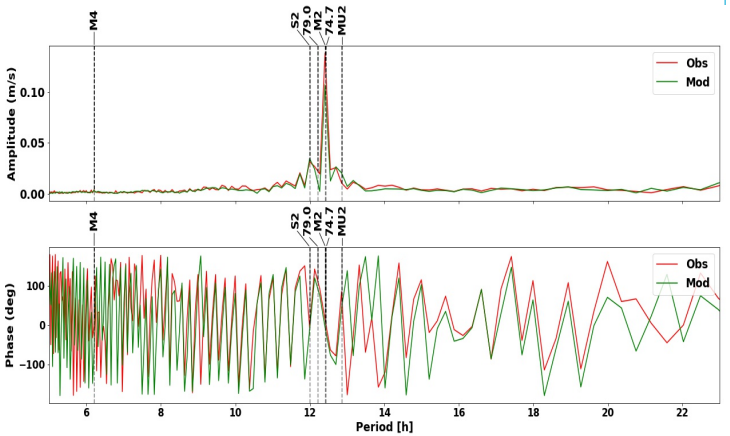

(d) 03:V

Figure 3.6.: Amplitude and phase plots of the velocities from beacon observations (red) and point model simulations (green) against time periods in the oscillations. The periods are in subdaily range (i.e. high frequency) from 5h to 23h. Apart from the inertial and tidal frequencies denoted by dotted lines, the remaining high frequency spectra are red noise. The subfigure captions denote the beacon number and the U and V correspond to δu or δv velocity respectively.

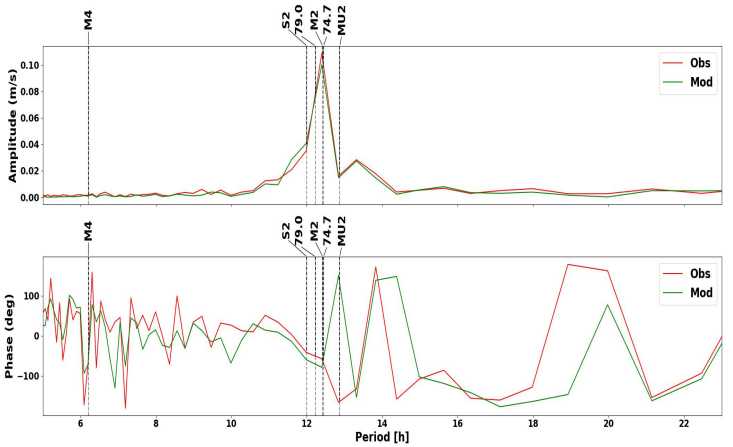

(e) 09:U

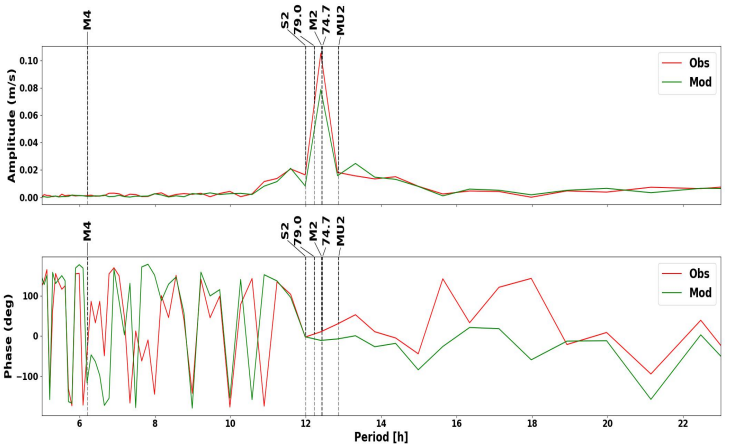

(f) 09:V

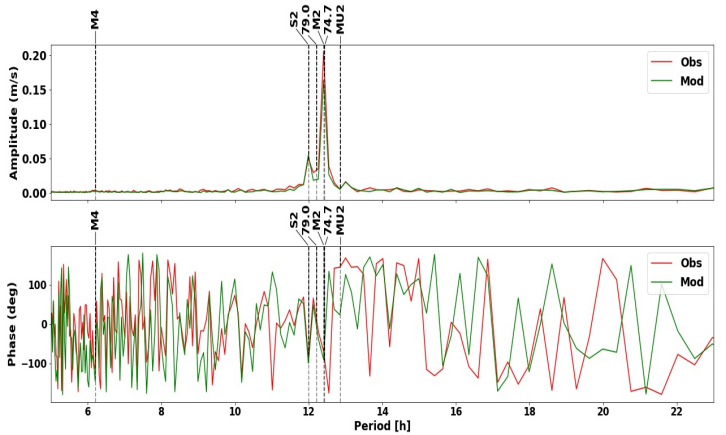

(g) 16:U

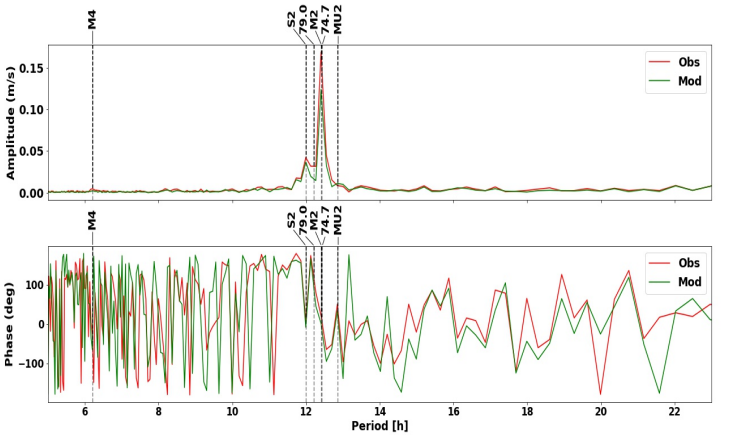

(h) 16:V

Figure 3.6.: Amplitude and phase plots of the velocities from beacon observations (red) and point model simulations (green) against time periods in the oscillations. The periods are in subdaily range (i.e. high frequency) from 5h to 23h. Apart from the inertial and tidal frequencies denoted by dotted lines, the remaining high frequency spectra are red noise. The subfigure captions denote the beacon number and the U and V correspond to δu or δv velocity respectively.

transform approach averages the changes in the oscillations over the entire time series which implies that the obtained/plotted amplitudes and phases here are time averages of the beacon trajectory.

Comparing the observed and modelled Fourier transforms (Figure 3.6), it can be seen that both the spectra have similar order of magnitudes of the amplitudes and phases at the tidal and inertial frequencies for all four beacons. For frequencies with low amplitudes, the phase, naturally, becomes very uncertain which is probably the reason for the noisy phases in the spectra.

Of the semi-diurnal frequencies, it is seen that the maximum amplitude in both the observed and modelled spectra occurs at the M_2 frequency. But the magnitudes of the modelled amplitudes for the dominant M_2 frequency are consistently lower than the observed amplitudes. In a more quantitative sense, the modelled amplitude at the M_2 frequency for δu and δv velocity oscillations are anywhere between $70-95\%$ of the observed values for all four beacons. Thus, based on the above qualitative comparison coupled with a good accuracy at the dominant M_2 frequency one can say that our 'simple' point model reasonably captures the amplitude and phase spectra as compared to the observed spectra. As such, our model is suitable to perform further analysis on the subdaily sea ice oscillations even if it does not reproduce the trajectories accurately. Next, we will evaluate the dissipation between the sea ice-tide interface by performing two analyses which study the correlation and causality of sea ice oscillations.

3.4. CORRELATION BETWEEN SEA ICE OSCILLATIONS AND TIDES

3.4.1. AIM AND METHODOLOGY

The aim is to investigate the relationship between tidal currents and the sea ice oscillations by comparing the observed oscillations to the point model oscillations and the tidal currents from the GTSM in the Barents Sea region.

For this analysis, we use the subdaily sea ice velocity signals (δu and δv) of point model simulations and observations obtained previously (Section 3.3) by high-pass filtering the beacon velocities. To compute the tides, the GTSM was run without any atmospheric forcing and as mentioned before, it does not include the effect of sea ice on tides. Thus, the tides can be considered independent of the wind and sea ice effects. To study the relationship, the velocity vectors of the subdaily oscillations (modelled and observed) and tidal velocity vectors are plotted on a time axis. The relationship is further quantified by computing the corresponding correlation coefficients.

3.4.2. RESULTS AND DISCUSSION

For each beacon, we have two plots, the vectors of beacon observations versus tidal velocity vectors and the vectors of beacon observations versus vectors of point model simulations. The plots for beacon 16 (Figure 3.7 and 3.8) are presented and discussed here.

It can be seen that all the velocity vectors loop clockwise along the time axis. This resembles the loops formed by an elongated spring where the loops have different radii corresponding to the magnitude of the vectors. One can view these plots as tidal ellipses stretched over time, but, since the beacon moves over time the shape of the ellipse depends on the tidal currents at the beacon location. On comparing the loops of the tidal velocity vectors or tides against the observations in Figure 3.7, it is seen that, in general, the highs and lows of the oscillations (vector magnitudes) occur at almost the same times and the loop inclinations (vector directions) are also, almost, the same throughout the length of the series. In the initial period, the tidal vectors and observed oscillations are seen to have a better match in terms of the magnitude and direction of the vectors. And, towards the end, the observations have a larger magnitude than the tides and their directions seem rotated. The larger amplitudes of the observed oscillations towards the end for this beacon is also evident from the larger loops/tidal ellipses in its trajectory (Figure 3.5f) in the region around Bear Island. The tidal currents (Figure 3.2) are also stronger in this region which hints to a correlation between the two. Another interesting part is when the tides seem to have died out or tidal velocity vectors have low amplitudes (Figure 3.7; time period April 7 to April 12) the corresponding observations are also very low, and, are almost of the same magnitude. Thus, it can be concluded that the observed oscillations and tidal velocity vectors have similar highs and lows along the entire time series.

Such a similar behaviour is also observed in the case of comparison between observed and modelled oscillations (Figure 3.8) with a difference only in the initial part of the trajectory where the point model oscillations are smaller (vector magnitudes lower) and the oscillations tilted to right (vectors are rotated clockwise). It implies that the point model captures the subdaily oscillations fairly well and is an additional validation of the point model results. For other beacons (plots shown in Online Resource 2), similar conclusions can be drawn.

To further quantify the agreement between the observed oscillations on the one hand and the tidal velocity vectors and the point model oscillations on the other hand, correlation coefficients were computed for the δu and δv velocities (Table 3.2). This is done for each of the 6 beacons.

	02		03		09		13		14		16	
	U	V	U	V	U	V	U	V	U	V	U	V
Tides-Obs	0.89	0.82	0.82	0.80	0.90	0.83	0.91	0.82	0.93	0.90	0.86	0.83
Mod-Obs	0.91	0.92	0.86	0.89	0.93	0.89	0.92	0.86	0.94	0.95	0.91	0.92

Table 3.2.: Correlation between beacon observed sea ice oscillations, GTSM derived tidal currents and point ice model based sea ice oscillations. The U and V represent the δu and δv velocity of the oscillations, respectively.

The correlations in both the cases are positive and large (> 0.8, for all beacons) suggesting a direct and strong relationship between the tides and sea ice oscillations. This in turn implies that the sea ice oscillations and the corresponding tidal currents move together in Barents Sea region. Moreover, it implies that the sea ice oscillations

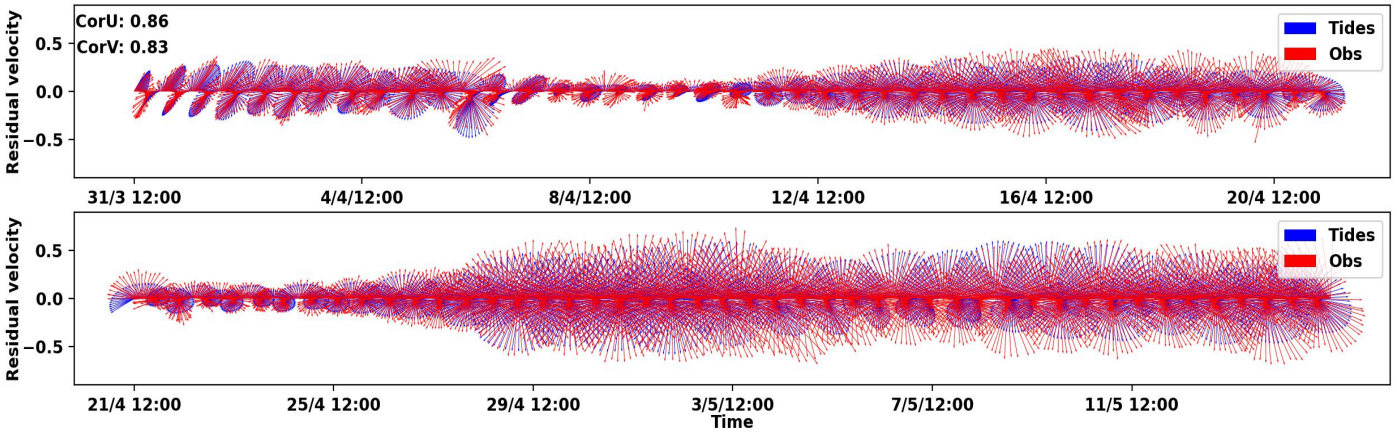

Figure 3.7.: Velocity vector plots of the time series of sea ice oscillations (δu and δv) with observations (red) and GTSM tides (blue) for beacon 16. The residual velocity vectors imply that the mean drift is removed from the beacon trajectories and the resulting subdaily residuals are plotted.

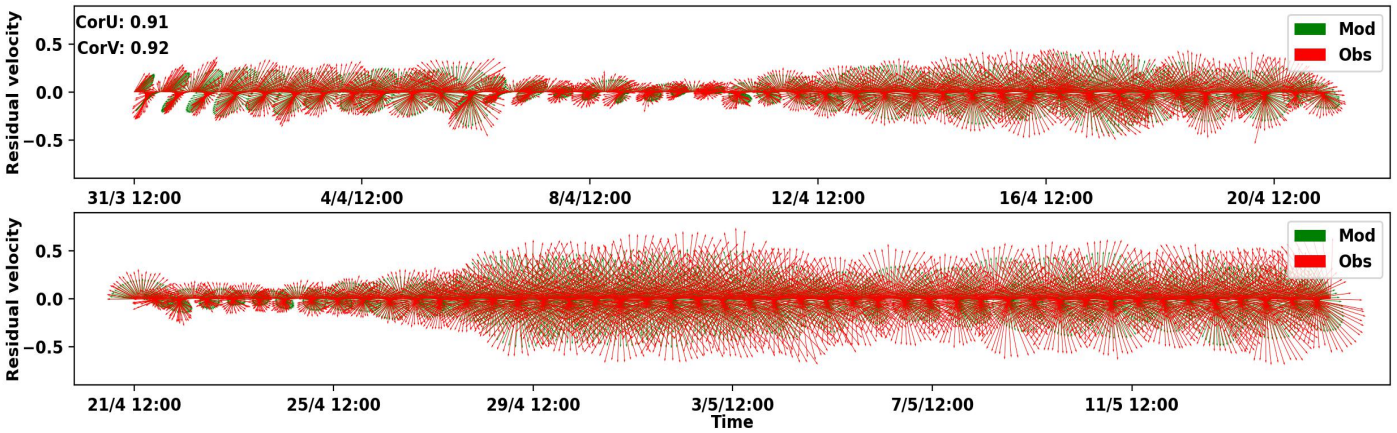

Figure 3.8.: Velocity vector plots of the time series of sea ice oscillations (δu and δv) with observations (red) and point model oscillations (green) for beacon 16. The residual velocity vectors imply that the mean drift is removed from the beacon trajectories and the resulting subdaily residuals are plotted.

have a dominant tidal signal as opposed to an inertial signal, a conclusion in line with Pease et al., 1995.

The correlation between observed and point model oscillations is similar to the observed oscillations and GTSM tidal current oscillations. This means that the forcing responsible for tides in GTSM and point model are similar suggesting that the tidal forcing could be a major cause of sea ice oscillations in this dataset. Next section will verify this with a sensitivity analysis.

3.5. CAUSALITY OF SEA ICE OSCILLATIONS

3.5.1. AIM

We have shown a strong and positive correlation between sea ice oscillations and tides/tidal currents. However, *correlation does not imply causality.* The cause of the sea ice oscillations is still unknown. There are many possible forcing which could cause the subdaily sea ice oscillations like, inertia or Coriolis forcing, wind drag (air-ice drag), pressure gradients from the sea surface heights associated with tides or the water-ice drag from tidal currents. Here, we aim to study the cause of the sea ice oscillations. When coupled with the previous analysis this will help to determine the energy dissipation between the sea ice-tide interface. We start by establishing an hypothesis, formed by performing a preliminary analysis of the dynamics between sea ice and tides followed by sensitivity tests to verify the hypothesis.

3.5.2. PRELIMINARY ANALYSIS OF THE DYNAMICS

From the results shown in Section 3.4, we hypothesize that tidal forcing is the major cause of sea ice oscillations. Moreover, from the equations of point model or free drift model (Equation (3.2)) it is clear that this forcing comprises of the pressure gradients from the tidal sea surface heights and water-ice tidal drag. One can argue that, in practice, these two are always present together, yet it is important to evaluate which of the two is the primary cause of the sea ice oscillations.

If it is pressure gradient forcing then it follows that the tidal model and sea ice model are forced by the same forcing and the bottom frictional stress from the shallow water region or the viscous term does not play a significant role. In such a case, the water-ice drag term is comparatively low and the connection between sea ice and tide is not strong, consequently, giving us a negligible dissipation from drag in the sea ice and tide interface. On the other hand, if water-ice drag term is the primary cause of the sea ice oscillations then the stress from this term is significant and the connection between sea ice and water is strong. This would further mean that the dissipation between the ice-tide interface needs to be evaluated to ascertain the nature.

To evaluate a priori which of the above two forcings might be a cause, we conduct a scaling analysis on Equation (3.2).

Consider U, H and T as scaling factors for the velocity, ice thickness and time, respectively. Then the subdaily (or tidal scale) ice velocity can be written as $\boldsymbol{u}_{it} = U\boldsymbol{u}^*_{it}$. Similarly, the remaining terms in the ice-drift Equation (3.2) are written

as $t = Tt^*$, $h_i = Hh_i^*$, $\boldsymbol{u}_t = U\boldsymbol{u}_t^*$.

Now, assuming that the water-ice drag from tides is a major significant force we have the local/inertial acceleration term equated with this drag which is further scaled with $\rho_w C_w U^2$ (water-ice tidal drag). Thus, the equation looks like,

$$\begin{aligned} &\rho_i h_i \frac{\partial \boldsymbol{u}_{it}}{\partial t} = \boldsymbol{\tau}_{wi}, \\ \Rightarrow &\frac{\rho_i HU}{T} \frac{\partial \boldsymbol{u}_{it}^*}{\partial t^*} = \rho_w C_w U^2 (\boldsymbol{u}_{it} * - \boldsymbol{u}_t^*)^2, \\ \Rightarrow &\frac{\rho_i H}{\rho_w C_w UT} \frac{\partial \boldsymbol{u}_{it}^*}{\partial t^*} = (\boldsymbol{u}_{it} * - \boldsymbol{u}_t^*)^2. \end{aligned} \tag{3.6}$$

The factor $\frac{\rho_i H}{\rho_w C_w UT}$ is the Strouhal's number (Sr). As we know that M_2 is the dominant frequency in the sea ice oscillations in the Barents Sea and also, it is very close to the inertial frequencies in the region, consider T as $T_{M_2} (\sim 4.4 \times 10^4 \text{s})$. Also, assuming $H = 1\text{m}$ and $U = 0.1\text{m/s}$ the value of $Sr \sim 3 \times 10^{-2}$. Thus, $Sr << 1$ which implies $\boldsymbol{u}_{it}^* \approx \boldsymbol{u}_t^*$ as per Equation (3.6). Thus, the sea ice oscillations and tidal velocities/tidal currents must be similar. As a result, the sea ice will be dragged along with the tides attaining almost the same velocity as tides. This would mean that the nonlinear connection between sea ice and water is strong and the water-ice tidal drag is large and a possible major cause of sea ice oscillations.

One can also calculate the time-scale for which the terms become of comparable magnitude, i.e. $Sr \sim 1$. Consequently, $T \sim 1.6 \times 10^3 \text{s}$ or approximately 0.5h is the actual inertial timescale of sea ice drift. Thus, on an M_2 tidal time scale, the sea ice attains a steady state equilibrium condition. Similar timescale of $T \sim 10^3 \text{s}$ is also shown in Leppäranta, 2011b.

As most of the sea ice is in steady state equilibrium on M_2 tidal time scale, we study the case of steady state ice drift equation but with only the pressure gradients from tidal sea surface heights to understand the significance of the forcing. The Equation (3.2) then, reduces to:

$$f e^{i\pi/2} \boldsymbol{u}_g = -g \boldsymbol{\nabla} \zeta_t. \tag{3.7}$$

This is a form of the geostrophic flow equation, where $\boldsymbol{u}_g$ is the steady state ice velocity originating only from the pressure gradient of tidal sea surface heights. The velocities are computed using the above equation for all the beacon trajectories. Then the mean of the magnitude of the resulting velocities ($|\overline{\boldsymbol{u}_g}|$) along the beacon trajectories is compared to the mean of the magnitude of tidal velocities ($|\overline{\boldsymbol{u}_t}|$) along the beacon trajectories. Then, for all the beacons we see that, $|\overline{\boldsymbol{u}_g}| \sim 20\%$ of $|\overline{\boldsymbol{u}_t}|$. Now, from the analysis present in Section 3.4, we know that the tidal velocities and subdaily sea ice velocities are very close. As a result, it can be said that forcing from pressure gradients of tidal sea surface heights might contribute around 20% to the sea ice oscillations. Hence, this forcing, although a cause of sea ice oscillations, is probably not a dominant one for this Barents Sea dataset.

Based on the above mathematical analyses we hypothesise that the water-ice tidal drag is the major reason behind the sea ice oscillations in this Barents Sea dataset.

3.5.3. SENSITIVITY ANALYSIS ON THE FORCING

To evaluate the hypothesis and strengthen our understanding, we perform a number of sensitivity tests on the beacon dataset for all the forcing and not only the tidal forcing. These tests are done on the parameters of the sea ice model Equation (3.2). In this analysis, the effects of different model and forcing parameters on the sea ice oscillations are assessed by switching the respective parameter or forcing off and running the model. The resulting model runs are compared to the *reference* model runs and the observations. Reference model here is defined as the model where all the forcing from the Equation (3.2) are included and the model results are the ones discussed in Section 3.3. Such a comparison provides the magnitude of the effect that respective forcing has on the sea ice oscillations.

As observed previously (Figure 3.6), the M_2 frequency is the dominant one in the observed oscillation spectrum and this is also very close to the inertial frequencies. Hence, we use the amplitude and phase at a frequency which falls close to the M_2 frequency in the observed and modelled spectra of oscillations as a comparison metric. And furthermore, the oscillations at this frequency will be referred to as *M_2 frequency oscillations*. Thus, for comparison the amplitude and phase of the M_2 frequency sea ice oscillations (δu_i and δv_i) are obtained from the reference model runs and model runs without a particular forcing parameter from Table 3.3.

Forcing	Parameters
Sea ice inertia	h_i
Wind Drag forcing	$\boldsymbol{u}_a$
Tidal forcing	$\boldsymbol{u}_t$;$\nabla\zeta_t$

Table 3.3.: Sensitivity tests conducted on the point model forcing and corresponding parameters. It should be noted that only the given parameters above are switched off in the respective tests, the remaining parameters are still present in the model simulations.

For the sea ice inertia (Table 3.3), the test involves performing model runs for varying sea ice thicknesses from 0.5 m to 3.0 m. Here it should be noted that the reference model thickness was 1.0 m. In the case of wind drag forcing, the test involves running the model by just switching off the winds ($\boldsymbol{u}_a$).

The last of the sensitivity analyses is based on tidal forcing where two tests were performed, one without pressure gradients from tidal sea surface heights (tidal pressure gradient forcing) and one without the tides/tidal currents in the water-ice drag. Note that removing the tides in water-ice drag is equivalent to not considering water-ice tidal drag when we are evaluating M_2 frequency oscillations.

The sensitivity analysis for ocean currents and their corresponding pressure gradients is not conducted because they have no tides in them and thus, they will not cause M_2 frequency oscillations.

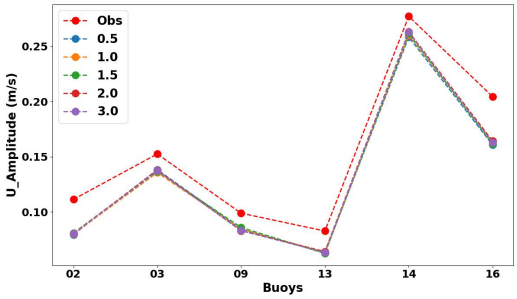

(a) U Amplitude

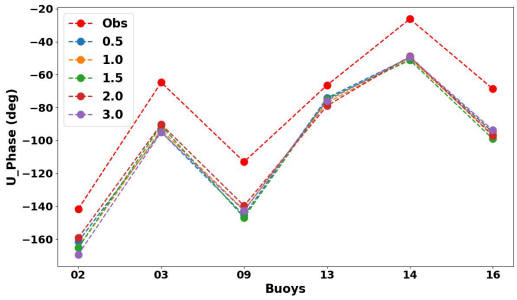

(b) U Phase

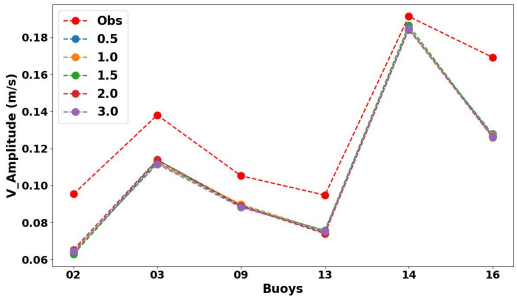

(c) V Amplitude

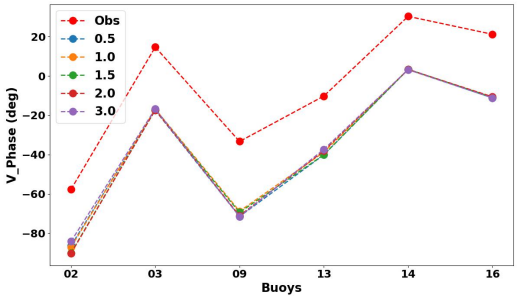

(d) V Phase

Figure 3.9.: Plots of M_2 amplitudes and phases of the δu and δv (in the sub-figures referred to as U and V, respectively) velocity components of the sea ice oscillations against the beacons. The beacon observations (red) are compared against the point model simulations with varying sea ice thicknesses. The M_2 frequency amplitude and phase are obtained from the Fourier transform plots (Figure 3.6).

EFFECT OF ICE THICKNESS

The results (Figure 3.9) shows that for all thicknesses and all beacons, observations have a larger amplitude and their phase is lagging for both the δu and δv velocity compared to model runs. The values of the amplitudes of the δu and δv velocity beacon observations vary from 0.1 m/s to around 0.25 m/s which is in line with the values noted in Section 3.3.

There are small variations in the amplitudes of the δu and δv velocity components in the model runs with varying sea ice thicknesses for all the beacons. These minor variations in the amplitudes and phases are low enough to be ignored and it can be said that the sensitivity analysis shows no effect of sea ice thickness on the amplitude and phase of M_2 frequency oscillations for a broad range of sea ice thicknesses for the beacon dataset. This is in line with Omstedt, 1980, who found using a sensitivity analysis of steady-state free drift sea ice motion that sea ice mass has no significant effect on free drift of sea ice.

The lack of any significant effect can also be seen from a dimensional analysis as presented in Section 3.5.2 where we evaluated based on Strouhal's number that the sea ice inertial timescale is $T \sim 0.5$ h. Now, the time scale of the M_2 tide is $T_{M_2} \sim 12.42$ h. Consequently, for sea ice thickness to have any significant effect on the oscillations at the M_2 frequency it should have a thickness of around 20 m for $U = 0.1$ m/s. This is unrealistic.

However, note that the results in Figure 3.9 are valid only when the model assumes a free drift sea ice. This is because even for the case of 2 m or 3 m thick ice (Figure 3.9) the sea ice internal stresses start to play a role and its effect on sea ice oscillations might be different.

EFFECT OF WIND DRAG FORCING

The results of these model runs (Figure 3.10) show that the observations are larger in amplitudes and lagging in phase compared to the reference model.

The δu amplitudes of model runs without the wind drag forcing are around $2-4\%$ higher than the reference model runs with the differences varying for all the beacons. These differences seem to scale with the initial magnitude of the reference model runs, cf. beacon 14 to beacon 13. A similar effect is observed for the δv amplitudes too. Thus, it can be said that the wind forcing tends to dampen the amplitudes of M_2 frequency oscillations of δu and δv velocity. Further, there is almost no change observed in the phases of both the δu and δv components by removing the wind drag in the model runs.

The results indicate that the wind drag forcing has a very small but noticeable influence on the δu and δv amplitudes of the sea ice oscillations (Figure 3.10). The large effect observed for beacon 14 could be explained by the comparatively short lifespan of this beacon as a result of which we cannot separate the M_2, S_2, and inertial frequencies in the spectrum. Consequently, their individual effects are aliased on each other magnifying the effect of inertial forcing.

The relatively small changes in the amplitude and phases due to wind drag forcing implies that the wind drag is not a major cause of the sea ice oscillations in our

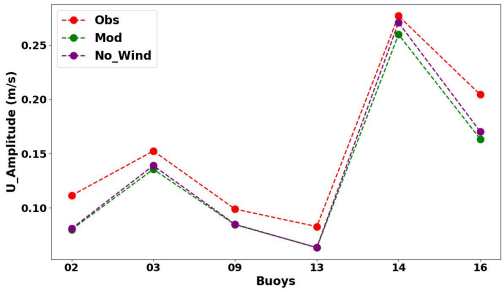

(a) U Amplitude

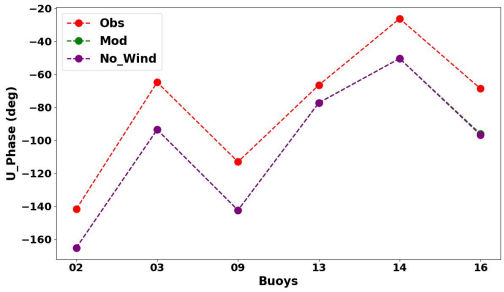

(b) U Phase

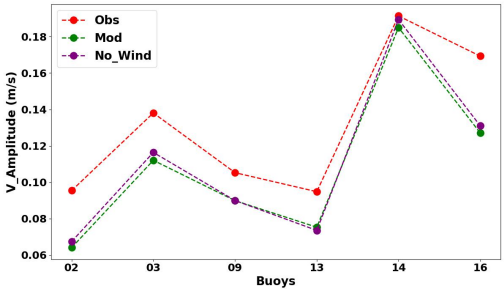

(c) V Amplitude

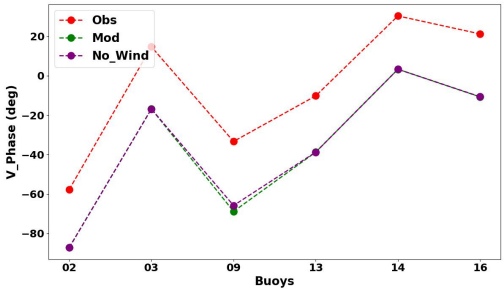

(d) V Phase

Figure 3.10.: Plots of M_2 amplitudes and phases of the δu and δv (in the sub-figures referred to as U and V, respectively) velocity components of the sea ice oscillations against the beacons. The beacon observations (red) are compared against the point model simulations with and without wind (air-ice drag) forcing. The reference point model simulation (referred to as Mod in legend; green colour) is the model run with all the forcing as given by Equation (3.2) and ice thickness of 1 m. The point model simulation without wind drag and Coriolis force is the one labelled as *No_Wind* (purple colour). The M_2 frequency amplitude and phase are obtained from the Fourier transform plots (Figure 3.6). Note that the Mod values (green) are, at some locations, overlapping with the No_Wind (purple) making them indistinguishable.

dataset. Thus, the inertial oscillations from this forcing are not dominant in the sea ice oscillation, which supports the conclusion of our first analysis (Section 3.4). This conclusion is in line with the analysis of Pease et al., 1995 and Kowalik, 1981, but in contradiction to Hibler et al., 2006. However, Hibler et al., 2006 model results were for the inertial wind forcing with sea ice drifting under strong internal stresses and their model domain was central Arctic and the Siberian Continental Shelf.

In the free drift subdaily sea ice velocity spectrum where the external forcing (wind or tidal drag) has periodic signals, a peak is observed when the frequency of external forcing is equal to the Coriolis frequency (Leppäranta, 2011a; Omstedt et al., 1996). This peak emerges from the analytical solution employing the free drift equation with a linear stress law for both air-ice and water-ice drag terms. The analytical and model results are given in Omstedt et al., 1996. Now, as the Coriolis frequency is almost the same as the semi-diurnal tidal frequencies in the Barents Sea region, the resulting sea ice velocity spectrum has a peak at the semi-diurnal tidal frequencies. This is evident from the beacon observed spectrum (Figure 3.6). For inertial forcing to significantly affect sea ice oscillations, it must exhibit strong semi-diurnal frequency signal constituents. In the current beacon experiment, the winds did not possess strong subdaily frequency signal and hence, their effect was low on sea ice oscillations. But in the case of storm surges, the winds might have stronger subdaily signals, which will have significant effects on the sea ice oscillations. One such example was noted in the strong cyclone-induced inertial sea ice oscillations in the Fram Strait (Lammert et al., 2009). Thus, we conclude that in the beacon dataset the wind drag is a cause of sea ice oscillations albeit not a dominant one. This is valid for the winds obtained from ERA5 (Hersbach et al., 2018) in which no strong subdaily scale signal was present.

EFFECT OF TIDAL FORCING

For the first test, the results indicate that for model runs without water-ice tidal drag, the amplitudes of the M_2 frequency oscillations of δu and δv velocity are very low ($< 0.03\,\mathrm{m/s}$). In terms of phases, it is observed that the δu-velocity phases lag behind the reference model, while the δv-velocity phases lead the reference model. The amount of lead and lag in the phases is varying for each beacon but for such low amplitudes phases are uncertain.

On the other hand, for the test without pressure gradients from tidal sea surface heights (Figure 3.12) there is a small reduction in δu and δv velocity amplitudes. It is seen that the reduction of δv velocity amplitudes is comparatively larger than for the δu velocity. Similarly, there is a small change of phase of a few degrees with the runs without pressure gradients leading the reference model runs. Beacon 14 again has a comparatively larger deviation in the amplitudes compared to reference model runs than other beacons. This is again attributed to the fact that the length of the velocity series for this beacon does not allow to separate the M_2, S_2, and inertial frequencies in the spectrum. From the results, it can be inferred that removing the tidal currents significantly dampens the amplitudes for all the beacons consistently. Further, the relatively small changes of amplitudes upon removing the pressure gradients from tidal sea surface heights implies that their effect on sea ice oscillations is low.

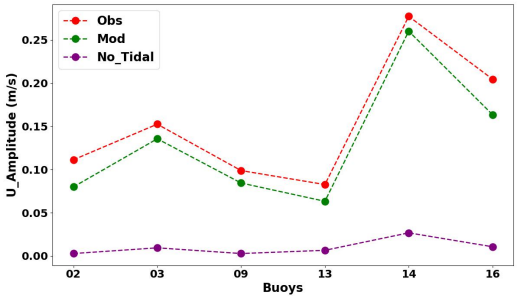

(a) U Amplitude

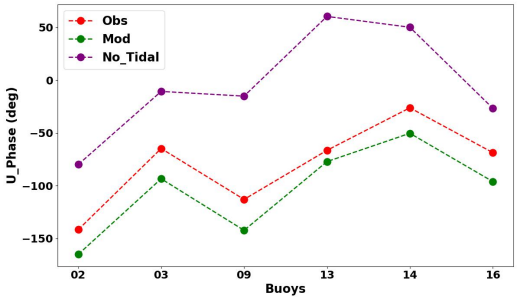

(b) U Phase

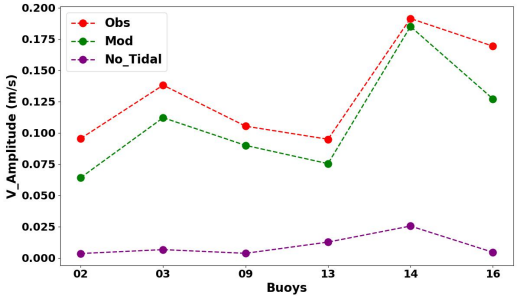

(c) V Amplitude

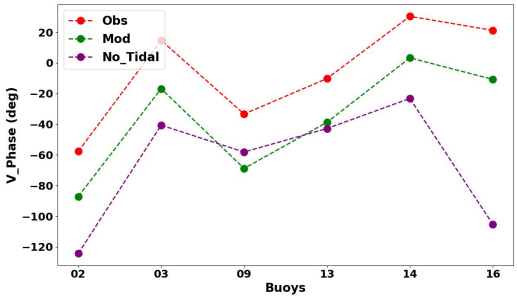

(d) V Phase

Figure 3.11.: Plots of M_2 amplitudes and phases of the δu and δv (in the sub-figures referred to as U and V, respectively) velocity components of the sea ice oscillations against the beacons. The beacon observations (red colour) are compared against the point model simulations with and without tidal currents. The reference point model simulation (referred to as Mod in legend; green colour) is the model run with all the forcing as given by Equation (3.2) and ice thickness of 1 m. The point model simulation without any tidal currents is the one labelled as *No_Tidal* (purple colour). The M_2 frequency amplitude and phase are obtained from the Fourier transform plots (Figure 3.6).

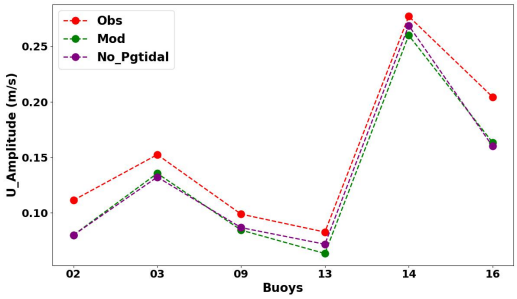

(a) U Amplitude

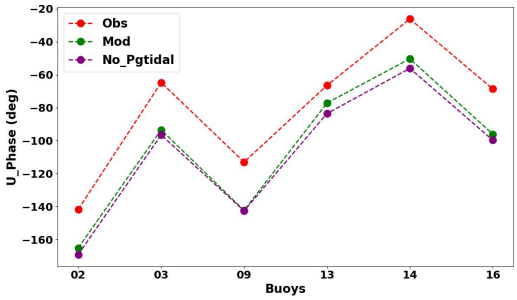

(b) U Phase

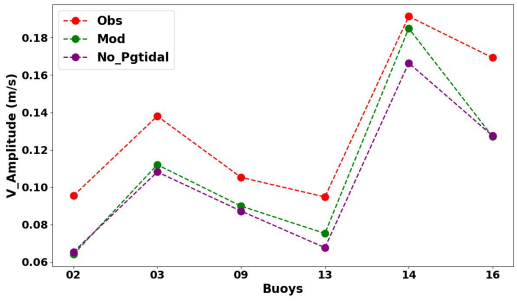

(c) V Amplitude

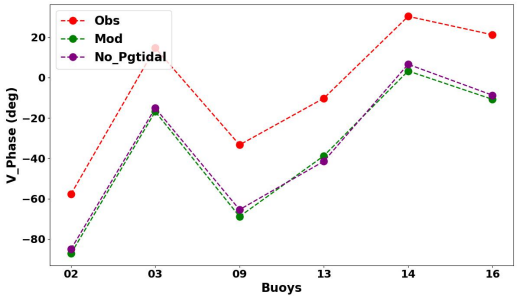

(d) V Phase

Figure 3.12.: Plots of M_2 amplitudes and phases of the δu and δv (in the sub-figures referred to as U and V, respectively) velocity components of the sea ice oscillations against the beacons. The beacon observations (red colour) are compared against the point model simulations with and without pressure gradients from tidal sea surface heights. The reference point model simulation (referred to as Mod in legend; green colour) is the model run with all the forcing as given by Equation (3.2) and ice thickness of 1 m. The point model simulation without the pressure gradients from tidal sea surface heights is labelled as *No_Pgtidal* (purple colour). The M_2 frequency amplitude and phase are obtained from the Figure 3.6.

This is in line with our hypothesis and was also noted in Steele et al., 1997. Thus, the analysis shows that tidal currents and the resulting drag is essential and a major cause for the dominant M_2 frequency sea ice oscillations in the observations of the Barents Sea.

In this dataset of the Barents Sea region there is a strong correlation between the sea ice oscillations and the underlying tides implying that the relative velocity between the two is low. It is also seen that the water-ice tidal drag is the main cause of the sea ice oscillations. This makes the coupling between sea ice and tides strong and hence, the shear stress between the two is large.

3.6. ANALYSIS ON ENERGY DISSIPATION

The quantitative nature of the energy dissipation between the air-ice and water-ice interface on a subdaily scale for the Barents Sea experiment is not straightforward. In this section, we evaluate energy loss/transfer due to both the drags in their respective interface. For this, we use the point model derived sea ice velocities to evaluate the energies since it uses the free drift Equation (3.2). Moreover, we use the tidal model dataset from GTSM that is based on Equation (3.1). The comparison metric for the computed energies is the energy loss of tidal energy to the bottom/bed friction since this friction is the main source of tidal dissipation globally. The expression for this is given by:

$$E_b = -\boldsymbol{\tau}_b.\boldsymbol{u}_t, \tag{3.8}$$

$$E_b = -\rho_w C_b |\boldsymbol{u}_t| \boldsymbol{u}_t.(\boldsymbol{u}_t),$$

$$\overline{E_b} = -\rho_w C_b \overline{|\boldsymbol{u}_t|^3}, \tag{3.9}$$

where E_b is the energy loss to bottom friction, $\boldsymbol{u}_t$ is the tidal velocity along the beacon trajectory, C_b (1.2×10^{-3}) is the bottom friction coefficient as used in the GTSM model runs. E_b is the energy loss over the entire trajectory of each beacon and it is different for each beacon. Hence, a time-average is computed over the M_2 period given by $\overline{E_b}$.

3.6.1. DISSIPATION FROM STRONG WINDS

In Sect. 3.5.3, our analysis, drawing from the work of Omstedt et al., 1996, adopted a linear drag law to evaluate the influence of wind drag on sea ice oscillations in the Barents Sea. The analysis led to the conclusion that wind drag significantly impacts these oscillations only in the presence of strong subdaily wind signals. Now, we use a quadratic drag law and this non-linear quadratic term in itself can have a dissipation part which might affect the subdaily sea ice oscillations.

The energy from wind drag (air-ice drag) on sea ice, is given by:

$$E_{ai} = \boldsymbol{\tau}_{ai}.(\boldsymbol{u}_i), \tag{3.10}$$

where E_{ai} is the energy loss from the air-ice drag $\boldsymbol{\tau}_{ai}$. The remaining terms are the same as in Equation (3.3). Then, the dissipation component in this wind stress is seen by performing a linearisation of the stress by Taylor's approximation.

$$\boldsymbol{\tau}_{ai} = \rho_a C_a \sqrt{u_a^2 + v_a^2} \begin{bmatrix} u_a \\ v_a \end{bmatrix} - 2\rho_a C_a \sqrt{u_a^2 + v_a^2} \begin{bmatrix} \delta u_i \\ \delta v_i \end{bmatrix} + \frac{\rho_a C_a (u_a \delta v_i - v_a \delta u_i)}{\sqrt{u_a^2 + v_a^2}} \begin{bmatrix} -v_a \\ u_a \end{bmatrix} + \text{Higher Order Terms}, \tag{3.11}$$

where u_a and v_a are wind speeds in $x-$ and $y-$ direction, respectively, likewise u_i and v_i are the sea ice velocities. The linearisation is performed around $u_i = v_i = 0$. The first term on the LHS in Equation (3.11) is the constant term which represents the energy transferred to the sea ice and the first-order terms are the dissipative components from the relative movement between sea ice and winds. The dissipation loss due to this component is given by an expression similar to Equation (3.10) and computed as:

$$E'_{ai} = \left(-2\rho_a C_a \sqrt{u_a^2 + v_a^2} \begin{bmatrix} \delta u_i \\ \delta v_i \end{bmatrix} + \frac{\rho_a C_a (u_a \delta v_i - v_a \delta u_i)}{\sqrt{u_a^2 + v_a^2}} \begin{bmatrix} -v_a \\ u_a \end{bmatrix} \right) \cdot \begin{bmatrix} \delta u_i \\ \delta v_i \end{bmatrix}, \tag{3.12}$$

where E'_{ai} is the energy loss from the first-order terms of the air-ice drag, δu_i and δv_i are the sea ice velocities around the mean. And, similar to the bottom friction energy loss, the time-average of this energy loss is given by $\overline{E'_{ai}}$.

To evaluate the dissipation on the subdaily motion of sea ice, the point model derived subdaily sea ice motion δu and δv, which we obtained by removing the low frequency mean drift, is used as the δu_i and δv_i. These are obtained from the reference model runs (Figure 3.4 and 3.5).

Using these ice velocities and the same values for parameters ρ_a and C_a as given in Section 3.3, the above energy dissipation Equation (3.12) and its time average are computed for winds (u_a and v_a) with constant directions and varying magnitudes for all the beacons.

The winds are assumed to be blowing 45° North-East with varying constant wind speeds from 1 m/s to 32 m/s scaled by a factor of 2. It is seen that (Figure 3.13) increasing the wind naturally increases the dissipation which, for a speed of 8 m/s is around 2 – 3% of the loss of energy due to the bottom frictional stress for all the beacons except beacon 13. This dissipation becomes quite significant for a wind speed of 32 m/s with values ranging from 10 – 20% of the loss to the bottom frictional stress for all beacons except, again beacon 13. Beacon 13 is an exception because in this case the bottom friction energy loss is in itself very low. Thus, it can be said that in this dataset of the Barents Sea region, on a subdaily scale the non-linear wind drag can cause dissipation at the air-ice interface and dissipation increases with increasing wind speeds. In comparison to energy loss of tides due to bottom friction, this effect is observed to be not very high for normal wind speeds of around 8 m/s.

Such a dissipation due to winds without any subdaily signal can in turn, affect the subdaily sea ice oscillations. In the case of the beacon dataset the wind speeds were

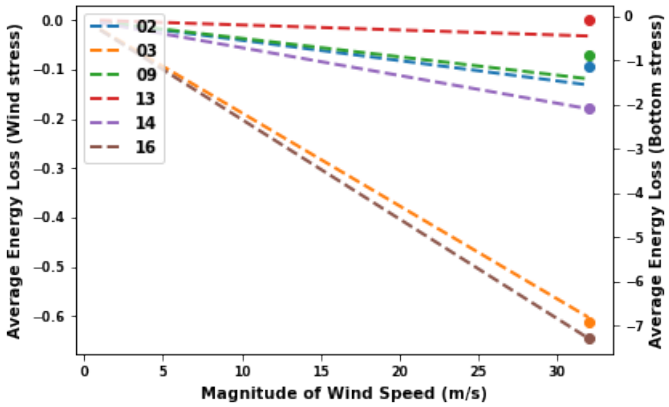

Figure 3.13.: Time-averaged energy loss computed using Equation (3.12) plotted against varying wind speed magnitudes. The dots correspond to time-averaged bottom energy loss for respective beacons with their values corresponding to the right vertical (y-) axis. The different coloured lines correspond to each beacon and the same colour of respective beacon is used to represent the time-averaged energy loss to the bottom friction.

low enough for this dissipation to be low. But in case there is a storm surge which does not have any subdaily signal, there is a chance that the sea ice subdaily motion might be affected due to the dissipation term seen in Equation (3.11). Although, the evaluation above is for the beacon dataset, the procedure is valid for any other buoy dataset and can help evaluate the significance of wind stress on a subdaily scale.

3.6.2. DISSIPATION AT ICE-TIDE INTERFACE

$$E_{wi} = -\boldsymbol{\tau}_{wit}.(\boldsymbol{u}_t - \boldsymbol{u}_{it}), \tag{3.13}$$

$$E_{wi} = -\rho_w C_w |\boldsymbol{u}_t - \boldsymbol{u}_{it}|(\boldsymbol{u}_t - \boldsymbol{u}_{it}).(\boldsymbol{u}_t - \boldsymbol{u}_{it}),$$

$$\overline{E_{wi}} = -\rho_w C_w \overline{|\boldsymbol{u}_t - \boldsymbol{u}_{it}|^3}, \tag{3.14}$$

where E_{wi} is the energy loss from the tidal part of the water-ice drag, $\boldsymbol{\tau}_{wit}$ is the water-ice drag from the tidal component only, $\boldsymbol{u}_t$ is the tidal velocity, $\boldsymbol{u}_{it}$ is the reference point model-derived sea ice oscillations obtained by removing the mean drift from model runs and a time-average given by $\overline{E_{wi}}$.

For a quantitative analysis, the comparison between this dissipation ($\overline{E_{wi}}$) and time-averaged loss to bottom friction ($\overline{E_b}$) is seen in Figure 3.14.

The average energy loss between the sea ice and tidal interface (blue dots) is just around 2 – 3% of the loss of energy of tides to the bottom friction for all the beacons except beacon 13. Again, beacon 13 is an exception because of the lower bottom frictional dissipation along its trajectory. Thus, we conclude that in the beacon dataset the drag from the tides is the major cause of sea ice oscillations yet the dissipation between the sea ice and tide interface is negligible. This conclusion

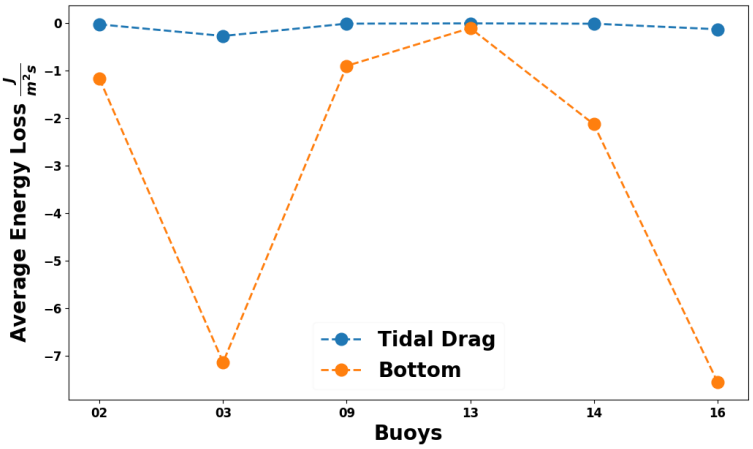

Figure 3.14.: Total average energy loss or gain of tides over the entire beacon trajectory (which is averaged over M_2 tidal period) is plotted for all the beacons. For comparison a loss of energy to sea bed bottom friction stress is used as a reference.

holds true under the condition that no storm surges are present and the winds have very low subdaily signals.

The analyses presented here relied on the point model simulations which in turn relied on external datasets i.e. ERA5, CMEMS and GTSM. There are no data on the uncertainty of these datasets in this region of the Barents Sea or near marginal ice zones. Yet to evaluate the consistency of our conclusions we did a sensitivity analysis on the results of our two analyses presented above by using other datasets than the three mentioned above. It was seen that the results of the two analyses we presented here were not very sensitive to the external datasets and as such, the conclusions remained consistent. Details of this sensitivity analysis can be found in Online Resource 4.

Now, we started off with the problem that in shallow water regions it is not clear if the dissipation at the ice and water interface is negligible on a tidal/subdaily scale. Through our study, it is clear that the ice-water tidal drag plays a significant role in sea ice oscillations, yet the role of dissipation at the ice-tide interface is negligible. Furthermore, the effect of bottom frictional drag in inducing a relative difference in ice and water velocities is low for our dataset. This conclusion is only valid for the current dataset. Yet, the hypothesis presented in Section 3.5.2 depends on the free drift and tidal equations for range of depths. So, we can hypothesise that the conclusion above is also valid for many other areas, which can be proved with the methodology used in the paper if a valid dataset is available for these areas.

3.7. SUMMARY AND CONCLUSIONS

Sea ice and its interaction with tides is one of the major challenges for global hydrodynamic tidal models (Stammer et al., 2014). The presence of sea ice leads

to a dissipation of tidal energy and most existing global tidal models include this by adding a dissipative term similar to the bottom friction term while assuming a stationary sea ice cover. However, in reality, the sea ice cover varies over the year and sea ice is drifting. The nature of frictional dissipation due to drifting sea ice is partly unknown.

In this chapter, we estimate the significance of the frictional dissipation due to free drift sea ice. There is little to no frictional dissipation between free drift sea ice and tides for deeper and open oceans. But for shallow water regions, the bottom friction plays a role and as such, the dissipation is not known. To study this, a dataset of beacon trajectories in the Barents Sea region showing subdaily sea ice oscillations is used. Along with the dataset, a physics-based point sea ice model was developed which tracked the beacon trajectories and was forced with external data from an ocean model, a tidal model, and an atmospheric model (Table 3.1). The spectrum of the subdaily oscillations showed that model and observations were in good agreement and that the M_2 tidal signal was the dominant spectral peak in the oscillations, but in this region, the Coriolis frequencies are also very close to the M_2 frequency.

Two analyses were done to evaluate the nature of the dissipation in this Barents Sea dataset. In the first analysis, a direct and strong relationship was observed between the sea ice oscillations from the observations and the tides and also between the observations and the model. This suggests that the observations had a large tidal signal and sea ice and tides move together. So the dominance at M_2 frequency in the spectrum is highly correlated to the tidal currents.

Next, we studied the causality and physical processes using sensitivity tests on the forcing in the model. It was noted that the oscillations are a result of the inertial forcing due to wind (air-ice) drag, the water-ice drag from tidal currents and the pressure gradients from the tidal sea surface heights. In our study, the effect of water-ice drag from tidal currents dominated the forcing and the influence of the tidal pressure gradients and the inertial (from air-ice drag) terms was comparatively low. This may be more balanced in deeper waters. Thus, based on the conclusions of the two analyses — tides and sea ice are strongly connected and the drag from the tidal currents being the main cause of oscillations — we can say that the sea ice follows the tides.

The dissipation between sea ice and tides was further evaluated for all the beacons (Figure 3.14) by computing the time-averaged energy loss and comparing it to the bottom friction energy loss of tides. It is seen that the dissipation is just $2-3\%$ of the equivalent bottom frictional energy loss of tides. Thus, we concluded that the tides do not have significant dissipation due to the free drift sea ice in this dataset of the Barents Sea region. This implied that the bottom frictional stress from the shallower Spitsbergen Shelf does not induce significant differences between the tidal and sea ice velocities, and as such, the dissipation remains negligible.

This conclusion corresponds to the experiment in the Barents Sea region where ERA5 data showed that the winds had low speed and no subdaily signals in them. It was seen in the sensitivity analysis that if the winds had a strong subdaily signal then the above conclusion might not hold true as the sea ice oscillations will have

a large inertial part too. Further, for the case of strong winds with no tidal signals we studied the effect of a non-linear air-ice drag term on sea ice oscillations in the beacon dataset. This effect was observed to be around $2-3\%$ of equivalent bottom friction energy loss for wind speed of $8\,m/s$ but increased to around 20% for strong constant wind of $32\,m/s$. Hence, stronger winds such as in the case of storm surges can also have significant impact on subdaily sea ice oscillations. This should be evaluated for each region and time separately.

Based on the mathematical analysis, we hypothesise that the similar conclusion of negligible dissipation between free drift sea ice and tides might hold true for other areas of the Arctic. To verify this, one would need more of such beacon observations in other areas in the free drift regime and for different time periods. The methodology presented here, is, in principle, applicable to any such dataset. Given this, for global tidal and storm surge models the dissipation from free drift sea ice on tides should be evaluated on a case-by-case basis. For deeper open oceans with low winds it can be said that the dissipation from such ice is negligible. But for shallow water regions the dissipation depends on the strength of the winds and needs to be evaluated based on local observations and the methodology presented here.

In the spectral analysis presented in this chapter, a Hamming low-pass filter was applied. A better choice would have been a Butterworth filter applied in forward and backward direction. We use this filter in Chapter 5.

Here, we have not studied the dissipation due to sea ice drifting under strong internal stresses. The analysis we did on sea ice drifting under strong internal stresses for the beacon dataset above the 78°N latitude was not conclusive due to the sparsity of the dataset. Hibler et al., 2006 saw amplification in the sea ice oscillation spectrum from the tides+winds forcing for the Arctic Central Basin, but this could very well be local and seasonal. It is expected that the internal stresses will dampen the sea ice oscillations. Hence, the resulting sea ice velocities will be different from the tidal velocities, which will imply larger dissipations. But the nature of this dissipation is not known and will be part of future study. It thus, remains to be seen what is the interaction between such sea ice drifting under strong internal stresses and tides and the resulting quantitative nature of the dissipation.

REFERENCES

Vasulkar, A., Verlaan, M., Slobbe, C., & Kaleschke, L. (2022). Tidal dissipation from free drift sea ice in the Barents Sea assessed using GNSS beacon observations. *Ocean Dynamics*, *72*(8), 577–597. https://doi.org/10.1007/s10236-022-01516-w

Stammer, D., Ray, R. D., Andersen, O. B., Arbic, B. K., Bosch, W., Carrère, L., Cheng, Y., Chinn, D. S., Dushaw, B. D., Egbert, G. D., Erofeeva, S. Y., Fok, H. S., Green, J. A. M., Griffiths, S., King, M. A., Lapin, V., Lemoine, F. G., Luthcke, S. B., Lyard, F., … Yi, Y. (2014). Accuracy assessment of global barotropic ocean tide models. *Reviews of Geophysics*, *52*(3), 243–282. https://doi.org/10.1002/2014RG000450

Kleptsova, O., & Pietrzak, J. D. (2018). High resolution tidal model of Canadian Arctic Archipelago, Baffin and Hudson Bay. *Ocean Modelling*, *128*, 15–47. https://doi.org/10.1016/j.ocemod.2018.06.001

Verlaan, M., De Kleermaeker, S., & Buckman, L. (2015). GLOSSIS: Global storm surge forecasting and information system. *Australasian Coasts & Ports Conference 2015: 22nd Australasian Coastal and Ocean Engineering Conference and the 15th Australasian Port and Harbour Conference*, 229–234.

Muis, S., Verlaan, M., Winsemius, H. C., Aerts, J. C., & Ward, P. J. (2016). A global reanalysis of storm surges and extreme sea levels. *Nature Communications 2016 7:1*, *7*(1), 1–12. https://doi.org/10.1038/ncomms11969

Padman, L., & Erofeeva, S. (2004). A barotropic inverse tidal model for the Arctic Ocean. *Geophysical Research Letters*, *31*(2). https://doi.org/10.1029/2003GL019003

Chen, C., Gao, G., Qi, J., Proshutinsky, A., Beardsley, R. C., Kowalik, Z., Lin, H., & Cowles, G. (2009). A new high-resolution unstructured grid finite volume Arctic Ocean model (AO-FVCOM): An application for tidal studies. *Journal of Geophysical Research*, *114*(C8). https://doi.org/10.1029/2008JC004941

McPhee, M. G. (1982). *Sea ice drag laws and simple boundary layer concepts, including application to rapid melting* (Report 82-4). United States Army Cold Regions Research; Engineering Laboratory.

Pease, C. H., Salo, S. A., & Overland, J. E. (1983). Drag measurements for first-year sea ice over a shallow sea. *Journal of Geophysical Research*, *88*(C5), 2853. https://doi.org/10.1029/JC088iC05p02853

Kagan, B. A., & Sofina, E. V. (2010). Ice-induced seasonal variability of tidal constants in the Arctic Ocean. *Continental Shelf Research*, *30*(6), 643–647. https://doi.org/10.1016/J.CSR.2009.05.010

Müller, M., Cherniawsky, J. Y., Foreman, M. G., & Von Storch, J. S. (2014). Seasonal variation of the M 2 tide. *Ocean Dynamics*, *64*(2), 159–177. https://doi.org/10.1007/s10236-013-0679-0

Bij de Vaate, I., Vasulkar, A. N., Slobbe, D. C., & Verlaan, M. (2021). The Influence of Arctic Landfast Ice on Seasonal Modulation of the M2 Tide. *Journal of Geophysical Research: Oceans*, *126*(5), e2020JC016630. https://doi.org/10.1029/2020JC016630

Mahoney, A. R. (2018). *Landfast Sea Ice in a Changing Arctic* (tech. rep.). Arctic Program NOAA. https://arctic.noaa.gov/Report-Card/Report-Card-2018/ArtMID/7878/ArticleID/788/Landfast-Sea-Ice-in-a-Changing-Arctic

Heil, P., & Hibler, W. D. (2002). Modeling the High-Frequency Component of Arctic Sea Ice Drift and Deformation. *Journal of Physical Oceanography*, *32*(11), 3039–3057. https://doi.org/10.1175/1520-0485(2002)032<3039:MTHFCO>2.0.CO;2

Hunke, E. C., & Dukowicz, J. K. (1997). An ElasticViscousPlastic Model for Sea Ice Dynamics. *Journal of Physical Oceanography*, *27*(9), 1849–1867. https://doi.org/10.1175/1520-0485(1997)027

McPhee, M. G. (1978). A simulation of inertial oscillation in drifting pack ice. *Dynamics of Atmospheres and Oceans*, *2*(2), 107–122. https://doi.org/10.1016/0377-0265(78)90005-2

Pease, C. H., Turet, P., & Pritchard, R. S. (1995). Barents Sea tidal and inertial motions from Argos ice buoys during the Coordinated Eastern Arctic Experiment. *Journal of Geophysical Research*, *100*(C12), 24705–24718. https://doi.org/10.1029/95jc03014

Hibler, I. D., Roberts, A., Heil, P., Proshutinsky, A. Y., Simmons, H. L., & Lovick, J. (2006). Modeling M2 tidal variability in Arctic Sea-ice drift and deformation. *Annals of Glaciology*, *44*, 418–428. https://doi.org/10.3189/172756406781811178

Kowalik, Z., & Proshutinsky, A. Y. (1994). The Arctic Ocean Tides. American Geophysical Union (AGU). https://doi.org/10.1029/gm085p0137

Zubov, N. (1945). Lćdy Arktiki. *Izdatelćstvo Glavsermorputi, Moscow*, 360 pp. English%20translation%201963%20by%20US%20Naval%20Oceanographic%20Office%20and%20American%20Meteorological%20Society,%20San%20Diego

McPhee, M. G. (1980). An Analysis of Pack Ice Drift in Summer. *Sea Ice Processes and Models*, 62–75.

Leppäranta, M. (2011a). Free drift. *The Drift of Sea Ice*, 185–212. https://doi.org/10.1007/978-3-642-04683-4{_}6

Omstedt, A., Nyberg, L., & Leppäranta, M. (1996). On the ice-ocean response to wind forcing. *Tellus, Series A: Dynamic Meteorology and Oceanography*, *48*(4), 593–606. https://doi.org/10.3402/tellusa.v48i4.12145

Furevik, T., & Foldvik, A. (1996). Stability at M2 critical latitude in the Barents Sea. *Journal of Geophysical Research: Oceans*, *101*(C4), 8823–8837. https://doi.org/10.1029/96JC00081

Middleton, J. H., & Denniss, T. (1993). The propagation of tides near the critical latitude. *Geophysical and Astrophyscial Fluid Dynamics*, *68*(1-4), 1–13. https://doi.org/10.1080/03091929308203559

Kaleschke, L., Tian-Kunze, X., MaaSS, N., Beitsch, A., Wernecke, A., Miernecki, M., Müller, G., Fock, B. H., Gierisch, A. M. U., Heinke Schlünzen, K., Pohlmann, T., Dobrynin, M., Hendricks, S., Asseng, J., Gerdes, R., Jochmann, P., Reimer, N., Holfort, J., Melsheimer, C., … Casal, T. (2016). SMOS sea ice product:

Operational application and validation in the Barents Sea marginal ice zone. *Remote Sensing of Environment*. https://doi.org/10.1016/j.rse.2016.03.009

Kaleschke, L., & Müller, G. (2022). Sea ice drift from autonomous measurements from 15 buoys, deployed during the IRO2/SMOSIce field campaign in the Barents Sea March 2014. *PANGAEA*. https://doi.org/https://doi.org/10.1594/PANGAEA.941334

Kowalik, Z. (1979). A note on the co-oscillating M2-tide in the Arctic Ocean. *Deutsche Hydrographische Zeitschrift*, *32*(3), 100–112. https://doi.org/10.1007/BF02226997

Gjevik, B., & Straume, T. (1989). Model simulations of the M ₂ and the K ₁ tide in the Nordic Seas and the Arctic Ocean. *Tellus A*, *41A*(1), 73–96. https://doi.org/10.1111/j.1600-0870.1989.tb00367.x

Dmitriev, N. E., Proshutinsky, A. Y., VlNJE, T., Yu, A., Yu Proshutinsky, A., & Scienr, A. (1991). Tidal ice dynamics in the area of Svalbard and Frans Josef Land. *Polar Research*, *9*(2), 193–205. https://doi.org/10.3402/POLAR.V9I2.6791

Beitsch, A., Kaleschke, L., & Kern, S. (2014). Investigating High-Resolution AMSR2 Sea Ice Concentrations during the February 2013 Fracture Event in the Beaufort Sea. *Remote Sensing 2014, Vol. 6, Pages 3841-3856*, *6*(5), 3841–3856. https://doi.org/10.3390/RS6053841

Leppäranta, M., & Omstedt, A. (1990). Dynamic coupling of sea ice and water for an ice field with free boundaries. *http://dx.doi.org/10.3402/tellusa.v42i4.11892*, *42*(4), 482–495. https://doi.org/10.3402/TELLUSA.V42I4.11892

Brown, R. A. (1981). Modeling the geostrophic drag coefficient for AIDJEX. *Journal of Geophysical Research: Oceans*, *86*(C3), 1989–1994. https://doi.org/10.1029/jc086ic03p01989

Hersbach, H., Bell, B., Berrisford, P., Biavati, G., Horányi, A., Muñoz Sabater, J., Nicolas, J., Peubey, C., Radu, R., Rozum, I., Schepers, D., Simmons, A., Soci, C., Dee, D., & Thépaut, J.-N. (2018). ERA5 hourly data on single levels from 1979 to present. 10.24381/cds.adbb2d47

Copernicus Marine Service. (2014). Global Ocean 1/12° Physics Analysis and Forecast. https://doi.org/https://doi.org/10.48670/moi-00016

Leppäranta, M. (2011b). Equation of drift ice motion. *The Drift of Sea Ice*, 143–184. https://doi.org/10.1007/978-3-642-04683-4{_}5

Omstedt, A. (1980). A sensitivity analysis of steady, free floating ice. *(RMK, Rapport Meteorologi och Klimatologi). SMHI. Retrieved from http://urn.kb.se/resolve?urn=urn:nbn:se:smhi:diva-2732*. https://www.diva-portal.org/smash/record.jsf?pid=diva2%3A948028&dswid=-4094

Kowalik, Z. (1981). A Study of the M-2 Tide in the Ice-Covered Arctic Ocean. *Modeling, Identification and Control: A Norwegian Research Bulletin*, *2*(4), 201–223. https://doi.org/10.4173/mic.1981.4.2

Lammert, A., Brümmer, B., & Kaleschke, L. (2009). Observation of cyclone-induced inertial sea-ice oscillation in Fram Strait. *Geophysical Research Letters*, *36*(10). https://doi.org/10.1029/2009GL037197

Steele, M., Zhang, J., Rothrock, D., & Stem, H. (1997). The force balance of sea ice in a numerical model of the Arctic Ocean. *JOURNAL OF GEOPHYSICAL RESEARCH*, *102*(C9), 61–82. https://doi.org/10.1029/97JC01454

4

NEW METHOD TO INCLUDE SEA ICE IN TIDAL MODELS

Arctic sea ice leads to a significant dissipation of tidal energy, necessitating its inclusion in global tidal models. However, most global tidal models either neglect or only partially incorporate the impact of sea ice on tides. This study proposes a method to model the dissipative forces exerted by sea ice on tides without directly coupling to a sea ice model, yet utilizing sea ice parameters such as thickness and concentration. Our approach involves (re)-categorizing the sea ice cover into regions dominated either by the velocity difference between sea ice and tides (Vertical Shear (VS)) or by the shear from drifting sea ice on tides (Horizontal Shear (HS)), which primarily govern the energy dissipation between tides and sea ice. The subdivision and resulting areas of these HS and VS regions are based on a nondimensional number referred to as the Friction number, *which is the ratio of the internal stress of the sea ice field to the ice-water frictional stress, and directly depends on the thickness and concentration of the sea ice. The new parameterization is validated through a performance assessment comparing it to a commonly used approach of assuming all the sea ice to be stationary (landfast). The seasonal modulation of the M_2 tidal component, quantified as the March-September difference, serves as the performance metric, demonstrating that the new parameterization has better agreement with observations from altimeter- and tide gauge-derived seasonal modulation. The results indicate that the physics of ice-tide interaction is better represented with the new parameterization of sea ice-induced dissipation, making it suitable for investigating the effects of declining sea ice thickness on tides.*

This chapter is published Vasulkar et al., 2024 as:
Vasulkar, A., Verlaan, M., Slobbe, C., & Kulikov, M. (2024). Modelling the effect of sea ice in an ocean tide model. Ocean Modelling, 190, 102405. https://doi.org/10.1016/J.OCEMOD.2024.102405

4.1. INTRODUCTION

Numerous studies have investigated the influence of tides on Arctic sea ice dynamics (e.g., Holloway and Proshutinsky, 2007 and Luneva et al., 2015, among others). However, there is limited knowledge regarding the impact of sea ice and its decline (Perovich & Richter-Menge, 2009; Meier, 2016) on future global tides and surges. Most global or regional ocean tide models do not model the effect of sea ice on tides (e.g., Lyard et al., 2021; Padman and Erofeeva, 2004; Pal et al., 2023), and as such, are not able to study the impact of sea ice and its decline on tides. Recent regional studies by Overeem et al., 2011 and Lintern et al., 2013 have demonstrated that the reduced sea ice extent provides greater fetch and wave action and, as such, allows higher storm surges to reach the shore. Other regional studies (St-Laurent et al., 2008; Kagan & Sofina, 2010; Müller et al., 2014; Kleptsova & Pietrzak, 2018; Kulikov et al., 2020) have shown a seasonal modulation of tides due to friction between the sea ice-tide interface. Bij de Vaate et al., 2021 observed in a global study a significant impact on the seasonal modulation of the M_2 tide by considering only the Arctic landfast sea ice.

To assess the impact of Arctic sea ice decline on global tides, global hydrodynamic tidal models should model the effect of sea ice on tides. Sea ice is known to cause a frictional dissipation force on tides, resulting in a loss of tidal energy (St-Laurent et al., 2008). Such loss, coupled with the seasonal and inter-annual variations in sea ice extent, leads to a modulation of tides. In the past, tidal models did not consider such modulation of tides from sea ice, assuming that the model errors were much larger than any modulation (Kleptsova & Pietrzak, 2018). As such, these models either ignored sea ice or assumed a constant yearly mean sea ice cover. In the latter case, the models incorporate the effect of dissipation from sea ice as an additional term, similar to sea bed (bottom) frictional stress.

A rigorous approach to include the effect of sea ice exploits a global 3D coupled ocean tide-sea ice model, resolving the effects of sea ice on tides and vice versa (e.g., STORMTIDE Müller et al., 2014, FESOM2.1 Song et al., 2023). However, these models employ coarse grids, leading to less accurate tidal dynamics (Song et al., 2023), while increasing grid resolution significantly increases computational costs. Despite the 3D nature of these ice-ocean models, they do not necessarily exhibit greater accuracy compared to most high-resolution 2D global tidal models. These 2D global tidal models have also improved in the past couple of decades, owing to improved modeling and data assimilation from satellite altimetry (Stammer et al., 2014). Nevertheless, an accurate representation of tides remains a challenge for these models in the poleward regions (above 66° latitude) (Kleptsova & Pietrzak, 2018; Stammer et al., 2014).

In the current state-of-the-art 2D hydrodynamic tidal models, the effect of sea ice dissipation and its resulting modulation is included by using a monthly mean sea ice cover instead of a yearly mean (time invariant) version, with sea ice assumed to be fixed, i.e., landfast ice (e.g., Kleptsova and Pietrzak, 2018; Cancet et al., 2016). The ice-friction stress is then simulated in Kleptsova and Pietrzak, 2018 using approaches proposed by Dupont et al., 2002; Dunphy et al., 2008; Collins et al., 2011, combining it with bottom frictional stress and varying the cumulative drag coefficient based on

sea ice concentration. In contrast, Cancet et al., 2016 simply multiplied the bottom frictional stress by a factor of 2 in the region covered by sea ice. These studies considered the entire sea ice cover/field for the month; however, Bij de Vaate et al., 2021 only considered monthly landfast sea ice cover. There, the ice-water frictional stress was again modeled by adding extra friction to the bottom frictional stress in the region of the landfast sea ice cover.

However, there are two main issues with these approaches. Firstly, the sea ice field is not entirely fixed, but partly fixed and partly drifting. In fact, only about 12% of the Northern Hemisphere sea ice is fixed/landfast (Mahoney, 2018). Modeling the ice-water frictional stress from drifting sea ice in a 2D tidal model requires a relative velocity between sea ice and water as input (Pease et al., 1983). For such drifting sea ice, the fixed sea ice cover assumption is physically incorrect and would lead to larger dissipation and erroneous results. The second issue is that these parameterizations do not include sea ice parameters like thickness and concentration, and as such, are not equipped to deal with the effect of the spatio-temporal variability of these parameters. In fact, the sea ice is thinning at a rapid rate with large variability (Mallett et al., 2021) in the Arctic. It should be noted here that Kleptsova and Pietrzak, 2018 include the sea ice concentration parameter in an indirect way through the drag coefficient.

The main objective of this paper is to present and analyse a new physically consistent sea ice parameterization that models the effect of sea ice-induced dissipation, incorporating sea ice thickness and concentration. Unlike the traditional division of the sea ice field into landfast and drifting categories with their corresponding dissipation effects, this parameterization identifies two distinct dissipation regimes. The first is referred to as Vertical Shear (VS), representing the dissipation arising from the velocity difference between sea ice and tides, where sea ice is either fixed (landfast) or drifting so slowly that it can be considered almost fixed (referred to as near-stationary sea ice). The second regime, known as Horizontal Shear (HS), accounts for dissipation due to the shear from drifting sea ice. The latter is modeled by integrating the ice-water momentum equations, similar to Heil and Hibler, 2002, resulting in a dissipative sea ice viscous internal stress term. The new parameterization addresses the two issues previously mentioned, i.e. the sea ice field as fixed and no consideration of the sea ice parameters. This is achieved by considering horizontal shear dissipation from drifting sea ice, separate from the vertical shear associated with fixed or near-stationary sea ice. Furthermore, the modelling of the horizontal shear also requires the sea ice thickness and concentration fields.

The new parameterisation is implemented in the Global Tide and Storm Surge Model (GTSM, Verlaan et al., 2015; Muis et al., 2016), and its performance is assessed by comparing the model-derived seasonal modulation of the M_2 tide with altimeter- and tide gauge-derived modulations for the years 2012, 2017, and 2019. These years were chosen because they represent the maximum, minimum, and average differences in ice extent between March and September. Note that the seasonal modulation of the M_2 tide is quantified as the March-September differences in tidal amplitudes and phases.

Moreover, a sea ice field is traditionally subdivided into Landfast sea ice and Drifting sea ice regions. The Drifting sea ice field is further subdivided into free drift sea ice and sea ice drifting under strong internal stresses. Such a division is also observed in Vasulkar et al., 2022, where it is noted that the dissipation from free drift sea ice on tides is (almost) negligible under low wind conditions. Meanwhile, in the absence of winds, the sea ice exerts no dissipation on tides (Vasulkar et al., 2022; M. G. McPhee, 1978; Leppäranta, 2011a). This implies that only landfast sea ice and sea ice drifting under strong internal stresses cause dissipation on tides. Following M. G. McPhee, 1980; Leppäranta and Omstedt, 1990, one can approximate, in a quantitative sense, that the sea ice field with concentrations less than 0.8 can be assumed to be free drift sea ice. Hence, in this paper, sea ice fields with concentrations above 0.8 will be considered, which would then be either landfast sea ice or sea ice drifting under strong internal stresses.

This chapter is organized as follows: Section 4.2 describes the dataset used in this study. Section 4.3 provides the detailed theory of our approach to model the dissipation of sea ice. Section 4.4 presents the results and discussions of the validation. Section 4.5 summarizes and concludes the main findings of this research.

4.2. DATA AND MODELS

4.2.1. SEA ICE DATASET

A global ocean reanalysis product from the Copernicus Marine Service (Copernicus Marine Service, 2019), having the GLORYS model underneath is used for the parameterization in this study. This product provides monthly mean sea ice thickness and concentration values in a gridded format and, is based on a global numerical model that includes the assimilation of sea ice concentration, among others. The years 2012, 2017, and 2019 were selected because most sea ice datasets have shown sufficient resolution and accuracy in the past decade, i.e., 2010-2020. Additionally, the March-September differences in monthly sea ice extent (obtained from NSIDC (Fetterer et al., 2017)) were maximum for 2012 ($\approx$ 11.6 million km^2) and minimum for 2017 ($\approx$ 9.4 million km^2), while the difference for 2019 is (almost) the average of the two extremes ($\approx$ 10.3 million km^2). The sea ice field with concentration larger than 0.8 is plotted for the year 2019 (Figure 4.1).

Although the GLORYS model includes the assimilation of sea ice concentration, it is known to suffer from inaccuracies. In particular, sea ice thicknesses are overestimated in the GLORYS model (Uotila et al., 2019). Ideally, remote sensing-based observational products of sea ice concentration and thickness are more accurate than those derived from the GLORYS model. However, utilizing these datasets presents multiple challenges. Firstly, for our analysis, these products must provide monthly average ice concentrations and thicknesses specifically for March and September in the years 2012, 2017, and 2019. Secondly, integrating different products may lead to inconsistencies; for example, regions with sea ice concentrations greater than 0.8 might lack corresponding thickness data due to disparities in the sources of the products. Although interpolation is possible to estimate these thicknesses, it inherently introduces additional errors. Furthermore, the resolution discrepancy

between the two products necessitates further interpolation, potentially degrading data quality. In contrast, model-derived products, despite their inherent inaccuracies, offer consistently aligned concentrations and thicknesses with monthly averages. These products also provide the flexibility to generate daily or weekly averages, which might be essential for future enhancements in tidal model simulations. We compare the sea ice extent from the GLORYS model with another dataset in Appendix E and compare the sea ice concentration and thickness from multiple remote sensing products in Appendix H.

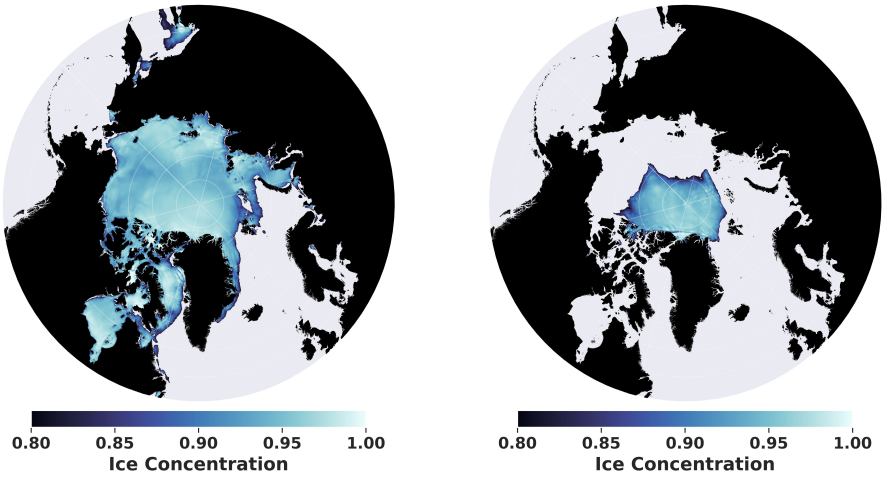

(a) March 2019 **(b)** September 2019

Figure 4.1.: Sea ice concentration field with values larger than 0.8 for March and September 2019 obtained from a global ocean reanalysis product (Copernicus Marine Service, 2019). The sub-figures (Figure 4.1a and 4.1b) show the March and September distribution.

4.2.2. ALTIMETER-DERIVED SEASONAL MODULATION IN THE ARCTIC

Bij de Vaate et al., 2021 estimated March-September differences in M_2 amplitude and phase from CryoSat-2 and Sentinel-3 altimeter data acquired between June 2010 to August 2019 (CryoSat-2) and between December 2016 to December 2019 (Sentinel-3). The area covered by the altimetry product includes the region north of 60řN and is extended to include the Hudson Bay area; 50°N60°N, 100°W45°W (Figure 4.7). UTide (Codiga, 2011) was used to perform tidal analysis using the major tides; K_1, O_1, Q_1, P_1, N_2, M_2 and S_2. This altimetry product is observed to exhibit significant spatial variability of seasonal modulation owing to spatial and temporal data scarcity (Bij de Vaate et al., 2021).

The March-September differences capture the *total* seasonal modulation from not only the seasonal sea ice cover but also other external seasonal forcings, i.e., wind forcing, spatial density differences, stratification, and inter-annual variations of sea ice (Bij de Vaate et al., 2021). However, in the Arctic region, many studies have

noted that the seasonal sea ice cover is a major contributor to seasonal modulation (St-Laurent et al., 2008; Müller et al., 2014; Kleptsova & Pietrzak, 2018; Bij de Vaate et al., 2021).

4.2.3. TIDE GAUGE-DERIVED SEASONAL MODULATION

This study uses two tide gauge datasets. The first dataset comprises tidal water level predictions at 15-minute intervals at 11 locations for the year 2019. These predictions, obtained from the Canadian Hydrographic Service (Fisheries and Ocean Canada-MEDS, 2019) and referred to as *CHS* in this chapter, include predictions for 154 locations. We selected these 11 locations because a Fourier Transform of the year-long time series revealed amplitudes larger than 1 cm for the α_2 (H_1) and β_2 (H_2) tidal frequencies, which are satellite constituents responsible for the seasonal modulation of the M_2 tide (Ray, 2022). From these tidal water level predictions at 11 tide gauge locations, we computed M_2, H_1, and H_2 constituents by performing a tidal analysis without considering the nodal factors. The second dataset includes the M_2, H_1, and H_2 tidal amplitudes and phases for 7 tide gauge records provided by Kulikov et al., 2020. The locations and names of the tide gauges for both datasets are shown in Figure 4.2.

Using the amplitudes and phases for the M_2, H_1, and H_2 components from both datasets, a year-long series is reconstructed without considering the nodal factors to eliminate interference with the seasonal modulation. From this reconstructed signal, the monthly average amplitudes and phases for the M_2 component are computed for both March and September (Figure 4.10). This tide gauge-derived dataset is referred to as *TG-derived* in this chapter.

4.3. SEA ICE PARAMETERIZATION FOR 2D OCEAN TIDE MODELS

4.3.1. GOVERNING EQUATIONS WITH SEA ICE DISSIPATION

Drifting and landfast sea ice exert different dissipation on tides, and as such, can be modelled separately based on their characteristics. The sea ice-induced dissipation of tides can be incorporated into the momentum equation of the depth-averaged shallow water equations of tidal models. These equations are similar to Equation 2.2 in most hydrodynamic 2D models. The resulting momentum equation is given by:

$$\frac{\partial \boldsymbol{u}}{\partial t} + f e^{i\pi/2}\boldsymbol{u} + \boldsymbol{u}.\boldsymbol{\nabla}\boldsymbol{u} = -g\boldsymbol{\nabla}(\zeta_n) + \nu_w(\boldsymbol{\nabla^2}\boldsymbol{u}) + \frac{\boldsymbol{\tau}_b}{\rho_w H_d} + \frac{\boldsymbol{\tau}_{IT}}{\rho_w H_d} + \left[\lambda\frac{\boldsymbol{\tau}_{wi}}{\rho_w H_d} + (1-\lambda)\frac{\boldsymbol{\nabla}.\boldsymbol{\sigma}}{\rho_w H_d}\right], \tag{4.1}$$

where the terms have same meaning as in Equation 2.2 apart from the sea ice terms with $\boldsymbol{\nabla}.\boldsymbol{\sigma}$ being the stress from the horizontal (2D) sea ice internal friction ($\boldsymbol{\sigma}$) with dimension force/length and $\boldsymbol{\tau}_{wi}$ is the water-ice surface frictional stress from the landfast (fixed) sea ice and is similar to the bottom frictional stress. λ is a parameter that controls the switch between the two shear forcing from sea ice on tides and is responsible for the classification of sea ice into landfast and drifting sea ice.

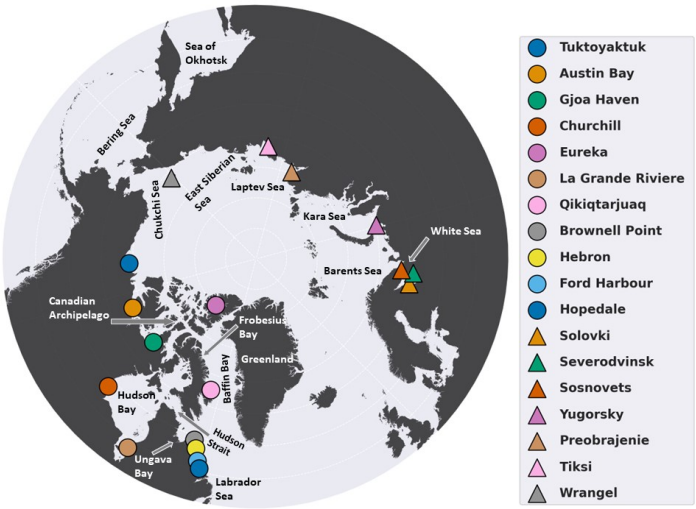

Figure 4.2.: Tide gauge locations with their respective names in the legend. The dots represent tide gauges from Fisheries and Ocean Canada-MEDS, 2019 and triangles represent tide gauges from Kulikov et al., 2020. The names of the regions referred to in the paper are also shown in the figure.

In the absence of winds, oceanic forcing is the main cause of sea ice drift. Then, it follows from Equation (4.1) that landfast sea ice will have a vertical shear owing to the velocity difference in frictional stress, wheras drifting sea ice will have a horizontal shear on tides as a result of its viscous internal stress. At times, the internal stress for compact sea ice is strong enough for the ice to move slowly and be considered (near) stationary. In such scenarios, sea ice exhibits dissipation characteristics similar to those of landfast sea ice, suggesting that a portion of drifting sea ice also shares similar dissipation characteristics as landfast ice.

Therefore, instead of adhering to the traditional classification (Figure 4.3), this paper proposes dividing sea ice with a concentration greater than 0.8 into Horizontal Shear (HS) and Vertical Shear (VS) regions. These names reflect the dominant physical interaction between sea ice and tides. The sea ice field must then be classified into these regions and modelled separately in ocean tide models according to the Equation (4.1).

4.3.2. MODELLING OF SEA ICE DISSIPATION WITH CLASSIFICATION

It can be shown with a scaling argument on Equation (4.1) that the horizontal shear is lower than the vertical shear, with its maximum potentially equaling the vertical shear. Thus, the upper limit of the horizontal shear is vertical shear and this limit serves to divide the sea ice cover into HS/VS regions.

To classify the ice field into the two shear regions, we introduce a non-dimensional number referred to as the *Friction number* (F). It is defined as the ratio of the

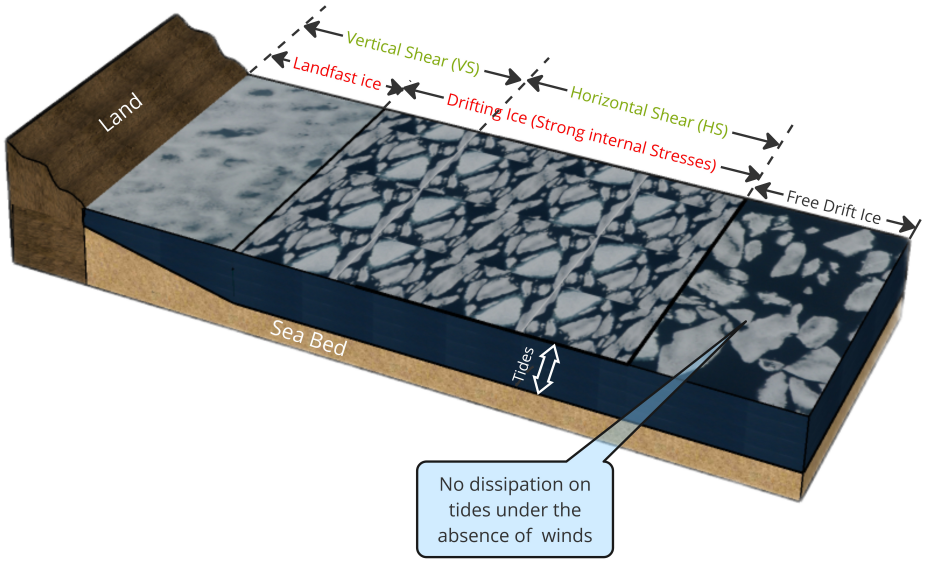

Figure 4.3.: Pictorial representation of the traditional sea ice field sub-division and the new sub-division into Horizontal and Vertical Shear (HS/VS). This is a representative figure and in reality the ratio of HS/VS can change based on the sea ice parameters and VS can even be larger than the landfast sea ice region.

frictional stress from the sea ice field internal friction and water-ice frictional shear stress with sea ice drift set to zero, i.e.,

$$F = \frac{\nabla.\boldsymbol{\sigma}}{\boldsymbol{\tau}_{wi}}, \tag{4.2}$$

where the terms are as described above in Equation (4.1). The value of F acts as the classification metric and for $F \geq 1$ the upper limit of horizontal shear is reached and the sea ice is almost stationary. Consequently, such sea ice only causes vertical shear on tides and is classified as VS region. Conversely, for $F < 1$ the sea ice is classified as HS region with the dissipation driven by the sea ice internal viscous stress.

Employing F, the switching parameter λ is utilized to classify into HS and VS regions and is defined as:

$$\lambda = H(F - 1), \tag{4.3}$$

where $H(.)$ is a Heaviside function which gives a binary switching between HS and VS regions based on the value of F.

To calculate F one needs expressions for the two stress terms. The water-ice frictional stress with sea ice velocity set to zero can be modelled similar to the bottom frictional stress. For most tidal models including GTSM, this is given by:

$$\boldsymbol{\tau}_{wi} = \rho_w C_f |\boldsymbol{u}| \boldsymbol{u}, \tag{4.4}$$

where C_f is the water-ice drag coefficient.

To model the stress from sea ice internal friction, a sea ice rheology is required. Almost all continuum and geophysical-scale sea ice models employ the Elastic-Viscous-Plastic (EVP) rheology, as proposed by Hunke and Dukowicz, 1997 and further discussed in Ólason et al., 2022. This rheology represents a numerically efficient implementation of the Viscous-Plastic (VP) rheology initially proposed by Hibler III, 1979. However, the EVP rheology is not without its shortcomings. Firstly, its underlying assumptions have been questioned (Coon et al., 2007). Secondly, models employing this rheology have exhibited a larger spread in thickness, concentration, and sea ice drift than what is observed in reality (Chevallier et al., 2017). These limitations have spurred the development of new rheologies, such as the recent Brittle Bingham-Maxwell (BBM) rheology (Ólason et al., 2022), which addresses some of the limitations inherent to the VP rheology. Additionally, there have been several enhancements to the original formulation of the VP rheology itself, aiming to mitigate some of its limitations (e.g., Lemieux et al., 2010; Kimmritz et al., 2016).

Nonetheless, modeling these rheologies requires significant time and effort, and we believe a simplified version of the VP rheology is more appropriate for our relatively simple parameterization. We adopt the original VP rheology formulation by Hibler III, 1979, with sea ice modeled as a Newtonian fluid similar to water, implying sea ice rheology is assumed to be linear, viscous, and incompressible. Such a Newtonian approximation, initially proposed by Laikhtman, 1958, is not representative of sea ice behavior but does provide first-order approximations for basin-wide sea ice circulation, as noted in Leppäranta, 2011b. Moreover, it simplifies the modeling of sea ice internal stress in tidal models because most tidal models

already include modeling for the diffusive viscous stress term of water (a Newtonian fluid), allowing the addition of sea ice horizontal shear viscosity to that term.

Given this Newtonian approximation is a simplified one, the viscous-plastic nature of sea ice is partially represented through the sea ice shear viscosity obtained from Hibler III, 1979's rheology:

$$\boldsymbol{\sigma} = \zeta \dot{\epsilon}_I + 2\eta \dot{\boldsymbol{\epsilon}} - \frac{P}{2}, \tag{4.5}$$

where $\zeta(h_i, A) = \frac{P(h_i,A)}{2\Delta_o}$ and $\eta(h_i, A) = \frac{\zeta(h_i,A)}{2e_c^2}$ are the horizontal (2D) bulk and shear viscosities (units kg/s), respectively, P is the strength of the sea ice field, Δ_o is the maximum viscous creep variant, e_c is the aspect ratio of the yield ellipse of the rheology, h_i is the sea ice thickness and A is the sea ice concentration. The expression for sea ice strength ($P = P^* h_i e^{-C(1-A)}$) leads to an expression for the shear viscosity of sea ice given by:

$$\eta = \frac{P^* h_i e^{-C(1-A)}}{4\Delta_o e_c^2}, \tag{4.6}$$

where P^* is the compressive strength of compact ice of unit thickness, C is a strength reduction constant for lead opening. This formulation implies that the sea ice internal stress and its resulting dissipation are functions of the spatially and temporally varying sea ice thickness (h_i) and concentration (A).

Using Equation (4.6) and assuming that the sea ice internal stress is modelled similarly to the diffusive water internal stress, the friction number F can be written as:

$$F = \frac{\eta(\boldsymbol{\nabla^2 u})}{\rho_w C_f \boldsymbol{u}^2}. \tag{4.7}$$

Note that the horizontal shear viscosity (η) in the depth-averaged shallow water equations is divided by $\rho_w H$ and hence is dimensionally equivalent to the horizontal kinematic viscosity of water (ν_w)

Further simplification of Equation (4.7) is achieved through scaling analysis. Assuming a scaling of $u = Uu^*$, $x = Lx^*$ and $y = Ly^*$ where L is the horizontal length scale, the friction number scales as:

$$\begin{aligned} F &\sim \frac{\eta(h_i, A)U}{\rho_w C_f U^2 L^2}, \\ F &\sim \frac{P^* h_i e^{-C(1-A)}}{4\Delta_o e_c^2 \rho_w C_f U L^2}, \\ F &\sim \alpha_i h_i e^{-C(1-A)}, \end{aligned} \tag{4.8}$$

where α_i is a scaling constant given by the expression:

$$\alpha_i = \frac{P^*}{4\Delta_o e_c^2 \rho_w C_f U L^2}. \tag{4.9}$$

This expression for F (Equation (4.8)) represents an exponential function of sea ice concentration A, linear in sea ice thickness h_i and scales with a constant α_i. Given the concentration and thickness vary spatially and temporally, F is also a function of space and time.

Classification based on F depends on the value of the scaling constant α_i given by Equation 4.9. The uncertainties associated with the value of the scaling parameter stem from the uncertainties of the underlying parameters. For instance, P^*, ranges from 10 kPa to 27.5 kPa (Massonnet et al., 2014) showing a large variability. Likewise, the other parameters also have their inherent uncertainties and their values are subject to calibration (See e.g.Massonnet et al., 2014). Consequently, we instead analyse the range of possible values of the scaling parameter (α_i) based on the resulting classification of sea ice.

Assuming $\alpha_i = 1$, the plot for F versus concentration A (Figure 4.4) illustrates exponential curves for fours different sea ice thicknesses, ranging from 0.5 m to 3.0 m.

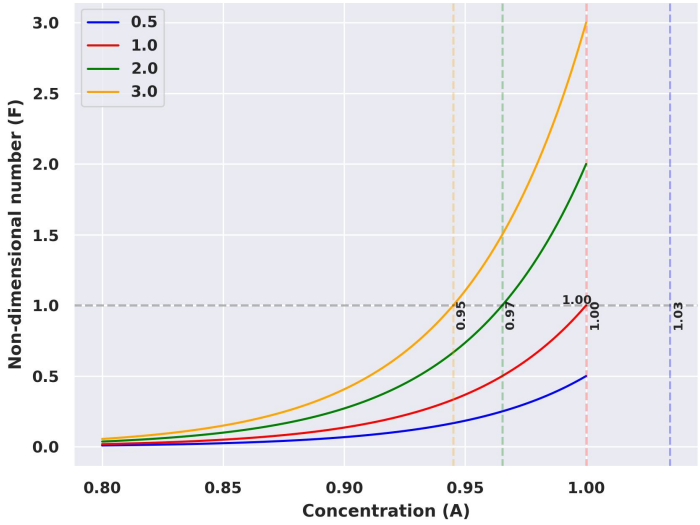

Figure 4.4.: Plots of non-dimensional friction number (F) versus concentration (A) for $\alpha_i = 1$. The colors correspond to the various sea ice thickness given in the legend. The minimum concentration considered is 0.8. The horizontal grey dotted line is the classification line between HS and VS regions. The abscissa of the point of intersection for each curve with this line gives the corresponding concentration for that thickness which is written along the dotted vertical lines for the respective thicknesses.

The horizontal grey dotted line at $F = 1$ demarcates the HS and VS regions with area/region below the line classified as HS and area/region above the line classified as VS region. As per Equation (4.8), it is clear that for a sea ice thickness ($h_i = 1$ m), $F = 1$ when concentration $A = 1$ and $\alpha_i = 1$. As the concentration (A) decreases below 0.8 the value of F goes exponentially to zero, suggesting the sea ice becomes free drift. This demonstrates that the design of the Equation (4.7) follows the free drift

condition. The equation also implies that increasing or decreasing the value of α_i changes the HS/VS classification.

The limiting value of α_i for the sea ice field to be entirely classified as VS occurs when $F = 1$ for a lowest possible concentration of 0.8. This limiting value is given by:

$$\alpha_i^{vs} = \frac{e^4}{h_i}. \tag{4.10}$$

Similarly, the entire field is classified HS when $F = 1$ for the maximum concentration of $A = 1.0$. The corresponding α_i is given by:

$$\alpha_i^{hs} = \frac{1}{h_i}. \tag{4.11}$$

Using Equations (4.11) and (4.10), the limiting α_i is evaluated for the same 4 sea ice thicknesses as in Figure 4.4. Since α_i is inversely proportional to h_i, the limiting classification of entire HS occurs for a maximum sea ice thickness $h_i (= 3.0\,\text{m}$ in our considered range of sea ice thicknesses) giving $\alpha_i^{hs} = 0.3$. Likewise, the limiting value for all VS classification occurs for a minimum thickness $h_i (= 0.5\,\text{m})$ giving $\alpha_i^{vs} = 109.2$.

Acknowledging the uncertainty with α_i's value, in this study we estimate its value based on assumptions regarding the parameters in Equation 4.9. We consider $P^* = 25\,\text{kPa}$, $C = 20$ and $e_c = 2$ which are the original values in (Hibler III, 1979) rheology. The sea ice-water friction coefficient (C_f) was assumed to be 5.5×10^{-3} as per M. G. McPhee, 1980. The maximum creep parameter Δ_o must be taken much smaller than typical strain-rates of sea ice for a good approximation of the plastic flow. Sea ice is seen to have strain rates from subdaily scale tidal and inertial forces of the order ranging from 10^{-6} to 10^{-7}s^{-1} (Heil & Hibler, 2002; Kwok et al., 2003). It is noted in Heil and Hibler, 2002 that due to high-frequency motion like in case of tides, the sea ice deformation is also higher with higher divergence or strain rates. So, here, the larger of the two Δ_o is considered i.e. $\Delta_o = 10^{-6}\text{s}^{-1}$.

U and L are the scaling parameters dependent on the physics of the problem. Since this involves sea ice-tide interaction, it serves as a criterion for the limit of sea ice drifting due to tidal movements. Hence, $U = 1\,\text{m/s}$ is assumed, representing a stronger tidal velocity. For L, the sea ice field on a continuum scale is considered, such a field is known to exist in shear and marginal zones when L is in the range of $10 - 15\,\text{km}$ (Leppäranta, 2011c). Here, we are using GTSM which has a maximum grid cell size of up to 25 km in open oceans, down to a minimum of 2.5 km. Based on this, L is assumed to be 15 km, which, on average, would show sufficient resolution for GTSM grid cells and also satisfies the sea ice continuum criterion in shear zones. With these values, α_i evaluates to 1.2. This value is closer to the all HS limit, implying that in practice, there is more sea ice with HS than with VS.

Utilizing this value of α_i alongside the sea ice thickness and concentration, the value of F follows from Equation (4.8). Implementing this value of F in Equation (4.3) gives the classification of the sea ice field in HS and VS regions. The subsequent step involves modelling the sea ice dissipation from VS region with Equation (4.4)

and from the HS region with:

$$\nabla.\boldsymbol{\sigma} = \eta(h_i, A)(\nabla^2 \boldsymbol{u}), \tag{4.12}$$

where sea ice horizontal shear viscosity, given by Equation (4.6), can also be expressed as:

$$\eta = F\rho_w C_f U L^2, \tag{4.13}$$

where $U = 1\,\mathrm{m/s}$ and $L = 15\,\mathrm{km}$.

4.3.3. IMPLEMENTATION OF THE PARAMETERIZATION

The new parameterization for sea ice-induced dissipation in ocean tide models, reliant on sea ice thickness and concentration, can be implemented in any ocean tide model as follows:

1. Obtain a suitable dataset with sea ice thickness and concentration fields for relevant regions with a sea-ice concentration larger than 0.8
2. Compute the value of the friction number F using Equation (4.8) with $\alpha_i (= 1.2)$. Note that this scaling parameter may require calibration.
3. Classify the sea ice field into HS and VS regions based on the switching parameter λ given by Equation (4.3).
4. Sea ice dissipation from the new classification (HS/VS) is then modelled in the shallow water equations of tide models by Equation (4.1) with:
   - Dissipation from VS is modelled with Equation (4.4) which is the same term as bottom frictional stress with different drag coefficient value.
   - Dissipation from HS is modelled with Equation (4.12) which is the same as viscous diffusion from water but with a spatially varying sea ice shear viscosity computed from Equation (4.13)

4.3.4. VALIDATION

Here, we outline the validation steps to assess the performance of our parameterization. Initially, we provide details of the validation for the HS/VS classification, followed by the steps undertaken to assess the performance of our method in comparison to altimetry and tide gauge datasets.

The initial step involves obtaining an HS/VS classification of the sea ice field from Sect. 4.2.1. Additionally, we consider another classification of HS/VS by assuming $\alpha_i = 0.7$, chosen to result in a classification with a predominantly large HS region and minimal VS region coverage. Modifying $\alpha_i (= 0.7)$ equates to adjusting the maximum creep parameters Δ_o from 1×10^{-6} to 1.64×10^{-6} in the Equation (4.9), altering the sea ice shear limits by modifying sea ice viscosity and thereby expanding the horizontal shear region. Using these two values of α_i, two sets of sea ice field classifications are obtained, denoted as *Exp HS_VS_1.2* for $\alpha_i = 1.2$ and *Exp HS_VS_0.7* for $\alpha_i = 0.7$ representing the two experiments.

Another classification, termed *Ex All_VS*, is similar to the current state-of-the-art method (Kleptsova & Pietrzak, 2018; Bij de Vaate et al., 2021; Cancet et al., 2016) where the entire sea ice field is assumed to be landfast ice or VS. The HS/VS region distribution resulting from these classifications is compared to the distribution of landfast and drifting sea ice using a gridded dataset from the National Snow and Ice Data Center (NSIDC) (U.S. National Ice Center, 2020). This dataset providing the landfast sea ice and total sea ice concentration data is based on the National Ice Center (NIC) charts derived from manual analysis of various satellite images. This dataset will be referred to as *NSIDC* in the chapter.

These classifications are implemented in GTSM with their corresponding dissipation characteristics. Model simulations are conducted for three settings: Exp All_VS, Exp HS_VS_1.2 and Exp HS_VS_0.7 for March and September months of the years 2012, 2017 and 2019, with a 7-day spin-up period. Water levels from the model simulation are used to compute M_2 amplitude and phase for March and September through tidal analysis with UTide (Codiga, 2011) using the major tides; K_1, O_1, Q_1, P_1, N_2, M_2 and S_2, consistent with the altimetry product (Sect. 4.2.2). The seasonal modulation of the M_2 tide is then evaluated as March-September differences in M_2 amplitude and phase.

Seasonal modulation from the model is compared to the altimeter- and TG-derived observations (Sect. 4.2.2 and 4.2.3). The altimeter-derived seasonal modulation serves as an average over the data years (2010-2019). In contrast, the CHS tide gauge predictions of 2019 are based on harmonic analysis of past data collected by the tide gauge, lacking precise information of the year of collection. On the other hand, the seasonal modulation from tide gauges in Kulikov et al., 2020 data is computed from data collected over years ranging from 1981 to 2014 with each tide gauge operational during different periods of time. These details imply that the observations of altimeter- and TG-derived modulations are not ideal for model comparisons over the Arctic but having reliable, accurate and sufficiently long datasets over the entire Arctic is a challenge.

To address this to an extent, model simulations were performed for the two extreme years (2012 and 2017) and average (2019) of sea ice cover, allowing an assessment of the range of seasonal modulation of tides from the model results and aiding in attributing discrepancies between observed- and model-derived seasonal modulation.

The parameterization is validated by doing qualitative and quantitative comparisons between model results and observations. For the altimetry dataset, a qualitative comparison presents the seasonal modulation of the M_2 amplitude and phase for both observations and model results. Quantitative comparison faces challenges due to significant variability in altimeter-derived data, as noted in Sect. 4.2.2. To reduce this variability, a coarser grid of resolution 875km × 875km is considered where the values at a grid cell are the median of all the observations/model results in that particular grid cell. A Pearson correlation coefficient is calculated between observed and model values on this coarser grid. Due to large variability, a p-value is also computed with the null hypothesis that the distribution underlying the samples is uncorrelated and normally distributed. A p-value below 0.05 is assumed to indicate

a statistically significant correlation. For tide gauges, the qualitative comparison is similar to the altimeter-derived product, whereas quantitative comparison involves calculating the median of the difference between observations and model results across various years.

4.4. RESULTS AND DISCUSSION

4.4.1. SEA ICE FIELD CLASSIFICATION FOR 2019

The gridded dataset from the NSIDC provides weekly outputs of landfast sea ice and total sea ice concentration. We consider the data from around mid-month as a representation of the mean for that month. The sea ice fields on March 21, 2019, and September 19, 2019, are shown (Figure 4.5a and 4.5b) with concentrations larger than 0.8, displaying the distribution of landfast and total sea ice. It is observed that in September (Figure 4.5b; summer), the sea ice cover is significantly reduced with no landfast sea ice present in the dataset, in contrast to March (Figure 4.5a; winter). This loss in landfast sea ice during summer periods since 2018 is also noted by Li et al., 2020. For landfast ice, the March extent is around 10% of the total sea ice extent.

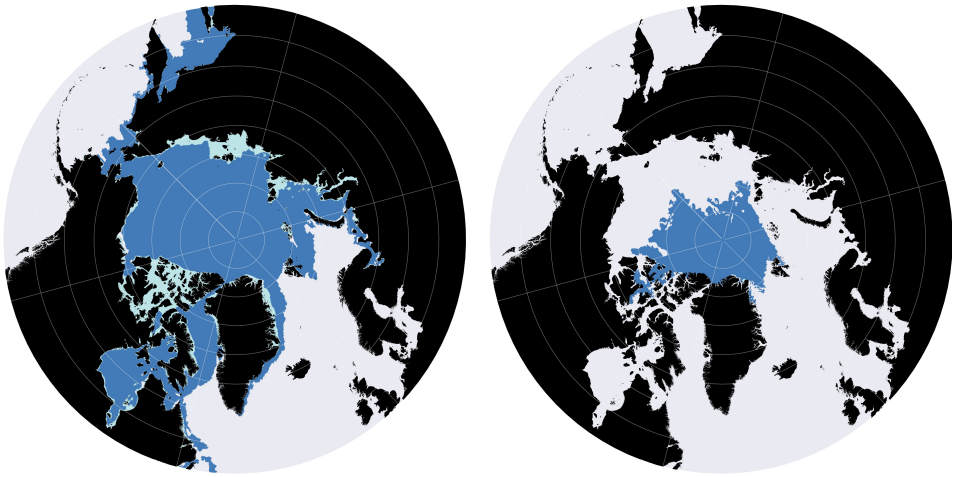

(a) March 2019 **(b)** September 2019

Figure 4.5.: Sea ice field for March and September 2019 obtained from NSIDC dataset. The sub-figures (Figure 4.5a and 4.5b) show the traditional sub-division of landfast sea ice (light blue) from the remaining sea ice (dark blue) obtained from NSIDC. Note that only the sea ice field with concentration > 0.8 is considered here.

The HS/VS classifications from Exp HS_VS_1.2 and Exp HS_VS_0.7 for the sea ice field of 2019 are shown in Figure 4.6. Similar figures showing classifications (Exp HS_VS_1.2 and Exp HS_VS_0.7) for the years 2012 and 2017 are available in Appendix F.

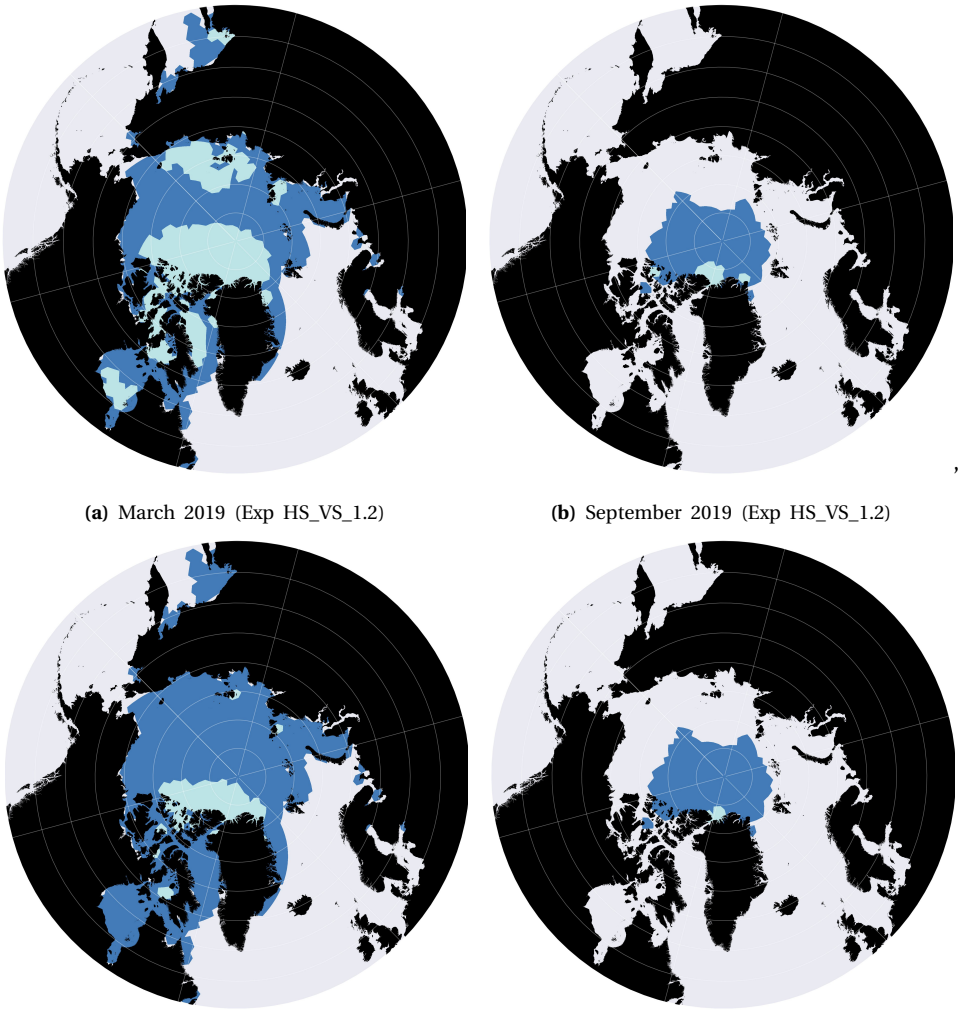

(a) March 2019 (Exp HS_VS_1.2)

(b) September 2019 (Exp HS_VS_1.2)

(c) March 2019 (Exp HS_VS_0.7)

(d) September 2019 (Exp HS_VS_0.7)

Figure 4.6.: HS (dark blue) and VS (light blue) classification of the sea ice field for March and September 2019 with the sea ice field obtained from Copernicus Marine Service, 2019. The sub-figures show HS/VS classification based on two α_i values for the same the sea ice field. Exp HS_VS_1.2 is with $\alpha_i = 1.2$ and Exp HS_VS_0.7 is with $\alpha_i = 0.7$. Note that only the sea ice field with concentration > 0.8 is considered here.

With Exp HS_VS_1.2, it is seen that for March (Figure 4.6a), approximately 30% of the sea ice field is classified as VS, which is significantly larger compared to the landfast ice coverage (10%, Figure 4.5a). The larger landfast ice regions, such as the Canadian Archipelago, the East Siberian Shelf Sea, and the Laptev Sea, are also identified as part of the VS regions, along with other areas in the Hudson Bay and the Central Arctic. On the other hand, the HS classification for March primarily encompasses regions with strong tidal velocities like Ungava Bay, Hudson Strait, and near the Kara Sea, as well as along the sea ice edge where horizontal shear is expected due to the drifting nature of the sea ice surrounded by ocean. For September (Figure 4.6b), a small region ($\sim$ 7% of the total) north of Greenland is classified as VS, while the remaining Central Arctic region and parts of the Canadian Archipelago are classified as HS, in contrast to the absence of landfast sea ice in September (Figure 4.5b). This HS/VS classification validates the physical notion that regions within the drifting sea ice, possessing strong internal stresses, can remain almost stationary under tidal influences, resulting in vertical shear on tides.

In comparison, Exp HS_VS_0.7 for March (Figure 4.6c) shows approximately 5% of the sea ice field as VS, mainly in the central Arctic north of the Canadian Arctic archipelago and Greenland. With the choice of $\alpha_i = 0.7$, this VS region is minimal compared to the HS region, indicating that much of the sea ice field behaves as drifting sea ice with horizontal shear. The VS region is considerably smaller than the landfast ice cover for March (Figure 4.5a). Likewise, for September (Figure 4.6d), there is (almost) no VS region ($\sim 1-2\%$) similar to absence of landfast sea ice cover (Figure 4.5b). Here again, it is seen that the HS classification is around the sea ice edge while the central sea ice field with compact and large internal stresses is classified as VS due to the high viscosity of the ice field.

It should be noted that the landfast ice coverage is not a mean for that month, but the mean is expected to be within $\pm 2\%$ of the current distribution, as there is not a significant variation within a month. The proportions of the HS/VS regions for March in both classifications exceed this range, and, for September, landfast ice is absent. Thus, the discussion remains valid even if a mean landfast ice coverage were available. Currently, no dataset provides a monthly mean landfast ice coverage.

4.4.2. COMPARING MODEL-DERIVED AND OBSERVATION-DERIVED SEASONAL MODULATION

RESULTS-ALTIMETRY DATASET

The model-derived and altimetry-derived March-September differences in the amplitude and phase of the M_2 tide for the year 2019 are shown in Figure 4.7. The plots obtained for the years 2012 and 2017 are shown in Appendix G.

Figure 4.8 displays the scatter plots of the altimeter-derived March-September amplitude and phase differences compared to their model-derived counterparts for the three years and each classification. The scatter plots are generated using the values on the coarser grid, and the map showing the median values for observations and model results is available in Appendix G. The resulting correlation coefficients

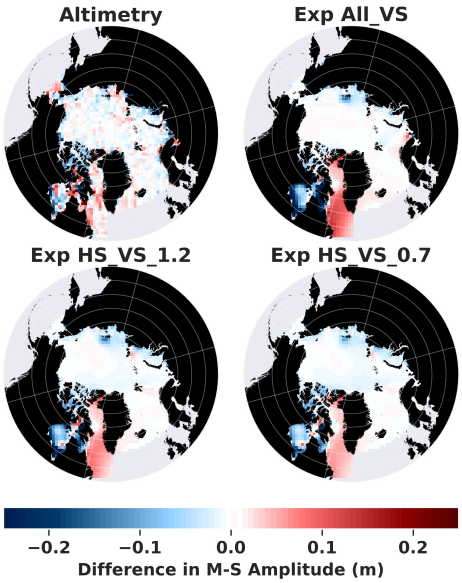

(a)

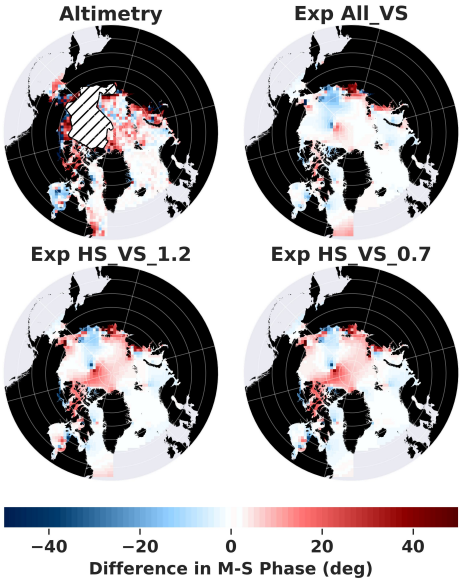

(b)

Figure 4.7.: Seasonal Modulation of M_2 tide quantified as March-September differences in amplitude and phases for the altimeter-derived product and the Exp All_VS, Exp HS_VS_1.2 and Exp HS_VS_0.7 runs for the year 2019. Differences in amplitude (4.7a) and phase (4.7b). Positive differences (red) denote that the March amplitude is larger/phase is leading than September, while negative differences (blue) denote the opposite.

and p-values are shown in Figure 4.9.

Amplitude modulations are minimal in the Central Arctic and radiate outward to the Canadian and Russian Arctic sides. A strong seasonal modulation of up to $\sim \pm 0.25$ m in the altimeter-derived estimates (Figure 4.7a) is observed for several regions in the Hudson Bay, Hudson Strait, Frobesius Bay, Canadian Archipelago, White Sea and Kara Sea. Positive modulations are evident in the western part of Hudson Bay, Ungava and Frobisher Bay, White Sea, Laptev Sea, and west and east of Greenland in Baffin Bay, Labrador Sea, and near Svalbard. Negative modulations are noted in the eastern part of Hudson Bay, Canadian Archipelago, Barents Sea, Kara Sea, East Siberian Shelf Sea, and parts of the Chukchi Sea and Sea of Okhotsk. In the Central Arctic, the amplitude modulations are very low (around $2-3$mm), as expected due to the low tidal amplitudes in this region.

In comparison, the amplitude modulations with Exp All_VS for the year 2019 (Figure 4.7a) exhibit much stronger seasonal modulation, up to approximately ± 0.7 m. The distribution of positive and negative modulation appears smoother compared to the altimeter-derived estimates in the region. The areas of positive and negative distribution largely align with the altimeter-derived estimates, with a few exceptions. These exceptions include the western Hudson Bay and Strait, Frobisher Bay, Ungava Bay, and the Laptev Sea, where negative modulation is observed, and the southern Barents Sea, which exhibits positive modulation. Moreover, the Central Arctic, Chukchi Sea, and Sea of Okhotsk show almost zero modulation. A quantitative comparison using scatter plots reveals that only points around 0 amplitude modulation lie on the $y = x$ line (dotted line in the figure), while the remaining points are scattered with no visible linear trend. This observation is supported by the resulting correlation coefficients, which average approximately 0.45 (Figure 4.9). Furthermore, the amplitude modulation remains consistent across different years (2012, 2017, and 2019), except for four points in the plot.

The model-derived amplitude modulations with Exp HS_VS_1.2 for the year 2019 (Figure 4.7a) also exhibit strong seasonal modulation, up to approximately ± 0.4 m, albeit lower than Exp All_VS. The positive-negative distribution is very similar to the Exp All_VS case, except for a section of Hudson Bay and Forbes Bay, where positive modulation is noted in Exp HS_VS_1.2. Additionally, the negative modulation in the Chukchi Sea and the southern region of Barents Sea diverges from Exp All_VS. The scatter plot (Figure 4.8b) for this case similarly shows points only around 0 lying on the $y = x$ line, but exhibits a better linear trend compared to Exp All_VS. The average correlation coefficient between years is 0.55 (Figure 4.9). Here, the scatter plot reveals varying amplitude modulations within different years, primarily for points distant from the $y = x$ line.

Lastly, the model-derived estimates for amplitude modulation with Exp HS_VS_0.7 for the year 2019 (Figure 4.7a) display a lower seasonal modulation (up to approximately ± 0.3 m) compared to the other two simulations but exceed the altimeter-derived estimates. The distribution of positive and negative modulation closely resembles Exp HS_VS_1.2, except for Frobisher Bay and some areas of Hudson Bay. In this region, Exp HS_VS_0.7 shows a broader spread of positive modulations compared to Exp HS_VS_1.2 and aligns with the altimetry-derived estimates. The

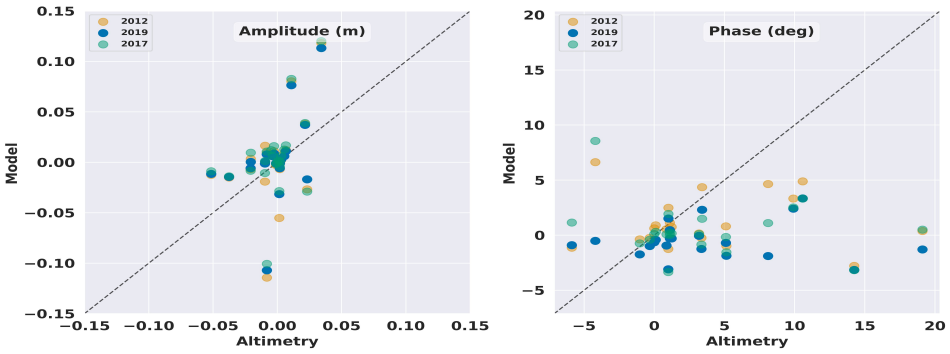

(a) Sea ice as Fixed

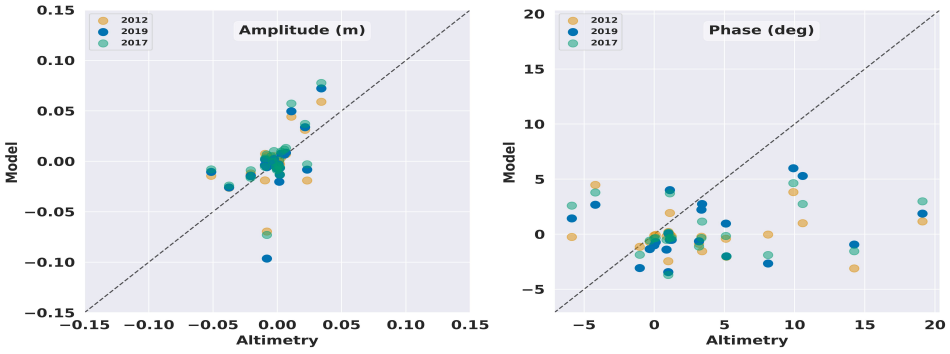

(b) Exp HS_VS_1.2

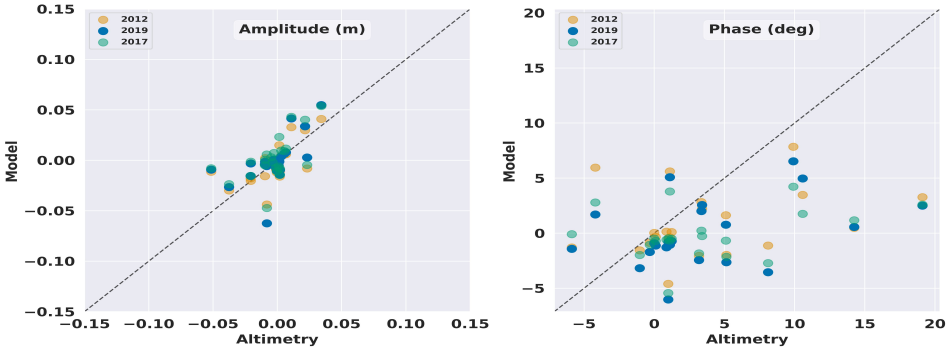

(c) Exp HS_VS_0.7

Figure 4.8.: Scatter plots showing a comparison between altimeter-derived seasonal modulation ($x-$ axis) versus the seasonal modulation (March-September differences of M_2 constituent) from the 3 Model results (Exp All_VS, I and II) ($y-$axis). Each sub-figure corresponds to the respective model simulation with the sub-title denoting the name of the simulation and the amplitude and phase modulations are compared separately. The color of the dots correspond to the year of the run. Note that each point corresponds to the value at the cell of the coarse grid and importantly, the phase differences of the cells lying in the hatched region (Figure 4.7b) are removed from the plotting.

	Amplitude						Phase					
	Exp All_VS		Exp HS_VS_1.2		Exp HS_VS_0.75		Exp All_VS		Exp HS_VS_1.2		Exp HS_VS_0.75	
	R	*P-value*	*R*	*P-value*	*R*	*P-value*	*R*	*P-value*	*R*	*P-value*	*R*	*P-value*
2012	0.42	0.04	0.55	0.005	0.65	0.001	-0.002	0.99	-0.04	0.85	0.28	0.20
2017	0.45	0.03	0.58	0.003	0.60	0.002	-0.19	0.40	0.11	0.62	0.30	0.18
2019	0.47	0.02	0.52	0.009	0.60	0.002	0.032	0.88	0.24	0.28	0.38	0.079
Mean	0.45	0.03	0.56	0.006	**0.62**	0.001	-0.05	0.76	0.10	0.59	0.32	0.15

Figure 4.9.: Pearson correlation (R) and corresponding P-value for the plots in Figure 4.8. The mean represents the mean of the values of the 3 years for that respective statistic with the green value denoting the model run with highest correlation in amplitude differences.

scatter plots (Figure 4.8c) includes points on the line $y = x$ that are not close to 0 and exhibit better linear trends compared to the other two simulations, with an average correlation coefficient of 0.6 (Figure 4.9) between years. Moreover, amplitude modulations vary between years for nearly all points.

The variations in amplitude modulation for the results Exp HS_VS_0.7 and Exp HS_VS_1.2 between years indicate that modulations on the Canadian Arctic side are larger in 2017 than in 2012, with 2019 serving as the median between them. Conversely, on the Russian Arctic side, 2017 has lower modulation, with 2012 exhibiting the largest among the three years. These modulations do not directly correlate with the fact that 2012 experienced the largest March-September differences in sea ice, while 2017 had the lowest.

Regarding phases, the hatched region in the phase plot of the altimeter-derived estimates (Figure 4.7b), as mentioned by Bij de Vaate et al., 2021, signifies that these phase differences are deemed unreliable due to large variability. Furthermore, the altimeter-derived estimates show considerable variability in phase modulation across the region, except for the Archipelago, where consistently positive differences are noted. Compared to altimeter-derived estimates, the model-derived estimates (Exp All_VS, Exp HS_VS_1.2, and Exp HS_VS_0.7, Figure 4.7b) for the year 2019 demonstrate less variability in phase modulations. Consequently, the overall alignment between altimeter-derived phase modulations and model-derived modulations in scatter plots (Figure 4.8a, 4.8b, 4.8c) is minimal, with insignificant correlation coefficients (Figure 4.9). This lack of agreement persists across all years.agreement holds true for all the years.

Among the three model-derived estimates, phase modulations from Exp All_VS (Figure 4.7b) are negligible in many regions, except for a few areas on the Russian side of the Arctic and the southern part of the Labrador Sea. In contrast, Exp HS_VS_1.2 and Exp HS_VS_0.7 simulations present phase modulations throughout the entire region, with a comparatively lower proportion of areas showing negligible modulation. Additionally, the large phase differences in the central Arctic across all model simulations can be disregarded as artifacts or uncertainties, given the low amplitudes in the region near the North Pole.

RESULTS-TIDE GAUGE DATASET

The comparison with TG-derived March-September differences in amplitude and phase for the year 2019 is shown in Figure 4.10. The results for the remaining years are provided in Appendix G. Figure 4.11 displays the TG-derived and model-derived (Exp All_VS, Exp HS_VS_1.2, and Exp HS_VS_0.7) estimates of amplitude and phase modulations for all the years, with the tide gauge names on the $x-$ axis.

TG-derived data indicate negative seasonal amplitude modulation across most CHS tide gauges, with the exception of those in the Labrador Sea (Figure 4.10a). The tide gauge at La Grande Riviere in Hudson Bay exhibits the largest absolute amplitude modulation, recorded at 0.3 m. Similarly, in the Russian Arctic, negative modulations were observed, notably at the Wrangel gauge in the Chukchi Sea.

Comparisons with all three model simulations (Exp All_VS, Exp HS_VS_1.2, and Exp HS_VS_0.7) show consistent signs of seasonal amplitude modulation with the observed data, except at three tide gauges in the Laptev and Chukchi Seas. Specifically, for the Wrangel tide gauge, model simulations suggest almost zero modulation, whereas observations indicate a modulation of −0.1 m. Among the model simulations, Exp All_VS exhibits larger amplitude modulations in absolute terms, while Exp HS_VS_1.2 and Exp HS_VS_0.7 generally align more closely with observed values. The median differences in amplitude modulation between observation-derived estimates and model-derived estimates (Figure 4.11d) indicate the best performance with Exp HS_VS_1.2 simulations and the poorest with Exp All_VS.

TG-derived phase modulation (Figs. 4.10b and 4.11) from CHS data, excluding a positive anomaly at Tuktoyaktuk (∼ 65°) in the Chukchi Sea, exhibit either negative or nearly zero seasonal modulation. Russian side gauges mostly show positive or neutral phase modulations, with a notable exception in the Laptev Sea displaying a small negative modulation (∼ −5°). The agreement between model-derived phase modulations for all simulations and observed values is poor, with deviations as high as 40° at four tide gauges.

Finally, variability among all the tide gauges between years of different model simulations is noted in Figure 4.11. The Exp All_VS case exhibits a narrower range of amplitude and phase modulations between years for all tide gauges, except for La Grande Riviere, compared to the other two simulations. For La Grande Riviere, the range is wider than the other two, but only for amplitudes.

DISCUSSION

The comparison between altimeter- and TG-derived versus model-derived March-September differences shows overall good agreement in terms of the signs (positive or negative) for the amplitude. However, in regions such as Ungava Bay, the Bering Sea, and some parts of the Laptev Sea, the direction of amplitude modulations does not align with the altimeter-derived values. A plausible explanation could be that the altimeter-derived seasonal modulation, as mentioned in Section 4.2.2, results from all seasonal forces (i.e. wind forcing, spatial density differences, stratification). On the other hand, the seasonal modulation of phases from altimeter- and TG-derived values is not captured very well by the model runs. In fact, model estimates of 4

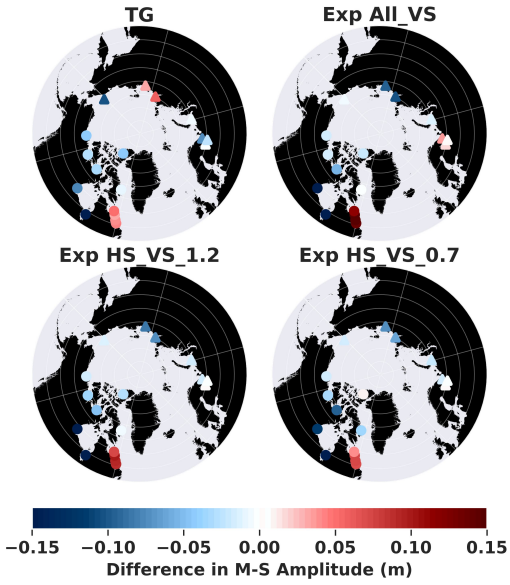

(a)

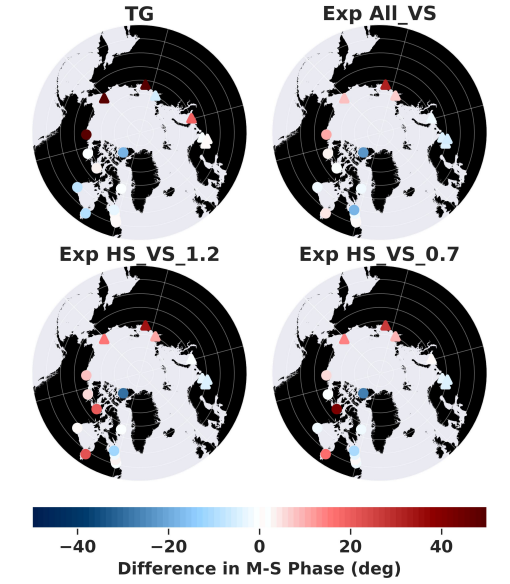

(b)

Figure 4.10.: Seasonal Modulation of M_2 tide quantified as March-September differences in amplitude and phases for the TG-derived product and the 3 model runs (Exp All_VS, Exp HS_VS_1.2 and Exp HS_VS_0.7) for the year 2019. Differences in amplitude (4.10a) and phase (4.10b). Positive differences (red) denote that the March amplitude is larger/phase is leading than September, while negative differences (blue) denote the opposite.

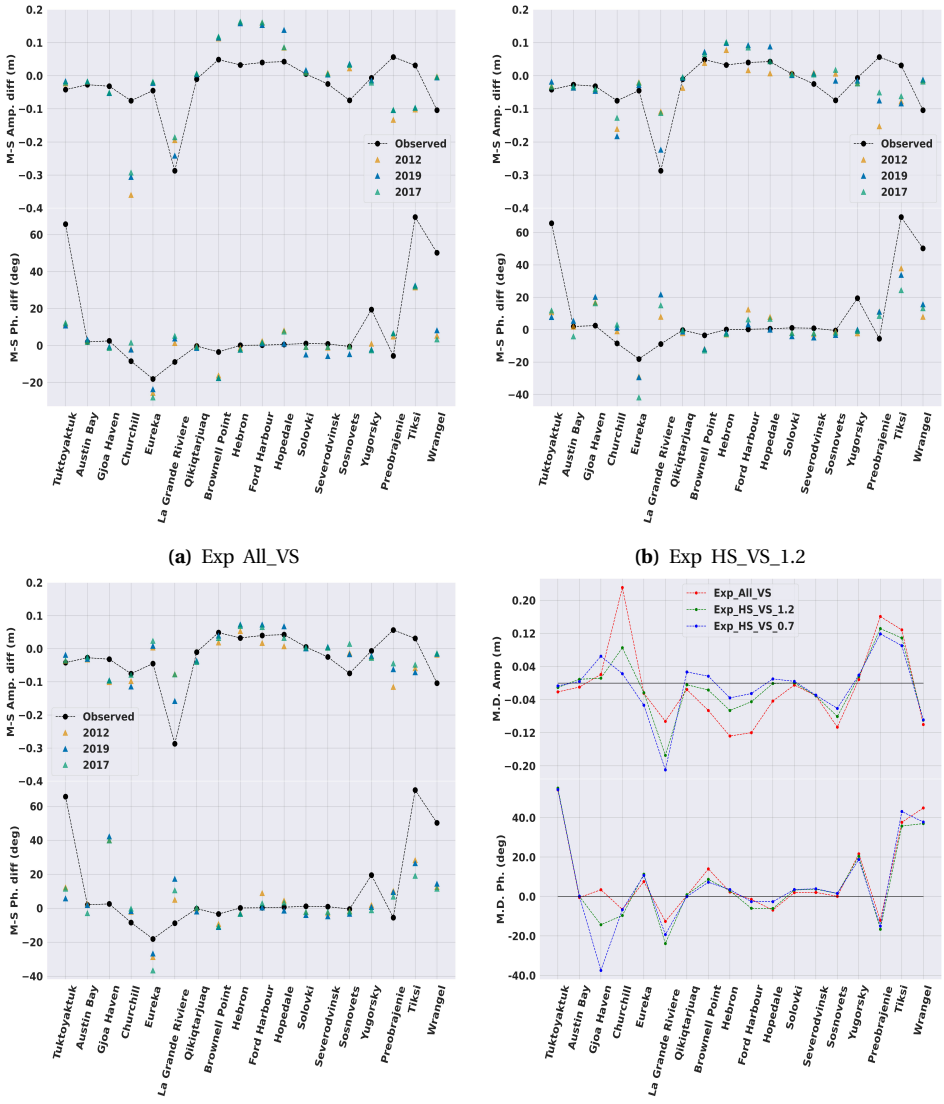

(a) Exp All_VS

(b) Exp HS_VS_1.2

(c) Exp HS_VS_0.7

(d) Median of differences

Figure 4.11.: Seasonal modulation per tide gauge with observations in black dots connected by dotted lines. The model results are shown by triangles with different colors corresponding to a particular year. The tide gauges are arranged on the $x-$ axis in order of increasing longitude (going anti-clockwise) starting from Tuktoyaktuk (Lon 133°W) to Wrangel (Lon 178°E). The first 11 tide gauges on the $x-$ axis are from the CHS data and the next 7 are from Kulikov et al., 2020. The first 3 sub-figure captions denote the type of model simulation among Exp All_VS, Exp HS_VS_1.2 and Exp HS_VS_0.7. The last sub-figure is the median of difference between model and observed values computed over 3 years. The colors in this sub-figure correspond to the three types of model runs. A value closer to zero indicates better agreement of the model simulation to the observed value.

tide gauges show deviations of around 40° from the observations.

Nevertheless, it should be noted that the observations are not without issues. The altimeter-derived values exhibit considerable variability and uncertainty. For tide gauges, we either lack knowledge of the year of data collection (CHS data) or the year of data collection differs from the model runs (Kulikov et al., 2020). For instance, this discrepancy could explain the poor performance observed at the Wrangel tide gauge, whose modulations are computed from data collected between 1981-1995. Model simulations show (almost) zero amplitude modulation for this tide gauge, while the observed modulation is −0.1 m. The period of 1981-1995 featured thicker and more extensive sea ice than the years in this study, which could have influenced the model-derived seasonal modulation at this tide gauge. With thicker ice conditions, the scaling parameter α_i would be higher than 1.2 due to a linear relationship between them, as this would increase the compressive strength, consequently leading to a larger VS region. Another issue with the tide gauge measurements is the presence of local seasonal forces. For instance, there are local forces like seasonal river discharges due to ice melting which could affect the observations or tide gauge damage due to winter sea ice conditions. Such issues were particularly noted for the tide gauge Churchill near the Hudson River (Ray, 2016).

The variations in sea ice cover can affect amplitude modulations far from their source, with no direct relationship to the variations. For instance, the March-September differences were maximum for 2012, yet the absolute amplitude modulations for 2012 were lower on the Canadian side of the Arctic than the 2017 modulations. Conversely, on the Russian Arctic side, absolute amplitude modulations for 2012 were larger than those in 2017.

Among all the types of model simulations, it is observed that Exp HS_VS_0.7 simulations (Figure 4.10 and 4.9) show the best overall agreement with the altimeter-derived values, while Exp HS_VS_1.2 simulations (Figure 4.11d) have the best overall agreement with the tide gauge results. The Exp All_VS case, which represents a current state-of-the-art in many tidal models, shows larger seasonal modulations of amplitude implying a larger dissipation from the sea ice on tides. This outcome is expected since a landfast ice assumption represents an extreme dissipation condition at the ice-water interface. The Exp HS_VS_1.2 and Exp HS_VS_0.7 simulations, which are based on the new parameterization derived in this paper, exhibit comparatively lower amplitude modulations. Here, the drifting sea ice is treated separately with its own dissipation characteristics modeled through the HS region. Such dissipation, by virtue of its construction (friction number formulation) in the parameterization, is lower than the dissipation from landfast ice. This can be verified in the results, as Exp HS_VS_0.7 has lower amplitude modulation than Exp HS_VS_1.2, while it has a larger HS area than Exp HS_VS_1.2.

Although some tidal models can change the ice-water drag coefficient in the landfast ice assumption to alleviate (to some extent) the problem of strong dissipation from the landfast ice assumption. In fact, Kleptsova and Pietrzak, 2018 proposed a solution wherein the drag coefficient varied with ice concentration. Nonetheless, these multiple approaches still do not account for drifting sea ice and its resulting

velocity gradients, which can lead to different dissipation characteristics. Our new parameterization is equipped to deal with such dissipation characteristics by modelling the dissipation with a diffusion term and sea ice viscosity. This diffusion term will lead to larger dissipation when sea ice velocity gradients are expected to be larger, for example, in regions like the Hudson Strait and Frobesius Bay.

Furthermore, the dissipation is also designed to handle the spatial and temporal variability of sea ice thickness (h_i) and concentration (A) through the value of sea ice viscosity and the classification in HS/VS regions. This inclusion of sea ice parameters helps in reducing dissipation when sea ice is thin and increasing dissipation for thicker sea ice. Given that such variability cannot be addressed with the simple assumption of landfast sea ice, it is observed that changes in sea ice cover between years does not have significant differences in seasonal modulation in Exp All_VS simulations. Our parameterization can deal with this variability making it suitable for studying the effects of sea ice decline on tides and thus, has a more accurate representation of sea ice-water physics than the simple landfast sea ice assumption.

Still, Exp HS_VS_1.2 and Exp HS_VS_0.7 model simulations, when compared against the observations used in this study, do not seem to exhibit very good accuracy. Apart from the fact that the observations have their own uncertainties, the parameterization developed here also incorporates some approximations and assumptions that can affect the model-derived results. Firstly, there is uncertainty in the scaling parameter (α_i) stemming from the uncertainty of the parameters in Equation 4.9. This value could further be fine-tuned through calibration using data assimilation principles to improve the HS/VS classification and the resulting model outcomes. Secondly, the ice-water drag coefficient C_f used here, and in most other studies, is obtained from M. G. McPhee, 1980. This coefficient is larger for recent first-year ice in the Arctic than for the experiments conducted in 1978 (M. McPhee, 2017). Moreover, the value of this drag coefficient is also known to exhibit a seasonal pattern (Brenner et al., 2021). Therefore, further research into better representation of drag coefficients will lead to more accurate dissipation values. Finally, the parameter λ for simplicity, is assumed to be a binary parameter switching between the two regions, i.e., HS/VS. However, a smooth transitioning parameter between the two regions (e.g., a sigmoid function) could provide better modelling, potentially altering the HS/VS classification and, thus, the results. Nonetheless, the current assumptions regarding these parameters represent a first step, and the values chosen here are based on tidal characteristics and a simplistic representation.

4.5. SUMMARY AND CONCLUSIONS

The impact of sea ice decline on global tides is still a topic of ongoing research. To study such an impact global hydrodynamic tidal models should include, in their modelling, the effect of sea ice induced dissipation on tides. Most models either ignore this effect or model it by assuming a monthly mean sea ice cover which is fixed i.e. landfast ice.

Here, we propose a novel parameterization to model sea ice-induced dissipation on tides, distinguishing between landfast and drifting sea ice through Horizontal

Shear (HS) and Vertical Shear (VS) regions, determined by a Friction Number (F). This number incorporates sea ice thickness (h_i), concentration (A), and a scaling parameter (α_i). From the range of values of α_i two were selected based on tidal characteristics and the nature of HS/VS regions, leading to classifications Exp HS_VS_1.2 and Exp HS_VS_0.7, showcased for March and September 2019 in Figure 4.6. This parameterization's efficacy was assessed within the Global Tide and Storm Surge Model (GTSM) by comparing three simulations–Exp All_VS, Exp HS_VS_1.2, and Exp HS_VS_0.7-to altimeter- and TG-derived observations, focusing on the seasonal modulation of the M_2 tide. The Exp All_VS simulation assumes the entire sea ice field as landfast which is the current state-of-the-art in many tidal models.

Overall, the simulation results from the Exp HS_VS_1.2 and Exp HS_VS_0.7 experiments demonstrate better agreement with observations than the Exp All_VS simulations, which exhibited larger seasonal modulation indicating higher sea ice-tidal dissipation. This discrepancy is expected because the Exp All_VS approach does not distinctly treat drifting sea ice, and its assumption of landfast sea ice implies extremum in dissipation. Furthermore, the new parameterization accounts for the spatial and temporal distribution of sea ice thickness and concentration, making it apt for studying the implications of recent decline in sea ice thickness. It is also notable that changes in sea ice can influence tidal modulation (or tides) distantly from its source, with the relationship being non-linear.

However, this study is limited by the observational dataset. The altimetry-derived seasonal modulation represents an average over the data collection years (2010-2019), while the year of data collection for TG-derived modulation is either unknown or does not coincide with the model simulation years of 2012, 2017, and 2019. Ideally, a desirable dataset would encompass spatially distributed tidal water levels from tide gauges corresponding to the year of the model simulations, facilitating a more accurate comparison. The Canadian Hydrographic service is doing great work on this end, but on the Russian side of the Arctic there is still a lack of publicly available data. However, due to issues pointed out in Ray, 2016 the tidal water levels from any such Arctic tide gauges should undergo a thorough quality check.

In case such an observational dataset is available, it would also help in further research on improving the estimations of the uncertain parameters like the scaling parameter (α_i) and the drag coefficient (C_f) through calibration or tuning. Another approach to improve the estimation of the scaling parameter (α_i) is the utilization of a sea ice velocity dataset. Such a dataset can aid in estimation of HS/VS regions and thereby assist in refining the scaling parameter. However, this approach requires investigation due to the temporal scale mismatch between the tides and the daily to monthly scales of sea ice velocities in the datasets.

The results of this study should be viewed in the context of the challenges in obtaining an accurate representation of sea ice concentration and thickness and the limitations of the GLORYS model. Due to over estimation of sea ice thickness, the VS region is more, consequently providing larger dissipation. Ideally, a monthly averaged remote sensing-based product providing both sea ice thickness and concentration or an accurate model-based product is desirable.

Here, we used the seasonal modulation of the M_2 tide as a performance metric. However, other tidal constituents, such as S_2, O_1, and K_1, also experience seasonal modulation as noted in Wang and Bernier, 2023. Seasonal modulation of these additional constituents could also serve as performance metrics, provided that suitable datasets are available.

We focused exclusively on Arctic sea ice, yet our parameterization can be extended to Antarctic sea ice, which is notably thinner due to the absence of multi-year ice and (almost) complete summer melt. This results in a lower ice-water drag coefficient for Antarctic sea ice–about 40% lower than Arctic averages (Schroeter & Sandery, 2022)--suggesting lower dissipation effects. Considering these differences, applying and investigating our parameterization for Antarctic sea ice could provide valuable insights.

In conclusion, this parameterization represents an initial step towards enhancing tidal models to incorporate sea ice dissipation effects on tides without necessitating coupling to a sea ice model. Such advancements promise a more realistic representation of sea ice in tidal models, aiding in the global analysis of the impacts of sea ice decline on tides and supporting coastal flood management strategies.

REFERENCES

Vasulkar, A., Verlaan, M., Slobbe, C., & Kulikov, M. (2024). Modelling the effect of sea ice in an ocean tide model. *Ocean Modelling*, *190*, 102405. https://doi.org/10.1016/J.OCEMOD.2024.102405

Holloway, G., & Proshutinsky, A. (2007). Role of tides in Arctic ocean/ice climate. *Journal of Geophysical Research: Oceans*, *112*(C4), 4–06. https://doi.org/10.1029/2006JC003643

Luneva, M. V., Aksenov, Y., Harle, J. D., & Holt, J. T. (2015). The effects of tides on the water mass mixing and sea ice in the Arctic Ocean. *Journal of Geophysical Research: Oceans*, *120*(10), 6669–6699. https://doi.org/10.1002/2014JC010310

Perovich, D. K., & Richter-Menge, J. A. (2009). Loss of sea ice in the arctic. *Annual Review of Marine Science*, *1*(1), 417–441. https://doi.org/10.1146/annurev.marine.010908.163805

Meier, W. N. (2016). Losing Arctic sea ice: observations of the recent decline and the long-term context. *Sea Ice: Third Edition*, 290–303. https://doi.org/10.1002/9781118778371.CH11

Lyard, F. H., Allain, D. J., Cancet, M., Carrère, L., & Picot, N. (2021). FES2014 global ocean tide atlas: Design and performance. *Ocean Science*, *17*(3), 615–649. https://doi.org/10.5194/OS-17-615-2021

Padman, L., & Erofeeva, S. (2004). A barotropic inverse tidal model for the Arctic Ocean. *Geophysical Research Letters*, *31*(2). https://doi.org/10.1029/2003GL019003

Pal, N., Barton, K. N., Petersen, M. R., Brus, S. R., Engwirda, D., Arbic, B. K., Roberts, A. F., Westerink, J. J., & Wirasaet, D. (2023). Barotropic tides in MPAS-Ocean (E3SM V2): impact of ice shelf cavities. *Geoscientific Model Development*, *16*(4), 1297–1314. https://doi.org/10.5194/GMD-16-1297-2023

Overeem, I., Anderson, R. S., Wobus, C. W., Clow, G. D., Urban, F. E., & Matell, N. (2011). Sea ice loss enhances wave action at the Arctic coast. *Geophys. Res. Lett*, *38*, 17503. https://doi.org/10.1029/2011GL048681

Lintern, D. G., Macdonald, R. W., Solomon, S. M., & Jakes, H. (2013). Beaufort Sea storm and resuspension modeling. *Journal of Marine Systems*, *127*, 14–25. https://doi.org/10.1016/j.jmarsys.2011.11.015

St-Laurent, P., Saucier, F. J., & Dumais, J. F. (2008). On the modification of tides in a seasonally ice-covered sea. *Journal of Geophysical Research: Oceans*, *113*(C11), 11014. https://doi.org/10.1029/2007JC004614

Kagan, B. A., & Sofina, E. V. (2010). Ice-induced seasonal variability of tidal constants in the Arctic Ocean. *Continental Shelf Research*, *30*(6), 643–647. https://doi.org/10.1016/J.CSR.2009.05.010

Müller, M., Cherniawsky, J. Y., Foreman, M. G., & Von Storch, J. S. (2014). Seasonal variation of the M 2 tide. *Ocean Dynamics*, *64*(2), 159–177. https://doi.org/10.1007/s10236-013-0679-0

Kleptsova, O., & Pietrzak, J. D. (2018). High resolution tidal model of Canadian Arctic Archipelago, Baffin and Hudson Bay. *Ocean Modelling*, *128*, 15–47. https://doi.org/10.1016/j.ocemod.2018.06.001

Kulikov, M. E., Medvedev, I. P., & Kondrin, A. T. (2020). Features of Seasonal Variability of Tidal Sea-level Oscillations in the Russian Arctic Seas. *Russian Meteorology and Hydrology*, *45*(6), 411–421. https://doi.org/10.3103/S1068373920060047/FIGURES/3

Bij de Vaate, I., Vasulkar, A. N., Slobbe, D. C., & Verlaan, M. (2021). The Influence of Arctic Landfast Ice on Seasonal Modulation of the M2 Tide. *Journal of Geophysical Research: Oceans*, *126*(5), e2020JC016630. https://doi.org/10.1029/2020JC016630

Song, P., Sidorenko, D., Scholz, P., Thomas, M., & Lohmann, G. (2023). The tidal effects in the Finite-volumE Sea ice-Ocean Model (FESOM2.1): a comparison between parameterised tidal mixing and explicit tidal forcing. *Geoscientific Model Development*, *16*(1), 383–405. https://doi.org/10.5194/GMD-16-383-2023

Stammer, D., Ray, R. D., Andersen, O. B., Arbic, B. K., Bosch, W., Carrère, L., Cheng, Y., Chinn, D. S., Dushaw, B. D., Egbert, G. D., Erofeeva, S. Y., Fok, H. S., Green, J. A. M., Griffiths, S., King, M. A., Lapin, V., Lemoine, F. G., Luthcke, S. B., Lyard, F., … Yi, Y. (2014). Accuracy assessment of global barotropic ocean tide models. *Reviews of Geophysics*, *52*(3), 243–282. https://doi.org/10.1002/2014RG000450

Cancet, M., Andersen, O., Lyard, F., Shulz, A., Cotton, P., & Benveniste, J. (2016). A New High Resolution Tidal Model in the Arctic Ocean. *Living Planet Symposium*, 67. https://ui.adsabs.harvard.edu/abs/2016ESASP.740E..67C

Dupont, F., Hannah, C., Greenberg, D., Cherniawsky, J., & Naimie, C. (2002). *Modelling system for tides for the Northwest Atlantic Coastal Ocean* (tech. rep.). Fisheries & Oceans Canada, Maritimes Region, Ocean Sciences Division, Coastal Ocean Science Section, Bedford Institute of Oceanography.

Dunphy, M., Dupont, F., Hannah, C., & Greenberg, D. (2008). *Revisions to a modelling system for tides in the Canadian Arctic Archipelago* (tech. rep.). Can. Tech. Rep. Hydrogr. Ocean Sci 259: 6-62.

Collins, A., Hannah, C., & Greenberg, D. (2011). *Validation of a High Resolution Modelling System for Tides in the Canadian Arctic Archipelago* (tech. rep.). Can. Tech. Rep. Hydrogr. Ocean Sci., 273.

Mahoney, A. R. (2018). *Landfast Sea Ice in a Changing Arctic* (tech. rep.). Arctic Program NOAA. https://arctic.noaa.gov/Report-Card/Report-Card-2018/ArtMID/7878/ArticleID/788/Landfast-Sea-Ice-in-a-Changing-Arctic

Pease, C. H., Salo, S. A., & Overland, J. E. (1983). Drag measurements for first-year sea ice over a shallow sea. *Journal of Geophysical Research*, *88*(C5), 2853. https://doi.org/10.1029/JC088iC05p02853

Mallett, R. D., Stroeve, J. C., Tsamados, M., Landy, J. C., Willatt, R., Nandan, V., & Liston, G. E. (2021). Faster decline and higher variability in the sea ice thickness of the marginal Arctic seas when accounting for dynamic snow cover. *Cryosphere*, *15*(5), 2429–2450. https://doi.org/10.5194/TC-15-2429-2021

Heil, P., & Hibler, W. D. (2002). Modeling the High-Frequency Component of Arctic Sea Ice Drift and Deformation. *Journal of Physical Oceanography*, *32*(11), 3039–3057. https://doi.org/10.1175/1520-0485(2002)032<3039:MTHFCO>2.0.CO;2

Verlaan, M., De Kleermaeker, S., & Buckman, L. (2015). GLOSSIS: Global storm surge forecasting and information system. *Australasian Coasts & Ports Conference 2015: 22nd Australasian Coastal and Ocean Engineering Conference and the 15th Australasian Port and Harbour Conference*, 229–234.

Muis, S., Verlaan, M., Winsemius, H. C., Aerts, J. C., & Ward, P. J. (2016). A global reanalysis of storm surges and extreme sea levels. *Nature Communications 2016 7:1*, *7*(1), 1–12. https://doi.org/10.1038/ncomms11969

Vasulkar, A., Verlaan, M., Slobbe, C., & Kaleschke, L. (2022). Tidal dissipation from free drift sea ice in the Barents Sea assessed using GNSS beacon observations. *Ocean Dynamics*, *72*(8), 577–597. https://doi.org/10.1007/s10236-022-01516-w

McPhee, M. G. (1978). A simulation of inertial oscillation in drifting pack ice. *Dynamics of Atmospheres and Oceans*, *2*(2), 107–122. https://doi.org/10.1016/0377-0265(78)90005-2

Leppäranta, M. (2011a). Free drift. *The Drift of Sea Ice*, 185–212. https://doi.org/10.1007/978-3-642-04683-4{_}6

McPhee, M. G. (1980). An Analysis of Pack Ice Drift in Summer. *Sea Ice Processes and Models*, 62–75.

Leppäranta, M., & Omstedt, A. (1990). Dynamic coupling of sea ice and water for an ice field with free boundaries. *http://dx.doi.org/10.3402/tellusa.v42i4.11892*, *42*(4), 482–495. https://doi.org/10.3402/TELLUSA.V42I4.11892

Copernicus Marine Service. (2019). Global Ocean Physics Reanalysis. https://doi.org/https://doi.org/10.48670/moi-00021

Fetterer, F., Knowles, K., Meier, W. N., Savoie, M., & Windnagel, A. K. (2017). Sea Ice Index, Version 3 [G02135]. https://doi.org/https://doi.org/10.7265/N5K072F8

Uotila, P., Goosse, H., Haines, K., Chevallier, M., Barthélemy, A., Bricaud, C., Carton, J., Fukar, N., Garric, G., Iovino, D., Kauker, F., Korhonen, M., Lien, V. S., Marnela, M., Massonnet, F., Mignac, D., Peterson, K. A., Sadikni, R., Shi, L., … Zhang, Z. (2019). An assessment of ten ocean reanalyses in the polar regions. *Climate Dynamics*, *52*(3-4), 1613–1650. https://doi.org/10.1007/S00382-018-4242-Z/FIGURES/26

Codiga, D. L. (2011). *Unified Tidal Analysis and Prediction Using the UTide Matlab Functions* (tech. rep. September). University of Rhode Island. https://doi.org/10.13140/RG.2.1.3761.2008

Fisheries and Ocean Canada-MEDS. (2019). Canadian Tides and Water Levels Data Archive. https://tides.gc.ca/tides/en/stations

Ray, R. D. (2022). Technical note: On seasonal variability of the M2 tide. *Ocean Science*, *18*(4), 1073–1079. https://doi.org/10.5194/OS-18-1073-2022

Hunke, E. C., & Dukowicz, J. K. (1997). An ElasticViscousPlastic Model for Sea Ice Dynamics. *Journal of Physical Oceanography*, *27*(9), 1849–1867. https://doi.org/10.1175/1520-0485(1997)027

Ólason, E., Boutin, G., Korosov, A., Rampal, P., Williams, T., Kimmritz, M., Dansereau, V., & Samaké, A. (2022). A New Brittle Rheology and Numerical Framework for Large-Scale Sea-Ice Models. *Journal of Advances in Modeling Earth Systems*, *14*(8), e2021MS002685. https://doi.org/10.1029/2021MS002685

Hibler III, W. D. (1979). A Dynamic Thermodynamic Sea Ice Model. *Journal of Physical Oceanography*, *9*(4), 815–846. https://doi.org/https://doi.org/10.1175/1520-0485(1979)009<0815:ADTSIM>2.0.CO;2

Coon, M., Kwok, R., Levy, G., Pruis, M., Schreyer, H., & Sulsky, D. (2007). Arctic Ice Dynamics Joint Experiment (AIDJEX) assumptions revisited and found inadequate. *Journal of Geophysical Research: Oceans*, *112*(C11), 11–90. https://doi.org/10.1029/2005JC003393

Chevallier, M., Smith, G. C., Dupont, F., Lemieux, J. F., Forget, G., Fujii, Y., Hernandez, F., Msadek, R., Peterson, K. A., Storto, A., Toyoda, T., Valdivieso, M., Vernieres, G., Zuo, H., Balmaseda, M., Chang, Y. S., Ferry, N., Garric, G., Haines, K., … Wang, X. (2017). Intercomparison of the arctic sea ice cover in global oceansea ice reanalyses from the ora-ip project. *Climate Dynamics*, *49*(3), 1107–1136. https://doi.org/10.1007/S00382-016-2985-Y/FIGURES/14

Lemieux, J. F., Tremblay, B., Sedláek, J., Tupper, P., Thomas, S., Huard, D., & Auclair, J. P. (2010). Improving the numerical convergence of viscous-plastic sea ice models with the Jacobian-free NewtonKrylov method. *Journal of Computational Physics*, *229*(8), 2840–2852. https://doi.org/10.1016/J.JCP.2009.12.011

Kimmritz, M., Danilov, S., & Losch, M. (2016). The adaptive EVP method for solving the sea ice momentum equation. *Ocean Modelling*, *101*, 59–67. https://doi.org/10.1016/J.OCEMOD.2016.03.004

Laikhtman, D. (1958). O vetrovom dreife ledjanykh poley. *Trudy Leningradskiy Gidrometeorologicheskiy Institut*, *7*, 129–137.

Leppäranta, M. (2011b). Sea ice rheology. In *The drift of sea ice* (pp. 107–143). Springer Berlin Heidelberg. https://doi.org/10.1007/978-3-642-04683-4{_}6

Massonnet, F., Goosse, H., Fichefet, T., & Counillon, F. (2014). Calibration of sea ice dynamic parameters in an ocean-sea ice model using an ensemble Kalman filter. *Journal of Geophysical Research: Oceans*, *119*(7), 4168–4184. https://doi.org/10.1002/2013JC009705

Kwok, R., Cunningham, G. F., & Hibler, W. D. (2003). Sub-daily sea ice motion and deformation from RADARSAT observations. *Geophysical Research Letters*, *30*(23). https://doi.org/10.1029/2003GL018723

Leppäranta, M. (2011c). Equation of drift ice motion. *The Drift of Sea Ice*, 143–184. https://doi.org/10.1007/978-3-642-04683-4{_}5

U.S. National Ice Center. (2020). U.S. National Ice Center Arctic and Antarctic Sea Ice Concentration and Climatologies in Gridded Format, Version 1 [G10033]. https://doi.org/https://doi.org/10.7265/46cc-3952

Li, Z., Zhao, J., Su, J., Li, C., Cheng, B., Hui, F., Yang, Q., & Shi, L. (2020). Spatial and Temporal Variations in the Extent and Thickness of Arctic Landfast Ice. *Remote Sensing 2020, Vol. 12, Page 64*, *12*(1), 64. https://doi.org/10.3390/RS12010064

Ray, R. D. (2016). On Measurements of the Tide at Churchill, Hudson Bay. *http://dx.doi.org/10.1080/07055900.2016.1139540*, *54*(2), 108–116. https://doi.org/10.1080/07055900.2016.1139540

McPhee, M. (2017). The sea iceocean boundary layer. In D. Thomas (Ed.), *Sea ice* (3rd ed., pp. 138–159). Wiley.

Brenner, S., Rainville, L., Thomson, J., Cole, S., & Lee, C. (2021). Comparing Observations and Parameterizations of Ice-Ocean Drag Through an Annual Cycle Across the Beaufort Sea. *Journal of Geophysical Research: Oceans*, *126*(4), e2020JC016977. https://doi.org/10.1029/2020JC016977

Wang, P., & Bernier, N. B. (2023). Adding sea ice effects to a global operational model (NEMO v3.6) for forecasting total water level: approach and impact. *Geoscientific Model Development*, *16*(11), 3335–3354. https://doi.org/10.5194/gmd-16-3335-2023

Schroeter, S., & Sandery, P. A. (2022). Large-ensemble analysis of Antarctic sea ice model sensitivity to parameter uncertainty. *Ocean Modelling*, *177*, 102090. https://doi.org/10.1016/J.OCEMOD.2022.102090

5

METHOD TO DERIVE TIDAL CURRENT CONSTITUENTS FROM GNSS BUOYS

Measurements of tides are relatively sparse in the Arctic. This paper studies GNSS buoy tracks to complement existing data. Existing methods to perform tidal harmonic analysis of the buoy data are inadequate in the Arctic region because these methods for tidal analysis combine data from multiple buoy tracks, which is often infeasible in the Arctic. Moreover, we find that there are significant spatial and temporal variations in amplitudes and phases in baroclinic zones. To address these complexities, we introduce a new approach–Model-derived Fitting Method–to estimate the tidal current constituents (TCC) from a single buoy trajectory.

Our study assesses the proposed method by analysing GNSS buoy data from three Arctic regions characterized by barotropic or baroclinic tidal currents. Through detailed case studies in the Barents Sea, Chukchi Sea, and Baffin Bay, our approach demonstrates accuracy, robustness, and operational capabilities. In the Barents Sea, TCC estimates from two buoys were compared at a common location within their trajectories and compared against model estimates. In the Chukchi Sea's barotropic dominant zone, our method's estimates were evaluated against nearby ADCP mooring data. In Baffin Bay, known for baroclinic currents, a synthetic evaluation confirmed the method's effectiveness. Our study also highlights that phase variations along buoy trajectories can lead to frequency shifts in the spectrum, similar to the Doppler shift effect, particularly notable in regions with baroclinic tides.

This chapter is under 1st Revision in AGU: Earth and Space Science as:

Vasulkar, A., Verlaan, M., Slobbe, C. (2024). Deriving Tidal Current Constituent Estimates from GNSS Buoy Data in the Arctic, Under Revision AGU: Earth and Space Science

5.1. INTRODUCTION

Tidal currents play a crucial role in the Arctic, impacting everything from the health of marine ecosystems to the subdaily scale sea ice dynamics (Luneva et al., 2015; Watkins et al., 2023). In addition, precise tidal current information is essential for navigation, fisheries, and resource exploration (Baumann et al., 2020), which are becoming increasingly vital as marine traffic intensifies with the ongoing decline in sea ice (Boylan, 2021).

Arctic tidal models provide insights into tidal currents, but there is limited data regarding the accuracy of their tidal current estimates e.g. (Lyard et al., 2021; Verlaan et al., 2015; Erofeeva & Egbert, 2018; Cancet et al., 2016; Müller et al., 2014, among others). Observations from Acoustic Doppler Current Profilers (ADCPs) give tidal current estimates at their mooring locations. The Arctic Tidal Current Atlas (Baumann et al., 2020) offers tidal current estimates based on historical mooring data, but it does not provide real-time information. Another challenge is the significant spatio-temporal variability in tidal current estimates, especially in the strong baroclinic tidal zones of the Arctic such as the Nares Strait (Baumann et al., 2020), which emphasize the need to have well-distributed ADCP network. But the harsh Arctic environment poses challenges for deploying the ADCPs (Munchow et al., 1995), compounded by the need for specialized equipment to prevent ice buildup on the instruments (Nyström, 2022). These issues highlight the need for new or additional data sources.

GNSS buoys that track surface ocean currents present a promising additional data source. Expeditions like the Multidisciplinary drifting Observatory for the Study of Arctic Climate (MOSAiC) (Bliss et al., 2022, among others) have enhanced buoy deployments in the Arctic. Innovations, such as the solar-powered Spotter buoy (Raghukumar et al., 2019) developed by Sofar Technologies, Inc, ensure extended operational periods even in severe Arctic winter conditions (Kodaira et al., 2021). The International Arctic Buoy Programme (IABP) further contributes by offering extensive real-time and historical data (IABP, 2020). Contemporary buoys, boasting high temporal resolution, typically ranging from 15 min to 6 h, grant detailed insights into the variability of tidal currents.

However, the presence of sea ice in the Arctic presents challenges for using these buoy data. Firstly, buoys cannot be deployed in landfast ice regions. In drifting sea ice regions, buoy trajectories result from air-ice-water interactions and may not accurately represent underlying tidal currents, as sea ice internal stress dampens tidal movements of the buoys (Koentopp et al., 2005). Moreover, the Arctic lies in the critical latitude of the semidiurnal tidal frequency, leading to potential contamination from the inertial frequency (Pease et al., 1983). These can be addressed to some extent by considering buoys only in the free drift regimes of the drifting sea ice. Vasulkar et al., 2022 have shown that under low wind conditions, in a free drift sea ice field the buoys move along with the tides and have the same movement as the underlying tidal currents. This makes it possible that at least part (free drift and open ocean) of the buoy trajectories can be used to estimate tidal surface currents in the Arctic. Consequently, however, doing so limits the availability of 'usable' buoy trajectories to estimate tidal current constituents (TCC) in the Arctic.

Other issues in TCC estimation from buoy data are challenges which are not encountered with traditional tidal harmonic analysis used in ADCPs. These buoys traverse both space and time, tracking surface tidal currents. In regions where surface tidal currents align with depth-averaged barotropic currents, buoys effectively track the barotropic flow. However, when these currents traverse rough topographies or steep inclines, a conversion from barotropic to baroclinic tides is observed (Simmons et al., 2004), resulting in surface currents that deviate from depth-averaged tidal flows. The smaller spatial scales of baroclinic tides compared to barotropic tides (Simmons et al., 2004; Apel, 2003) can cause a Doppler shift in the tidal frequencies observed by the buoy, rendering traditional tidal harmonic analysis ineffective. Another challenge is that the changes in stratification can result in changes to the baroclinic tides and as a consequence, TCCs are not constant along the buoy trajectory.

Several methods target TCC estimation from buoy trajectories, with most of them focussing on barotropic tides. Lie et al., 2002 presented two methods for the Yellow and East China Sea. Their *correction method* segments trajectories into semidiurnal and diurnal components. And each of the components is estimated separately to obtain the amplitude and phase for M_2 and K_1 with other components (S_2, N_2, O_1, P_1) derived using constant amplitude ratios and phase differences with respect to these components. These fixed amplitude ratios and phase differences were obtained from observations in the region. Addressing the limitations of this approach, they proposed what is referred to as the *fitting method*. This approach builds on top of the correction method but considers varying amplitudes and phases, fitting them to n^{th}-order polynomials. While adaptable to regions with baroclinic tides, its treatment of Doppler shift remains unclear. Here, selecting the proper order of the polynomial is also challenging without knowing the variations of amplitude and phase. The methods rely on a large number of buoy data, where estimates from multiple buoy trajectories in the region are used to compute an average estimate for the region. Moreover, accounting for the non-linear interaction between tides and the mean current would make the optimization challenging.

Poulain and Centurioni, 2015 created a global tidal current dataset (excluding poleward regions) from extensive drifter data over 15 years. Their method involved a tidal harmonic analysis of the buoy trajectories using an approach similar to Lie et al., 2002. They sub-divided the buoy trajectories into 15−day periods for eight constituents and averaged estimates over a $2^\circ \times 2^\circ$ grid. These were benchmarked against global ocean tide models, showing good accuracy but with notable standard deviation. A challenge of their method for the Arctic is the reliance on extensive multi-year buoy data, and the assumption of constant TCCs, which may not apply in baroclinic dominant regions. Kodaira et al., 2016 adjusted the constant tidal current assumption of Poulain and Centurioni, 2015 in baroclinic zones by using a finer $0.5^\circ \times 0.5^\circ$ grid. Their method multiplies slow-moving polynomial-fitted buoy positions by harmonic terms for the M_2 amplitude and phase. However, in this method, too, the need for large amount of buoy data remains a challenge for the Arctic.

Overall, existing methods are inadequate in addressing the unique challenges

presented by the Arctic environment. This inadequacy is evident in the need for accurate TCC estimates from single buoy trajectories, a requirement stemming from the limited availability of buoy data in the Arctic. Additionally, the significant spatio-temporal variability in amplitudes and phases, coupled with the potential frequency shift in buoy trajectory spectra, further emphasize the need for precise and adaptable tidal estimation procedures tailored to Arctic conditions.

In this paper, we introduce a method for conducting tidal harmonic analysis of single buoy trajectories accounting for space-time variations: the *Model-derived Fitting method*. The accuracy and applicability of this method will be validated through case studies involving buoys located in three distinct Arctic regions: the Barents Sea, Chukchi Sea (barotropic zones), and Baffin Bay (baroclinic zone). Furthermore, we demonstrate that the Doppler shift phenomenon can lead to frequency shifts in the angular frequency of tidal harmonics as observed by the buoy. We analysed the spectrum of two buoy trajectories in regions with both barotropic and baroclinic tidal current dominance in the Arctic. In this analysis, observed frequency shifts are compared with theoretical shifts in the spectrum, focussing on the peak for the M_2 tidal frequency.

In Section 5.2, we outline the proposed method for tidal analysis on buoy trajectories along with the mathematics of the Doppler shift. Section 5.3 delineates the data and models utilized in the study. Section 5.4 shows the results of the Doppler shift experiment with the following section (Section 5.5) focussing on the three case studies. Finally, Section 5.6 summarizes the key conclusions of this paper.

5.2. TIDAL ANALYSIS OF THE BUOYS

5.2.1. HARMONIC ANALYSIS–PRELIMINARIES

The GNSS buoys provide trajectory data, which we refer to as *position time series* in this chapter. Using these series, we can calculate velocity time series through a central difference scheme. This velocity series can be decomposed into two components: a low-frequency currents and high-frequency (i.e. tidal) currents:

$$\boldsymbol{u}(x,y,t) = \boldsymbol{u}_m(x,y,t) + \boldsymbol{u}_t(x,y,t), \tag{5.1}$$

where $\boldsymbol{u}$ represents the velocity vector of the buoy, $\boldsymbol{u}_m$ denotes the low-frequency currents, and $\boldsymbol{u}_t$ represents the high frequency (tidal currents). The functions $y(t)$ and $x(t)$ correspond to the latitude and longitude of the buoy's position at time t. The low-frequency currents can be removed by filtering or polynomial fitting e.g. (Vasulkar et al., 2022; Lie et al., 2002; Kodaira et al., 2016, among others). Some authors (e.g. Lie et al., 2002) also include a wind-driven and inertial component. For simplicity, we'll postpone this discussion until later.

The tidal component can be approximated by a tidal harmonic expansion, as shown below:

$$u_t(x,y,t) = \sum_{i \in \mathrm{TC}} H_i(x,y,t)\cos(\omega_i t - \phi_i(x,y,t)), \tag{5.2}$$

where u_t is the meridional component of $\boldsymbol{u_t}$, TC denotes the list of tidal harmonics, and ω_i represents the angular frequency of the i^{th} harmonic with its corresponding amplitude H_i and phase ϕ_i. Similarly, for the zonal component of the velocity (v_t), we have,

$$v_t(x,y,t) = \sum_{i \in \mathrm{TC}} G_i(x,y,t)\cos(\omega_i t - \theta_i(x,y,t)), \tag{5.3}$$

where the amplitude (G_i) and the phase (θ_i) correspond to the i^{th} harmonic. For a thorough decomposition of the time series, nodal factors and initial phase considerations are essential. Although, for brevity in this text, we've left out these factors from the discussed expressions. Nonetheless, we have incorporated the nodal factors in our calculation of the tidal harmonics. The magnitude and nature of Arctic tidal currents can be seen in the Arctic tidal current atlas from Baumann et al., 2020 which provides a spatio-temporal distribution of the tidal currents.

5.2.2. CHALLENGES IN DOING A TIDAL ANALYSIS

Performing a traditional tidal harmonic analysis on GNSS buoy data presents unique challenges due to the non-stationary nature of the buoys. The key issues are as follows:

SPATIO-TEMPORAL VARIABILITY IN AMPLITUDES AND PHASES

The amplitude and phase of the tidal harmonic fitting to the velocity time series of the buoy are functions of both space and time. The amplitude and phase of the TCCs can vary along the trajectory, differing from what would be observed at a fixed point. When this spatio-temporal variability is not taken into account, the movement of the buoy at best leads to an averaging of the amplitude and phase estimates over the trajectory of the buoy. But this averaging can lead to large errors in regions with large spatial variations in amplitudes and phases.

FREQUENCY SHIFT DUE TO PHASE VARIABILITY

Due to the dependence of the phase on space and time, the angular frequency of the tidal harmonics observed by the buoy is affected. In this section, we show this mathematically for the phase of the meridional velocity. Doing a first-order Taylor approximation of the phase ($\phi_i(x,y,t)$) in the cosine component of Equation (5.2), we get:

$$\hat{\phi}_i^n \approx \omega_i t - \phi_i^0 - \frac{\partial \phi_i}{\partial x}\Delta x - \frac{\partial \phi_i}{\partial y}\Delta y, \tag{5.4}$$

where $\hat{\phi}_i^n$ is the total (net) phase within the brackets of the cosine term, Δx is the average buoy movement in the $x-$ direction and likewise, Δy is the average buoy movement in the $y-$ direction. ϕ_i^0 is the phase at the initial position of the position time series. The subscript (i) denotes that this is for the i^{th} TCC. $\phi_i(x,y,t)$ being a function of time alters the frequency ω_i. To see this, consider the average velocity of the buoy given by:

$$\overline{\boldsymbol{u}} = \left[\overline{u}, \overline{v}\right]^T,$$

then, we can say that, $\Delta x = \overline{u}t$ and $\Delta y = \overline{v}t$, giving us approximately,

$$\begin{aligned}\hat{\phi}_i^n &= \omega_i t - \phi_i^0 - \frac{\partial \phi_i}{\partial x}\overline{u}t - \frac{\partial \phi_i}{\partial y}\overline{v}t, \\ &= \left(\omega_i - \frac{\partial \phi_i}{\partial x}\overline{u} - \frac{\partial \phi_i}{\partial y}\overline{v}\right)t - \phi_i^0. \end{aligned} \tag{5.5}$$

Equation (5.5) shows that the angular frequency in the meridional velocity series of the buoy is shifted by a factor dependent on the phase gradients and the average buoy velocities.

Since the buoy is moving in a tidal wave, the buoy net phase ($\hat{\phi}_i^n$) can be compared to the phase in a travelling wave with a wavenumber.

Considering the phase gradients are the wavenumbers projected on the x and y directions, i.e. $k_{ix} = \frac{\partial \phi_i}{\partial x}$ and $k_{iy} = \frac{\partial \phi_i}{\partial y}$. Then, Equation (5.5) can be re-written as:

$$\begin{aligned}\hat{\phi}_i^n &= \left(\omega_i - k_{ix}\overline{u} - k_{iy}\overline{v}\right)t - \phi_i^0, \\ &= \left(\omega_i - \boldsymbol{k_i}.\overline{\boldsymbol{u}}\right)t - \phi_i^0 = (\omega_i - \Delta\omega_i)\,t - \phi_i^0. \end{aligned} \tag{5.6}$$

where $\boldsymbol{k_i}$ is the directional wavenumber of the wave corresponding to the i^{th} TCC. Although a wavenumber is a scalar quantity, for a tidal wave propagating in a particular direction on the globe, it can be decomposed into longitude (x) and latitude (y) directions with their respective wavenumbers.

From Equation (5.6), it becomes apparent that the tidal harmonics in the buoy velocity time series are shifted by a factor of $\Delta\omega_i (= \boldsymbol{k_i}.\overline{\boldsymbol{u}})$. It should be noted that traditional tidal analysis uses a model (Equation (5.2)) that is based on fixed and known tidal frequencies. If the above shift is significant, performing a traditional tidal harmonic analysis on the buoy data directly considering the TCCs in TC will lead to erroneous results. This issue arises because the harmonic analysis attempts to fit to standard tidal frequencies in the buoy velocity times series, whereas, these frequencies are actually shifted.

The shift is significant when the order of magnitude of $\boldsymbol{k_i}.\boldsymbol{u}$ is comparable or larger than ω_i, which can be evaluated by a simple scaling analysis. For M_2 and S_2 constituents $\omega_i \sim 10^{-4}$rad/s. Considering an average buoy velocity of 1 m/s, the wavenumber (k_i) can be estimated using the underlying tidal wavelength (λ_i) via their inverse relationship. For barotropic tidal waves, the wavelengths are in the order of 1000 km, making the shift negligible. On the other hand, for baroclinic tidal waves, the order of wavelengths ranges from 10 km to 1000 km (Simmons et al., 2004; Apel, 2003), and the shift can be in the order of the tidal frequency making it significant. These shifts are similar to the Doppler shift phenomenon where the buoy is moving in a medium (i.e. the tidal wave).

5.2.3. MODEL-DERIVED FITTING METHOD

For TCC estimations from single buoy trajectories, it is imperative to address challenges arising from the space-time variation of amplitudes and phases. This variability can be approximated by a first-order Taylor Series expansion:

$$H_i(x,y,t) \approx H_i(x_0,y_0) + \left.\frac{\partial H_i}{\partial x}\right|_{(x_0,y_0)}(x-x_0) + \left.\frac{\partial H_i}{\partial y}\right|_{(x_0,y_0)}(y-y_0), \quad (5.7)$$

$$\phi_i(x,y,t) \approx \phi_i(x_0,y_0) + \left.\frac{\partial \phi_i}{\partial x}\right|_{(x_0,y_0)}(x-x_0) + \left.\frac{\partial \phi_i}{\partial y}\right|_{(x_0,y_0)}(y-y_0), \quad (5.8)$$

where the subscript 0 denotes the values at the start of the buoy trajectory. By substituting in Equation (5.2), we obtain:,

$$u_t(x,y,t) = \sum_{i\in \mathrm{TC}} {H_i}^0 \cos({\omega_i t - {\phi_i}^0 + \boldsymbol{\nabla_{\phi_i}}\cdot\boldsymbol{\Delta x}}) + \boldsymbol{\nabla_{H_i}}.\boldsymbol{\Delta x}\cos({\omega_i t - {\phi_i}^0 + \boldsymbol{\nabla_{\phi_i}}\cdot\boldsymbol{\Delta x}}), \quad (5.9)$$

where the gradients, $\boldsymbol{\nabla_{\phi_i}}$ and $\boldsymbol{\nabla_{H_i}}$, are the gradient vectors evaluated at (x_0, y_0), and the dot product is taken with the displacement vector $\boldsymbol{\Delta x} = [(x-x_0),(y-y_0)]^T$.

Likewise, a similar equation for the v_t component is given by:

$$v_t(x,y,t) = \sum_{i\in \mathrm{TC}} {G_i}^0 \cos({\omega_i t - {\theta_i}^0 + \boldsymbol{\nabla_{\theta_i}}\cdot\boldsymbol{\Delta x}}) + \boldsymbol{\nabla_{G_i}}.\boldsymbol{\Delta x}\cos({\omega_i t - {\theta_i}^0 + \boldsymbol{\nabla_{\theta_i}}\cdot\boldsymbol{\Delta x}}), \quad (5.10)$$

where the gradients, $\boldsymbol{\nabla_{\theta_i}}$ and $\boldsymbol{\nabla_{G_i}}$, are the gradient vectors evaluated at (x_0, y_0).

Equation (5.9) has the same form as the equation used for tidal estimation in Lie et al., 2002, which employs a linear polynomial for amplitude and phase. This implies that the coefficients of the polynomial in the method from Lie et al., 2002 represent derivatives of amplitudes and phases, with first-order derivatives for a linear polynomial, second-order for a quadratic polynomial, and so on.

However, for a single buoy in the case of a unidirectional flow, attempting to estimate the gradient in the orthogonal direction would result in a singular matrix implying an ill-conditioned problem, leading to erroneous estimations of amplitude and phase. This issue could also affect the method by Kodaira et al., 2016, which utilizes a third-order polynomial. Nonetheless, these methods may perform adequately due to the averaging of estimates from numerous buoys within a region or grid cell.

Additionally, adopting a linear polynomial approximation necessitates estimating six parameters per TCC: the initial amplitude and phase, along with their gradients in both the x and y directions. If TC includes n constituents, then $6n$ parameters must be estimated, significantly more than the $2n$ parameters in standard tidal harmonic analysis. This increased parameter count necessitates a trajectory with a high sampling frequency, i.e., a large number of data points. The complexity of estimation escalates with the polynomial order.

In the newly proposed, Model-derived Fitting Method (reffered to as MdF henceforth), as the name implies we capitalize on a tidal model to obtain initial estimates of the amplitudes and phases (Equations 5.7 and 5.8). Consequently, we have:

$$H_i(x,y,t) = \alpha_i H_i^m(x,y,t), \quad (5.11)$$

$$\phi_i(x,y,t) = \phi_i^m(x,y,t) + \beta_i, \quad (5.12)$$

where H_i^m and ϕ_i^m are the amplitude and phase of TCC i obtained from a tidal model at location x, y. Tidal models, particularly in the Arctic, have limited accuracy. The parameter α_i is the multiplicative correction applied to the amplitude derived from the model, and parameter β_i is the additive correction to the phase for each TCC. Here, we assume these parameters are constant over the region covered by the buoy trajectory since this results in $2n$ parameters to estimate which is same as a standard tidal harmonic analysis.

Substituting this into Equation (5.2), we obtain:

$$u_t(x,y,t) = \sum_{i \in \mathrm{TC}} \alpha_i H_i(x,y,t) \cos(\omega_i t - \phi_i(x,y,t) + \beta_i), \tag{5.13}$$

These parameters can be estimated through a least squares fit with the resulting cost function given by:

$$J(\boldsymbol{q}) = \sum_{j=0}^{N} \left(u_t(x_j, y_j, t_j) - f(t_j, \boldsymbol{\omega}, \boldsymbol{\Delta x}_j, \boldsymbol{q})\right)^2, \tag{5.14}$$

5

where N equals the number of points in the velocity time series, f is a function representing the right-hand side of Equation (5.13), $\boldsymbol{\omega}$ denotes the vector of angular frequencies for the n TCCs, and $\boldsymbol{q}$ is the parameter vector with elements:

$$\boldsymbol{q} = \left[\alpha_i, \beta_i\right], i \in \mathrm{TC}.$$

To avoid unrealistic parameter values, we impose constraints on the parameters as follows:

$$0 \leq \alpha_i \leq C, \tag{5.15}$$
$$0 \leq \beta_i \leq 2\pi, \tag{5.16}$$

where the constant C is a maximum threshold value which we set as 5 in this paper. The maximum limit in the amplitudes has a notion that if the parameters reach this limit one can expect that the model amplitudes are significantly different than the truth and the method would benefit from a different model with better first approximation.

We can re-write the Equation (5.13) as:

$$u_t(x,y) = \sum_{i \in \mathrm{TC}} \alpha_i \cos(\beta_i) H_i(x,y,t) \cos(\omega_i t - \phi_i(x,y,t)) - \alpha_i \sin(\beta_i) H_i(x,y,t) \sin(\omega_i t - \phi_i(x,y,t), \tag{5.17}$$
$$= \sum_{i \in \mathrm{TC}} A_i H_i(x,y,t) \cos(\omega_i t - \phi_i(x,y,t)) - B_i H_i(x,y,t) \sin(\omega_i t - \phi_i(x,y,t)), \tag{5.18}$$

where A_i and B_i are the new parameters to be estimated for the i^{th} TCC. This is now a linear estimation problem in A_i and B_i and is akin to a tidal harmonic analysis, albeit with a different coefficient matrix. This matrix now includes an initial approximation of the amplitude and phase from the model.

By substituting the estimated parameters into Equation (5.13), one can determine the velocity in the region covered by the buoy trajectory as long as our approximation

holds true. Additionally, given the parameters, we can compute the amplitude and phase of a TCC at a specific location in the region using Equations 5.11 and 5.12.

As with a regular tidal harmonic analysis, the number of parameters in this method is $2n$ but with constraints (Equations 5.15 and 5.16). This, along with obtaining initial approximations from a model and a reformalisation as per Equation (5.18) lends this method robustness and suitability for operational purposes. Furthermore, as the first estimates of the amplitudes and phases are obtained from the model, the space time variations of the amplitudes and phases are also indirectly a part of it.

The method focusses on estimation of the the four principal TCCs (M_2, S_2, O_1, K_1). Due to lack of knowledge of the signal-to-noise level of the buoy trajectories we use a simple Rayleigh criteria (Foreman & Henry, 1989) to select 15-day buoy trajectories for distinguishing these TCCs. A similar trajectory length in days has also been employed in Lie et al., 2002; Poulain and Centurioni, 2015; Kodaira et al., 2016, which have noted that extended trajectories can lead to significant amplitude and phase variations.

5.3. MODELS AND DATA

5.3.1. BAROTROPIC AND BAROCLINIC TIDAL MODELS

For the initial estimates in the MdF Method, we utilize tidal models suitable for the specific nature of tidal currents in the study areas. One barotropic and one baroclinic model are employed for regions with dominant barotropic and baroclinic tidal currents, respectively. The Arctic barotropic tide model employed is the Global Tide and Storm Surge Model (GTSMv4.1) (Verlaan et al., 2015). GTSMv4.1 is a global depth-averaged barotropic model forced by a full tide-generating potential, i.e., all tidal constituents are included. It is developed within the Delft3D Flexible Mesh suite from Deltares, using an unstructured grid. The grid resolution varies, with 25 km in the open ocean and 2.5 km near coastal regions. The model utilises the GEBCO2019 gridded bathymetry (GEBCO Bathymetric Compilation Group, 2019) which has been further calibrated globally in Wang et al., 2021.

The GTSM is governed by the depth-averaged shallow water equations and incorporates parameterizations of the Self-Attraction and Loading (SAL) and internal tidal wave drag (Irazoqui Apecechea et al., 2017). Additionally, the effects of Arctic sea ice dissipation on tides have been integrated into the model (Vasulkar et al., 2024). The GTSM data used in this research is drawn from runs for the year 2014 which contain only tides, and no wind forcing.

For the baroclinic region analysis, the Arctic Tidal Analysis and Forecast product was utilized (E.U.Copernicus Marine Service Information (CMEMS), 2018). This product operates on a 3D TOPAZ6 model, integrating atmospheric forcing and tidal boundary conditions from the FES2014 dataset (Lyard et al., 2021). Outputs are provided on a 3 km × 3 km grid and include sea surface elevation and surface ocean currents, which are informed by ocean general circulation, wind-driven effects, and tidal currents, and available from 2018.

5.3.2. GNSS BUOY DATA SOURCES

Arctic GNSS buoy data were sourced from a Barents Sea expedition and the IABP portal. In an expedition to the Barents Sea region in March 2014 (Kaleschke & Müller, 2022) an array of 15 drifting ice buoys were deployed. Termed as beacons by their manufacturer, they came equipped with a GNSS receiver that recorded buoy positions every 15 min. The details of the 15 buoys and their drifting trajectories are discussed in Vasulkar et al., 2022.

From the IABP, we utilized a LEVEL 1 data product (IABP, 2014) with a 3-hourly resolution, featuring different types of buoys operational from 1979 to 2016. The year 2014 had the highest number of operational buoys (327) in this dataset. We selected a buoy from this dataset that was operational in the western Chukchi Sea in 2014 (Figure 5.5). The data for this buoy had no gaps or quality issues during our study period and thus required no additional processing.

We also used a LEVEL 2 data product (IABP, 2018) for a buoy in Baffin Bay in 2018 (Figure 5.7). This product, encompassing data from 2015 to 2021, included a total of 329 buoys and underwent processing to remove 'obvious spikes' and the beginning of the data record. The selected buoy from this data set exhibited no missing data.

5

PROCESSING FOR BUOY VELOCITY TIME SERIES

For all the buoys, a buoy-derived velocity time series was computed using a central difference approach. This series was then bandpass filtered with cutoff frequencies corresponding to periods of 10 h and 30 h to capture the tidal band currents (TBC) of the meridional (u_t) and zonal (v_t) components. For bandpass filtering we used a second order Butterworth filter and applied in both forward and backward directions to realise a zero-phase filter. This technique aligns with Poulain and Centurioni, 2015 and Baumann et al., 2020. We employed the Hatyan tidal analysis and prediction software (Veenstra, 2023) to evaluate Equation (5.2) while computing the cost functions for the least squares.

5.3.3. ARCTIC TIDAL CURRENT ATLAS

For robust validation, we leveraged the Arctic-wide tidal current atlas compiled by Baumann et al., 2020. This atlas aggregates data from 429 moored current measurements, primarily from Acoustic Doppler Current Profilers (ADCPs), collected over two decades (2000-2020). This comprehensive compilation provides predictions for tidal currents, TBC, and tidal ellipse parameters over a uniform depth grid. Additional details of the data used from this dataset are provided later.

5.4. STUDY ON FREQUENCY SHIFT IN BUOY TRAJECTORIES

5.4.1. DETAILS OF EXPERIMENT

The purpose of this analysis is to discern a possible frequency shift in buoy trajectories where we focus only on the dominant M_2 tidal frequency. To investigate this phenomenon, we examined the velocity time series (u_t and v_t) from two buoy trajectories. The first buoy trajectory is the Buoy Baf from the IABP dataset located

in the baroclinic dominant Baffin Bay (Figure 5.7). The second is Buoy 16 sourced from the Barents Sea dataset (Figure 5.2).

Amplitude peaks of tidal currents near the M_2 frequency from these buoy trajectories are scrutinized in the frequency domain. To do this, we apply a Fast Fourier Transform (FFT). The magnitudes from the FFT are scaled by a factor of $2/N$, where N represents the number of points in the truncated velocity series, to obtain the amplitude spectrum. Peaks with values greater than 1 cm/s, within a range of ± 2 h from the M_2 frequency, are identified.

For buoys that exhibit peaks deviating from the M_2 frequency, these peak frequencies are compared to theoretical values derived from Equation (5.5), re-written as:

$$\hat{\phi}_i^n = (\omega_i + \Delta\omega_i)\, t - \phi_i^0, \tag{5.19}$$

where

$$\Delta\omega_i = -\frac{\partial \phi_i}{\partial x}\overline{u_t} - \frac{\partial \phi_i}{\partial y}\overline{v_t}. \tag{5.20}$$

The primary objective here is to ascertain if the magnitude of the observable shift in the M_2 frequency in the buoy spectrum corresponds to the magnitude of the theoretical frequency shifts, thus potentially validating our hypothesis. Here, we do not take into account the orientation (x or y) of the M_2 phase changes and direction of the current. Thus, the magnitude of average frequency shift can be given by:

$$\begin{aligned} |\Delta\omega_i| &= |k_i||\overline{u}|, \\ &= \frac{\omega_i}{c_i}|\overline{u}|, \qquad (5.21) \\ &= \frac{2\pi}{\lambda_i}|\overline{u}|, \qquad (5.22) \end{aligned}$$

where $\overline{u}$ is the average buoy velocity, c_i is the tidal wave speed and λ_i is the wavelength for the TCC $i \in$ TC.

The net angular frequency (ω_i^n) tracked by the buoy is then,

$$\omega_i^n = \omega_i \pm \frac{2\pi}{\lambda_i}|\overline{u}|. \tag{5.23}$$

Here, a positive (+) or negative (−) shift depends on the direction of the gradients. Using this equation, we can compute the new shifted frequencies and their corresponding time periods in both positive (added to the time period) and negative (subtracted from the time period) directions.

We are analysing the M_2 tidal wave, which has a period of 12.42 h. Since the wavelengths or the wave speed of the M_2 tidal wave in the region of the buoys are unknown, we analyse the average theoretical frequency shifts using Equation (5.22) for a range of wavelengths from 50 to 1000 km. This range facilitates the analysis of

behavior in the presence of baroclinic tides until it reaches the limit of barotropic tides around the wavelength of 1000 km. Additionally, examining this range aids in determining the magnitude range of the frequency shift

5.4.2. RESULTS AND DISCUSSION

Figure 5.1 illustrates the positions of two buoys, alongside the spectra of their u_t and v_t velocity.

Table 5.1.: Theoretical shifts in hours (computed using Equation (5.23)) of the M_2 tidal frequency for u_t and v_t components for the buoy in Baffin Bay

	Positive Period Shift		Negative Period Shift	
λ (km)	Value	Shift	Value	Shift
50	14.45	2.03	10.90	-1.52
100	13.36	0.94	11.60	-0.82
300	12.72	0.3	12.13	-0.29
1000	12.51	0.09	12.33	-0.09

A clear observation from the spectrum of the buoy in the region with barotropic tidal currents (top two of Figure 5.1) reveals that both u_t and v_t velocities peak precisely at the M_2 frequency, suggesting no shift. Conversely, in the baroclinic dominant tidal region, the peaks for both u_t and v_t trajectories are displaced from the M_2 frequency. Specifically, the u_t component peaks at a time period of 12.10 h (a negative shift from M_2), while the v_t component peaks at 12.51 h (a positive shift from M_2). The other peaks shown in the u_t and v_t spectrum of the buoy in baroclinically dominant region are possibly the shifts from nearby TCCs apart from M_2.

From Table 5.1 we can note that the average theoretical shifts corresponding to range of wavelengths less than 1000 km align well with the observed shifts in the spectrum for the buoy in Baffin Bay. This shows that the theoretical shifts have similar order of magnitudes as the observed shifts.

In the barotropic case, one can approximate the wave speed as $c_i = \sqrt{gD}$, where g is the acceleration due to gravity and D is the water depth. At the median location of the buoy, the water depth as obtained from GTSM is approximately 50 m. Using this value, $c_i = 22.36$ m/s for this buoy, and the shift using Equation (5.21) can be evaluated. The resulting shift was negligible (< 0.001 h) which aligns with the observed result of no shift for the buoy.

In both regions, M_2 is the dominant tidal forcing (Pease et al., 1983; Vasulkar et al., 2022; Kodaira et al., 2016). Consequently, these results indicate that although the external forcing on the buoy in the Baffin Bay is from the M_2 tide, the resulting spectrum of the buoy has peaks at different frequencies. This discrepancy is attributed to the Doppler shift effect, as previously discussed in Section 5.2.2, and can be approximately calculated using Equation (5.22). The magnitude of this frequency shift is inversely proportional to the M_2 tidal wavelength in the region. As

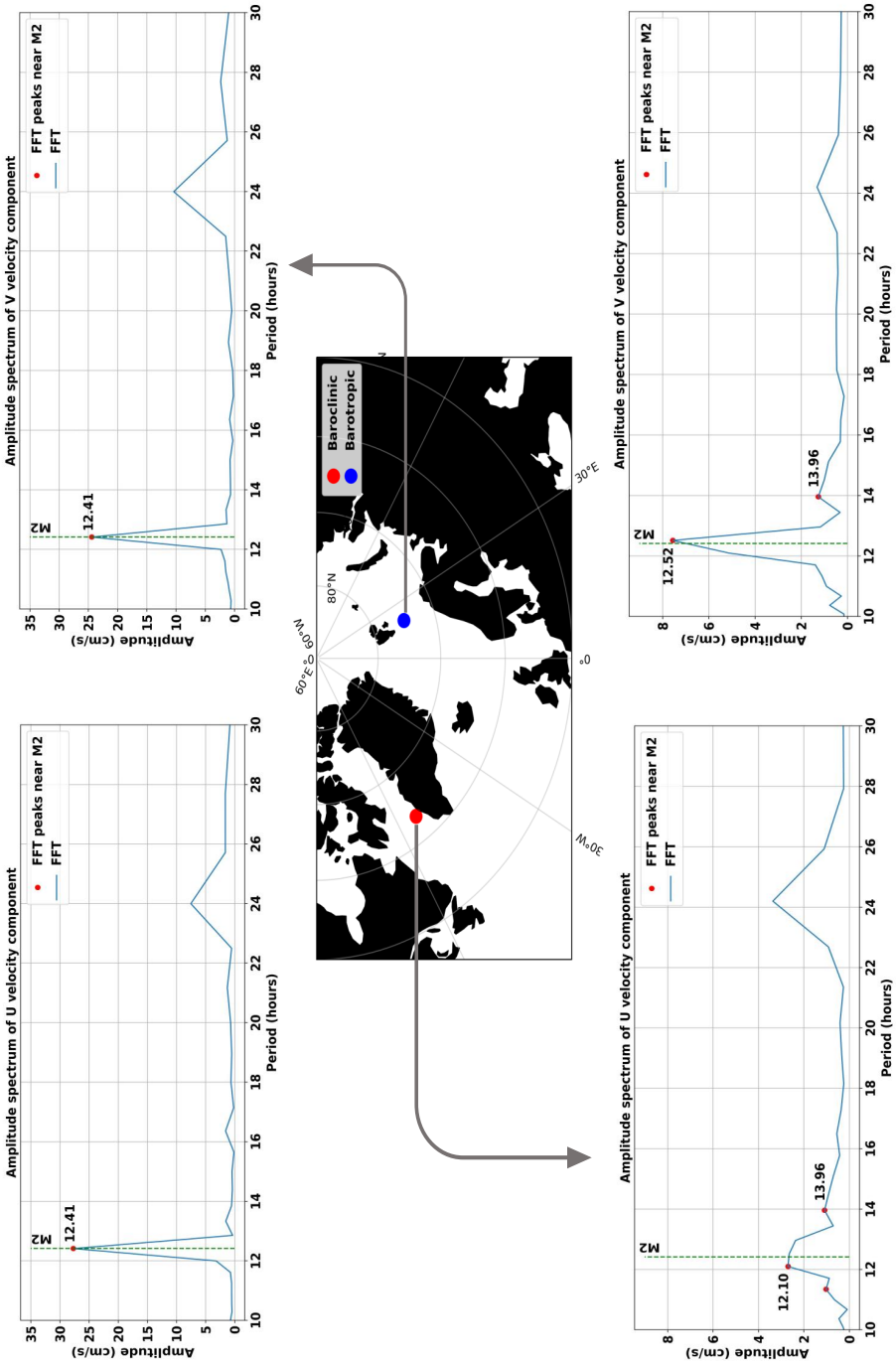

Figure 5.1.: Depiction of the median location of the two buoy trajectories analysed in this study. The blue dot represents the buoy in the predominantly barotropic tidal current region, while the red dot represents the buoy in the baroclinic dominant region. The arrows point to the Fourier spectra of their amplitudes: the top two are for the barotropic buoy and the bottom two for the baroclinic buoy. The amplitude spectra for the u_t and v_t components of the buoy velocities are shown with a dotted green line marking the M_2 frequency. Peaks and their respective frequencies near the M_2 frequency are highlighted with red dots and annotations.

a result, in areas where barotropic tides with large wavelengths dominate, such as the Barents Sea, the frequency shift becomes negligible. However, in regions with strong baroclinicity with smaller wavelengths, significant frequency shifts are likely to occur. Furthermore, these shifts suggest that applying traditional tidal harmonic analysis, which performs curve fitting by assuming a known M_2 frequency, might lead to erroneous estimations, as the actual spectrum displays peaks at frequencies different from the assumed M_2 tidal frequency.

5.5. CASE STUDIES IN THREE REGIONS

5.5.1. CASE 1: BARENTS SEA-BAROTROPIC

DETAILS OF THE EXPERIMENT

From the Barents Sea expedition dataset (Section5.3.2), we selected two trajectories of CALIB (Compact Air-Launched Ice Beacons) sea ice buoys for analysis (Figure 5.2). These buoys drifted in a free drift ice field between Hopen and Bear Island in the Barents Sea, an area characterized by barotropic tidal currents (Baumann et al., 2020; Teigen et al., 2010). Both buoys were operational during the same 15-day period from 1-15 May 2014.

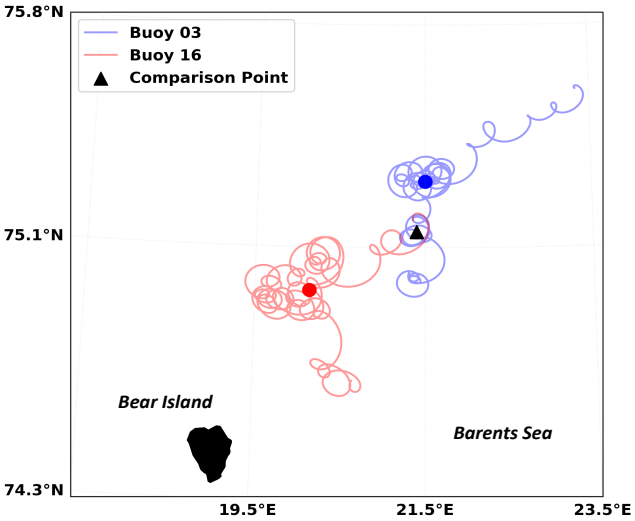

Figure 5.2.: Trajectories of two buoys in the Barents Sea region near Spitsbergen Shelf (between Hopen and Bear Island) during 1-15 May 2014, recording data at a 15 min interval. The red and blue dots represent the median location of each buoy's trajectory. The black triangle indicates the comparison point at $(21.4^{\circ}E, 75.15^{\circ}N)$, covered by both trajectories.

To assess the accuracy and robustness of our TCC estimation method, we initially compared the tidal velocities estimated by our method against the actual velocities derived from the buoy data. This comparison also involved GTSM outputs, with the Root Mean Square Error (RMSE) serving as a quantitative metric for the analysis.

Given both buoys operated within the same region, we compared the analysis at a *comparison point* (as shown in Figure 5.2) instead of at the median location for each buoy separately to reduce the impact of the spatial variability. Here, we evaluated the estimates from the MdF method applied to both buoys against GTSM outputs. This analysis included the computation of tidal ellipses for the four principal TCCs – M_2, S_2, O_1, and K_1. The computation of these current ellipses is facilitated by the amplitudes and phases of the u_t and v_t components, following the procedure outlined by Zhigang, 2002. Additional details of the individual TCC estimates from the buoys are provided in Appendix I.

RESULTS AND DISCUSSION

Figures 5.3a and 5.3b illustrate the meridional (u_t) and zonal (v_t) components of the tidal currents for Buoys 03 and 16, respectively. The RMSE values between buoy-observed tidal velocities and GTSM-derived tidal currents are [0.1 m/s, 0.11 m/s] for Buoy 03 and [0.15 m/s, 0.16 m/s] for Buoy 16 where the values in the vectors correspond to u_t and v_t components, respectively. The fit of the MdF estimated tidal currents has almost 50% lower RMSE of [0.05 m/s, 0.07 m/s] for Buoy 03 and [0.07 m/s, 0.08 m/s] for Buoy 16. The lower RMSE is expected as the GTSM currents are used as initial values for the estimation which is then optimised making use of the buoy data.

Furthermore, it is seen that the GTSM currents have smaller amplitudes than the buoy-observed estimates in all 4 panels i.e. u_t and v_t for Buoy 03 and 16. On the other hand, the estimates from MdF have larger amplitudes than the buoy-observed currents. The signal of the buoy-observed data seems to be predominantly tidal.

The tidal current ellipses presented in Figure 5.4 offer a comparative view of the tidal current estimations from our approach applied to Buoys 03 and 16 and the underlying GTSM values.

For the M_2 constituent, semi-major axis estimates from MdF method for both the buoys are approximately 0.05 m/s larger than GTSM values, with the values from Buoy 16 being the largest. In the case of the S_2 and K_1 constituents, the values from Buoy 03 align more closely with GTSM, while Buoy 16's values are marginally higher ≈ 0.01 m/s. Yet, both MdF estimates point in the same direction compared to GTSM. These results inspire confidence in the method. As for the O_1 constituent there is no coherence between the estimates and GTSM, with semi-major axes values less than 0.01 m/s, suggesting lower confidence in these estimates.

The location of the comparison point is around the critical latitude for the M_2 constituent where its frequency is very close to the inertial oscillations (Pease et al., 1983; Vasulkar et al., 2022). The absence of wind effects in the GTSM might explain the lower ellipse values for the M_2 constituent when compared to buoy-derived estimates. It is also possible that the surface currents are a bit larger than the depth-averaged currents from GTSM.

Regarding the O_1 constituent, random and systematic error in the receiver positions may contribute to the incoherent results. Given the 15 min sampling interval and an average speed of 0.01 m/s, the resultant travel distance is approximately 9 m. This distance may fall below the GNSS receiver's threshold of accuracy, leading

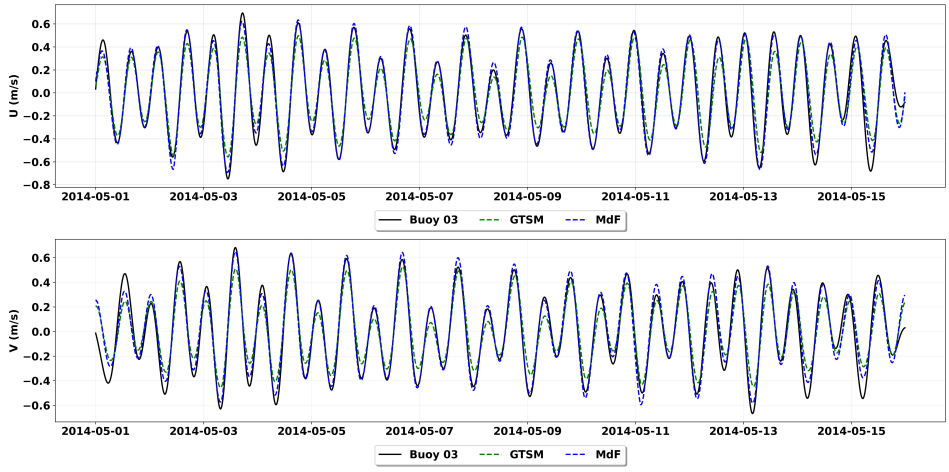

(a) Buoy 03

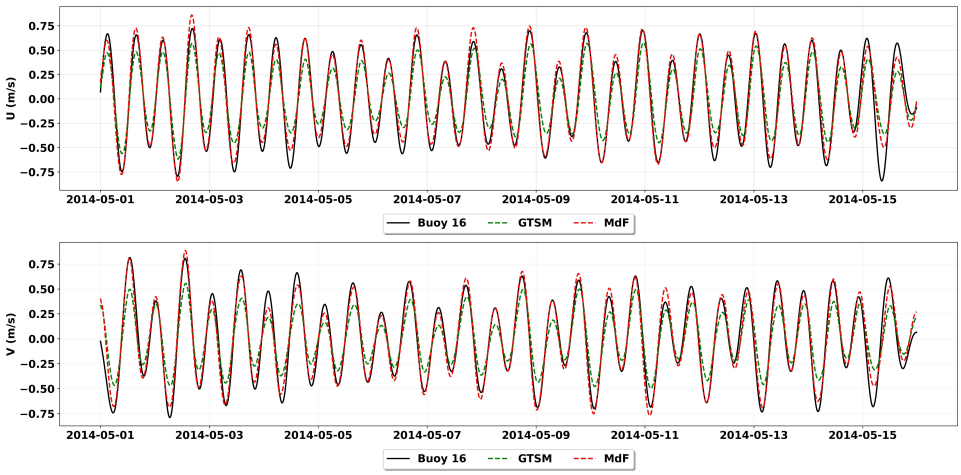

(b) Buoy 16

Figure 5.3.: Comparison of tidal current velocities for Buoys 03 (a) and 16 (b) over a 15-day period starting May 1, 2014. The plots display the meridional (u_t) and zonal (v_t) velocity components derived from buoy observations alongside the values from GTSM (green) and the estimates from the MdF method. Note that the red and blue colors correspond to the respective Buoy 03 and Buoy 16 from figure 5.2 while the black is for the observed tidal currents from the buoys.

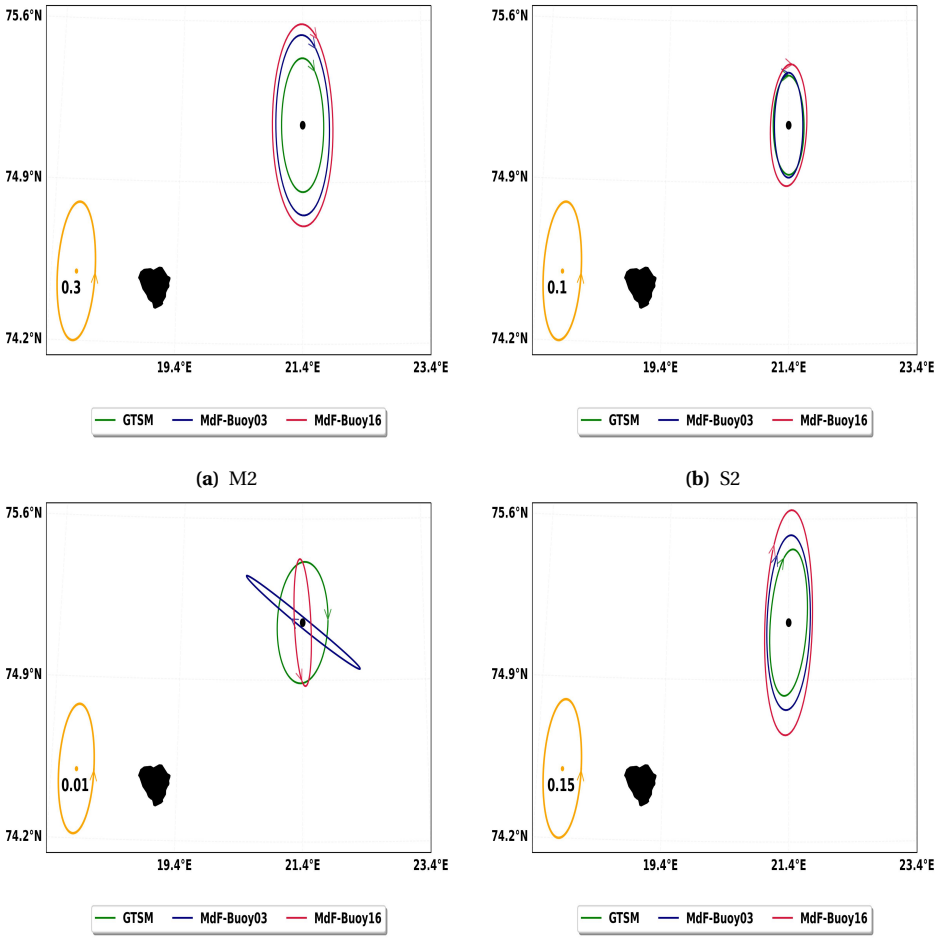

(a) M2 **(b)** S2

(c) O1 **(d)** K1

Figure 5.4.: Tidal current ellipses for the 4 TCCs-M_2 (a), S_2 (b), O_1 (c), K_1 (d). The centre of the ellipse indicates the comparison point $(21.4°E, 75.15°N)$; arrows on the ellipse represent its rotation. The comparison is between GTSM (green), MdF applied to Buoy 03 (blue) and MdF applied to Buoy 16 (red). The lower-left ellipse demonstrates the scale, with the magnitude of the semi-major axis given at the center in m/s.

to uncertainties in estimations, especially for low-value measurements. However, without specific details on the GNSS receiver's instrument accuracy, we can only hypothesize about the nature of these errors. Systematic errors may also arise during phase estimation, particularly since O_1's amplitudes are an order of magnitude lower than those of other constituents. To ensure the analysis remains coherent and minimize uncertainties, here, we establish a criterion that any TCC with a semi-major axis less than 0.01 m/s will not be considered for comparison. This decision helps

avoid potential inaccuracies associated with such low-value estimations, thereby enhancing the robustness of the analysis.

The quality of the fit of the MdF estimates along with its good agreement with GTSM values for the both the buoys at the comparison point sheds light on its accuracy and robustness. The marginally larger values observed in Buoy 16's estimates could be attributed to its more distant median location from the comparison point, as seen in Figure 5.2.

5.5.2. CASE 2: CHUKCHI SEA-BAROTROPIC

DETAILS OF THE EXPERIMENT

In this study, the Chukchi Sea buoy, referred to as *Buoy Chuk* (Figure 5.5), was obtained from the IABP's LEVEL 1 data product for 2014. It had a sampling interval of three hours during the period 1 July to 15 July. Mounted on an ice floe, this surface velocity profiler buoy, with ID *300234061367150*, traversed the region west of Hanna Shoal, known for its predominantly barotropic tidal currents (Fang et al., 2022).

The buoy was chosen for its complete data set, noting its drift through a free drift ice field with ice concentrations ranging from 0 to 0.8, as confirmed by sea ice data from (Copernicus Marine Service, 2014). Another selection criterion was the buoy's proximity to a nearby ADCP mooring (*ADCP Chuk*), situated at a geodesic distance of 15.2 km from the buoy's median location and intersecting its trajectory, thereby providing a valuable independent observation for validation purposes.

We evaluate the accuracy of the tidal estimates from our MdF approach on Buoy Chuk using GTSM as the underlying model. The TCCs from GTSM were derived from the simulations corresponding the buoy's operational period (1-15 July 2014). For validation, we obtained the tidal ellipse parameters from the Full Record (FR) data of the ADCP Chuk and averaged it over the depth. This depth-averaged FR data from the tidal current atlas is suitable for comparison with barotropic TCCs as suggested by Baumann et al., 2020.

The analysis focuses on the M_2 tide, predominant in this region, and excludes other constituents since their amplitudes are below 8 mm/s. Tidal ellipses for the M_2 constituent are plotted at both the ADCP location and the buoy's median location for visual comparison. For a quantitative assessment, the Vector Difference (VD) is calculated by comparing the buoy-derived and GTSM estimates at the mooring location against the mooring values. The VD is defined by Provost et al., 1995:

$$\mathrm{VD}_i = \sqrt{\left(A_i^o \cos(\phi_i^o) - A_i^e \cos(\phi_i^e)\right)^2 + \left(A_i^o \sin(\phi_i^o) - A_i^e \sin(\phi_i^e)\right)^2}, \tag{5.24}$$

where VD_i stands for the vector difference between the observation (represented by superscript o) and the estimated values from our methods (denoted by superscript e) for each TCC $i \in \mathrm{TC}$.

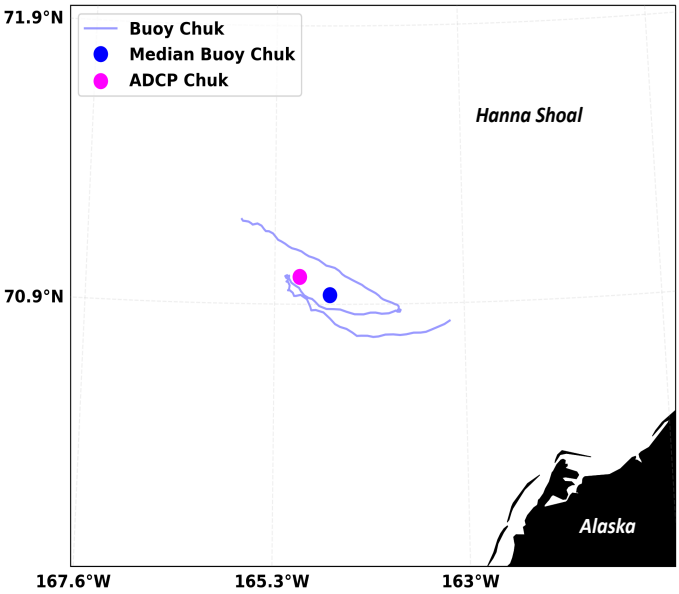

Figure 5.5.: Trajectory of *Buoy Chuk* in the barotropically dominant region west of the Hanna Shoal in the Chukchi Sea. The median location of the buoy (blue dot) and the nearby moored observation point from the Arctic Tidal Atlas (see Sec. 5.3.3) are also shown.

Table 5.2.: Comparison of the M_2 TCC estimates at the ADCP Chuk location. H is for amplitude, ϕ is for phase.

	u_t			v_t		
	H (m/s)	ϕ (deg)	VD (m/s)	H (m/s)	ϕ (deg)	VD (m/s)
ADCP Chuk	0.022	161.0	0.0	0.026	59.7	0.0
GTSM	0.025	165.0	0.004	0.018	88.8	0.017
Buoy Chuk	0.025	160.0	0.003	0.023	54.9	0.003

RESULTS AND DISCUSSION

Figure 5.6 presents tidal current ellipses for the M_2 tide at the median buoy location and the mooring site (ADCP Chuk). Amplitudes, phases, and vector differences (VD) at the mooring location can be found in Table 5.2.

The GTSM values for the meridional component closely match the moored observations in amplitude and phase. However, the GTSM values for the zonal component are noticeably less than those from ADCP Chuk, leading to a reduced semi-major axis in GTSM's tidal ellipse. In contrast, the MdFs estimates for Buoy Chuk show a better resemblance to ADCP Chuk for both zonal and meridional components, as indicated by the smaller VD compared to GTSM. The tidal ellipse from the MdF method is similar to those from ADCP Chuk but displays a slight

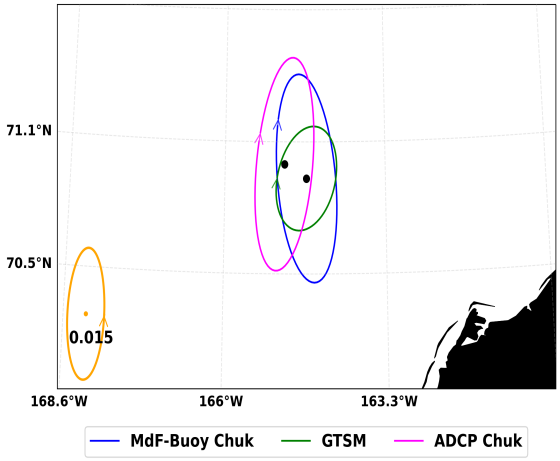

(a) M_2

Figure 5.6.: Tidal current ellipses for the M_2 constituent in the Chukchi Sea region. The ellipse's center indicates the dataset's location, arrows on the ellipse represent its rotation, while the ellipse's color denotes the dataset type. The lower-left ellipse demonstrates the scale, with its semi-major axis measuring 0.015 m/s.

angular offset, likely due to the approximate 5° phase disparity in the zonal component. The VDs with MdF are less than 0.01 m/s which are quite small given that these are based on a single buoy.

The results indicate that the estimates from the MdF method have a better agreement with the ADCP observations than GTSM. Lack of inertial oscillations in GTSM could be a possible reason for its poor performance.

The examples in Sections 5.5.1 and 5.5.2 validate the TCC estimation of our MdF method, demonstrating its accuracy in Arctic regions with barotropic conditions. The method's robustness is evidenced by its model-derived estimates, which effectively capture spatio-temporal variability. This ensures consistent tidal estimates across different conditions. Furthermore, obtaining similar estimates from different buoys at the same location lends additional credibility to the method's robustness. The results are encouraging, but the number of collocation points we could find was very limited.

A broader validation, encompassing additional buoys across diverse Arctic regions, would ideally substantiate the reliability of our method for barotropic conditions. However, the harsh Arctic environment and the scarcity of independent validation datasets present significant hurdles to such expansive verification.

5.5.3. CASE 3: BAFFIN BAY-BAROCLINIC

DETAILS OF THE EXPERIMENT

Multiple factors influenced the selection of a buoy in the Baffin Bay region. Firstly, Baffin Bay is known for having tidal currents with strong baroclinicity (Baumann et al., 2020). Secondly, the 3D model TOPAZ6 data were available only from the year 2018. Thirdly, the arctic tidal atlas had one of the largest number of moorings in this region. Based on this, we selected a buoy in Baffin Bay, referred to as *Buoy Baf* (Figure 5.7).

It was sourced from the IABP's LEVEL2 data product (Section 5.3.2), featuring a 3-hour sampling interval from October 28 to November 11, 2018. The buoy's ID in the original dataset is *300234064501660* with no details on the type of buoy or its instrument accuracy. We anticipate that it is a surface open ocean current tracking buoy, considering its operation in open waters during a period typically free of sea ice in Baffin Bay based on sea ice concentration from GLORYS global reanalysis (Copernicus Marine Service, 2014).

Moorings named *ADCP Baf C4* and *ADCP Baf C6* (Figure 5.7) were selected based on their proximity to the buoy trajectory. TBC data, spanning the entire depth from these moorings, were obtained and computed through bandpass filtering with cutoff frequencies corresponding to periods of 10-30 hours (Baumann et al., 2020). At each location, the dataset included TBC for five distinct durations.

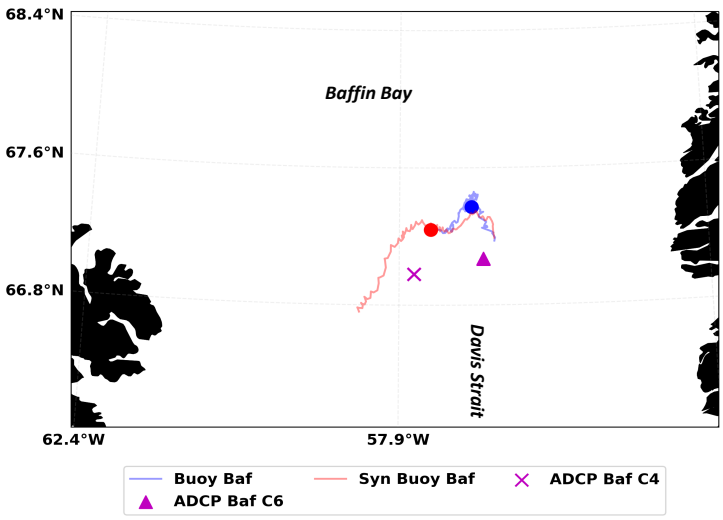

Figure 5.7.: Trajectories and mooring observation locations in Baffin Bay. Trajectory period October 28–November 11, 2018 for Buoy Baf and the corresponding synthetic trajectory for the same period. The corresponding medians positions for the trajectories are given by dots. The ADCP mooring locations in magenta are for *ADCP Baf C4* and *ADCP Baf C6* data locations.

SPATIO-TEMPORAL VARIABILITY OF M_2 TIDAL ELLIPSES IN BAFFIN BAY

Technically, at the two locations of ADCP Baf C4 and ADCP Baf C6 in Figure 5.7, there were multiple expeditions to install ADCPs at approximately the same location over a number of years. Further technical details regarding these ADCP observations are found in Wu et al., 2013. From this data, we evaluate M_2 tidal ellipses by doing a tidal analysis on the TBC in the period from October 28 to November 11 and from November 11 to November 28 for the 5 years of data availability. The first 15-day period corresponded to the Buoy Baf period and the next 15-day period for 5 years was plotted to show the temporal variability. These M_2 ellipses are plotted for both the locations for the surface currents and the depth-averaged currents (Figures 5.8 and 5.9).

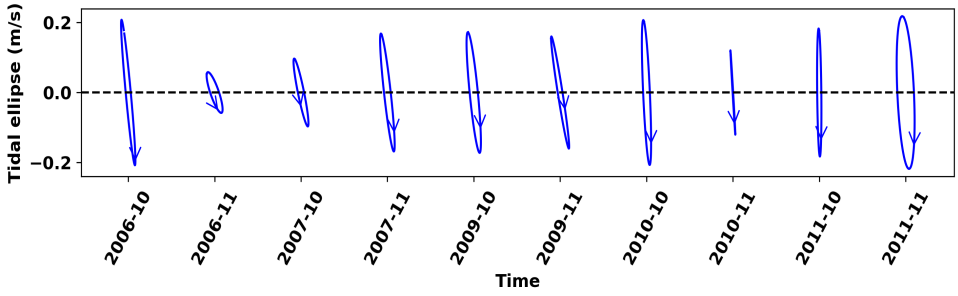

(a) Surface

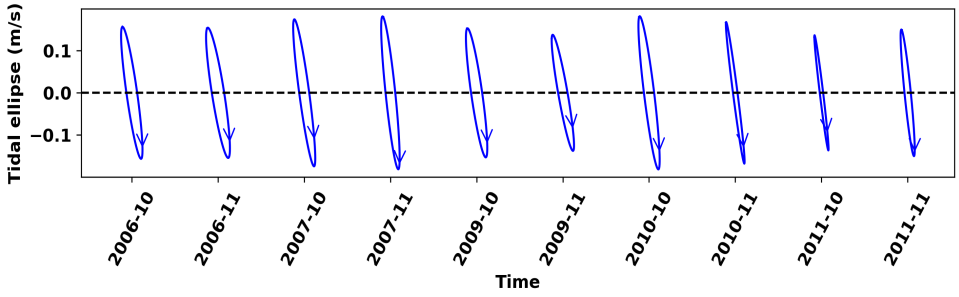

(b) Depth-averaged

Figure 5.8.: Tidal ellipses of the M_2 constituent measured by mooring ADCP Baf C4. Figure 5.8a shows the surface component over time. Figure 5.8b shows the depth-averaged component over time.

Significant temporal variability is observed at both locations for the surface tidal ellipses, with a standard deviation of approximately 5 cm/s. Conversely, the depth-averaged tidal ellipses exhibit a standard deviation of less than 1 cm/s. The mean values for depth-averaged currents are equal to or less than those for surface currents, suggesting that surface tidal currents are stronger or equivalent to depth-averaged currents. Spatial variability in tidal currents is also evident, with ADCP Baf C4 displaying a larger semi-major axis compared to ADCP Baf C6.

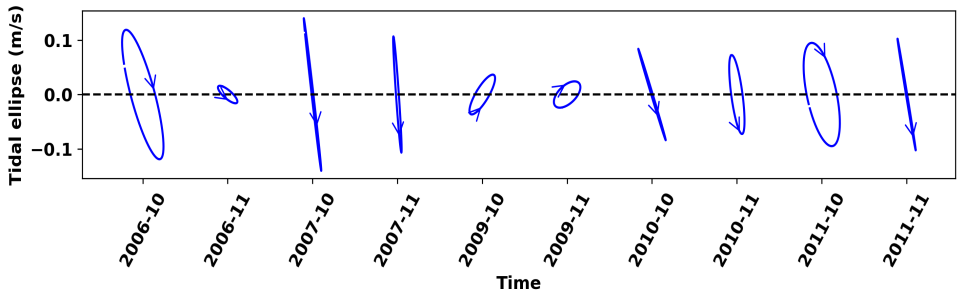

(a) Surface

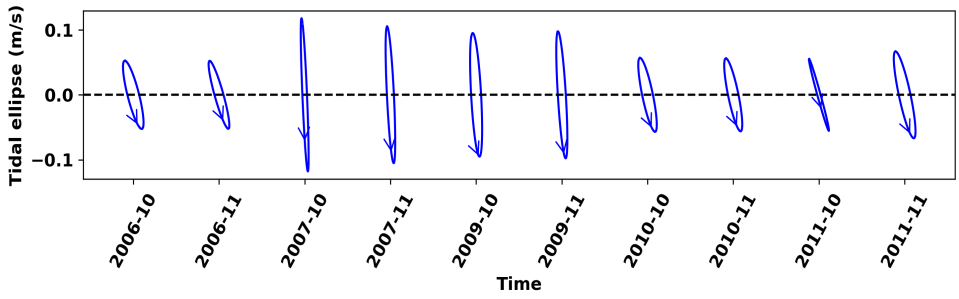

(b) Depth-averaged

Figure 5.9.: Tidal ellipses of the M_2 constituent measured by mooring ADCP Baf C6. Figure 5.8a shows the surface component over time. Figure 5.8b shows the depth-averaged component over time.

Table 5.3.: Variability of the semi-major axis of M_2 tidal ellipses at the two ADCP locations computed as mean and standard deviation with units in m/s.

	Surface		Depth-averaged	
	Mean	Std.	Mean	Std.
ADCP Baf_C4	0.18	0.04	0.19	0.01
ADCP Baf _C6	0.16	0.05	0.12	0.009

The substantial spatio-temporal variability in the surface tidal currents in this region corroborates the presence of strong M_2 baroclinic currents. This implies the need for mooring data that closely aligns in time and location with the buoy trajectory for accurate comparison using the estimates from the MdF method applied to the buoy.

In such baroclinic zones, the challenges are twofold: the substantial temporal and spatial variability, and the potential deviation of surface currents from depth-averaged currents. While the latter may be mitigated by employing a 3D tidal model, the former necessitates precisely matching mooring data in location and time.

We applied the MdF method to the Buoy Baf trajectory and computed the M_2

tidal ellipse. This estimate was compared to the underlying 3D TOPAZ6 model and evaluated against the standard deviation observed at the nearby ADCP locations (Table 5.3). Note that there was no mooring observation in 2018 near the buoy location to validate.

RESULTS-REAL BUOY DATA

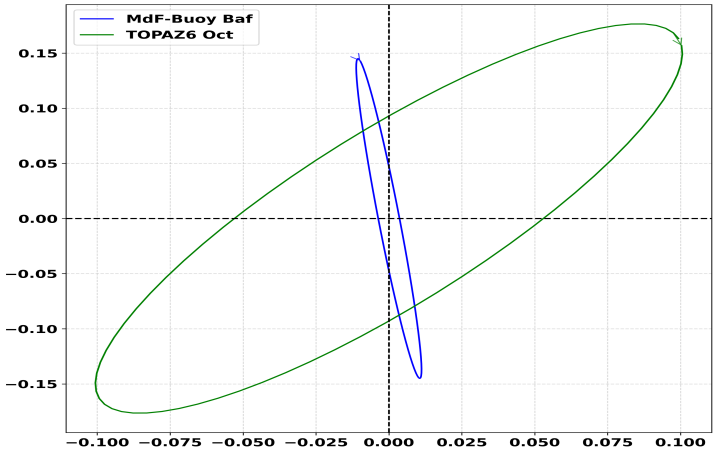

Figure 5.10.: M_2 tidal ellipses from the MdF estimation on Buoy Baf (blue) and the underlying TOPAZ6 (green) value for the October 2018 period. The axes labels are in m/s.

Figure 5.10 illustrates the M_2 tidal ellipses, comparing the MdF estimates for Buoy Baf with those from TOPAZ6 at the same location for October 28 to November 11 period. The Buoy Baf's estimated semi-major axis is 0.15 m/s, falling within the standard deviation range observed in Table 5.3. However, the TOPAZ6 estimate, at 0.2 m/s, exceeds this range. This suggests that the MdF method's estimate is in a realistic range, though its accuracy remains undetermined.

The absence of a mooring dataset at exact spatial location and temporal duration for validation in this baroclinically dominant Baffin Bay region with large spatio-temporal variability prompted us to conduct a synthetic test.

SYNTHETIC EXPERIMENT

This experiment involved constructing a synthetic buoy trajectory using the following equation:

$$\frac{\partial \boldsymbol{x}}{\partial t} = \boldsymbol{u} + \boldsymbol{\epsilon}, \tag{5.25}$$

where $\boldsymbol{x}$ represents the synthetic buoy's position vector, $\boldsymbol{u}$ is the surface velocity vector derived from the model (TOPAZ6), and $\boldsymbol{\epsilon}$ denotes a zero-mean Gaussian noise with standard deviation of 0.01 m/s.

This equation was integrated over time with a forward Euler scheme having a time step of 15 min. This integration over time, starting from the actual buoy's initial position ($\boldsymbol{x_0}$) on October 28, produces a synthetic trajectory (Figure 5.7) referred to as *Syn Buoy Baf* for 15-day period. Since the underlying model is TOPAZ6, we obtain the TCC values at the median location of the synthetic buoy trajectory from the model providing us the *synthetic truth*.

Considering the month-to-month variability in TCCs, we utilize model data from a subsequent 15-day period starting on November 12. With this model data as the initial data and the synthetic buoy trajectory we use the MdF method to estimate TCC parameters. These estimates are subsequently compared with the synthetic truth to evaluate the method's performance in this region. This assessment includes calculating tidal ellipses and vector differences, as previously conducted in Section 5.5.2.

RESULTS AND DISCUSSION

Figure 5.11 shows the tidal ellipses for the synthetic truth, initial estimates from the TOPAZ6 model, and MdF estimation from the Syn Buoy Baf trajectory. The vector differences (VD_i) relative to the synthetic truth are detailed in Table 5.4. The O_1 TCC is omitted since its amplitude is < 1 cm/s.

Table 5.4.: Vector Difference (VD_i) between the initial and predicted values against the truth for the meridional (v_t) and zonal (u_t) components.

	Vector Differences for u_t		Vector Differences for v_t	
	TOPAZ6 Initial	MdF-Syn Buoy Baf	TOPAZ6 Initial	MdF-Syn Buoy Baf
M_2	0.030	0.004	0.077	0.005
S_2	0.022	0.006	0.028	0.003
K_1	0.027	0.002	0.016	0.015

The estimations from the MdF method appear to be in close agreement with the synthetic truth values. There is a noticeable phase discrepancy of approximately $5-10^\circ$ for the S_2 and K_1 constituents between the estimated and actual values, resulting in a slight angular difference between the ellipses. In contrast, the initial estimates from the TOPAZ6 model differ significantly from the synthetic truth, as evidenced by the larger vector differences.

The MdF method's accuracy in the synthetic case suggests its applicability in regions with dominant baroclinic tides. Although this conclusion stems from a synthetic test, the outcomes imply that model-derived gradients in amplitude and phase can aid in accurately estimating tidal parameters from buoy trajectories. The substantial difference between the initial model estimates and the synthetic truth, coupled with the agreement between the synthetic buoy-derived estimates and the true values, lends credibility to the method's effectiveness.

Synthetic experiments enable the computation of realistic estimates of expected accuracy of the method by comparing against known truths within the simulation framework. However, the reliability of these estimates depends upon the accuracy of

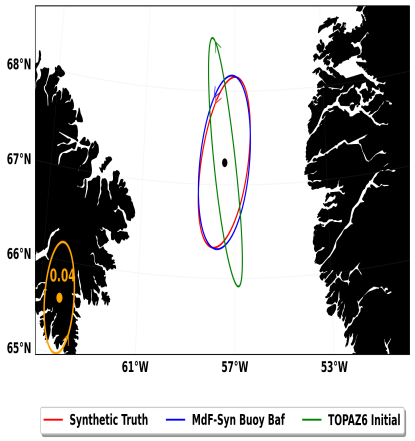

(a) M_2

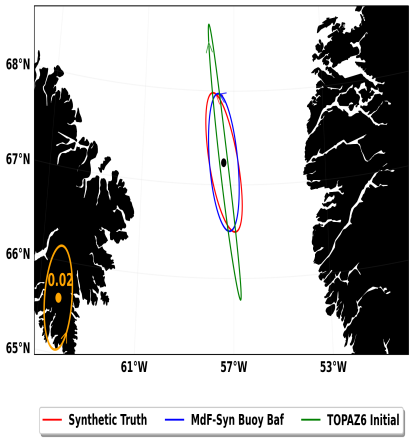

(b) S_2

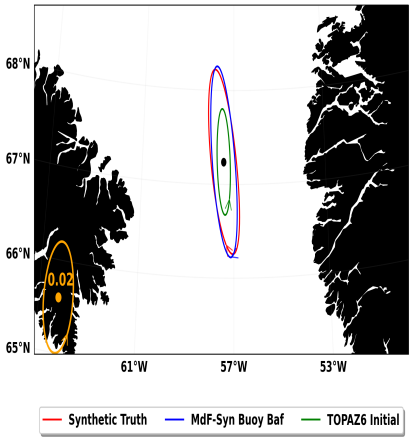

(c) K_1

Figure 5.11.: Tidal current ellipses for M_2, S_2 and K_1 constituents in the Baffin Bay region. The ellipse's center indicates the dataset's location, arrows on the ellipse represent its rotation, while the ellipse's color denotes the dataset type. The lower-left ellipse demonstrates the scale with the value at the center for the semi-major axis.

the uncertainties factored into the computation. Such experiments may yield overly optimistic results if the underlying uncertainties are not accurately represented.

A more definitive assessment of the MdF method's ability in baroclinic dominant regions would need a validation against independent observational data. Securing such a dataset for baroclinic dominant regions, which must closely correspond in location and time with the model and buoy trajectory, remains a substantial challenge. Future opportunities to access such data would further validate the reliability and usefulness of these buoy-derived estimates in such complex regions.

Since this approach depends on reliable initial estimates from a model, it necessitates the availability of a model to derive estimates from buoy trajectories. This reliance forms a significant limitation in scenarios where such models are unavailable. Additionally, our method assumes constant multiplicative factors in the estimation process (see Equation (5.13)). This assumption could be a potential constraint in regions where it may not be applicable. To address this, one could either reduce the length of the trajectory or introduce variability in these factors. However, such modifications necessitate further research.

5.6. SUMMARY AND CONCLUSIONS

In this paper, we proposed a novel method to estimate the tidal current constituents from a single buoy trajectory addressing the limitations in the Arctic.

We show that traditional harmonic analysis applied to buoy velocities does not only suffer from the spatial variability of the tides, but the interaction between mean flow and tides may also introduce frequency shifts in buoy-observed amplitudes, challenging the efficacy of traditional tidal harmonic analysis. This phenomenon, similar to Doppler shift, was empirically investigated using buoy data from both barotropic and baroclinic dominant regions. We found that in barotropic dominant regions, such shifts are negligible due to the large tidal current wavelengths, typically around 1000 km. In contrast, the shifts in the baroclinic dominant regions can be approximately computed by the Doppler shift formula.

Three case studies were conducted to assess the accuracy, robustness, and operational efficiency of our proposed method. In case 1 (Section 5.5.1), we demonstrated the method's accuracy and robustness through comparison with model results and noting the consistency of estimates derived from two different buoys. Case 2 (Section 5.5.2) involved a comparison with an independent moored observation in the barotropic dominant region of the Chukchi Sea, confirming the accuracy of the MdF method for estimating TCCs in such regions. In a baroclinic tidal region, the performance of the method is yet to be determined based on real control data. However, a simple synthetic experiment (case 3 Section 5.5.3) may be seen as an indication that the method can be applied in complex baroclinic environments.

In summary, our method has shown promising results when applied to buoys in various Arctic regions. It effectively incorporates spatio-temporal variations by utilizing model-based initial estimates. Additionally, the estimation of $2n$ parameters like in a standard tidal harmonic analysis coupled with a linearized estimation

process makes it operationally efficient. However, a more comprehensive validation, involving a wider range of buoys and independent observational data across both barotropic and baroclinic zones, is necessary to fully substantiate its applicability across the diverse Arctic regions. Furthermore, additional validation can be achieved by comparing the fixed amplitude ratios for S_2 and O_1 against M_2 and K_1 TCC respectively, between the model values and the buoy-derived estimates. Such validations are crucial for testing the assumptions, such as the constant multiplicative factor used in the MdF Method (Equation (5.13)). A representation of variable parameters with polynomials is one solution which can be investigated however, care should be taken that this might also lead to an illconditioned problem in the estimation similar to the methods from Lie et al., 2002 and others. Moreover, the reliance on good initial model estimates is a limitation when compared to existing approaches like those proposed by Lie et al., 2002 and Kodaira et al., 2016, although such models are becoming more readily available in recent years.

REFERENCES

Luneva, M. V., Aksenov, Y., Harle, J. D., & Holt, J. T. (2015). The effects of tides on the water mass mixing and sea ice in the Arctic Ocean. *Journal of Geophysical Research: Oceans*, *120*(10), 6669–6699. https://doi.org/10.1002/2014JC010310

Watkins, D. M., Bliss, A. C., Hutchings, J. K., & Wilhelmus, M. M. (2023). Evidence of Abrupt Transitions Between Sea Ice Dynamical Regimes in the East Greenland Marginal Ice Zone. *Geophysical Research Letters*, *50*(15), e2023GL103558. https://doi.org/10.1029/2023GL103558

Baumann, T. M., Polyakov, I. V., Padman, L., Danielson, S., Fer, I., Janout, M., Williams, W., & Pnyushkov, A. V. (2020). Arctic tidal current atlas. *Scientific Data 2020 7:1*, *7*(1), 1–11. https://doi.org/10.1038/s41597-020-00578-z

Boylan, B. M. (2021). Increased maritime traffic in the Arctic: Implications for governance of Arctic sea routes. *Marine Policy*, *131*, 104566. https://doi.org/10.1016/J.MARPOL.2021.104566

Lyard, F. H., Allain, D. J., Cancet, M., Carrère, L., & Picot, N. (2021). FES2014 global ocean tide atlas: Design and performance. *Ocean Science*, *17*(3), 615–649. https://doi.org/10.5194/OS-17-615-2021

Verlaan, M., De Kleermaeker, S., & Buckman, L. (2015). GLOSSIS: Global storm surge forecasting and information system. *Australasian Coasts & Ports Conference 2015: 22nd Australasian Coastal and Ocean Engineering Conference and the 15th Australasian Port and Harbour Conference*, 229–234.

Erofeeva, S., & Egbert, G. (2018). Arc5km2018: Arctic Ocean Inverse Tide Model on a 5 kilometer grid. https://doi.org/10.18739/A21R6N14K

Cancet, M., Andersen, O., Lyard, F., Shulz, A., Cotton, P., & Benveniste, J. (2016). A New High Resolution Tidal Model in the Arctic Ocean. *Living Planet Symposium*, 67. https://ui.adsabs.harvard.edu/abs/2016ESASP.740E..67C

Müller, M., Cherniawsky, J. Y., Foreman, M. G., & Von Storch, J. S. (2014). Seasonal variation of the M 2 tide. *Ocean Dynamics*, *64*(2), 159–177. https://doi.org/10.1007/s10236-013-0679-0

Munchow, A., Coughran, C., Hendershott, M., & Winant, C. (1995). Performance and Calibration of an Acoustic Doppler Current Profiler Towed below the Surface. *Journal of Atmospheric and Oceanic Technology*, 435444.

Nyström, L. (2022). *Acoustic Doppler Current Profiling for streamflow measurements in subarctic climate* (Doctoral dissertation). Luleå University of Technology. Luleå. https://urn.kb.se/resolve?urn=urn:nbn:se:ltu:diva-92666

Bliss, A., Hutchings, J., Anderson, P., Anhaus, P., Belter, H. J., Berge, J., Bessonov, V., Cheng, B., Cole, S., Costa, D., Cottier, F., Cox, C. J., Torre, P. R. D. L., Divine, D. V., Emzivat, G., Fang, Y.-C., Fons, S., Gallagher, M., Geoffrey, M., … Zuo, G. (2022). Raw files for sea ice drift tracks from the Distributed

Network of autonomous buoys deployed during the Multidisciplinary drifting Observatory for the Study of Arctic Climate (MOSAiC) expedition 2019 - 2021. https://doi.org/10.18739/A2WW77163

Raghukumar, K., Chang, G., Spada, F., Jones, C., Janssen, T., & Gans, A. (2019). Performance Characteristics of Spotter, a Newly Developed Real-Time Wave Measurement Buoy. *Journal of Atmospheric and Oceanic Technology*, *36*(6), 1127–1141. https://doi.org/10.1175/JTECH-D-18-0151.1

Kodaira, T., Waseda, T., Nose, T., Sato, K., Inoue, J., Voermans, J., & Babanin, A. (2021). Observation of on-ice wind waves under grease ice in the western Arctic Ocean. *Polar Science*, *27*, 100567. https://doi.org/10.1016/J.POLAR.2020.100567

IABP. (2020). Deployment Plans. https://iabp.apl.uw.edu/overview_deploymentplans.html

Koentopp, M., Eisen, O., Kottmeier, C., Padman, L., & Lemke, P. (2005). Influence of tides on sea ice in the Weddell Sea: Investigations with a high-resolution dynamic-thermodynamic sea ice model. *Journal of Geophysical Research: Oceans*, *110*(C2), 1–12. https://doi.org/10.1029/2004JC002405

Pease, C. H., Salo, S. A., & Overland, J. E. (1983). Drag measurements for first-year sea ice over a shallow sea. *Journal of Geophysical Research*, *88*(C5), 2853. https://doi.org/10.1029/JC088iC05p02853

Vasulkar, A., Verlaan, M., Slobbe, C., & Kaleschke, L. (2022). Tidal dissipation from free drift sea ice in the Barents Sea assessed using GNSS beacon observations. *Ocean Dynamics*, *72*(8), 577–597. https://doi.org/10.1007/s10236-022-01516-w

Simmons, H. L., Hallberg, R. W., & Arbic, B. K. (2004). Internal wave generation in a global baroclinic tide model. *Deep Sea Research Part II: Topical Studies in Oceanography*, *51*(25-26), 3043–3068. https://doi.org/10.1016/J.DSR2.2004.09.015

Apel, J. R. (2003). A New Analytical Model for Internal Solitons in the Ocean*. *Journal of Physical Oceanography*, *33*(11), 2247–2269. https://doi.org/10.1175/1520-0485(2003)033<2247:ANAMFI>2.0.CO;2

Lie, H.-J., Lee, S., & Cho, C.-H. (2002). Computation methods of major tidal currents from satellite-tracked drifter positions, with application to the Yellow and East China Seas. *Journal of Geophysical Research: Oceans*, *107*(C1), 3–1. https://doi.org/10.1029/2001JC000898

Poulain, P. M., & Centurioni, L. (2015). Direct measurements of World Ocean tidal currents with surface drifters. *Journal of Geophysical Research: Oceans*, *120*(10), 6986–7003. https://doi.org/10.1002/2015JC010818

Kodaira, T., Thompson, K. R., & Bernier, N. B. (2016). Prediction of M2 tidal surface currents by a global baroclinic ocean model and evaluation using observed drifter trajectories. *Journal of Geophysical Research: Oceans*, *121*(8), 6159–6183. https://doi.org/10.1002/2015JC011549

Foreman, M. G., & Henry, R. F. (1989). The harmonic analysis of tidal model time series. *Advances in Water Resources*, *12*(3), 109–120. https://doi.org/10.1016/0309-1708(89)90017-1

GEBCO Bathymetric Compilation Group. (2019). *The GEBCO_2019 Grid - a continuous terrain model of the global oceans and land* (tech. rep.). British Oceanographic Data Centre, National Oceanography Centre, NERC, UK. GEBCO.

Wang, X., Verlaan, M., Apecechea, M. I., & Lin, H. X. (2021). ComputationEfficient Parameter Estimation for a HighResolution Global Tide and Surge Model. *Journal of Geophysical Research: Oceans*, *126*(3), e2020JC016917. https://doi.org/10.1029/2020JC016917

Irazoqui Apecechea, M., Verlaan, M., Zijl, F., Le Coz, C., & Kernkamp, H. (2017). Effects of self-attraction and loading at a regional scale: a test case for the Northwest European Shelf. *Ocean Dynamics*, *67*(6), 729–749. https://doi.org/10.1007/s10236-017-1053-4

Vasulkar, A., Verlaan, M., Slobbe, C., & Kulikov, M. (2024). Modelling the effect of sea ice in an ocean tide model. *Ocean Modelling*, *190*, 102405. https://doi.org/10.1016/J.OCEMOD.2024.102405

E.U.Copernicus Marine Service Information (CMEMS). (2018). Arctic Ocean Tidal Analysis and Forecast. https://doi.org/10.48670/moi-00005

Kaleschke, L., & Müller, G. (2022). Sea ice drift from autonomous measurements from 15 buoys, deployed during the IRO2/SMOSIce field campaign in the Barents Sea March 2014. *PANGAEA*. https://doi.org/https://doi.org/10.1594/PANGAEA.941334

IABP. (2014). LEVEL 1 Data Product. https://iabp.apl.uw.edu/Data_Products/BUOY_DATA/3HOURLY_DATA/

IABP. (2018). LEVEL 2 Data Product. https://iabp.apl.uw.edu/WebData/LEVEL2/

Veenstra, J. (2023). hatyan: Tidal Analysis and Prediction. https://github.com/Deltares/hatyan

Teigen, S. H., Nilsen, F., & Gjevik, B. (2010). Barotropic instability in the West Spitsbergen Current. *Journal of Geophysical Research: Oceans*, *115*(C7), 7016. https://doi.org/10.1029/2009JC005996

Zhigang, X. (2002). *Ellipse Parameters Conversion and Velocity Profiles for Tidal Currents in Matlab* (tech. rep.). Maurice Lamontagne Institute, Fishries and Oceans Canada. https://doi.org/http://dx.doi.org/10.13140/RG.2.1.2515.4000

Fang, Y. C., Janout, M., Kawaguchi, Y., & Statscewich, H. (2022). Semidiurnal Internal Tides Observed on the Eastern Flank of Hanna Shoal in the Northeastern Chukchi Sea. *Journal of Geophysical Research: Oceans*, *127*(11), e2021JC018232. https://doi.org/10.1029/2021JC018232

Copernicus Marine Service. (2014). Global Ocean Physics Reanalysis. https://doi.org/https://doi.org/10.48670/moi-00021

Provost, C. L., Genco, M.-L., & Lyard, F. (1995). Modeling and Predicting Tides Over the World Ocean. In *Coastal and estuarine studies* (pp. 175–201). American Geophysical Union (AGU). https://doi.org/10.1029/CE047P0175

Wu, Y., Hannah, C., Petrie, B., Pettipas, R., Peterson, I., Prinsenberg, S., Lee, C., & Moritz, R. (2013). *Ocean current and sea ice statistics for Davis Strait* (tech. rep.). Fisheries and Oceans Canada. Darthmouth-Nova Scotia.

6

Conclusions and Recommendations

The objective of this thesis is twofold: First, develop a physically-consistent parameterisation that can be used in barotropic global tide models without modelling tide resolving currents in a 3D coupled ice-ocean model framework; and second, to devise a method for deriving tidal constituents from GNSS buoy data in the Arctic, thereby introducing a new data source for the calibration and validation of tidal models. This led to four research questions (RQ). In this chapter, we will answer those questions, reflect upon the research objectives, and provide recommendations for future research.

6.1. Conclusions

6.1.1. Research Questions Summary

RQ1: What is the extent and magnitude of the impact of seasonal variations in landfast sea ice on the model-derived seasonal modulation of M_2 tide in the Arctic, and what are the implications for tides away from the landfast ice?

In Chapter 2, we assessed the impact of seasonal landfast ice variations on the Arctic M_2 tide for 2013 and 2017 using the 2D Global Tide and Storm Surge Model (GTSM). These years represent the maximum and minimum extremes in winter landfast ice cover over the decade (2010-2020) with September having (almost) no landfast ice. We modelled frictional stress from landfast ice by adding it to the bottom frictional stress.

The differences in amplitudes and phases of M_2 constituent between March and September are used to study the seasonal and interannual modulation. March-September differences for 2013 showed significant seasonal modulation with differences reaching upto 0.25 m, especially in the regions of Hudson Bay, Hudson Strait, and the Canadian Archipelago. While the interannual differences in landfast ice cover between March 2013 and March 2017 showed that landfast ice variations

in Canadian Archipelago and Russian Shelf can influence seasonal modulation in Hudson and Baffin Bays, with amplitude differences reaching up to 0.05 m.

Our results highlighted the significant influence of landfast ice on Arctic tidal patterns, particularly during maximum ice coverage. The effect on amplitudes can be far reaching in areas where there is no landfast ice present throughout the year. This underscored the need for further research into the effect of ongoing decline in Arctic sea ice on global ocean tides.

RQ2: How significant is the tidal dissipation from free drift sea ice field on tides under the presence of varying wind speeds and in shallow water regions?

In deeper and open oceans, frictional dissipation between sea ice and tides was found to be negligible, but the dynamics in shallow water regions were not fully understood. In Chapter 3, beacon trajectories in the Barents Sea displaying subdaily sea ice oscillations are analyzed using a physics-based point sea ice model, forced by external ocean general circulation, tidal, and atmospheric model data. In this region, the M_2 tidal signal is dominant in the sea ice oscillations, but the region is also a critical latitude for the Coriolis (inertial) frequency.

Two key analyses were conducted. The first evaluated a strong correlation (> 0.8 for all beacons) between sea ice oscillation and tidal movements implying a direct and strong relationship between the two. This indicated that sea ice and tides moved together, especially at the dominant M_2 frequency. The second analysis uses sensitivity tests to determine the causes of these oscillations. Water-ice drag from tidal currents was identified as the primary driving force and the major cause of energy dissipation. On the other hand, the tidal pressure gradients and wind-induced inertial forces had minor contributions.

Numerical evaluation of the energy loss due to this water-ice tidal drag showed that dissipation is only about 2-3% of the bottom frictional energy loss from tides, indicating negligible tidal dissipation due to free drift sea ice in the Barents Sea. In this dataset, low wind speeds and lack of subdaily signals in ERA5 data led to negligible sea ice-tide dissipation. However, sensitivity analysis indicated that strong subdaily wind signals could significantly alter this outcome, potentially increasing the sea ice's inertial response. Furthermore, if there are strong constant winds then the non-linear drag can infact lead to additional dissipation on a subdaily scale. For instance, we saw that for winds of 32 m/s, the dissipation from non-linear air-ice drag on subdaily sea ice oscillations was about 20% compared to bottom friction energy loss.

These findings suggested that the dissipation from free drift sea ice on tides was negligible in shallow water regions under low wind conditions. In strong wind conditions, the dissipation can be significant and it needs to be analyzed on a case-by-case basis.

RQ3: To what extent can the dissipation from all three categories of Arctic sea ice–Landfast, free drift, and drift under strong internal stresses–on tides be accurately modelled with the novel physically-consistent parameterization?

We presented a new physics-consistent parameterization for modeling sea ice-induced dissipation on tides in Chapter 4. With focus on the case without winds, the dissipation from free drift sea ice is negligible resulting in dissipation only from drifting sea ice under strong internal stresses and landfast ice.

In the new approach, we re-categorize these two sea ice regimes into: Horizontal Shear (HS) for drifting ice and Vertical Shear (VS) for (near) stationary ice. The division was based on a Friction Number (F), calculated using sea ice thickness (h_i), concentration (A), and a scaling parameter α_i. We demonstrate this classification with March and September 2019 examples, using two α_i values leading to classifications named $HS\_VS\_1.2$ and $HS\_VS\_0.7$.

The implementation of this parameterization into the GTSM allowed us to evaluate its performance by comparing three model simulations: Exp All_VS (based on the assumption of landfast ice, representing the current state-of-the-art), Exp HS_VS_1.2, and Exp HS_VS_0.7 against observations derived from altimeter and tide gauge data. The metric for comparison is the seasonal modulation of the M_2 tide, defined by March–September differences in amplitude and phase. The model simulations were done for March and September months of the years 2012 (maximum sea ice extent), 2017 (minimum sea ice extent) and 2019 (average sea ice extent of the remaining two years) in the last decade.

Our findings from these model simulations revealed that Exp HS_VS_0.7 exhibited the highest Pearson correlation (0.6) with altimetry-derived amplitude modulation across all years, followed by Exp HS_VS_1.2 with a correlation of 0.54, while Exp All_VS showed the lowest correlation at 0.4. As for phase modulation, the dataset exhibited significant variability and uncertainty, making it challenging to draw definitive conclusions. Regarding tide-gauge derived seasonal modulation, Exp HS_VS_1.2 outperformed the others, displaying the lowest median difference with observed modulation for both amplitude and phase at all tide gauges. Exp HS_VS_0.7 also outperformed Exp All_VS in all but 4 tide gauges.

These analyses illustrated that our approach performed better than Exp All_VS, which had shown larger dissipation than observations. Furthermore, from both the comparisons, it is seen that the variability in seasonal modulation with variability in sea ice is (almost) negligible in Exp All_VS. On the other hand, our new approach which accounts for the spatial and temporal variations in sea ice thickness and concentration shows large variability between sea ice configurations for both the simulations.

In conclusion, our parameterization has a better physics-based representation of the dissipation from sea ice on tides. It is suitable to study the effect of sea ice (and its decline) on global tides. Due to the consideration of sea ice dynamics we were able to have a better representation of sea ice's impact on tidal dynamics as against the simple approach of assuming all ice as fixed.

However, it is essential to note that the study's limitations include the lack of seasonal modulation from observations corresponding to the period of the model simulations. The altimetry-derived estimates of seasonal modulation were an average over the data years i.e. 2010-2019. While the tide-gauge derived seasonal modulation was based on tidal analysis conducted on data collected at different instances in

the past 30 years. This emphasized the need for future data to further validate the parameterization.

RQ4: How can tidal harmonic constituents of tidal currents be obtained from single buoy trajectories, accounting for the spatial and temporal variations in amplitude and phase along these trajectories? What is the validity of the resulting method in estimating tidal currents in both barotropic and baroclinic regions?

In Chapter 5, our objective was to derive accurate tidal current constituents (TCC) from a single GNSS buoy data in the Arctic, addressing the region's unique challenges, including limited data availability and significant spatio-temporal variability of amplitudes and phases. To overcome these issues/challenges, we introduced a novel method: Model-derived Fitting (MdF) method, to derive tidal current constituents from single buoy trajectory.

This method effectively accounted for spatiotemporal variations by utilizing initial estimates derived from a model. It required the estimation of $2n$ parameters for n tidal constituents, which aligned with the number of parameters in a standard tidal harmonic analysis, highlighting the method's operational efficiency.

To assess the accuracy and applicability of our method, we conducted three case studies. The first study in a barotopic dominant Barents Sea region compared MdF estimates from two buoys at a common point with the GTSM results. We observed that the estimate from two different buoys at a common location were (almost) the same as the GTSM for S_2 and K_1. For M_2, GTSM values are around 0.01 m/s lower than the MdF estimates for the two buoys.

In the second study in barotropic region of the Chukchi sea, we saw that MdF estimates of the M_2 tide from a buoy were almost the same as a near by mooring observation where GTSM exhited poor performance. Finally, in the baroclinic Baffin Bay region due to lack of availability of mooring observations at exact location and time we conducted a synthetic experiment to ascertain the accuracy of our method. The synthetic experiment results of TCC estimates for M_2, S_2 and K_1 using MdF method showed good accuracy when compared to synthetic truth with vector differences lower than 5 mm/s. This indicated the applicability of MdF method in the baroclinic tidal regions, however, a comparison with independent observations is still lacking.

Overall, the MdF method has shown promising results when applied to buoys across three distinct Arctic regions. These indicate the accuracy and robustness of our method except in baroclinic regions where suitable real control data were lacking but a synthetic test showed promise. Furthermore, a comprehensive validation across the diverse Arctic regions, involving a wider range of buoys and independent observational data, is necessary to thoroughly assess its efficacy. This validation process was crucial for testing the assumptions underpinning the method, such as the constant multiplicative factor used in the approach. Additionally, it's important to note that this method relies on initial model estimates, making it less autonomous compared to existing approaches.

Nevertheless, this method represented an advancement as it enables the accurate

extraction of tidal current constituents from single buoy trajectories in barotropic regions, providing a new data source for tidal currents in the Arctic through GNSS buoy data.

6.1.2. REFLECTION ON THE MAIN RESEARCH OBJECTIVE

Addressing the first main research objective involved an exploration of the impact of dissipation from both landfast and free drift sea ice on tides. In the absence of winds, landfast ice was found to have a substantial influence on tides, whereas free drift sea ice had negligible dissipation in shallow and deep oceans. These insights aided in the development of a new parameterization designed to model the dissipation from both landfast and drifting sea ice under strong internal stresses. In this approach we do not have a direct coupling with a sea ice model or need sea ice velocities at tidal timescales. Its simplicity helps in easy integration into existing barotropic tide models. Furthermore, the parameterization incorporates data on sea ice thickness and concentration, along with a simplified representation of internal ice field stresses, ensuring a physically-consistent modelling of the sea ice dynamics and tidal interactions.

This refined parameteric model can be a valuable tool for researchers and policymakers alike, aiding in the understanding and researching of future changes in tidal patterns due to the ongoing changes in the Arctic's sea ice. The model's ability to account for changes in sea ice over time allows for a more accurate assessment of how ongoing climatic change may alter tidal patterns, which is a critical consideration for coastal planning and management. This parameterization contributes meaningfully to the body of research on sea ice decline and its broader environmental implications.

However, the validation of this new approach remains partial, given the tide gauge data and altimetry were historical data and not in exact years of model simulations. The challenge of obtaining such validation data in the Arctic is indeed formidable.

This challenge prompted an exploration of the utilization of GNSS buoy data as an additional observational source. In the second part of our research objective, a new method for deriving tidal current constituents from single GNSS buoy data was successfully developed and tested. The approach exhibited efficacy in both barotropic and baroclinic Arctic regions. This methodology holds promise in helping us develop a novel data source for tidal currents in the Arctic, with potential implications for enhancing the validation and calibration of Arctic tidal models. Rigorous evaluation of the Arctic tidal models in estimating the tidal currents is still lacking and can benefit from a such a data source. Furthermore, accurate information of Arctic tidal currents is also very important in marine navigation and Arctic ecosystem research.

6.2. RECOMMENDATIONS FOR FUTURE WORK

The work presented in this thesis has enhanced the body of knowledge in the field of modelling the dissipation from sea ice and estimating tidal constituents from

GNSS buoy data. Yet, there is still much to gain by adding to this research. Below we provide some important recommendations.

1. **Refining the scaling parameter**: The novel parameterization introduced for modelling sea ice-induced dissipation relies on the accurate determination of the scaling parameter, denoted as α_i which ranges from 0.33 to 109.2. Further research aimed at refining and accurately representing this parameter is essential to enhance the precision of the parameterization. Potential avenues for improvement may include leveraging sea ice velocity data to gain insights into HS/VS regions, or utilizing additional data related to the seasonal modulation of tides for parameter calibration.

2. **Including the effect of winds**: The present thesis primarily focused on modelling the dissipation from sea ice on tides in the absence of winds in GTSM. However, a significant enhancement to the parameterization can be achieved by incorporating the influence of winds. Past studies, such as that by McPhee, 1982 noted that the addition of winds introduces an angular motion between sea ice and water. This effect has been modelled in studies like Heil and Hibler, 2002 using ice-ocean coupled models. Including winds along with sea ice in GTSM will have estimates of TWLs which are influenced by sea ice. This will aid in understanding the global impact of sea ice on TWLs. Furthermore, this enhancement is also particularly significant for systems like GLOSSIS, which utilizes GTSM in the backend for surge forecasting.

3. **Arctic-wide GTSM validation**: It is recommended to conduct an extensive year-long simulation using the new parameterization. This simulation should be rigorously evaluated against tide gauge data from the ArcTICA (Hart-Davis et al., 2023) dataset. By doing such an extended simulation and comparing the model's performance with observed tidal patterns over an entire year, a more comprehensive validation of the new GTSM with sea ice capabilities can be achieved. This will provide data into the model's overall accuracy in the Arctic region,

4. **Impact of declining Arctic sea ice on tides**: One can consider performing a comprehensive climatology study, potentially spanning over three decades, to investigate the impacts of declining sea ice on global tides. This extensive analysis can be connected to long-term changes in tidal patterns using either a tide gauge dataset or satellite altimetry data such as that by Bij de Vaate et al., 2022. Consequently, highlighting the potential contribution of declining sea ice on long-term tidal changes. This research would greatly contribute to our understanding of the broader oceanographic consequences of climate change.

5. **Antarctic sea ice modelling**: While this thesis has predominantly focused on Arctic sea ice and its dissipation modelling, there also exists Antarctic sea ice. Notably, Antarctic sea ice presents distinctive characteristics compared to Arctic, primarily characterized by lower sea ice thickness. This disparity arises because Antarctica lacks multi-year sea ice, with almost all sea ice melting

during the summer season. Moreover, the lack of multi-year sea ice also leads to reduced occurrence of ridge formations in Antarctica which results in a significantly lower ice-water drag coefficient, averaging around 3.2×10^{-3} (Schroeter & Sandery, 2022) – approximately 40% lower than average Arctic values. These distinctions suggest that dissipation from Antarctic sea ice would be considerably lower than that from Arctic sea ice. Nonetheless, it is worthwhile to incorporate this dissipation using the new parameteric approach and explore its influence on tidal modulation. Conducting such studies could help in having more information on the influence of Antarctic sea ice on tides, contributing to a more comprehensive understanding of polar regions' tidal dynamics.

6. **Buoy-derived tidal current atlas**: Similar to Baumann et al., 2020, one can develop a comprehensive dataset of buoy-derived tidal current constituents in the Arctic. For this, one can use a 3D ocean-tide model with our newly developed–MdF method. The first step would involve the validation of the MdF method in baroclinic regions with real control data. Once a validity is established, the MdF approach can used to develop a dataset using buoys spread out over the Arctic. This dataset would prove invaluable for calibrating tidal models, especially in data-scarce regions like the Arctic. Additionally, it would serve as a valuable resource for validation of global tidal models, addressing the existing gap in tidal current validation.

REFERENCES

McPhee, M. G. (1982). *Sea ice drag laws and simple boundary layer concepts, including application to rapid melting* (Report 82-4). United States Army Cold Regions Research; Engineering Laboratory.

Heil, P., & Hibler, W. D. (2002). Modeling the High-Frequency Component of Arctic Sea Ice Drift and Deformation. *Journal of Physical Oceanography*, *32*(11), 3039–3057. https://doi.org/10.1175/1520-0485(2002)032<3039:MTHFCO>2.0.CO;2

Hart-Davis, M., Howard, S., Ray, R., Andersen, O., Padman, L., Nilsen, F., & Dettmering, D. (2023). Arctic Tidal Constituent Atlas (ArcTiCA): A database of tide elevation constituents for the Arctic region from 1800 through present day. https://doi.org/10.18739/A2D795C4N

Bij de Vaate, I., Slobbe, D. C., & Verlaan, M. (2022). Secular Trends in Global Tides Derived From Satellite Radar Altimetry. *Journal of Geophysical Research: Oceans*, *127*(10), e2022JC018845. https://doi.org/10.1029/2022JC018845

Schroeter, S., & Sandery, P. A. (2022). Large-ensemble analysis of Antarctic sea ice model sensitivity to parameter uncertainty. *Ocean Modelling*, *177*, 102090. https://doi.org/10.1016/J.OCEMOD.2022.102090

Baumann, T. M., Polyakov, I. V., Padman, L., Danielson, S., Fer, I., Janout, M., Williams, W., & Pnyushkov, A. V. (2020). Arctic tidal current atlas. *Scientific Data 2020 7:1*, *7*(1), 1–11. https://doi.org/10.1038/s41597-020-00578-z

APPENDIX A.

VELOCITY PLOTS OF POINT ICE MODEL RUNS

This Appendix contains all the velocity plots of the point model runs for all the beacons along with the corresponding observations corresponding to Chapter 3.

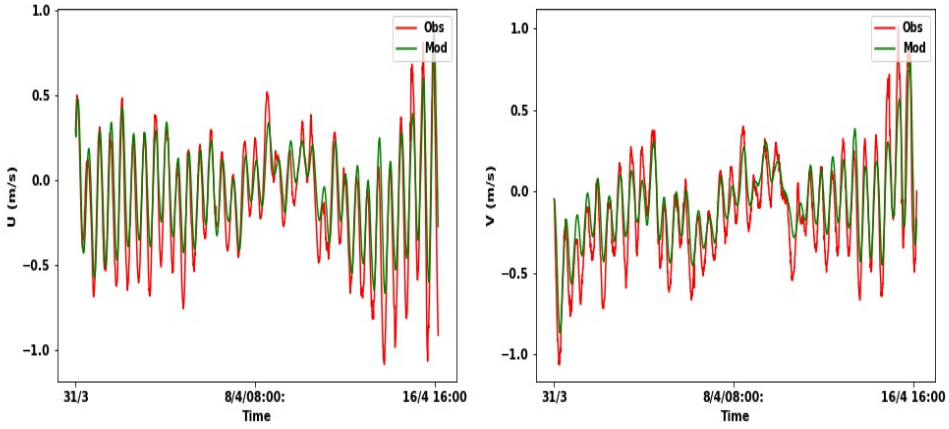

Figure A.1.: Time series plot for the longitudinal (u) and latitudinal (v) velocities for beacon 02. Observations are in red and point model simulations are in green. Time on the $x-$axis is given in format DD/M HH:MM with year being 2014. The velocities are plotted at the same time of the observations of the beacon positions, and thus, are separated by a time step of 15 min.

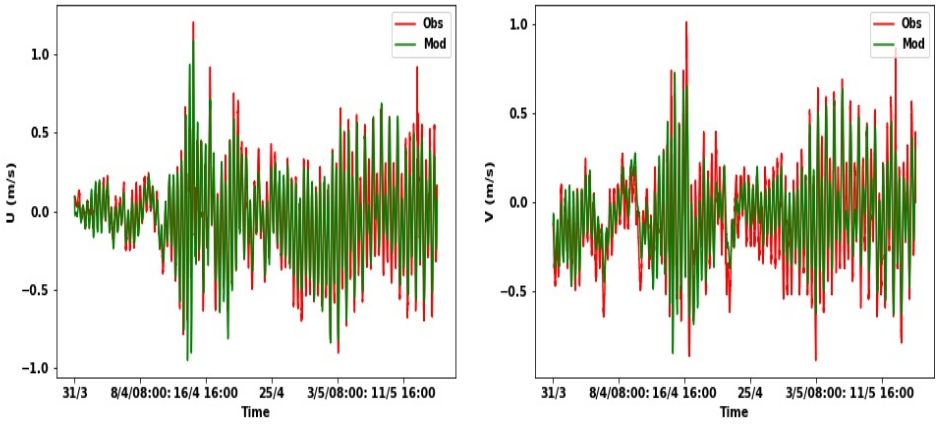

Figure A.2.: Time series plot for the longitudinal (u) and latitudinal (v) velocities for beacon 03. Observations are in red and point model simulations are in green. Time on the $x-$axis is given in format DD/M HH:MM with year being 2014. The velocities are plotted at the same time of the observations of the beacon positions, and thus, are separated by a time step of 15 min.

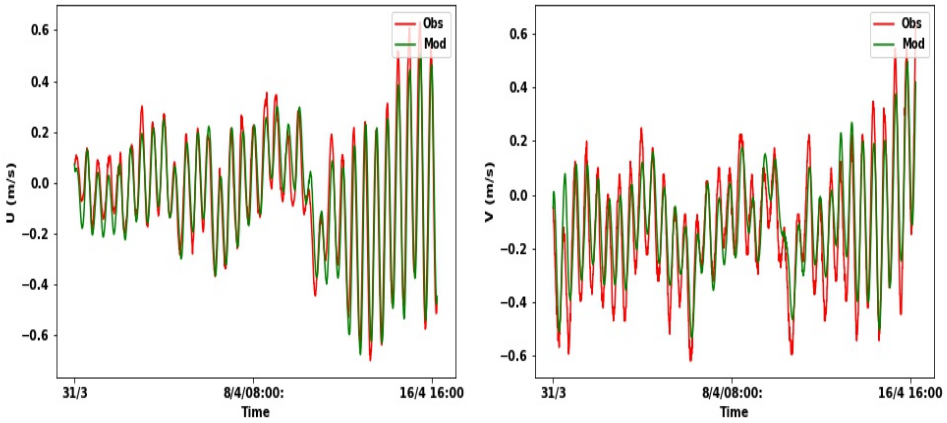

Figure A.3.: Time series plot for the longitudinal (u) and latitudinal (v) velocities for beacon 09. Observations are in red and point model simulations are in green. Time on the $x-$axis is given in format DD/M HH:MM with year being 2014. The velocities are plotted at the same time of the observations of the beacon positions, and thus, are separated by a time step of 15 min.

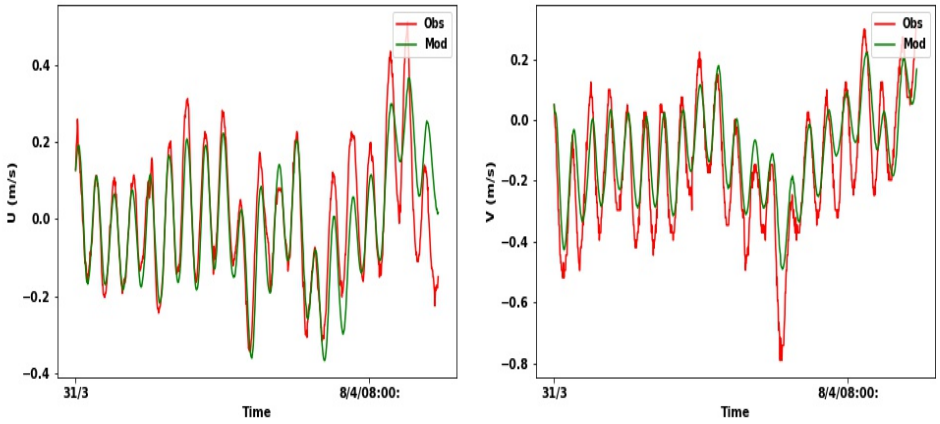

Figure A.4.: Time series plot for the longitudinal (u) and latitudinal (v) velocities for beacon 13. Observations are in red and point model simulations are in green. Time on the $x-$axis is given in format DD/M HH:MM with year being 2014. The velocities are plotted at the same time of the observations of the beacon positions, and thus, are separated by a time step of 15 min.

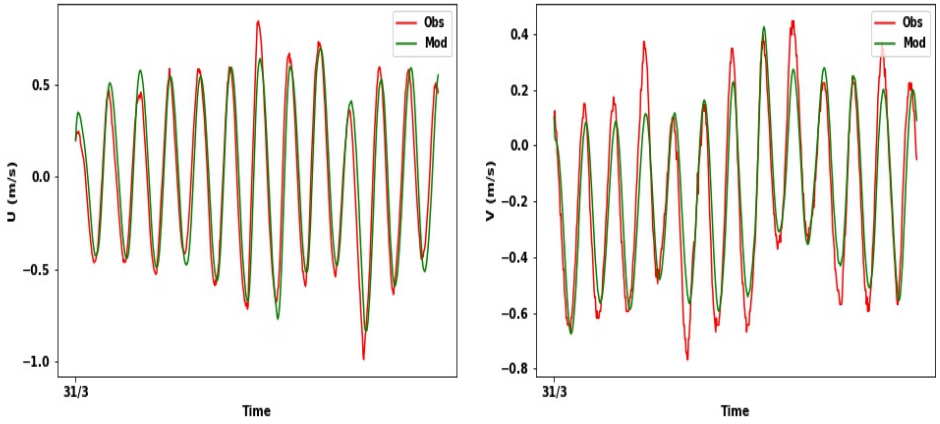

Figure A.5.: Time series plot for the longitudinal (u) and latitudinal (v) velocities for beacon 14. Observations are in red and point model simulations are in green. Time on the $x-$axis is given in format DD/M HH:MM with year being 2014. The velocities are plotted at the same time of the observations of the beacon positions, and thus, are separated by a time step of 15 min.

APPENDIX B.

TIDAL VELOCITY VECTOR TIME SERIES

This appendix contains all the plots of the residual velocity vectors for beacons in Chapter 3. Each page contains one plot for one beacon. Please note that the plots are according to the beacon time series length. So some plot might look incomplete at first sight, but that is just because the beacon was only operational for a limited time. Furthermore, we wanted similar comparison figures so the plots weren't adjusted based on beacon lengths.

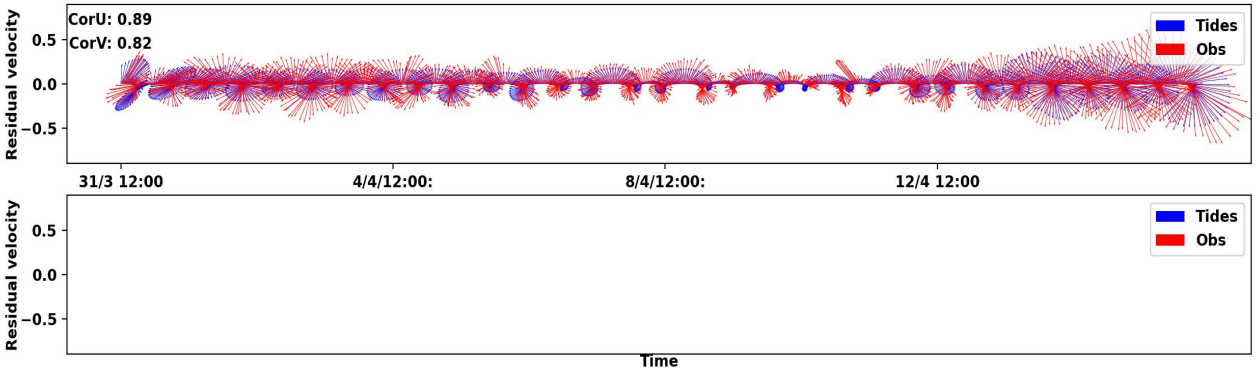

Velocity vector plots of the time series of sea ice oscillations (observations) (red) and GTSM tides (blue) for beacon 02. The residual velocity vectors imply that the mean drift is removed from the beacon trajectories and the resulting subdaily residuals are plotted.

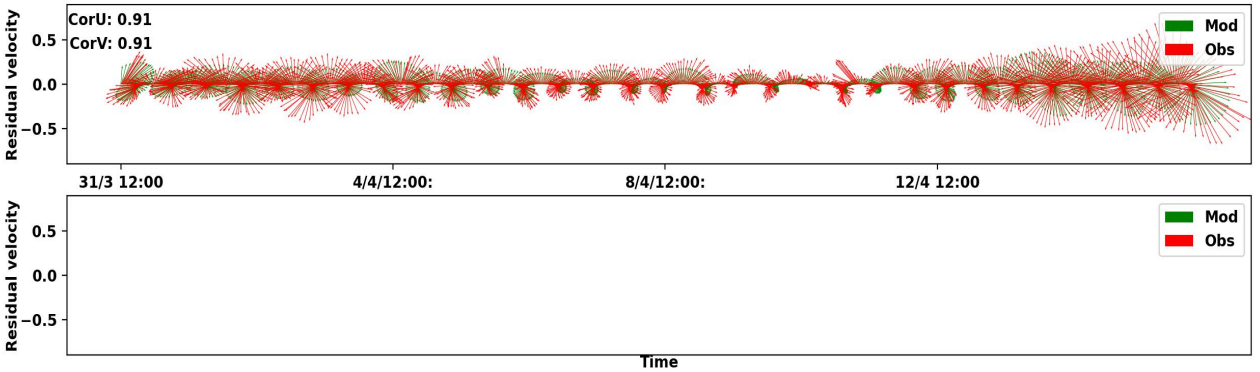

Velocity vector plots of the time series of sea ice oscillations (observations) (red) and point model oscillations (green) for beacon 02. The residual velocity vectors imply that the mean drift is removed from the beacon trajectories and the resulting subdaily residuals are plotted.

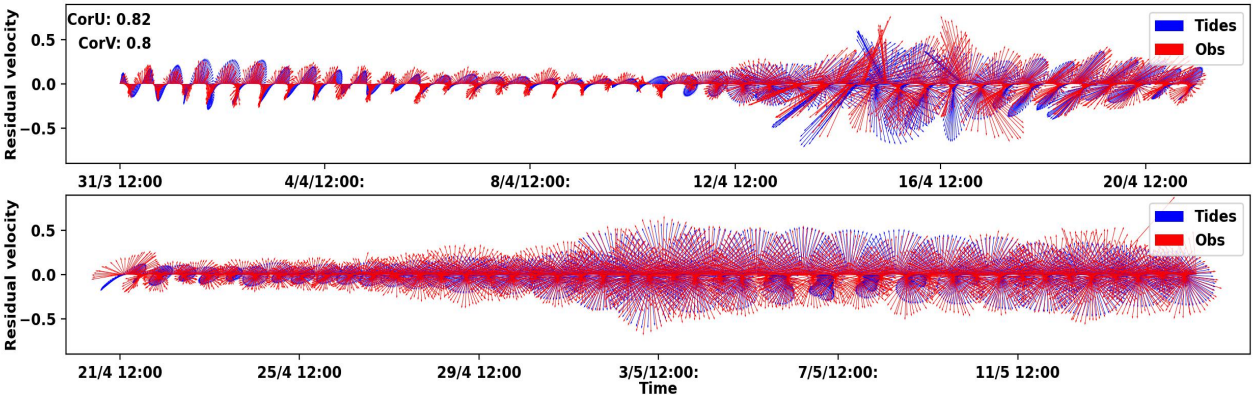

Velocity vector plots of the time series of sea ice oscillations (observations) (red) and GTSM tides (blue) for beacon 03. The residual velocity vectors imply that the mean drift is removed from the beacon trajectories and the resulting subdaily residuals are plotted.

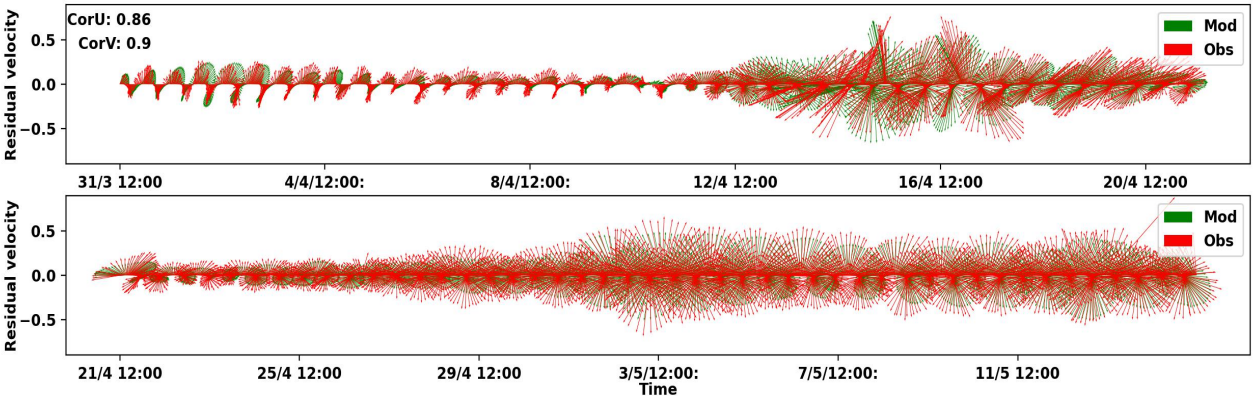

Velocity vector plots of the time series of sea ice oscillations (observations) (red) and point model oscillations (green) for beacon 03. The residual velocity vectors imply that the mean drift is removed from the beacon trajectories and the resulting subdaily residuals are plotted.

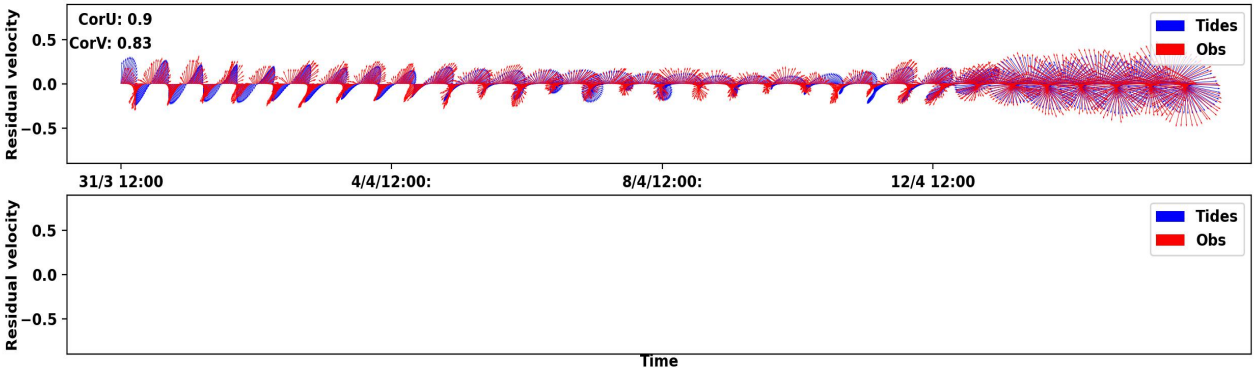

Velocity vector plots of the time series of sea ice oscillations (observations) (red) and GTSM tides (blue) for beacon 9. The residual velocity vectors imply that the mean drift is removed from the beacon trajectories and the resulting subdaily residuals are plotted.

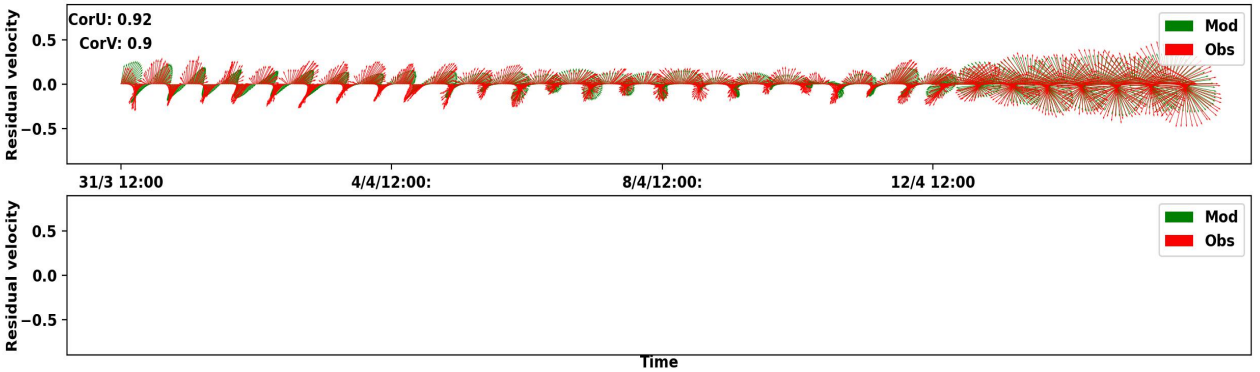

Velocity vector plots of the time series of sea ice oscillations (observations) (red) and point model oscillations (green) for beacon 9. The residual velocity vectors imply that the mean drift is removed from the beacon trajectories and the resulting subdaily residuals are plotted.

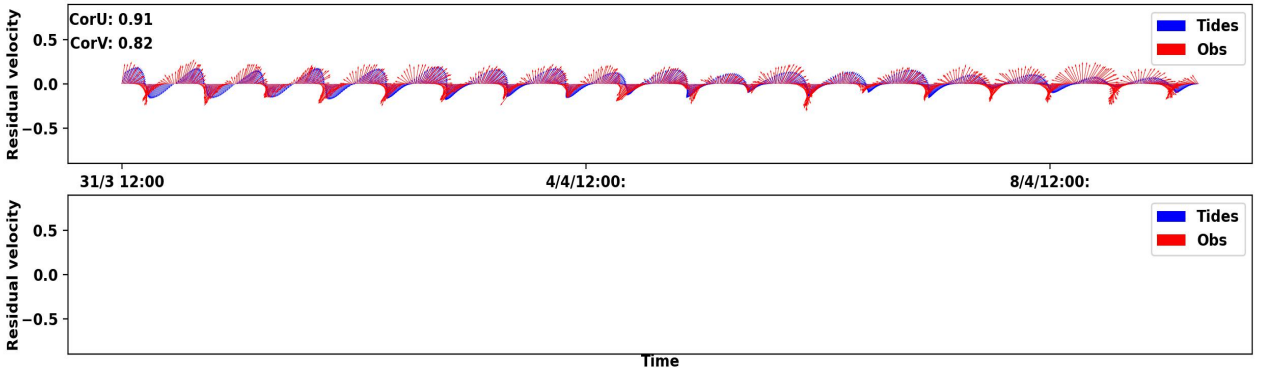

Velocity vector plots of the time series of sea ice oscillations (observations) (red) and GTSM tides (blue) for beacon 13. The residual velocity vectors imply that the mean drift is removed from the beacon trajectories and the resulting subdaily residuals are plotted.

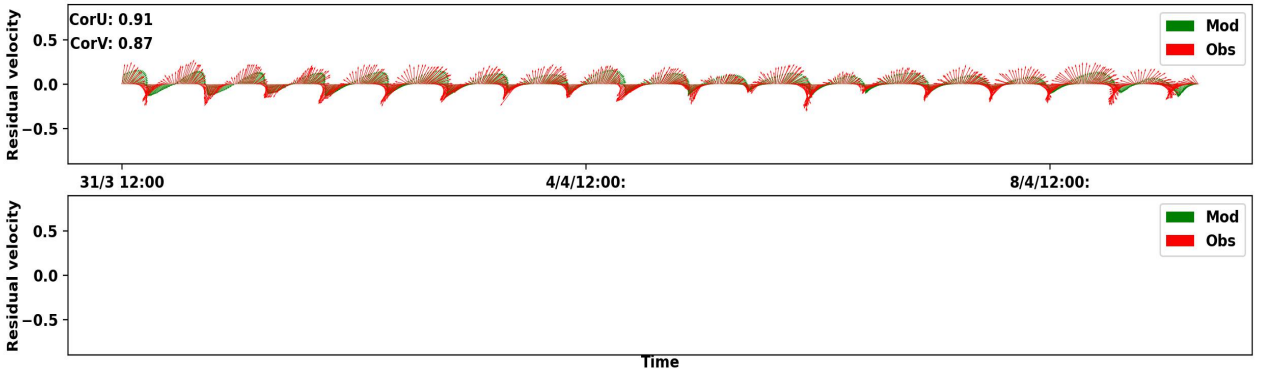

Velocity vector plots of the time series of sea ice oscillations (observations) (red) and point model oscillations (green) for beacon 13. The residual velocity vectors imply that the mean drift is removed from the beacon trajectories and the resulting subdaily residuals are plotted.

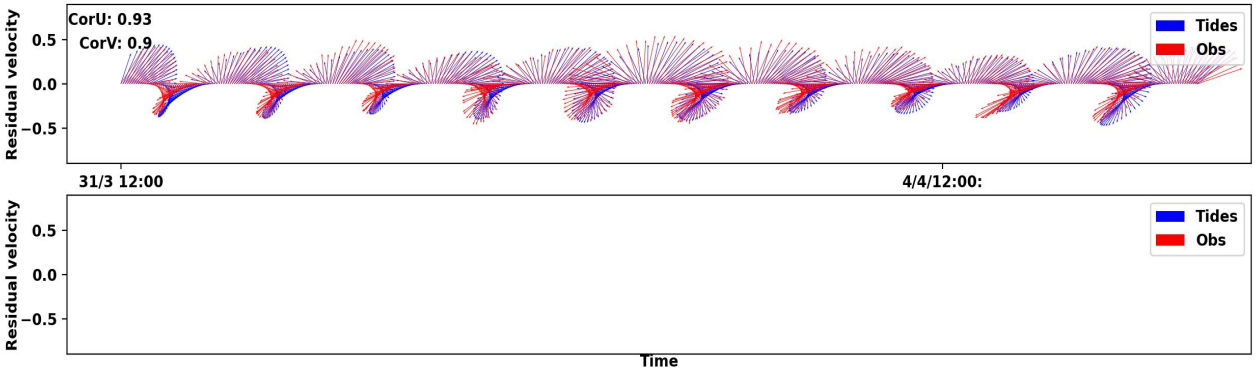

Velocity vector plots of the time series of sea ice oscillations (observations) (red) and GTSM tides (blue) for beacon 14. The residual velocity vectors imply that the mean drift is removed from the beacon trajectories and the resulting subdaily residuals are plotted.

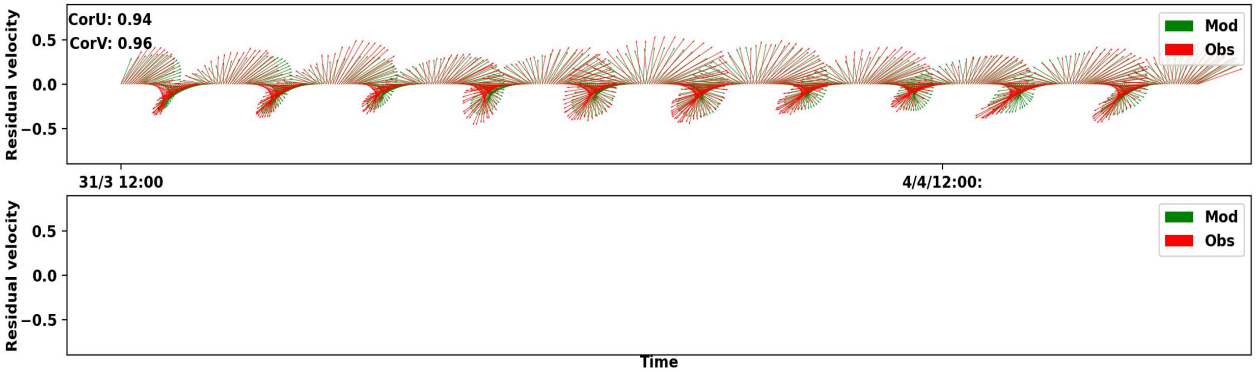

Velocity vector plots of the time series of sea ice oscillations (observations) (red) and point model oscillations (green) for beacon 14. The residual velocity vectors imply that the mean drift is removed from the beacon trajectories and the resulting subdaily residuals are plotted.

APPENDIX C.

COMPARISON OF SEA ICE CONCENTRATION AROUND THE BEACONS

This appendix contains sea ice concentration plots for 3 dates using the AMSR2 product and serves as additional supporting material for Chapter 3. There is a plot using the CMEMS ocean product for comparison on the same date as AMSR2.

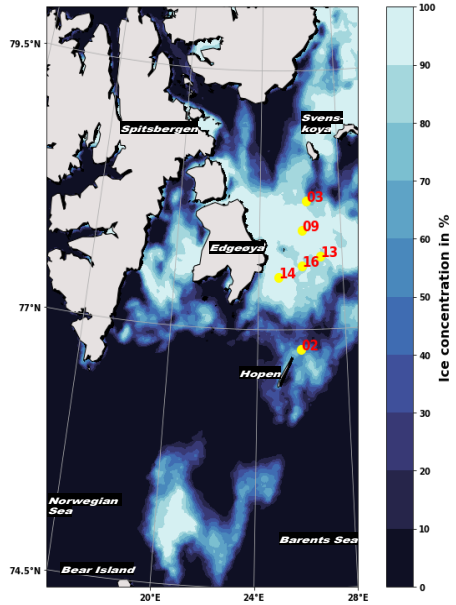

Figure C.1.: Sea ice concentration obtained from the AMSR2 product for March 31. The individual beacon positions are shown on this day with the yellow colored markers.

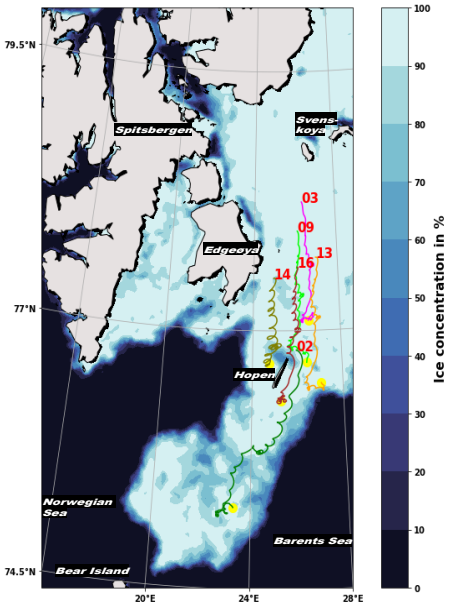

Figure C.2.: Sea ice concentration obtained from the AMSR2 product for April 28, 2014. The individual beacon tracks are shown starting from March 31, 2014 with the yellow colored markers showing the beacon positions on April 28, 2014.

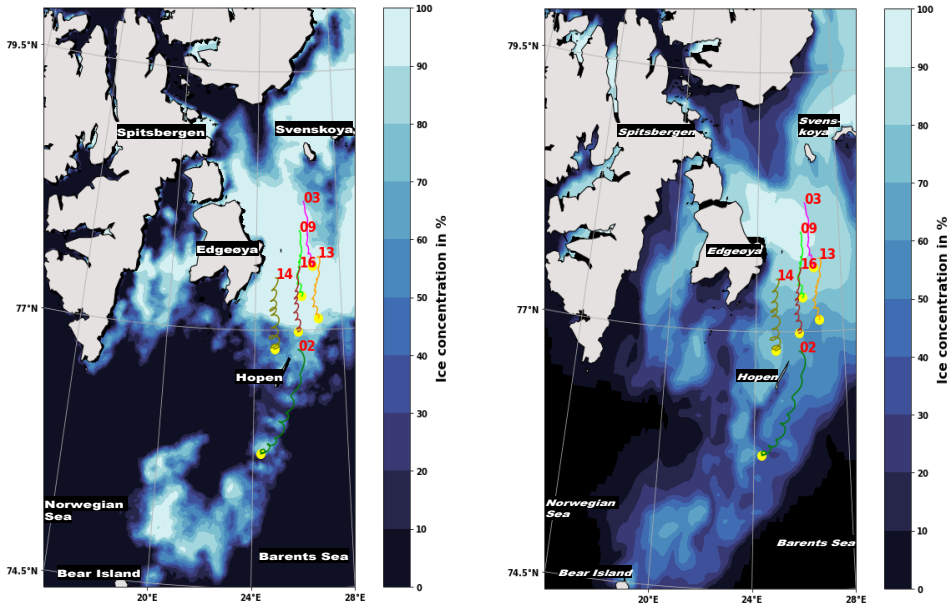

(a) AMSR2

(b) CMEMS

Figure C.3.: Sea ice concentration obtained from the AMSR2 product (left) and the CMEMS product for April 3. The individual beacon tracks are shown starting from March 31, 2014 with the yellow colored markers showing the beacon positions on April 3.

APPENDIX D.

SENSITIVITY OF THE FREE DRIFT DISSIPATION TO EXTERNAL DATASETS

This analysis corresponds to the study conducted in Chapter 3. A sensitivity analysis is performed on the external datasets (ocean, wind and tidal) to check if the analysis we conducted is sensitive to the underlying datasets. We use other similar verified datasets for the ocean, wind and tidal models and run our point ice model using these datasets. The resulting model runs are then used to check for the effect on dissipation between sea ice and tides and the correlation between the point model derived sea ice oscillations and the observations.

We have two comparison metrics here, namely,

1. Correlation coefficient between the sea ice oscillations from point model simulations and beacon observations.

2. Dissipation between the ice-tide interface calculated using $\boldsymbol{\tau_{wit}}$ and Equation (3.14) (in Chapter 3).

Now we evaluate the sensitivity of our model simulations by changing the external datasets. We start with winds.

SENSITIVITY TO WINDS

Currently, we use the ERA5 reanalysis product (Hersbach et al., 2018) which gives hourly winds. We replace this product with the reanalysis data from NCEP/NCAR (NOAA, 2014). This dataset is available every 6 hours and is provided on an unstructured T62 Gaussian grid (Hortal & Simmons, 1990). This dataset has a lower spatial and temporal resolution than ERA5, however, for a sensitivity analysis the comparison is effect on correlation and dissipation. Consequently, the spatial and temporal resolution is not of concern since we can interpolate the point ice model data to the resolution dataset. Now we run our point model with the winds from this NCEP/NCAR dataset instead of the ERA5 one and compute the above two metrics.
Correlation Coefficient: A correlation coefficient between the point model and

beacon observed sea ice oscillations is computed similar to Table 3.1 in Chapter 3. It is clear that there is almost no change in the correlation coefficient (Table 1) of

	02		03		09		13		14		16	
	U	V	U	V	U	V	U	V	U	V	U	V
$(\text{Mod-Obs})_E$	0.91	0.92	0.86	0.89	0.93	0.89	0.92	0.86	0.94	0.95	0.91	0.92
$(\text{Mod-Obs})_N$	0.91	0.92	0.86	0.89	0.93	0.89	0.93	0.87	0.94	0.95	0.91	0.92

Table D.1.: Correlation between beacon observed sea ice oscillations and the point model derived sea ice oscillations using winds from ERA5 (subscript E) and NCEP/NCAR (subscript E) datasets. The U and V represent the δu and δv velocity of the oscillations, respectively.

subdaily scale motion by changing the winds dataset. Vector plots of the oscillations (similar to Figure 3.7 and 3.8 in Chapter 3) look similar too.

Energy loss in dissipation The energy loss in the ice tide interface is computed using Equation (3.14). This energy is computed with the ice velocity values from the new model runs and it is compared to bottom friction energy loss.

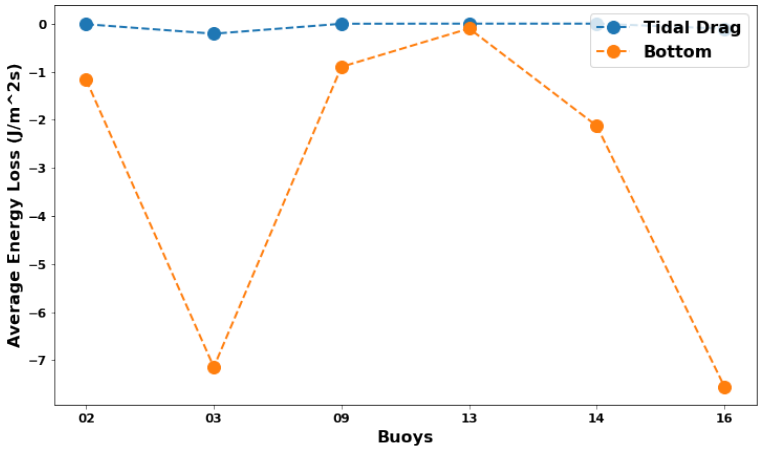

Figure D.1.: Total average energy loss or gain of tides over the entire beacon trajectory (which is averaged over M_2 tidal period) is plotted for all the beacons. For comparison a loss of energy to sea bed bottom friction stress is used as a standard.

This energy loss (Figure D.1) is compared to the energy loss using the ERA5 dataset (See Table D.2) there appears almost no difference. Also see Figure 3.14 in Chapter 3. It was concluded in the chapter that the energy loss due to the dissipation at the ice-tide interface is in the range of $2-3\%$ of the loss to corresponding bottom friction. Changing the winds dataset, this conclusion still stands true (Table D.2).

Beacon	%($ERA5_{bf}$)	%($NCEP_{bf}$)
02	1.7	1.1
03	3.3	2.9
09	0.1	0.3
13	0.3	0.1
14	0.1	0.1
16	1.6	1.4

Table D.2.: Percentage of the average energy loss from the ice-tide interface compared to the loss to bottom friction for each beacon.

SENSITIVITY TO OCEAN CURRENTSL

Similar to the analysis conducted for wind effects, this study explores the impact of utilizing an alternative ocean model output, specifically replacing the currently employed CMEMS (Copernicus Marine Service, 2014) with output from the HYCOM model, as documented in the Global Ocean Forecasting System (Cummings & Smedstad, 2013), version GOFS 3.1. This model provides ocean currents and sea surface heights at a 3-hourly temporal resolution and a spatial resolution of 0.04° poleward. However, it was observed that data were not consistently available for all time instances within the selected period, resulting in a total of 13 data points being absent from March 31 to June 02, 2014. To address this issue, linear interpolation was employed to estimate values at these missing points.

Subsequent simulations of the point model incorporated ocean currents and associated pressure gradients derived from HYCOM, while inputs from other models, namely ERA5 and GTSM, remained unchanged. This approach facilitates an evaluation of the specific influence exerted by the choice of ocean model on the outcomes of point model simulations. Similar to the approach adopted for the wind sensitivity tests, the correlation coefficient and energy loss were calculated to assess the implications of this model substitution.

Correlation Coefficient:

	02		03		09		13		14		16	
	U	V	U	V	U	V	U	V	U	V	U	V
$(Mod\text{-}Obs)_C$	0.91	0.92	0.86	0.89	0.93	0.89	0.92	0.86	0.94	0.95	0.91	0.92
$(Mod\text{-}Obs)_H$	0.92	0.91	0.86	0.89	0.92	0.89	0.92	0.87	0.94	0.95	0.9	0.92

Table D.3.: Correlation between beacon observed sea ice oscillations and the point model derived sea ice oscillations using CMEMS output (subscript C) and HYCOM output (subscript H) datasets. The U and V represent the δu and δv velocity of the oscillations, respectively.

Minor changes in the modelled sea ice oscillations are observed by changing the ocean model. (Table D.3).

Energy loss in dissipation: Now we compute the energy loss and plot it as a comparison to the loss to bottom friction.

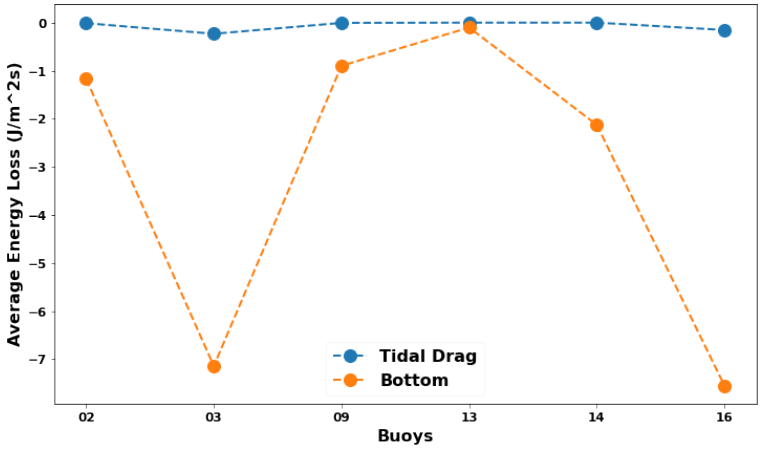

Figure D.2.: Total average energy loss or gain of tides over the entire beacon trajectory (which is averaged over M_2 tidal period) is plotted for all the beacons. For comparison a loss of energy to sea bed bottom friction stress is used as a standard.

Observations indicate that altering the ocean currents and pressure gradients derived from sea surface heights in the ocean model results in negligible changes to the dissipation at the sea ice-tide interface. As documented in Table D.3, the variation in energy loss values relative to bottom friction remains approximately $2-3\%$. Consequently, the previously established conclusionthat the loss accounts for $2-3\%$ relative to bottom frictionremains valid. This outcome is anticipated given that ocean models typically do not incorporate tidal effects, suggesting that their influence on tidal time scale solutions is limited. Likely, any observed impacts arise from the non-linear dynamics associated with the ice-water drag coefficient.

Beacon	%($CMEMS_{bf}$)	%($HYCOM_{bf}$)
02	1.7	1.0
03	3.3	3.2
09	0.1	0.6
13	3.0	0.1
14	0.1	0.1
16	1.6	2.0

Table D.4.: Percentage of the average energy loss from the ice-tide interface compared to the loss to bottom friction for each beacon.

TIDAL MODEL

Finally, we replace the GTSM (Verlaan et al., 2015) with FES2014 (Lyard et al., 2021) in a similar set of experiments. It should be noted that we were not able to obtain the tidal currents from FES2014 but only the sea surface heights. Hence, in the following results only the pressure gradients from the sea surface heights of FES2014 are used and the tidal currents are still from GTSM.

Correlation Coefficient

	02		03		09		13		14		16	
	U	V	U	V	U	V	U	V	U	V	U	V
$(\text{Mod-Obs})_G$	0.91	0.92	0.86	0.89	0.93	0.89	0.92	0.86	0.94	0.95	0.91	0.92
$(\text{Mod-Obs})_F$	0.91	0.91	0.86	0.9	0.92	0.89	0.91	0.87	0.94	0.96	0.91	0.92

Table D.5.: Correlation between beacon observed sea ice oscillations and the point model derived sea ice oscillations using GTSM derived pressure gradients (subscript G) and FES2014 derived pressure gradients (subscript F) datasets. The U and V represent the δu and δv velocity of the oscillations, respectively.

The changes in correlation coefficient by changing the tidal model (Table D.5) are almost negligible. There is still a strong and positive correlation between the observations and model simulations. Thus, the conclusions in the manuscript are still valid. Now we perform the energy loss experiment as done for other model tests.

Energy Dissipation: The computed energy loss is plotted against bottom friction loss and, again, it is seen that there is almost no change in the dissipation from ice-tide interface as compared to the bottom frictional loss. We compute the percentage of this energy loss compared to the bottom friction as we did previously.

Again, we notice that the energy loss is between $2-3\%$ and our conclusion in the chapter 3 remains true.

Beacon	$\%(\text{GTSM}_{bf})$	$\%(\text{FES}_{bf})$
02	1.7	2.0
03	3.3	3.5
09	0.1	0.1
13	3.0	2.7
14	0.1	0.1
16	1.6	1.8

Table D.6.: Percentage of the average energy loss from the ice-tide interface compared to the loss to bottom friction for each beacon.

Based on the above sensitivity analyses conducted, it is observed that variations in external datasets do not significantly impact the correlations and dissipation

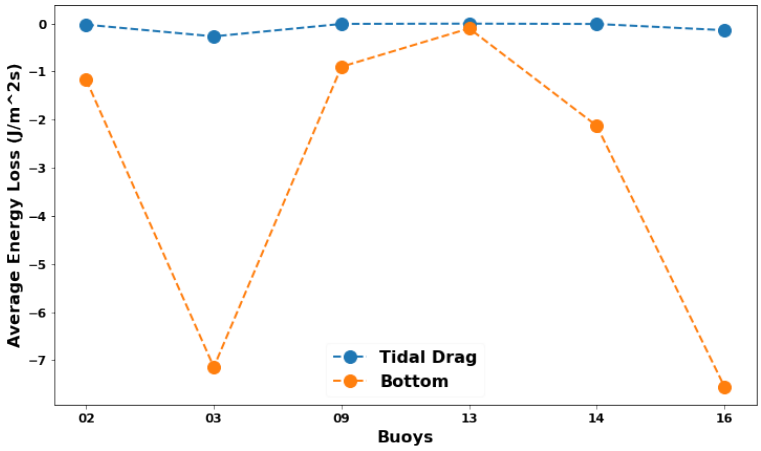

Figure D.3.: Total average energy loss or gain of tides over the entire beacon trajectory (which is averaged over M_2 tidal period) is plotted for all the beacons. For comparison a loss of energy to sea bed bottom friction stress is used as a standard.

conclusions drawn in this study. Furthermore, the influence of discrepancies originating from different models is minimal on the point model solutions at a subdaily scale. The findings presented in Chapter 3 indicate that tidal currents and the resultant drag are the primary drivers of the oscillations observed. Therefore, it could have been anticipated that alternative external datasets would not substantially affect the dissipation at the ice-tide interface. This analysis, however, serves to corroborate the assertion that the impact of other external forces on the point ice model is indeed marginal.

REFERENCES

Hersbach, H., Bell, B., Berrisford, P., Biavati, G., Horányi, A., Muñoz Sabater, J., Nicolas, J., Peubey, C., Radu, R., Rozum, I., Schepers, D., Simmons, A., Soci, C., Dee, D., & Thépaut, J.-N. (2018). ERA5 hourly data on single levels from 1979 to present. 10.24381/cds.adbb2d47

NOAA. (2014). *The NCEP/NCAR 40-Year Reanalysis Project: March, 1996 BAMS* (tech. rep.). https://psl.noaa.gov/data/gridded/data.ncep.reanalysis.html

Hortal, M., & Simmons, A. (1990). Use of reduced Gaussian grids in spectral models. https://doi.org/10.21957/v413vy4fg

Copernicus Marine Service. (2014). Global Ocean 1/12° Physics Analysis and Forecast. https://doi.org/https://doi.org/10.48670/moi-00016

Cummings, J. A., & Smedstad, O. M. (2013). Variational Data Assimilation for the Global Ocean. *Data Assimilation for Atmospheric, Oceanic and Hydrologic Applications (Vol. II)*, 303–343. https://doi.org/10.1007/978-3-642-35088-7{_}13

Verlaan, M., De Kleermaeker, S., & Buckman, L. (2015). GLOSSIS: Global storm surge forecasting and information system. *Australasian Coasts & Ports Conference 2015: 22nd Australasian Coastal and Ocean Engineering Conference and the 15th Australasian Port and Harbour Conference*, 229–234.

Lyard, F. H., Allain, D. J., Cancet, M., Carrère, L., & Picot, N. (2021). FES2014 global ocean tide atlas: Design and performance. *Ocean Science*, *17*(3), 615–649. https://doi.org/10.5194/OS-17-615-2021

APPENDIX E.

COMPARING SEA ICE EXTENT FROM GLORYS WITH NSIDC

The accuracy of the parameterization of the effect of sea ice developed in Chapter 4 depends, among others, on the sea ice dataset providing the sea ice thickness and concentration. Currently, we used the dataset from Copernicus Marine Service, 2019 which was a model derived reanalysis product. Here, we show the comparison of the the sea ice cover from that product to the sea ice cover obtained from the NSIDC dataset which also gives the landfast ice cover. This product was also used previously to compare the area of HS/VS classification with landfast ice. The NSIDC product was also used in the landfast ice study of Bij de Vaate et al., 2021. The sea ice extent with concentrations larger than 0.8 is obtained from this dataset for the year 2019 (Figure E.1).

This dataset does not have monthly mean data but an output every two weeks. Here, we consider the data for around mid of the respective months and assumed that this data is a representation of the mean for that month. The sea ice field on March 21, 2019 and September 19, 2019 are shown (Figure 4.5a and 4.5b) with concentrations larger than 0.8 and landfast (light blue) and total sea ice (dark blue) regions. It is seen that in September (Figure E.1b; summer) the sea ice cover is very low with no landfast sea ice in the dataset as compared to March (Figure 4.5a; winter) This is also noted in Li et al., 2020 that there is almost no landfast sea ice in the summer periods since 2018. Furthermore, this NSIDC landfast ice estimate will represent a physical lower bound of the VS region in our analysis. This can also give an idea of the value of the scaling parameter (α_i). However, it should be with a caveat that these charts from NSIDC are produced by a manual analysis on satellite images. So the region of landfast ice might vary.

The monthly mean sea ice cover for March and September from Copernicus Marine Service, 2019 is seen in Figure E.2. On comparison, the sea ice cover from both the datasets have very similar coverage with some small discrepancies. The noted discrepancies off the coast of Japan, Bering Sea and southern Labrador Sea could be due to the fact that the Copernicus Marine Service, 2019 dataset is a monthly mean where as NSIDC provides for a value at a particular day. Or possibly that the sea ice-ocean coupled models (including GLORYS used in the CMEMS product) often suffer from biases. For instance, the GLORYS model is known to have larger sea ice thicknesses than observed due to the underlying EVP rheology.

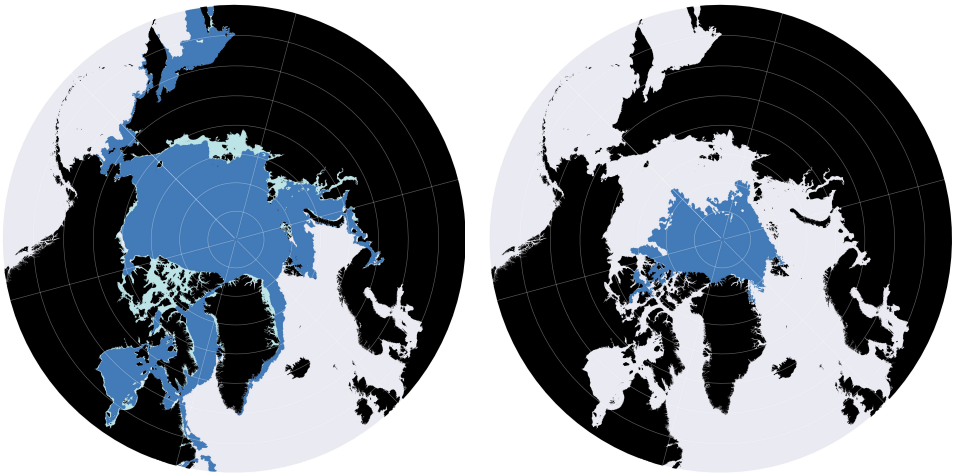

(a) March 2019 **(b)** September 2019

Figure E.1.: The sea ice field for March and September 2019 obtained from NSIDC dataset. The sub-figures (Figure E.1a and E.1b) show the traditional sub-division of landfast ice (light blue) from the remaining sea ice (dark blue) obtained from NSIDC. Note that only the sea ice field with concentration > 0.8 is considered here.

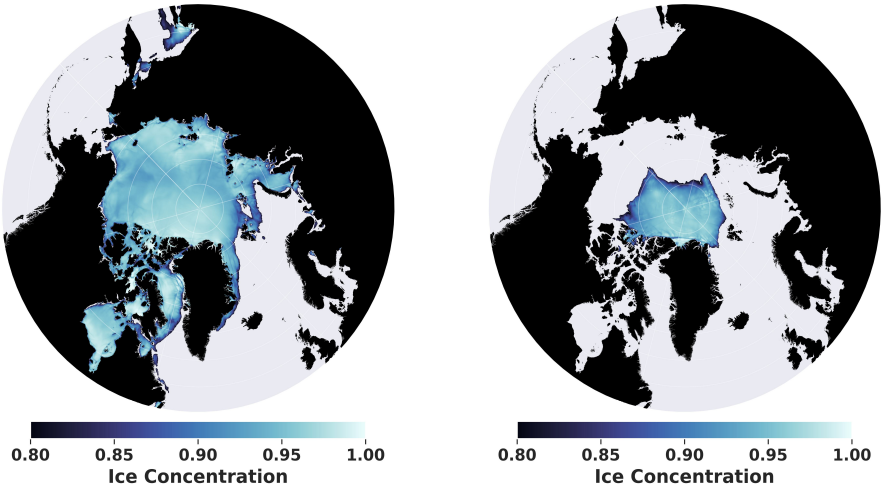

(a) March 2019 **(b)** September 2019

Figure E.2.: Sea ice concentration field with values larger than 0.8 for March and September 2019 obtained from a global ocean reanalysis product (Copernicus Marine Service, 2019). The sub-figures (Figure 4.1a and 4.1b) show the March and September distribution..

REFERENCES

Copernicus Marine Service. (2019). Global Ocean Physics Reanalysis. https://doi.org/https://doi.org/10.48670/moi-00021

Bij de Vaate, I., Vasulkar, A. N., Slobbe, D. C., & Verlaan, M. (2021). The Influence of Arctic Landfast Ice on Seasonal Modulation of the M2 Tide. *Journal of Geophysical Research: Oceans*, *126*(5), e2020JC016630. https://doi.org/10.1029/2020JC016630

Li, Z., Zhao, J., Su, J., Li, C., Cheng, B., Hui, F., Yang, Q., & Shi, L. (2020). Spatial and Temporal Variations in the Extent and Thickness of Arctic Landfast Ice. *Remote Sensing 2020, Vol. 12, Page 64*, *12*(1), 64. https://doi.org/10.3390/RS12010064

APPENDIX F.

SEA ICE CLASSIFICATION FOR 2012 AND 2017

This appendix corresponds to Chapter 4 where we show the remaining plots of the sea ice classifications. The model runs were done for 3 years; 2012, 2017 and 2019 with the respective sea ice fields for those years. Here, we show the results from the Exp HS_VS_1.2 and Exp HS_VS_0.7 classification for the two months; March and September for the years 2012 and 2017. These years as mentioned previously, represent the maximum and minimum differences of the sea ice cover between March and September. Figure F.1 shows the classification for 2012 while Figure F.2 gives the classification for 2017.

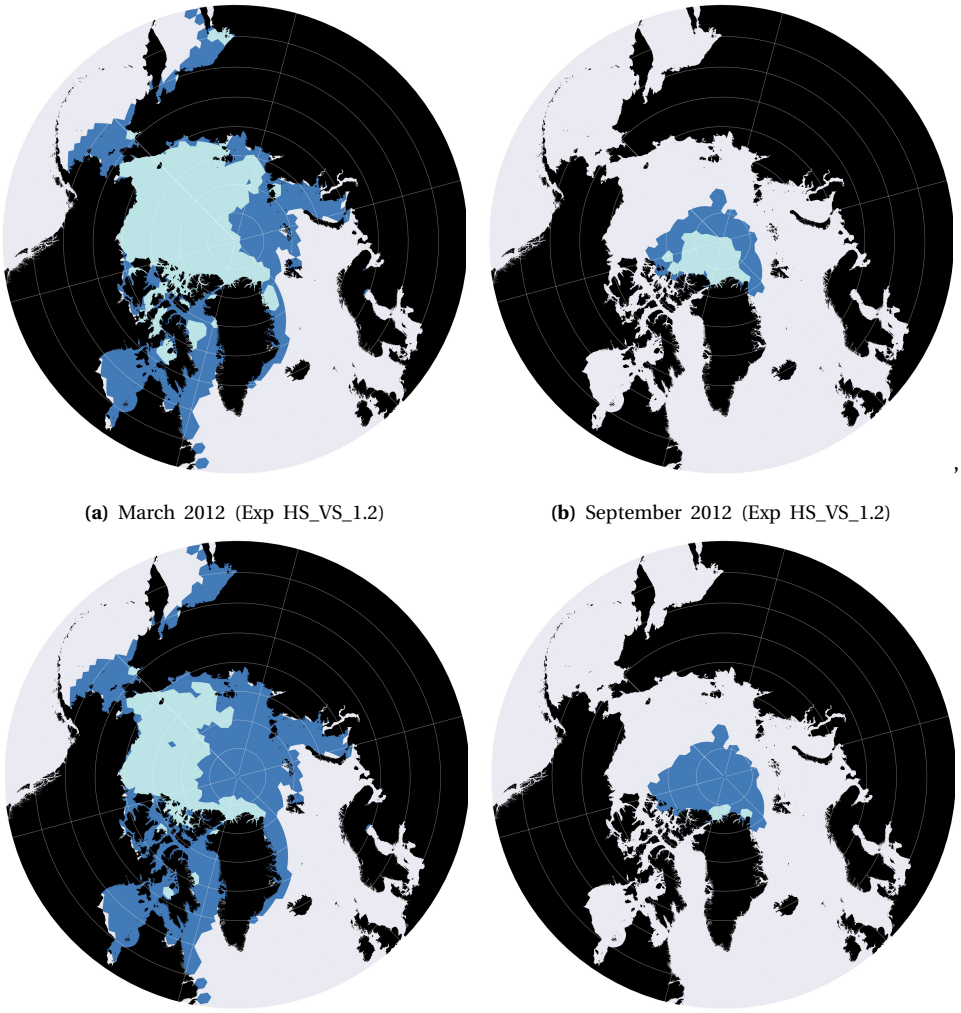

(a) March 2012 (Exp HS_VS_1.2)

(b) September 2012 (Exp HS_VS_1.2)

(c) March 2012 (Exp HS_VS_0.75)

(d) September 2012 (Exp HS_VS_0.75)

Figure F.1.: HS (dark blue) and VS (light blue) classification of the sea ice field for March and September 2012 with the sea ice field obtained from Copernicus Marine Service, 2019. The sub-figures show HS/VS classification based on two α_i values for the same sea ice field. Exp HS_VS_1.2 is with $\alpha_i = 1.2$ and Exp HS_VS_0.7 is with $\alpha_i = 0.7$. Note that only the sea ice field with concentration > 0.8 is considered here.

(a) March 2017 (Exp HS_VS_1.2)

(b) September 2017 (Exp HS_VS_1.2)

(c) March 2017 (Exp HS_VS_0.75)

(d) September 2017 (Exp HS_VS_0.75)

Figure F.2.: HS (dark blue) and VS (light blue) classification of the sea ice field for March and September 2017 with the sea ice field obtained from Copernicus Marine Service, 2019. The sub-figures show HS/VS classification based on two α_i values for the same sea ice field. Exp HS_VS_1.2 is with $\alpha_i = 1.2$ and Exp HS_VS_0.7 is with $\alpha_i = 0.7$. Note that only the sea ice field with concentration > 0.8 is considered here.

REFERENCES

Copernicus Marine Service. (2019). Global Ocean Physics Reanalysis. https://doi.org/https://doi.org/10.48670/moi-00021

APPENDIX G.

ADDITIONAL MODEL VALIDATION

Here we show additional model validation results of Chapter 4 for the years 2012 and 2017.

G.0.1. COMPARISON WITH ALTIMETRY

The map of model-derived March-September differences in M_2 amplitude and phase at altimeter product locations for the years 2012 and 2017 are given in Figure G.1 and G.2, respectively.

The altimetry data has noise which was reduced by first considering a coarser grid (875 km × 875 km). Then, all the points from the altimetry product which were part of a particular grid cell were selected and a median of these points was computed. This median value was a representation of that grid cell/area of the region. The resulting values on the coarser grid was used to compute the correlation plots (Figure 4.8). The coarse grid values of March-September differences for 2019 are shown here in Figure G.3.

G.0.2. COMPARISON WITH TIDE GAUGES

The map of model-derived March-September differences in M_2 amplitude and phase at tide gauge locations for the years 2012 and 2017 are given in Figure G.4 and G.5 respectively.

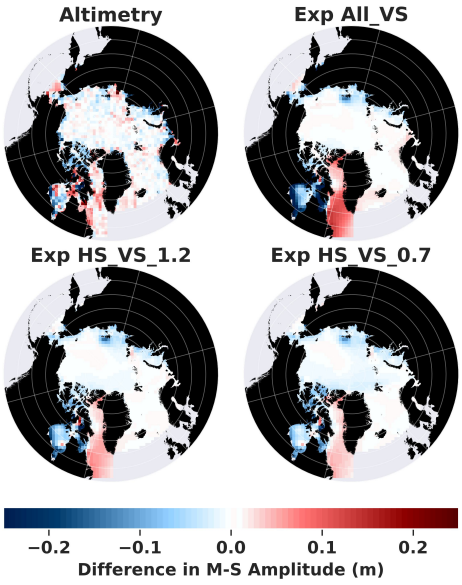

(a)

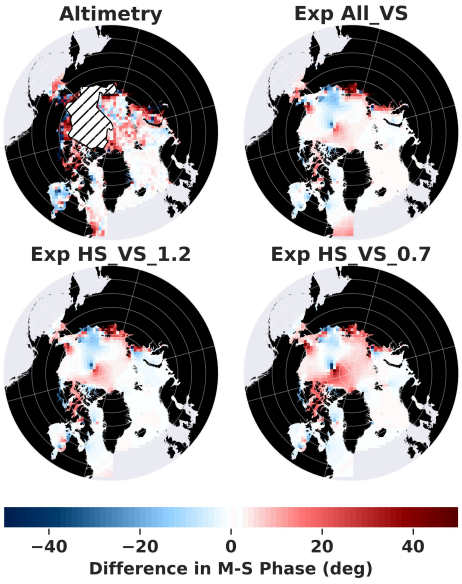

(b)

Figure G.1.: Seasonal Modulation of M_2 tide quantified as March-September differences in amplitude and phases for the altimeter-derived product and the Exp All_VS, Exp HS_VS_1.2 and Exp HS_VS_0.7 runs for the year 2012. Differences in amplitude (G.1a) and phase (G.1b). The positive differences (red) denote that the March amplitude is larger/phase is leading than September, while negative differences (blue) denote the opposite.

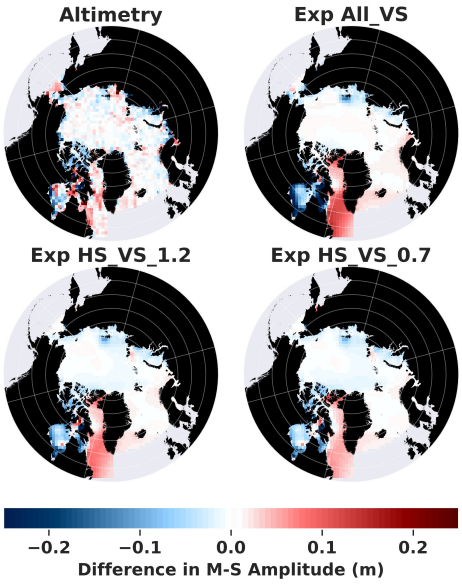

(a)

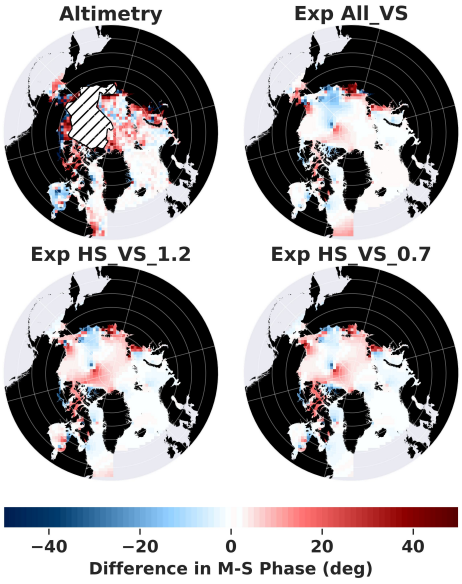

(b)

Figure G.2.: Seasonal Modulation of M_2 tide quantified as March-September differences in amplitude and phases for the altimeter-derived product and the Exp All_VS, Exp HS_VS_1.2 and Exp HS_VS_0.7 runs for the year 2017. Differences in amplitude (G.2a) and phase (G.2b). The positive differences (red) denote that the March amplitude is larger/phase is leading than September, while negative differences (blue) denote the opposite.

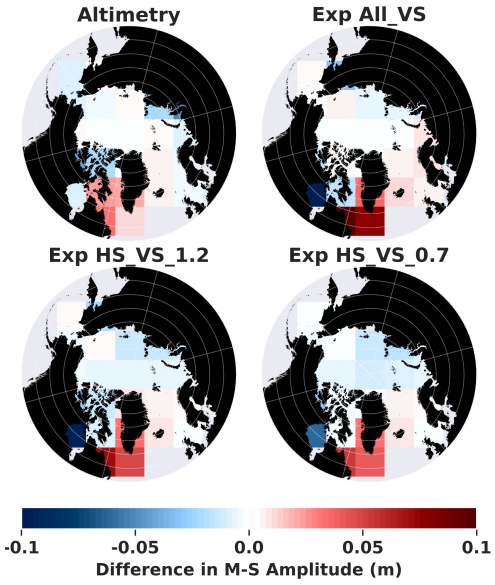

(a)

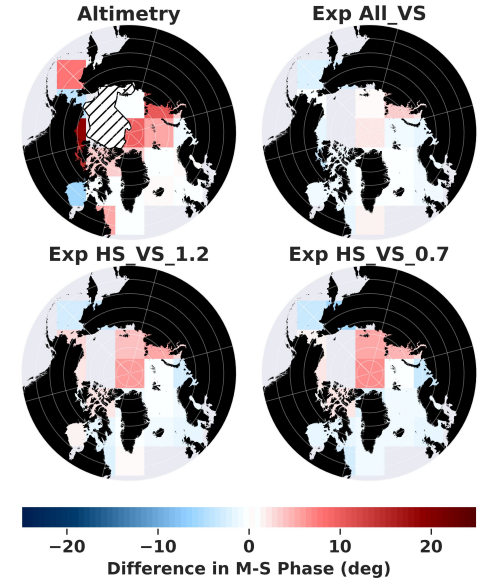

(b)

Figure G.3.: March-September differences of M_2 tide on a coarse grid for the altimeter-derived product and the Exp All_VS, Exp HS_VS_1.2 and Exp HS_VS_0.7 runs for the year 2019. Differences in amplitude (G.3a) and phase (G.3b). The positive differences (red) denote that the March amplitude is larger/phase is leading than September, while negative differences (blue) denote the opposite.

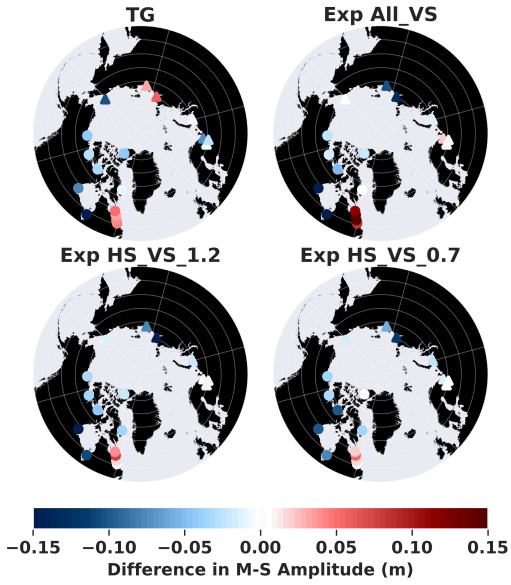

(a)

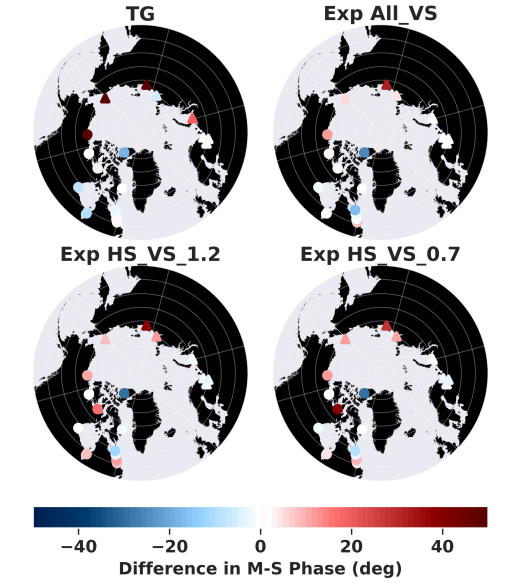

(b)

Figure G.4.: Seasonal Modulation of M_2 tide quantified as March-September differences in amplitude and phases for the TG-derived product and the 3 model runs (Exp All_VS, Exp HS_VS_1.2 and Exp HS_VS_0.7) for the year 2012. Differences in amplitude (G.4a) and phase (G.4b). The positive differences (red) denote that the March amplitude is larger/phase is leading than September, while negative differences (blue) denote the opposite. The circles correspond to CHS data and triangles correspond to Kulikov et al., 2020 dataset.

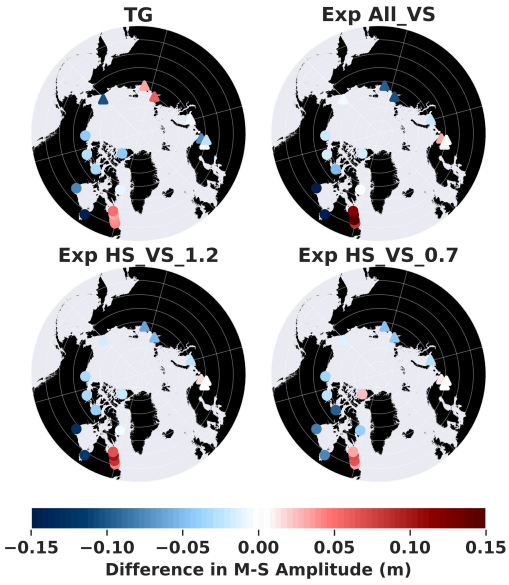

(a)

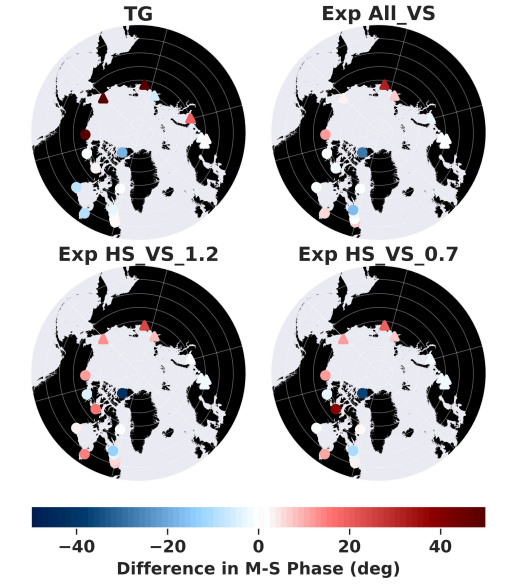

(b)

Figure G.5.: Seasonal Modulation of M_2 tide quantified as March-September differences in amplitude and phases for the TG-derived product and the 3 model runs (Exp All_VS, Exp HS_VS_1.2 and Exp HS_VS_0.7) for the year 2017. Differences in amplitude (G.5a) and phase (G.5b). The positive differences (red) denote that the March amplitude is larger/phase is leading than September, while negative differences (blue) denote the opposite. The circles correspond to CHS data and triangles correspond to Kulikov et al., 2020 dataset.

APPENDIX H.

COMPARING SEA ICE PARAMETERS FROM REMOTE SENSING PRODUCTS

We compared the concentration and thickness of sea ice from different remote sensing products to evaluate their efficacy. Sea ice concentration data were obtained from EUMETSAT Ocean and Facility, 2022 (OSISAF-450a product), and sea ice thickness data were obtained from Landy et al., 2022. We compared the data output for March 9, 2012, and September 8, 2012, from both datasets, as these were the matching dates we could find in our simulation years of 2012, 2017, and 2019. No monthly averages from these products were available.

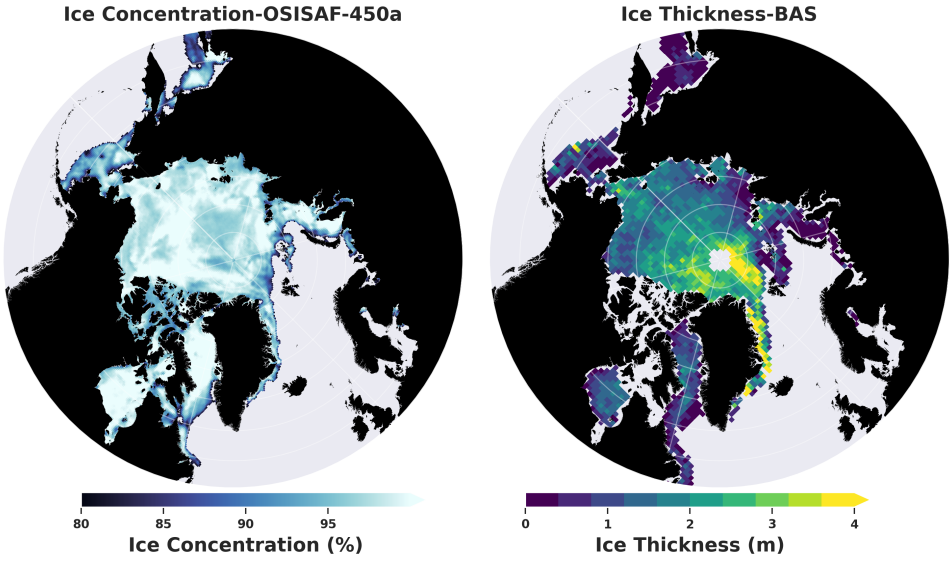

Figure H.1.: Sea ice concentration and thickness obtained from two different observation products for March 9, 2012. The concentration is derived from the OSISAF-450a product, while the sea ice thickness is from Landy et al., 2022, which evaluates thicknesses using CryoSat-2. BAS refers to the British Antartic Survery as this product was released by them.

From the sea ice thickness and concentration plots (Figure H.1), data gaps were

observed in the sea ice thickness product, particularly in the Canadian Archipelago, Hudson Bay, and Hudson Strait. These regions are significant in the context of sea ice-induced dissipation. The comparison for September (summer) also revealed mismatches between the concentrations and thickness data (Figure H.2).

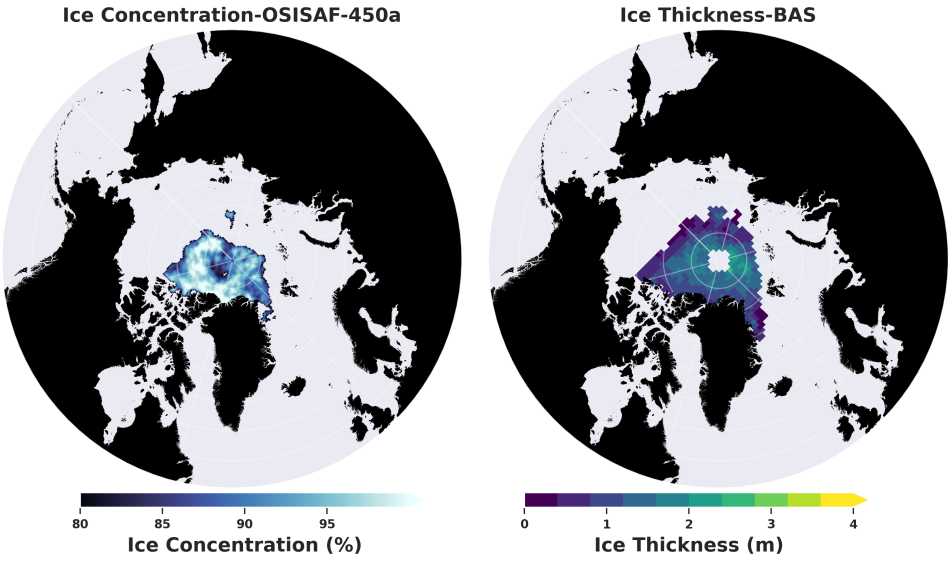

Figure H.2.: Sea ice concentration and sea ice thickness obtained from two different observation products for September 8, 2012. The concentration is obtained from OSISAF-450a product. The sea ice thickness is obtained from Landy et al., 2022 which evaluates thicknesses from CryoSat2. BAS refers to the British Antartic Survery as this product was released by them.

Further comparisons were made with a sea ice thickness dataset from SMOS and CryoSat-2 provided by AWI (CS2SMOS product Ricker et al., 2017). This dataset, available only for March, provided monthly averages.

The monthly average from CS2SMOS (Figure H.3) when compared with the sea ice concentration on March 9, 2012 from OSISAF-450a showed that for the sea ice concentration from the Bering Sea, there was no corresponding sea ice thickness in the CS2SMOS product. Additionally, the thickness product missed some regions in the Canadian Archipelago.

This analysis highlights the potential data mismatches and spatio-temporal challenges associated with using remote sensing products. However, with improvements in remote sensing technologies, it is expected that future products will provide better quality data with the required spatio-temporal coverage, allowing for their direct use in place of model-based products in our new parameterisation.

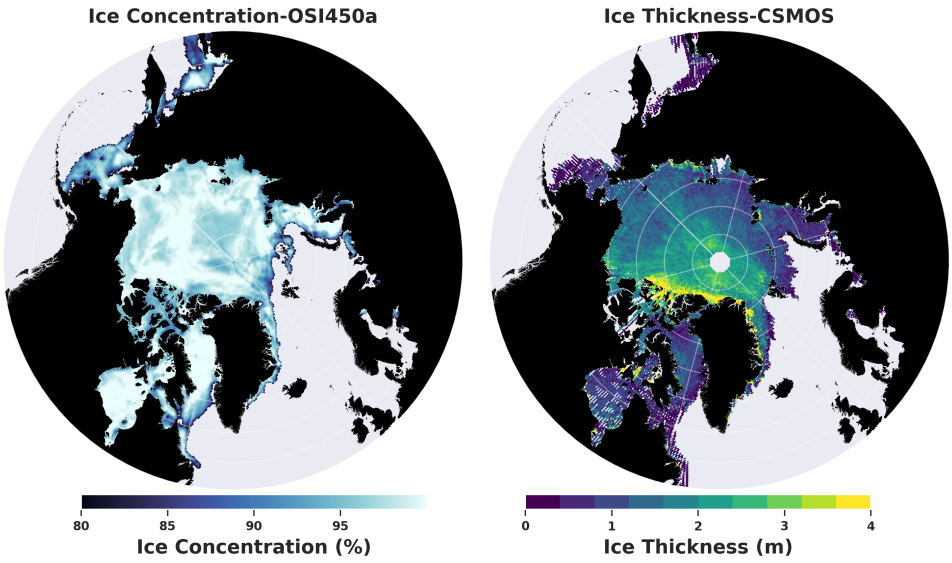

Figure H.3.: Sea ice concentration and sea ice thickness obtained from two different observation products for March 9, 2012. The concentration is obtained from the OSISAF-450a product. The sea ice thickness is obtained from the CS2SMOS product, which evaluates thicknesses from CryoSat-2 and SMOS and provides monthly averages.

APPENDIX I.

ADDITIONAL BARENTS SEA RESULTS

This appendix corresponds to the additional buoy-derived estimation from Chapter 5. Here we show the actual estimates of the tidal current constituents for the Buoy 03 and Buoy 16 at their median location in a tabular format.

Table I.1.: Tidal constituent estimates with the MdF method applied to Buoy 03 and corresponding GTSM values at the buoy median location. Amplitudes are in m/s and phases are in degrees.

	U				V			
	GTSM		Buoy 03		GTSM		Buoy 03	
	Amp	Ph	Amp	Ph	Amp	Ph	Amp	Ph
M_2	0.17	260	0.22	267	0.14	352	0.19	358
S_2	0.03	259	0.03	256	0.02	349	0.02	344
O_1	0.01	196	0.008	61.1	0.017	267	0.01	300
K_1	0.06	320	0.07	487	0.07	110	0.08	124

Table I.2.: Tidal constituent estimates with the MdF method applied to Buoy 16 and corresponding GTSM values at the buoy median location. Amplitudes are in m/s and and phases are in degrees.

	U				V			
	GTSM		Buoy 16		GTSM		Buoy 16	
	Amp	Ph	Amp	Ph	Amp	Ph	Amp	Ph
M_2	0.19	2590	0.27	266	0.16	357	0.24	318
S_2	0.03	271	0.03	254	0.02	166	0.02	135
O_1	0.01	248	0.01	32	0.01	70	0.008	319
K_1	0.05	25	0.07	45	0.07	112	0.1	132

ACKNOWLEDGEMENTS

This is the moment to reflect informally on the PhD journey. The last few years have been wonderful, filled with many ups and downs. The ups were motivating and mentally stimulating, while the downs were equally challenging, testing my mental resilience. Throughout these highs and lows, I was fortunate to have the support of family, friends, teachers, advisors, and support staff who celebrated my successes and backed me during difficult times. I would like to express my gratitude to each and every one of them.

First and foremost, I want to thank my promoter and daily supervisor, Martin Verlaan. I am grateful for the opportunity he provided and his constant support throughout this process. Every discussion with him was a learning experience, and his thought process and approach to problem-solving have significantly contributed to my development as an independent researcher. Next, I extend my heartfelt thanks to Cornelis Slobbe, my co-supervisor, who was equally involved in this thesis. His approach to writing with precise formulations has helped me hone my paper-writing skills. I will also cherish our informal discussions about life in general. I am also grateful to my promoter from CiTG, Roland Klees. His feedback has greatly improved the technical quality and language of this work.

I would like to express my sincere gratitude to Julie Pietrzak, Roderik van de Wal, Henk Schutelaars, and Pieter Smit for being my committee members. Their time in reviewing this thesis and providing valuable suggestions is greatly appreciated.

During this PhD process, we had weekly meetings with supervisors and colleagues from similar projects. I am particularly grateful to Inger, Henrique, Yosra, and Frithjof for their discussions and input, as well as for our outings, like the memorable wakeboarding adventure! Inger, we have been co-partners in the FAST4NL project, and I am grateful for all our long discussions and your help with even the silliest questions. Furthermore, I would also like to thank Jelmer Veenstra from Deltares, who was always ready to assist with technical challenges related to DFlow-FM and other operational aspects at Deltares.

Beyond those directly involved in my PhD work, there were many wonderful people at DIAM whom I would like to thank. To my current and former PhD friends-Avelon, Senlei, Xiaohui, Zhen, Feyza, Donna, Marco, Merel, Andrea, Marieke, Frederik, Matthijs[2]–and fellow colleagues at the MP group, thank you for all those coffee chats and outings. To Avelon, thank you for the help in the Dutch translation of the summary of this thesis. During my PhD, I was part of the SIAM Student Chapter board, the University PhD council, and the PhD Forum. I am especially grateful to the people I met in these forums; I truly enjoyed the countless meetings and discussions. These experiences provided me with a deeper insight into PhD life and the processes across the university while also hon-

ing my managerial, organizational, and communication skills.

At DIAM, I was fortunate to have people who supported me in managing the operational aspects of this PhD. I am grateful to Dorothee and Evelyn for arranging countless things like printing posters, managing budgets, getting forms signed, etc. Without them, it would have been a hassle, and they were always welcoming and ready to help. I am also grateful to Kees Lemmens for providing me with the opportunity to be a teaching assistant for the PDE course and for giving me the platform to teach the course while providing constructive feedback.

At TU Delft, apart from DIAM I had a strong support system in my friends. Niels, you have been there even before my PhD journey began and have seen it all. I am grateful for your presence throughout this process, for being a patient listener, our coffee chats, fun outings and above all, your unique Dutch perspective to things. Henrique, you were the first person Martin introduced me to, during the PhD, and we transitioned from being colleagues to friends. Our conversations have always been enlightening, with your immense breadth of knowledge turning every talk into a 'today I learned' session. Thank you for being there during this process and for our incessant conversations on PhD life. Niels and Henrique, special thanks for agreeing to be my paranymphs and for helping me arrange things for this defense. Andres, my ever-cheerful friend. I will never forget the summer school in Romania, which forged our lifelong friendship. Your calming presence was a much-needed comfort during difficult times, and your equally fun party spirit and those classic dance moves are unforgettable.

Outside of TU Delft and the PhD life, I had a wonderful group of friends with whom I could unwind and relax. This was particularly helpful in reminding me that there is more to life than just the PhD. I would like to thank my friends Nihar, Palash, Sakshi, Aarzu, Yash, Sukanya, Rajesh, Chinmay, Shreyas, Devendra, Vedangi, Sneha, Zoë, Shobhit, Jenny, Marco, and Sjors. Our parties, meetups, and festivals provided the much-needed breaks to reset my mind. Special thanks to Sneha for helping me in the cover layout of this thesis. In India, I am grateful to Amar and Nikita, who were always there for me during tough times, ready to listen to my rants about PhD challenges and life in general, and offering calming advice.

Finally, my family has been my main source of support. My sisters, Swapna and Sonal, have stood by me like a rock throughout my entire life. Their work ethic and steadfastness in the face of adversity have been a constant source of motivation for me. Thank you both.

आई आणि बाबा, पीएचडी करण्यासाठी मला समजावणारे तुम्हीच पहिले व्यक्ती होता. संशोधन करावे कि नोकरी घ्यावी या बद्दल मला शंका असताना, तुमच्या दृढ विश्वासानेच मला आत्मविश्वास मिळाला. आई, तुझ्याकडून मी कष्ट आणि शिस्त यांचे महत्व शिकलो. बाबा, तुम्ही मला कामात संपूर्णता आणणे शिकवले, जरी त्याचा अर्थ काम हळू अथवा सावकाश करणे असले तरी. या स्किल्स माझ्या रीसरच मध्ये खूप आवश्यक ठरल्या आहेत. तुम्ही दोघांनी दिलेले मार्गदर्शन, मी कसे वागावे अथवा वावरावे आणि कोणत्या गोष्टींशी सावध राहावे हे फार महत्वाचे होते आणि या तश्या लाइफ स्किल्स आहेत. धन्यवाद

तुम्हा दोघांचे.

Last but not least, I would like to extend my deepest gratitude to my best friend and wife, Sharayu. Words cannot fully express how grateful I am for your unwavering support throughout this PhD journey. I honestly cannot imagine having accomplished this without you by my side. We both know that this PhD was a joint effort. Our talks most evenings focussed on my day at work even if at times repetitive you were still a patient listener. You provided me with strength during the challenging times and were always celebrating the achievements.

During this PhD journey, we also experienced significant milestones in our personal lives, including getting married, moving in together, and buying a house. You seamlessly took over many of my responsibilities without hesitation, understanding that I was sometimes preoccupied. For this, and for countless other acts of kindness and support, I am sincerely grateful. Also, thank you for helping me create the animated illustrations and the cover for this thesis.

Finally, I would like to acknowledge that this is not an exhaustive list of all the amazing people who have supported me along the way. To everyone who has played a role in this journey, thank you from the bottom of my heart.

CURRICULUM VITÆ

Amey Nandkumar VASULKAR

Amey Vasulkar was born on March 5, 1993, in Pune, India. From 1998 to 2008, he attended Rosary High School for his primary and secondary education. He then attended Sir Parshurambhau Junior College from 2008 to 2010, specializing in Science and Technology. He pursued a Bachelor of Technology in Mechanical Engineering at COEP Technological University from 2011 to 2014. During this time, he developed an interest in Computational Science and Engineering, which he further explored the next couple of years in the role of a Design and Analysis Engineer at Tata Technologies.

In 2016, seeking to deepen his knowledge in the field, he enrolled in the COSSE program for his masters studies. He began his studies at TU Berlin, focusing on Scientific Computing courses, and continued at TU Delft. His master's thesis concentrated on Numerical Methods for solving coupled elliptic PDEs and ODEs. This work led to two masters degrees: one in Scientific Computing from TU Berlin and another in Applied Mathematics from TU Delft.

His experiences during his master's thesis inspired him to continue research and remain in academia. He began a PhD program with a focus on mathematical modeling and practical applications of data. He joined the Mathematical Physics group at DIAM, TU Delft, under the supervision of Prof. Dr. ir. Martin Verlaan and co-supervision of Dr. ir. Cornelis Slobbe. The PhD was part of the project Forecasting Arctic Surges and Tides for the Netherlands (FAST4NL) (https://fast4nl.nl/)

List of Publications

- Bij de Vaate, I., Vasulkar, A. N., Slobbe, D. C., & Verlaan, M. (2021). The Influence of Arctic Landfast Ice on Seasonal Modulation of the M2 Tide. *Journal of Geophysical Research: Oceans, 126*(5), e2020JC016630. https://doi.org/10.1029/2020JC016630

- Vasulkar, A., Verlaan, M., Slobbe, C., & Kaleschke, L. (2022). Tidal dissipation from free drift sea ice in the Barents Sea assessed using GNSS beacon observations. *Ocean Dynamics, 72*(8), 577–597. https://doi.org/10.1007/s10236-022-01516-w

- Vasulkar, A., Verlaan, M., Slobbe, C., & Kulikov, M. (2024). Modelling the effect of sea ice in an ocean tide model. *Ocean Modelling, 190*, 102405. https://doi.org/10.1016/J.OCEMOD.2024.102405

- Vasulkar, A., Verlaan, M., & Slobbe, C. (2024). Deriving Tidal Constituent Estimates from GNSS Buoy Data in the Arctic. *AGU: Earth and Space Science, Under Review*

List of Conference Presentations

Oral Presentations

- Vasulkar, A.N., Verlaan, M., and Slobbe, D.C.: Two Step Calibration of a regional tidal model. Presented at 8^{th} International Symposium on Data Assimilation (ISDA 2022). Colorado State University, Fort Collins, Colorado, USA, June 6th-10th, 2022.
- Vasulkar, A.N.: How to include sea ice in a tidal model? Presented at COSSE Workshop Meeting 2022. TU Delft, Netherlands, February, 2022
- Vasulkar, A.N., Verlaan, M., Veenstra, J., and Slobbe, D.C. Inclusion of sea ice induced seasonal modulation in a tidal model. AGU Fall Meeting 2021, id: OS33A-04. New Orleans, LA, 13-17 December 2021.
- Vasulkar, A.N., Verlaan, M., and Slobbe, D.C.: Towards the inclusion of sea-ice into a global tidal model. Presented at vEGU21. 1930 April 2021. https://doi.org/10.5194/egusphere-egu21-15359
- Vasulkar, A.N., Kaleschke, L., Verlaan, M., and Slobbe, D.C.: Analysis of tidal sea-ice movement using a drifting ice beacon array in the Barents Sea. Presented at EGU20. Online. 48 May 2020 https://doi.org/10.5194/egusphere-egu2020-7544

Poster Presentations

- Vasulkar, A.N., Verlaan, M., and Slobbe, D.C.: Modeling the effect of sea ice in a tidal model. Presented at Netherlands Polar Programme Symposium 2022. The Hague. 19 May, 2022.
- Vasulkar, A.N., Verlaan, M., and Slobbe, D.C.: Modeling the effect of sea ice in a tidal model. Presented at Living Planet Symposium 2022. Bonn, Germany. 23-27 May 2022.
- Vasulkar, A.N., Verlaan, M., and Slobbe, D.C.: Towards understanding the impact of declining sea ice on tides. Presented at Netherlands Polar Programme Symposium 2022. The Hague. 21 November, 2019.
- Vasulkar, A.N., Verlaan, M., and Slobbe, D.C.: Impact of Arctic ice decline on tides and surges. Presented at 9th International Workshop on Sea ice Modelling, Data Assimilation and Verification organized by IICWG. Bremen, Germany. 17-19 June 2019.